Dissertation zur Erlangung des Doktorgrades

der Fakultät für Chemie und Pharmazie

der Ludwig-Maximilians-Universität München

Expanding the Scope of Single-Molecule Energy Transfer with Gold Nanoparticles and Graphene

Johann Robert Bohlen

aus

Bremerhaven, Deutschland

2022

Erklärung

Diese Dissertation wurde im Sinne von §7 der Promotionsordnung vom 28. November 2011 von Herrn Prof. Dr. Philip K. J. Tinnefeld betreut.

Eidesstattliche Versicherung

Diese Dissertation wurde eigenständig und ohne unerlaubte Hilfe erarbeitet.

München, den 31.01.2022 Johann Robert Bohlen

Dissertation eingereicht am: 31.01.2022

1. Gutachter: Prof. Dr. Philip K. J. Tinnefeld

2. Gutachter: Prof. Don C. Lamb, PhD

Mündliche Prüfung am: 10.03.2022

Abstract

Förster resonance energy transfer (FRET) is a common tool to measure the distances between a donor and an acceptor fluorophore and is employed as a spectroscopic ruler. This non-radiative energy transfer is utilized to not only measure distances but also to observe dynamics in the field of biophysics and medicine. However, main limitations of FRET are the limited time resolution and working range between donor and acceptor molecules of 10 nm. To increase the application of FRET, this limitation can be circumvented by the introduction of different materials in the close proximity. For characterization of the altered distance dependence, a precise distance control between the dyes and the applied material is required, which here is provided by the DNA origami technique. In DNA origami, DNA self-assembles into programmable, complex, and robust structures, which can be easily modified with dyes and other entities with nanometric control.

DNA origami nanoantennas constructed of a pair of gold nanoparticles have recently been introduced to substantially increase the obtainable fluorescence signal that yields a higher time resolution in biophysical single-molecule FRET experiments. In this context, it is crucial to understand the influence of the gold nanoparticles on the FRET process itself. In this work, gold nanoparticles are placed next to FRET pairs using the DNA origami technique (see publication I). A measurement procedure to accurately determine energy transfer efficiencies is established and reveals that in the intermediate coupling regime, the energy transfer efficiency drops in the presence of nanoparticles whereas the energy transfer rate constant from the donor to the acceptor is not significantly altered.

Next, graphene is introduced to increase the range of energy transfer. Graphene is a 2D carbon lattice, which can also be employed as an unbleachable broadband acceptor without labeling. To understand the principles of the energy transfer between a fluorophore and the graphene surface, the distance dependence of the energy transfer from a fluorophore to graphene is investigated (see publication II). As such experiments require high quality graphene surfaces, a cleaning and transferring procedure to generate reproducible graphene-on-glass-coverslips is established (see publication III) and characterized by different spectroscopic methods. Finally, the full potential of graphene-on-glass coverslips as microscopy platforms are highlighted by adopting graphene in the fields of biosensing, biophysics and super-resolution microscopy (see publication IV). The designed biosensors are capable to detect a DNA target, a viscosity change, or the binding of a biomolecule. In addition, FRET between two dyes is expanded by additional graphene energy transfer (GET) that reveals the relative orientation of the FRET pairs to the graphene surface. Finally, GET is used in super-resolution experiments to reach isotopic nanometric 3D-resolution and track a single fluorophore that undergoes 6-nm

jumps. The developed techniques and assays have the potential to become the basis for numerous new applications in single-molecule sensing, biophysics, and super-resolution microscopy.

Table of Contents

1. Introduction 1
1.1. Extending FRET with Plasmonic Nanoparticles 2
1.2. Graphene Energy Transfer 3
1.2.1. Quantitative GET 4
1.2.2. Transfer and Cleaning of Graphene 4
1.2.3. Application of GET 5
1.2.4. Biosensor 5
1.2.5. Combining GET and FRET 6
1.2.6. 3D Super-Resolution 7
2. Theoretical Background 9
2.1. Fluorescence 9
2.2. Förster Resonance Energy Transfer 12
2.3. Graphene and Graphene Energy Transfer 14
2.4. Plasmonic Nanoparticles 16
2.5. Dye Stabilization 19
2.6. DNA Origami Technique 21
3. Material and Methods 23
3.1. Confocal Microscopy 23
3.2. Wide-Field Microscopy 24
3.2.1. Super-Resolution and DNA-PAINT 25
3.3. Atomic Force Microscopy 28
4. Summary of Publications 29
4.1. Publication I: Plasmon-assisted Förster resonance energy transfer at the single-molecule level in the moderate quenching regime 29
4.2. Publication II: Distance Dependence of Single-Molecule Energy Transfer to Graphene Measured with DNA Origami Nanopositioners 31
4.3. Publication III: Graphene-on-Glass Preparation and Cleaning Methods Characterized by Single-Molecule DNA Origami Fluorescent Probes and Raman Spectroscopy 32

4.4. Publication IV: Graphene Energy Transfer for Single-Molecule Biophysics, Biosensing, and Super-Resolution Microscopy 33

5. Conclusion and Outlook 36

6. References.....44

7. Calculation of the Shifted FRET Distance in Presence of a NP 59

8. Publication.....60

8.1. List of Publications 60

8.2. List of Conference Contribution 61

8.3. Publication I.....62

8.4. Publication II.....81

8.5. Publication II.....111

8.6. Publication IV 163

9. List of Figures.....226

10. Table of Abbreviations 230

11. Acknowledgement 232

1. Introduction

Resonance energy transfer in nature e.g. occurs in the process of photosynthesis, where light is guided to a photosynthetic reaction center by chromophores.[1–4] The principle of photosynthesis is a prominent example for the interest of mankind to disassemble objects, understand their basic functions, and adapt them for their own purpose. Thus, for example, solar cells are based on the fundamental understanding of energy transfer such as in photosynthesis. During the last decades, non-radiative resonance energy transfer has been established in the field of microscopy. Theodor Förster described the distance dependence of a non-radiative energy transfer between a donor and a red-shifted acceptor fluorophore, the so-called Förster resonance energy transfer (FRET). Besides the spectral overlap between the emission spectrum of the donor and the absorption spectrum of the acceptor, also the dipole orientations of the fluorophores and the distance between the donor and the acceptor dye are important to observe FRET.[5] As FRET is decaying inversely with the sixth power of the donor-acceptor distance, it can be utilized as a spectroscopic ruler[6,7] in the field of biology and nanoscience to determine distances between the donor and acceptor.[8–14] However, a drawback of this assay is the limitation of the donor-acceptor distance to 10 nm, as distances beyond 10 nm show only marginal energy transfer. To overcome this drawback, new approaches have to be developed to extend FRET beyond a donor-acceptor distance of 10 nm. Previous work focused on the design of complex donor-acceptor constructs, like in multi chromophoric FRET cascades[15–18] or a variety of acceptor or donor fluorophores to increase the FRET efficiency.[19–21] However, this kind of systems suffer from complex sample preparation, sophisticated microscopes, and the challenge to find suitable fluorophores for FRET. These issues make multi chromophoric systems not practicable for the implementation in biological systems. Therefore, in this thesis, the energy transfer of fluorophores to unbleachable acceptors is investigated, and the results are applied to the field of biosensors, biophysics, and super-resolution.

In our single-molecule experiments, a precise positioning of the fluorophores to each other as well as to the examined unbleachable acceptor is necessary. This positioning is guaranteed by the DNA origami technique, which is based on the folding of DNA into a predesigned structure at the nanoscale.[22] In more detail, a circular single stranded (ss) DNA scaffold with the length of about 8000 nt is folded into a defined shape by an excess of 200 ss oligonucleotides (staple strands) with a length of about 60 nt in a buffered environment. The advantages of the self-assembled DNA origami structures are high yields, the possibility to modify the DNA origami structures with e.g. dyes, biomolecules, or binding sites for NPs, and a nanometric-controlled positioning of these modifications. DNA origami structures are, for example, used as nanorulers in super-resolution microscopy to determine the possible resolution of a setup.[23–26]

1.1. Extending FRET with Plasmonic Nanoparticles

An unbleached acceptor studied in this work is a plasmonic nanoparticle (NP). NPs are much smaller than the wavelength of light and their electrons start to oscillate when they get excited with light, the so-called localized surface plasmon resonance (LSPR). A nearfield coupling of the excited NP and a fluorophore takes place when the fluorophore and the NP are in close proximity to each other.[27–30] This coupling, which depends on the orientation between dye, NP, and excitation laser beam, can either lead to an increase[31–35] or a quenching of the fluorescence intensity[36–38] (see Figure 1). Furthermore, the radiative and non-radiative rate constants are altered, which also affects the fluorescence lifetime and quantum yield.[31,39] The influence of the NP depends on the material, shape, and diameter of the NP itself. A common method to increase the influence of an NP on the fluorophore is the coupling of two NPs. This coupling results in the formation of a hot spot of the electric field between the NPs,[34] which, for example, can be used to increase the signal-to-noise ratio in bioassays.[33,35]

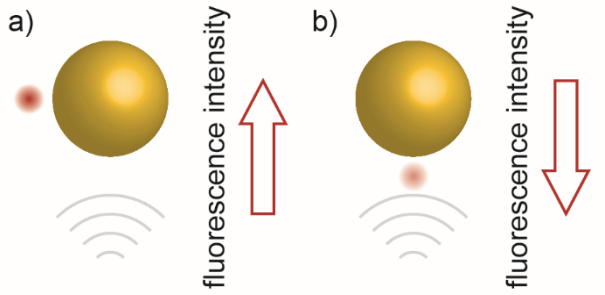

Figure 1: Influence of different orientations between dye, NP, and excitation laser beam. a) When the dye and NP are orthogonal orientated to the propagation direction of the laser beam the fluorescence intensity is enhanced. b) The orientation of the dye and NP aligned with the propagation direction of the excitation laser beam results in a quenching of the fluorescence intensity.

Furthermore, a great effect of nanoantennas is the ability to photostabilize dyes,[31] which leads to a higher time resolution. This can be used to extend the application of FRET. A fundamental understanding of FRET close to an NP is essential for a later application of FRET and NPs. Numerous studies[40–46] already investigated FRET close to plasmonic structures and reported on different results with regard to the FRET efficiency and rate constant. This on the one hand originates from the different designs of the assay, like donor-acceptor distances as well as material and shape of the nanomaterials. On the other hand differences arise from a variety of uncertainties faced in the previous works. One major uncertainty, for example, is the precise placement of the FRET pair in a defined distance to the plasmonic structure, which results in a heterogeneous fluorescence enhancement. The orientation of the NP-FRET assay to the excitation laser beam is another measure, which can yield an enhancement[31–35] or quenching of the fluorescence intensity[36–38] (see Figure 1). Furthermore, ensemble and solution meas-

urements are difficult to analyze in terms of distinguishing between fully and partially assembled assays like assays without donor, acceptor, or NP. To gain accurate FRET values, correction factors have to be extracted from the measurements. The correct and precise extraction of these factors together with the complex influence of the NP on the fluorophores by radiative and non-radiative processes, are important to gain reliable results.

The task of this work is to circumvent the aforementioned issues by combining single-molecule FRET experiments with an NP on a rectangular DNA origami structure (see chapter 4.1 and related publication I). The DNA origami structure spaces the donor and the acceptor as well as the FRET pair and the NP with a defined distance. Additionally, the NP and FRET pair are located on different sides of the DNA origami structure to avoid contact quenching between the dyes and the NP. An immobilization of the DNA origami structures to the glass surface guarantees the same orientation between the fluorophore-NP construct and the excitation laser beam, which results in homogenous data compared to previous studies. Our single-molecule experiments make it easy to distinguish between fully or only partially assembled nanostructures, like donor only, acceptor only, and without NP. Furthermore, we applied the acceptor bleaching approach for data acquisition, which alternates between donor and acceptor excitation on the second time scale. This method has the advantage that no prior knowledge of the system is needed. The alternating excitation enables the extraction of the individual influence of the NP on the donor in presence and absence of the acceptor, as well as on the acceptor only. Based on the controlled and more homogenous sample preparation presented here, the influence of different sized NPs on a static FRET is studied. From the fluorescence lifetime and intensity-based data, the FRET efficiency and rate constant is extracted and compared to numerical simulations.

1.2. Graphene Energy Transfer

Besides NPs also graphene, a monolayer of carbon, is a promising candidate as an unbleachable acceptor. Graphene has outstanding mechanical strength as well as electrical, and thermal conductivity.[47] In terms of absorption, the material shows an additive behavior in which an additional absorption of 2.3% per layer in the visible (vis) and infrared (IR) range is described.[48–53] Therefore, graphene is not only an unbleachable but also a broadband acceptor in the visible and infrared range with a working range up to 40 nm between a dye and the graphene surface.[9] A fluorophore in close proximity to the graphene surface experiences a non-radiative energy transfer from the fluorophore to the graphene surface, the so-called graphene energy transfer (GET).

1.2.1. Quantitative GET

For the implementation of GET in single-molecule experiments, a fundamental understanding of the energy transfer from the fluorophore to the graphene surface is crucial. In previous work the distance dependence between one fluorophore and a graphene surface has already been measured and a decaying GET has been concluded, which is inversely proportional to the fourth power of the distance between the fluorophore and the graphene surface. But these works also reported different results of the characteristic distance, where the energy transfer efficiency is 50%.[51,54–57] The reason for these discrepancies on the one hand lies in the defined positioning of the fluorophore to the graphene surface. On the other hand, quenching effects from dye-dye interactions could occur due to dyes without a controlled spacing. And last the use of fluorophores with heterogenous photophysical properties gives rise to uncertainties.

In our approach (see chapter 4.2 and related publication II) the stated problems are circumvented by the implementation of DNA origami structures, which enable a controlled spacing of the dyes to the graphene surface. Additionally, the high selectivity of DNA origami structures ensures that only one fluorophore is attached, which avoids dye-dye interactions. The implementation of organic fluorophores guarantees homogenous photophysical properties. In our work three different DNA origami structures with in total six different distances between the graphene surface and the fluorophore are designed to confirm the distance dependence and to extract the distance where 50% of GET occurs. For the immobilization of the DNA origami structures on the graphene surface, we modify the DNA origami structures with pyrene labelled oligonucleotides. With this non-invasive binding via π-π stacking between the pyrene and the graphene surface the graphene properties are not influenced. Our fluorescence intensity and lifetime-based results are compared to calculations of a semi classical model.

1.2.2. Transfer and Cleaning of Graphene

Another critical point for the realization of GET experiments in the field of super-resolution or biophysics is the transfer of graphene from a graphene coated cupper foil to a glass coverslip and the cleaning of graphene from synthesis residues. Previous works show various ways to transfer the graphene,[58–61] but by applying these in our single-molecule experiments heterogeneous results are observed. Therefore, we combine existing protocols[59–65] and screen in total ten different methods to achieve graphene-on-glass-coverslips with a quality for single-molecule experiments, the so-called single-molecule quality (see chapter 4.3 and related publication III). The quality control of these samples is performed with the combination of fluorescence lifetime imaging (FLIM),[66] Raman spectroscopy, and atomic force microscopy (AFM). The quality of the graphene-on-glass coverslips in FLIM measurements is verified by a static

dye at dye-graphene distance where 50% of energy transfer occurs. For further validation, a dynamic DNA origami sample can sense the distance dependent quenching from the graphene surface.

1.2.3. Application of GET

Our work of quantitatively analyzing GET[49] as well as transfer and cleaning of graphene with single-molecule quality[50] are fundamental for the implementation of GET in a broad range of interest. Our experiments (see chapter 4.4 and related publication IV) illustrate the easy application of graphene-on-glass-coverslips to answer questions, which previously needed complex microscopes and/or sample preparation. In first experiments, we use a two color assay to reveal if spectrally separated fluorophores at different distances to the graphene surface can be resolved at the same time. Furthermore, the orientation of a DNA origami structure to the graphene surface is validated with a two color assay. Moreover, we create a plethora of DNA origami samples to use GET as an acceptor in biosensor assays, in combination with FRET, and in the field of super-resolution to demonstrate the whole potential of graphene as a label free, unbleachable acceptor in the vis and IR range.

1.2.4. Biosensor

Biosensors are devices to detect e.g. biomolecules (target) like DNA or antibodies, which can have an optical readout.[67–69] A hairpin structure with an optical transduction mechanism, for example, is a simple biosensor with a binary readout, where in the beginning a fluorophore is close to a quencher and therefore is completely quenched. After the binding of a target that opens the hairpin structure, the fluorophore is switched to a “bright” state as it is spatially separated from the quencher, which disables the energy transfer between the fluorophore and the quencher (see Figure 2).[70,71] To increase the contrast, biosensors can also be placed in the hot spot region of a plasmonic dimer antenna to detect single-molecules even with a smartphone camera.[33,35] Fluorescence quenchers employed in bioassays, which could also be a FRET acceptor, can be replaced by graphene. Therefore, a bleachable acceptor gets substituted by an unbleachable acceptor. In our experiments two different DNA origami biosensors on graphene are implemented. The first biosensor has a binary readout, where in the beginning the fluorophore is quenched and after addition of the DNA target the fluorophore is less quenched, similar to the explained hairpin assay. In the second biosensor we checked for the influence of the surrounding medium of different viscosity and the influence of biomolecule binding on the diffusion behavior of a double stranded DNA tether. The advantages of GET over FRET or quencher-based assays are the increased distance range between donor and

acceptor of 40 nm (GET) compared to 10 nm (FRET and quencher), and the larger spectral range of GET ranging from the vis to the IR range. The larger working distance can be utilized to detect multiple targets at once, and the broad spectral range makes GET feasible as a biosensor for multiplex detection.

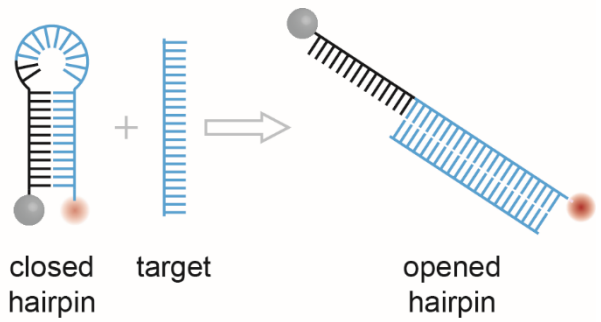

Figure 2: Hairpin as a biosensor. Before addition of the target the dye (red) is quenched by the quencher (grey). The target binds to the blue region of the hairpin and opens the hairpin, which separates the dye and quencher from each other that no energy transfer from the dye to the quencher occurs.

1.2.5. Combining GET and FRET

As discussed above FRET is limited to a range of approximately 10 nm, which can be expanded e.g. by additional donor and acceptor fluorophores. However, multi chromophoric FRET systems[15–21] suffer from a complex sample preparation, sophisticated microscopes, and it is challenging to find suitable fluorophores for FRET. While the difficulty in sample preparation is addressed by the DNA origami structures, graphene is a good substitute for the acceptor in FRET studies. In order to decrease the complexity of samples and microscopes, graphene is used as graphene-on-glass-coverslips. Furthermore, the combined information of GET and FRET in our experiments reveal the relative orientation of the donor and acceptor in space. Here, FRET resolves the distance between donor and acceptor, while from GET the distance to the graphene surface is extracted.

To illustrated the full power of combining GET and FRET, we designed static as well as dynamic FRET assays on DNA origami structures. The dynamic FRET sample is equipped with a dye labelled staple strand protruding from the DNA origami structure, which can transiently bind to two protruding binding sites on the DNA origami structure. Both binding sites differ by the distance to the graphene and the distance to the acceptor fluorophore, which leads to a different quenching of the donor fluorophore by GET and FRET in both positions. To observe the individual influence from the graphene surface to the donor and acceptor fluorophore and

therefore obtain reliable data the acceptor bleaching approach is used. With the help of fluorescence lifetime data, the influence of FRET to GET and *vice versa* is discussed.

1.2.6. 3D Super-Resolution

In FRET assays, the orientation between two dyes plays an important role but also the separation distance. The distances in FRET assays are very small with only a few nanometers. In conventional light microscopy, the distance of two emitters that can be resolved is limited by the Abbé criterion. The Abbé criterion states that the resolution or distance between two fluorophores is limited to half the excitation wavelength in the x/y plane and to the excitation wavelength in z. In single-molecule localization microscopy (SMLM) the Abbé criterion is circumvented by introducing blinking to the molecules. Each localization of a molecule is fitted, and a super-resolved image is gained.[72–74] With SMLM a resolution of 6 nm and lower in the x/y plane is achieved.[75–81] But an isotropic resolution in all three dimensions (x, y, and z) remains still challenging. Previous work[38,82,83] could not take the obstacle of isotropic resolution, only new more sophisticated microscopes are able to take this hurdle.[84] The drawbacks of previous works are difficult sample handling, the need of complex setups, calibration of the microscopes, and a low sensitivity of the methods.

We demonstrate the possibilities of GET in super-resolution microscopy with two different DNA origami structures. As a super-resolution method we utilize DNA-PAINT (point accumulation in nanoscale topography),[85] in which blinking of the fluorophores is achieved by the transient binding of dye labelled imager strands to binding sites at the structure of interest. While the resolution in the x/y-plane is achieved by the stochastic blinking, GET introduces a distance dependent fluorescence intensity quenching. This quenching facilitates a z-resolution with high accuracy. GET in combination with DNA-PAINT delivers the additional advantage that unspecific binding of the imager to the graphene surface is negligible because the imager is completely quenched. The first DNA origami sample investigated in this work has binding sites for DNA-PAINT imager strands at different distances to the graphene surface. Our second super-resolution method is the tracking of a single fluorophore. In order to realize the tracking, a DNA origami structure is modified with a protruding staple strand, which is labelled with a fluorophore and can transiently bind to three different binding sites at the DNA origami structure. To distinguish between the binding sites, they are placed at different distances to the graphene surface, which causes a different quenching to the fluorophore.

This work highlights the influence of unbleachable acceptors to dyes on the single-molecule level. These unbleacheable acceptors are applied to FRET, in the field of super-resolution, biophysics, and biosensing. Furthermore, the distance dependence of a fluorophore to the

graphene surface is investigated, and a protocol to obtain graphene-on-glass-coverslips with single-molecule quality is established. The results of this thesis set out the basis for further investigations in physics, biology, and material science. Examples on how to expand and improve the presented studies are discussed in the outlook.

2. Theoretical Background

This chapter gives a theoretical overview about the utilized methods in this work. Besides the basics of fluorescence (chapter 2.1), also FRET (Förster resonance energy transfer, chapter 2.2), GET (graphene energy transfer, chapter 2.3), plasmonic nanoparticles (chapter 2.4) and dye stabilization (chapter 2.5) are discussed. As a breadboard for placing fluorophores or NPs in close distance to each other, the DNA origami technique is introduced in chapter 2.6.

2.1. Fluorescence

In the Bohr atomic model, electrons are moving along quantized levels around the nucleus of the atom. Without any interaction the molecule is in the ground state (S_0) and can be excited with light of the energy E_{Photon} into a higher singlet state, this process is called absorption.

$$E_{Photon} = h\nu = \frac{hc}{\lambda} = hc\bar{\nu} \qquad (Eq. 2.1)$$

The energy E_{Photon} can be calculated from Plancks law (Eq. 2.1)[86] with the frequency ν, the wavelength λ or the wave number $\bar{\nu}$, the fundamental physical constant of the speed of light *c,* and the Planck constant *h*.[87]

Before the excitation process the molecule is in the vibrational ground state ($v'' = 0$) of the singlet (S_0) state. After absorption (Figure 3, continuous purple arrow) of a photon the molecule is excited to an energetically higher lying singlet state (S1 or higher) and can also change the vibrational state to a higher level. According to Kasha's rule fluorescence occurs from the lowest vibrational state of S_1 back to S_0.[88] Therefore, if the molecule is excited to a higher singlet state than S_1, it first has to relax to the lowest state of S_1 before emitting a photon. After internal conversion (waved green arrow) to the vibrational ground state of S_1, the molecule relaxes back to the singlet ground state S_0. This can either happen as a non-radiative (waved blue arrow) or radiative relaxation (continuous blue arrow), known as fluorescence. Another way to relax from the excited state (S_1) to the S_0 is *via* intersystem crossing (waved orange arrow) to the triplet state (T_1). After internal conversion (waved green arrow) to the vibrational ground state of T_1 the molecule can relax either radiatively as phosphorescence (continuous red arrow) or non-radiatively (waved red) by heat dissipation.[89]

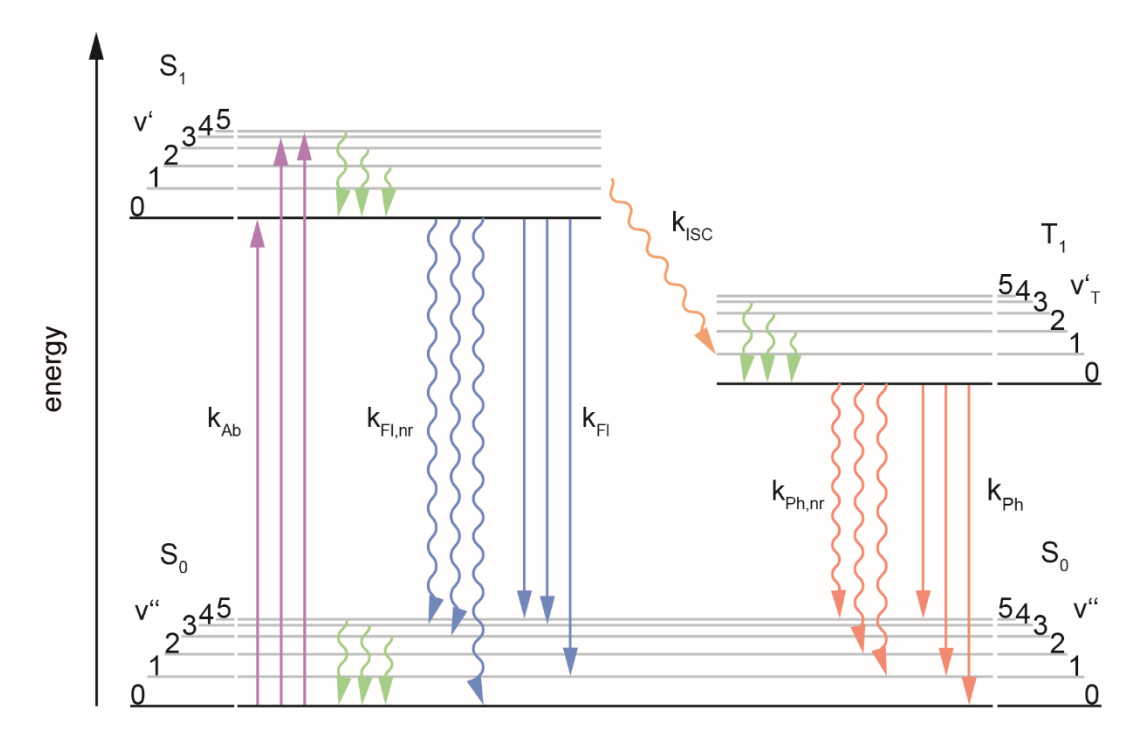

Figure 3: Jablonski diagram illustrating transition of a fluorescence molecule, including the singlet states S_1 and S_0 and the triplet state T_1 with the corresponding vibrational levels v. Besides the radiative transitions of absorption (purple arrow), fluorescence (blue arrow) and phosphorescence (red arrow), which are depicted as continuous lines, also non-radiative transitions in waved lines like internal conversion (green arrow) and inter system crossing (orange arrow) are shown. For a better overview, not all possible transitions as well as higher singlet and triplet states are illustrated.

Figure 3 illustrates all rate constants *k* that are connected to transitions, e.g. k_{ab} is the rate constant of the absorption. From the rate constants, the lifetime τ, which is the dwell time in a state can be determined. The lifetime can be calculated from the reciprocal of the rates depopulating the excited state. An example for the fluorescence lifetime τ_{Fl} is shown in (Eq. 2.2), including the rate constant of the fluorescence k_{Fl}, the non-radiative relaxation from the S_1 $k_{Fl,\,nr}$, and the intersystem crossing k_{ISC}.

$$\tau_{Fl} = \frac{1}{k_{Fl} + k_{Fl,nr} + k_{ISC}} \qquad (Eq.\,2.2)$$

As the names singlet and triplet might imply, both states have different spins. While the singlet states have an antiparallel spin, the triplet has a parallel spin. Due to the spin flip the transition probability from singlet to the triplet state and *vice versa* is low, which results in a longer lifetime of the triplet state in comparison to the singlet state. While the fluorescence lifetime (S_1) is in the range of 10^{-9}-10^{-8} s, the phosphorescence lifetime (T_1) is in the range of 10^{-3}-10^{0} s (detailed information on the fluorescence lifetime measurements can be found in chapter 3.1). The quantum efficiency is an indicator of how often a molecule relaxes *via* a specific transition. For example, the quantum efficiency of the fluorescence Φ_{Fl} is the fraction of molecules which undergo fluorescence to relax from the S_1 to the S_o and is shown in (Eq. 2.3.).[89]

$$\Phi_{Fl} = \frac{k_{Fl}}{k_{Fl} + k_{Fl,nr} + k_{ISC}} = k_{Fl}\,\tau_{Fl} \qquad (Eq.\,2.3)$$

The probability of a molecule to reach distinct vibrational states in an excited state is described by the Franck Condon principle.[90,91] This principle is based on the Born Oppenheimer approximation, which assumes that the heavier nucleus is rigid during excitation of the lighter electron.[92] Transitions between states are more likely the more the vibrational wave functions are symmetric to each other. In Figure 4 a)), for example, the symmetry or the overlap of the wave function (orange area) of *v''* = 0 and *v'* = 2 is higher than of *v''* = 1 and *v'* = 2, which makes the first transition more likely than the second. This leads to a higher intensity in the absorption spectrum (see Figure 4 b)). The absorption and fluorescence spectra also illustrate that the fluorescence spectrum compared to the absorption spectrum is shifted to higher wavelengths or lower energies, which is called Stokes shift. This on the one hand is caused by electronic relaxation from a higher excited state (Kasha's rule) or vibrational relaxation (internal conversion) where non-radiative transitions take place and energy is lost. On the other hand, the dipole of a molecule can change depending on the singlet state. A changed dipole in a higher excited state can lead to a rearrangement of the solvent molecules around the dye, which can either in- or decrease the energy of the singlet state and therefore blue or red shift the fluorescence with respect to the absorption.[93] The so-called mirror image between absorption and fluorescence (or phosphorescence) spectrum can also be explained by the Franck Condon principle, because it also states that the probability going from *v''* = 0 to *v'* = 1 is the same as going from *v'* = 0 to *v''* = 1, which explains similar intensities.[87,89]

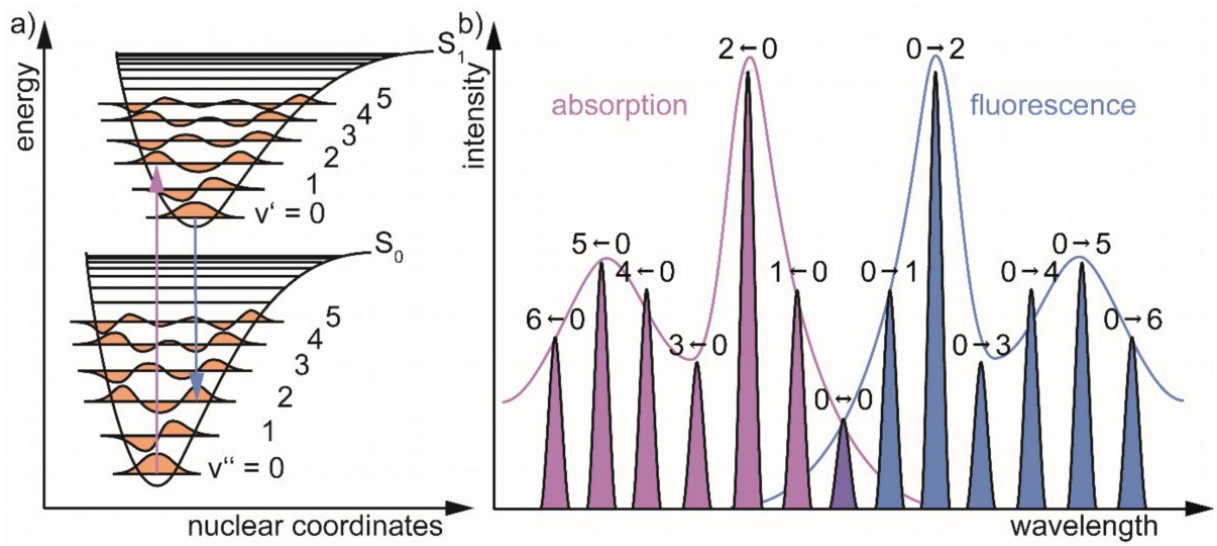

Figure 4: Schematic presentation of the Franck Condon principle. a) Transition of a molecule between to singlet states S_1 and S_0; including the vibrational wave functions illustrated in orange. b) Absorption and fluorescence spectra of a molecule as a results of a). In both figures the absorption is purple and the fluorescence is blue.

2.2. Förster Resonance Energy Transfer

The Förster resonance energy transfer (FRET) is a non-radiative energy transfer between a donor and an acceptor dye.[5] This simple, elegant, and easy to implement technique makes it possible to answer biological and medical questions regarding dynamics and distances at distances up to 10 nm.[8,11,13]

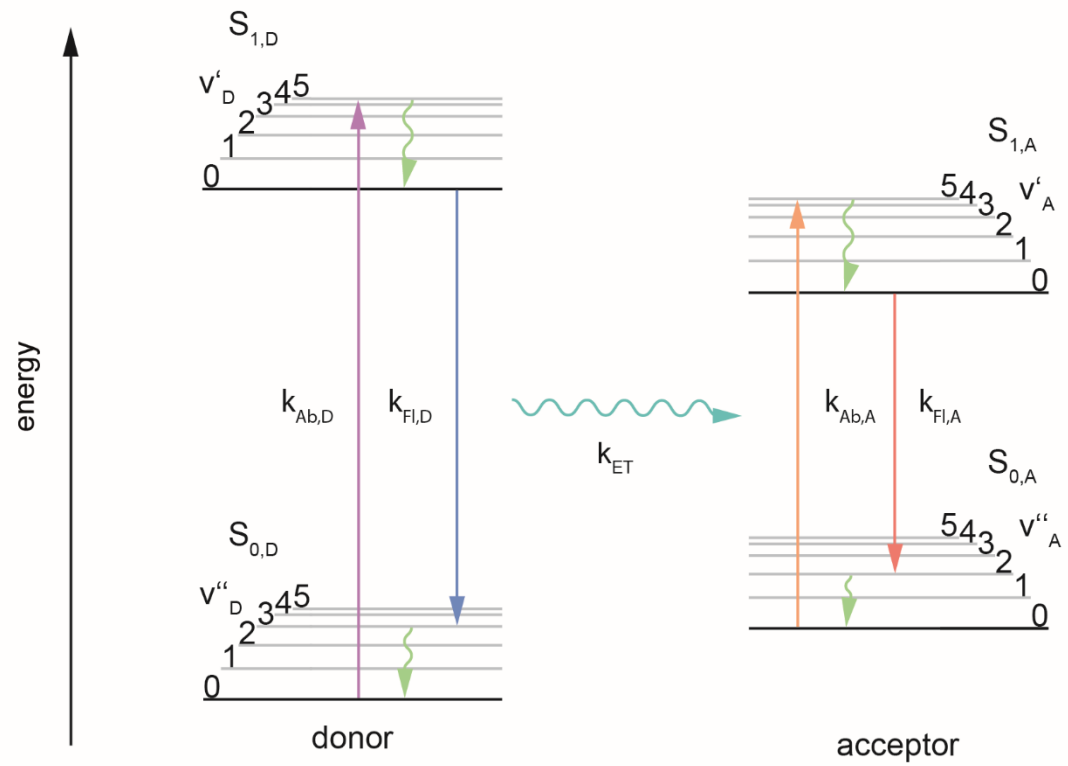

Figure 5: Jablonski diagram for Förster resonance energy transfer (FRET). Similar to Figure 3 the donor dye is excited through light absorption (continuous purple arrow) to a higher singlet state ($S_{1,D}$) and the molecule relaxes back to the singlet ground state $S_{0,D}$ via emission (continuous blue arrow) after internal conversion (waved green arrow). If another dye (acceptor) is in close proximity to the first dye (donor) an additional path is possible. Via non-radiative energy transfer the acceptor can get excited (continuous orange arrow) during the relaxation of the donor (waved turquois arrow). The excited acceptor ($S_{1,A}$) after internal conversion can relax radiatively (continuous red arrow) to the singlet ground state ($S_{0,A}$). For a better overview not all possible transitions as well as higher singlet states and vibrational levels are illustrated.

A Jablonski diagram with two dyes interacting *via* FRET is illustrated in Figure 5. First the donor is absorbing energy (continuous purple arrow) and populates the singlet excited state of the donor $S_{1,D}$. After internal conversion (waved green arrow) the molecule can relax (continuous blue arrow) to the ground state $S_{0,D}$ of the donor. When an acceptor molecule is in close proximity to the donor dye, the acceptor can get excited by the donor (waved turquois arrow). After reaching the excited singlet state of the acceptor $S_{1,A}$ the molecule can relax radiatively (continuous red arrow) to the ground sate of the acceptor $S_{0,A}$.

Three parameters have to be considered to describe FRET: the orientation factor κ^2, the overlap integral *J*, and the distance *r* between the donor and acceptor as illustrated in

Figure 6. κ^2 describes the relative orientation between the donor and acceptor diploes and can be calculated from the angle between the plane of the donor dipole and the acceptor dipole θ_{DA} as well as from the angles of the donor (θ_D) and the acceptor dipoles (θ_A) (Eq. 2.4,

Figure 6 a)).

$$\kappa^2 = (sin\theta_D \cdot sin\theta_A \cdot cos\theta_{DA} - 2\, cos\theta_D \cdot cos\theta_A)^2 \qquad \text{(Eq. 2.4)}$$

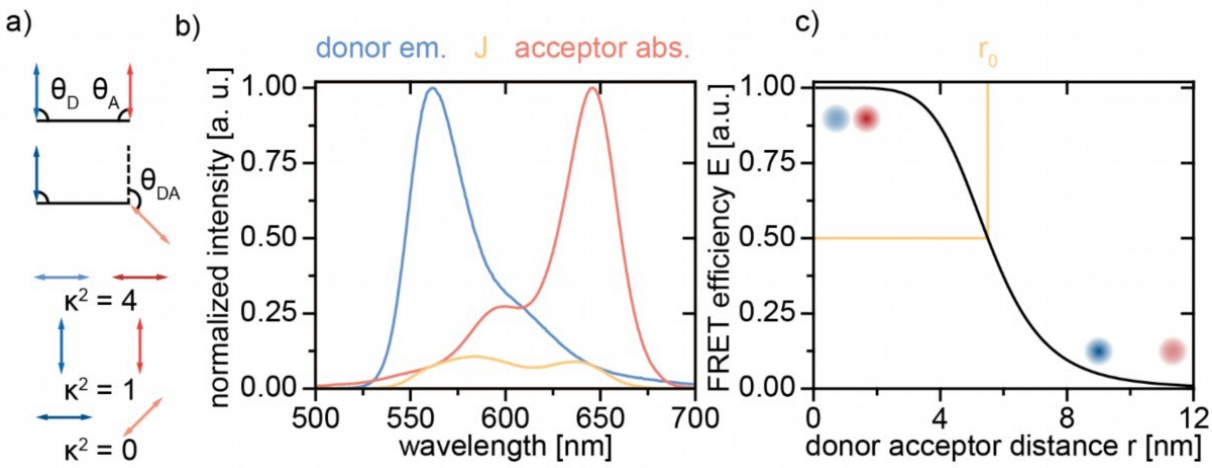

Figure 6: FRET requirements. a) Top: Angles to determine κ^2. Button: Example orientations of acceptor (red) and donor dipoles (blue) including the corresponding κ^2 values, a free rotating dye pair has a κ^2 of 2/3. b) Donor emission (blue) and acceptor absorption spectra (red) including the overlap integral J (orange) are illustrated. Here Atto542 is chosen as a donor and Atto647N as an acceptor were chosen. c) Distance dependence of the FRET efficiency for the FRET pair described in b) is shown with an r_0 of 5.5 nm.

When the dipoles are aligned head-to-head κ^2 is 4, when they are aligned parallelly 1 and perpendicularly 0, which indicates that no energy transfer takes place. If the dyes are freely rotating κ^2 is 2/3,[94] which is the case for the observed samples of this work. Fixed dyes can be observed by embedding them into a polymer matrix[95] or if they are interacting with DNA.[96] For FRET also a spectral overlap *J* between the donor emission and the acceptor absorption spectra is important. *J* is illustrated in

Figure 6 b). Except from FRET between two spectrally separated dyes, energy transfer can also be observed between similar dyes, which is called homo FRET.[97] The distance against the FRET efficiency *E* in dependence of the distance between donor and acceptor is shown in

Figure 6 c).

$$E = \frac{k_{ET}}{k_{Fl,D} + k_{nr,D} + k_{ISC,D} + k_{ET}} = \frac{r_0^6}{r_0^6 + r^6} = 1 - \frac{\tau_{DA}}{\tau_D}$$

$$= \frac{9\,\kappa^2 \ln 10}{128\pi^5\, n^4}\, N_A\, r^6 \frac{\Phi_E^D}{\tau_D} \int \varepsilon_A(\lambda)\, I_F^D(\lambda)\, \lambda^4\, d\lambda \qquad (Eq.\,2.5)$$

E indicates the amount of energy transferred from the donor to the acceptor. It can be calculated from the rate constants depopulating the $S_{1,D}$ and the FRET rate constant k_{ET}, the FRET pair specific distance r_0 where 50% of energy transfer is observed, and the distance between donor and acceptor *r*. For the theoretical calculation besides the fundamental physical constants like π and the Avogadro constant N_A, also the orientation factor κ^2, the diffraction index of the medium *n*, the quantum yield of the donor Φ_E^D and the fluorescence lifetime of the donor τ_D are required. The overlap integral *J* between the emission spectrum of the donor and the absorption spectrum of the acceptor includes the wavelength λ, the molar extinction coefficient $\varepsilon_A(\lambda)$, and the normalized donor emission intensity $I_F^D(\lambda)$ (see Eq. 2.5).

In general FRET can be used to study distances between 2 and 10 nm. For shorter distances other types of energy transfer (e.g. Dexter energy transfer[98,99]) are observed and for larger distances the change in *E* is too small to be detected. To design a sensitive FRET assay the FRET pair should be positioned around r_0.[87,89]

2.3. Graphene and Graphene Energy Transfer

Graphene is a two-dimensional monolayer containing sp^2-hybridized carbon atoms (see Figure 7 a)). The elaboration of the pristine material properties like mechanical strength, electrical, and thermal conductivity was rewarded with the noble prize in 2010.[47] Nowadays, it is for example used in material science and electronic devices.[100–102] In fluorescence experiments graphene can be used as an unbleachable universal broad band acceptor, which can answer questions in the area of biology,[103,104] photo physics, and super-resolution.[9]

As an optical property graphene absorbs only 2.3% of the incident light per monolayer of graphene.[48] Furthermore, for fluorophores placed at a distance *d* below 40 nm to graphene the two dimensional material is acting as a broad range acceptor along the whole visible and infrared range. To be more precise: if the excited donor fluorophore is relaxing back to the ground state an electron from the valence band of graphene can be excited to the conduction band. Afterwards the electron relaxes back under emission of heat,[51,105,106] phonon or plasmon emission[107] (see Figure 7 b)). To quantify the graphene energy transfer (GET), the GET efficiency η can be calculated from the GET rate constant k_G divided by the sum of the rate constants depopulating the S_1 state. Also a calculation of η using the dye graphene distance *d* including d_0, where 50% of the energy is transferred to the graphene surface, or the fluorescence lifetime

on graphene τ_{Gr} and glass τ_{Gl} is possible (Eq. 2.6). Instead of the fluorescence lifetime also fluorescence intensities can be used.

$$\eta = \frac{k_G}{k_{Fl} + k_{nr} + k_{ISC} + k_G} = \frac{1}{1 + \left(\frac{d}{d_0}\right)^4} = 1 - \frac{\tau_{Gr}}{\tau_{Gl}} \qquad (Eq. 2.6)$$

Equation 2.6 is similar to those already introduced for FRET (see chapter 2.2, Eq. 2.5). However, the difference is that FRET decays with a distance dependence of r^{-6} [87,89] while GET has a distance dependence of d^{-4}.[49,51–53] The different distance dependences are caused by the different type of acceptors. While in FRET the acceptor is a freely rotating dipole in GET the dipole is orientated along the 2D surface of graphene. This leads to a longer working range of GET (~40 nm) compared to FRET (~10 nm). If in FRET the single acceptor is exchanged with an array of acceptors the distance dependence and working range is similar to GET.[21]

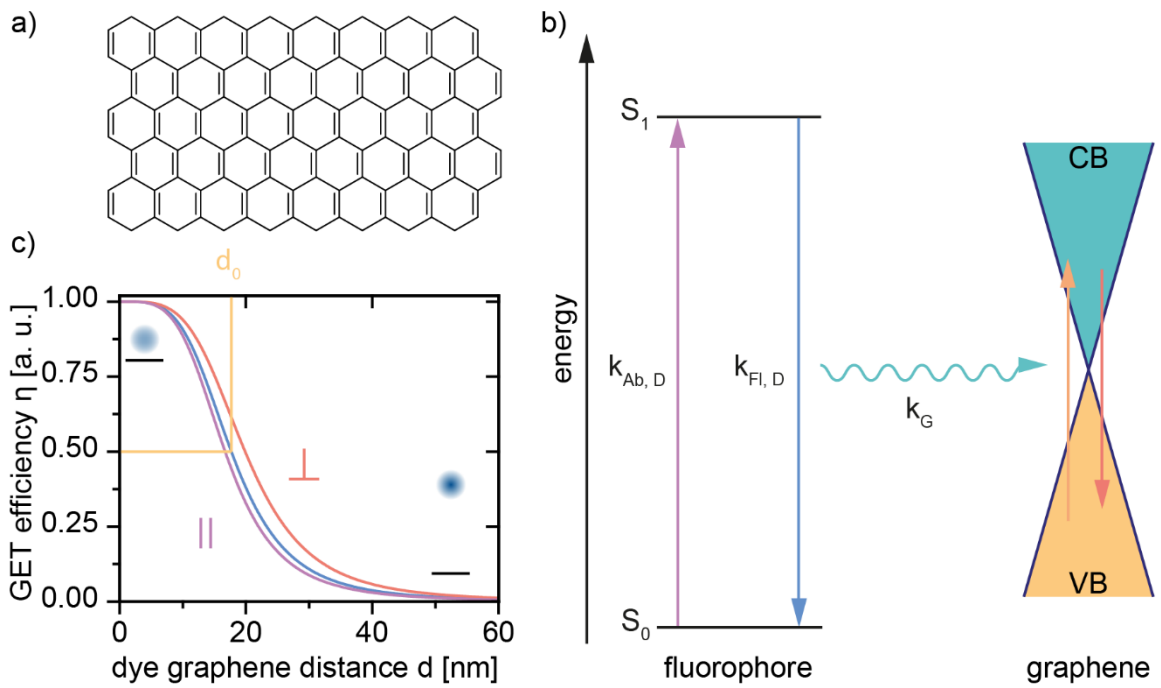

Figure 7: a) Chemical structure of sp²-hybridized carbon lattice graphene. b) Jablonski diagram of a fluorophore close to the graphene surface (< 40 nm). The excited electron can not only relax back to the ground state S_0 via radiative emission (straight blue) also a relaxation via non-radiative energy transfer (waved turquois arrow) known as graphene energy transfer (GET) can occur. In case of GET an electron from the valence band (VB) of the graphene is excited (orange arrow) to the conduction band (CB) and relaxes back to the VB (red arrow). c) Illustration of the GET efficiency η against the distance d. Besides the measured distance dependence of Atto542 with a d_0 of 17.7 nm (blue) also the theoretical calculations of the same fluorophore with perpendicular (red) of parallel (purple) orientation of the dipole based on equation 2.7 are shown.

For theoretical calculations of the GET efficiency η_{theo}, besides the fine structure constant α and the permittivity of the substrate ε also the orientation factor ν has to be taken into account (Eq. 2.7). The value of the orientation factor ν is 2 for a perpendicular orientation of both dipoles

and 1 for a parallel orientation of both (see Figure 7 c)), perpendicular: red; parallel: purple).[53,56] Equation. 2.7 shows that η_{theo} and therefore also d_0 depend on the emission wavelength λ causing a shift of d_0 from 17.7 ± 0.5 nm (Atto542, λ_{em} = 562 nm) to 18.5 ± 0.7 nm (Atto647N, λ_{em} = 664 nm).[49,52,53]

$$\eta_{theo} = 1 - \frac{1}{1 + \frac{9\,\nu\,\alpha}{256\,\pi^3\,(\varepsilon+1)^2}\left(\frac{\lambda_{em}}{d}\right)^4} \qquad (Eq.\,2.7)$$

2.4. Plasmonic Nanoparticles

The properties of NPs are strongly dependent on their size, material, and shape, which opens up a broad field of applications, like in medicine,[108,109] energy conversion,[27] and arts.[110] In this work, the interaction between spherical gold NPs with light and the influence on a fluorophore in close proximity to an NP are discussed.

NPs irradiated with an electromagnetic wave exhibit a collective oscillation of the electrons (Figure 8 a) blue), which is illustrated as a relative displacement to the nucleus. A condition, which has to be fulfilled is that the NPs have to be smaller than the wavelength of the incident light. The created positive charges (Figure 8 a) salmon) apply a counterforce, dragging the electrons in the opposite direction. This collective oscillation is called localized surface plasmon resonance (LSPR), which creates an electric field surrounding the NP (Figure 8 b)).[27–30]

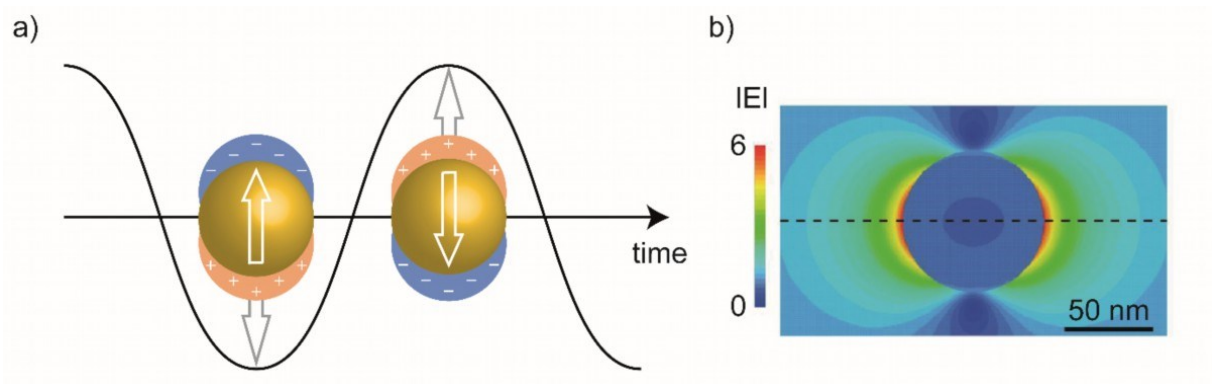

Figure 8: a) Interaction of a spherical gold nanoparticle with the electromagnetic field of light. The light displaces the electrons (blue) in the NP from the nucleus. A counterforce (gray arrow) from the positively charged nucleus (salmon) is replacing the electrons back to its starting position. b) The collective oscillation of the electrons is creating an electric field which can interact with the dyes in close proximity to the NP. The dashed line illustrates the orientation of the electrical component of light (modified from [111]).

As an indicator for the polarizability of an NP the permittivity ε can be described by the Drude model with the plasma frequency ω_p (given in Eq. 2.9), the frequency of the applied field ω, the ionic background of the metal ε_∞, and the damping term γ.

$$\varepsilon = \varepsilon_\infty - \frac{\omega_p^2}{\omega^2 + i\gamma\omega} \qquad \text{(Eq. 2.8)}$$

$$\omega_P = \sqrt{\frac{Ne^2}{\varepsilon_0 m_e}} \qquad \text{(Eq. 2.9)}$$

In Eq.2.9 N is the number of electrons, e the electron charge, ε_0 the permittivity in vacuum, and m_e the electron mass.

If only spherical NPs much smaller than the wavelength of light are considered the polarizability α is given by the so-called Rayleigh approximation with R being the radius of the NP and the dielectric constant of the medium ε_m.

$$\alpha = 4\,\pi\,\varepsilon_0 R^3 \frac{\varepsilon - \varepsilon_m}{\varepsilon + 2\,\varepsilon_m} \qquad (Eq.2.10)$$

The scattering and absorption cross-sections are given by Eq. 2.11 and Eq. 2.12, which include the wave vector k.[29]

$$\sigma_{sca} = \frac{k^4}{6\pi\varepsilon_0^2}\,\alpha^2 \qquad (Eq.2.11)$$

$$\sigma_{abs} = \frac{k}{\varepsilon_0}\,Im\,(\alpha) \qquad (Eq.2.12)$$

By combining Eq. 2.10 with either Eq. 2.11 or Eq. 2.12 a R^6-dependence for the scattering process and a R^3-dependence for absorption becomes clear, which shows that larger NPs are dominated by scattering and smaller NPs are dominated by absorption.[29] The damping of the light induced oscillation occurs *via* heat or light scattering.[112]

The external electric field of a NP created by the oscillating charges can influence the photo-physical properties of a dye situated in close proximity. Thus from Eq. 2.13 it is clearly visible that the excitation rate constant k_{ex} of a fluorophore is given by the local electric field intensity E and transition dipole p.

$$k_{ex} = |p\,E^2| \qquad (Eq.2.13)$$

This equation underlines that a higher local field will have a stronger impact on the fluorophore. A higher local field for example can be generate by using larger NPs[37] or the coupling of two

NPs with each other.[34] The NP is not only changing one rate constant of the fluorophore like for example in FRET or GET, but it changes the radiative and non-radiative rate constants.[31] The non-radiative rate constant decays similarly to FRET with a distance dependence of r^{-6}. However, for the radiative decay the distance dependence is dominated by a r^{-3} dependence together with an additional r^{-6} dependence, which occurs from radiative damping processes.[39]

Also the relative position of the fluorophore and NP to the polarization of the incident light is important for the modification of the photophysical properties. Another important factor in the dye-NP coupling is the relative orientation of the fluorophore with respect to the NP. As Figure 8 b) illustrates, a fluorophore located in the red area of the *E*-field distribution experiences a strong coupling, which results in an enhanced fluorescence intensity and a reduction of the fluorescence lifetime.[31,32,34] If the fluorophore is at the top or bottom of the NP (see Figure 8 b), dark blue area) a quenching of the dipole's fluorescence intensity and lifetime takes over.[36,37]

2.5. Dye Stabilization

In this chapter several approaches to stabilize fluorophores and collect more photons before the dye is photobleached are discussed.

As already explained (see Figure 9) when a molecule enters the triplet state it also changes the spin from antiparallel to parallel, which leads to a longer lifetime of the triplet compared to the singlet state. In case of a parallel spin the dye is a biradical and can interact with the biradical oxygen that can destroy the π-system of the dye and therefore photons are not emitted from the dye anymore. This is also called photobleaching. To reduce photobleaching, two different methods will be introduced: a reducing and oxidizing system (ROXS) and an oxygen scavenging system (OSS).

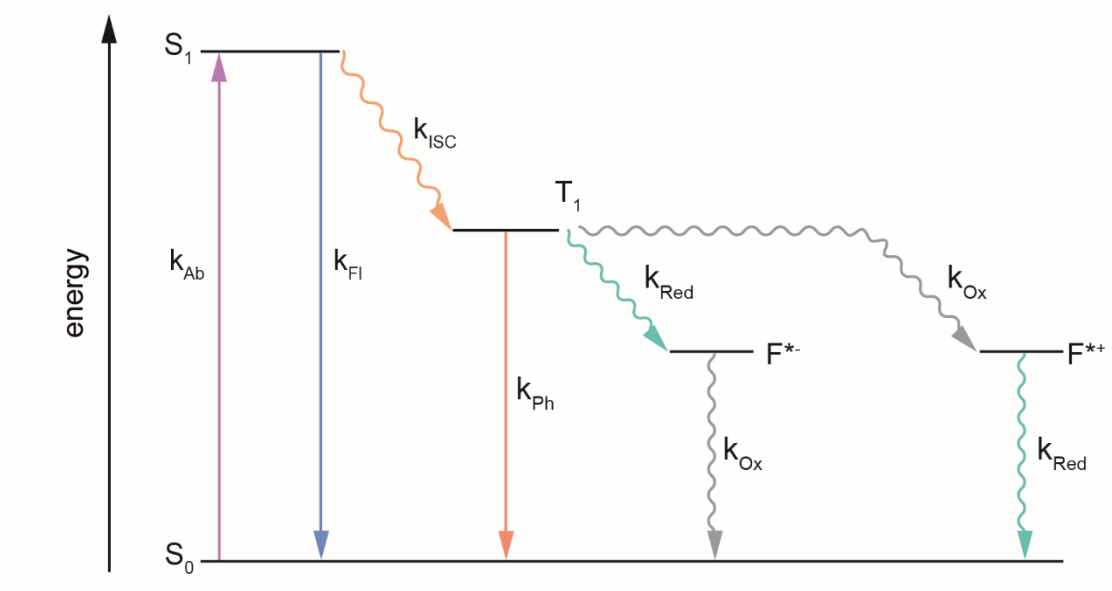

Figure 9: Jablonski diagram for ROXS. Besides the already explained transition to the S_1 and from the S_1 to the T_1 (Figure 3), the transitions for ROXS are pictured. In presence of ROXS the molecule can get reduced (waved turquois) and afterwards oxidized (waved gray) via a radical anion state (F^{*-}) or vice versa over a radical cation state (F^{*+}).

ROXS contains an oxidizing and a reducing agent, which either first reduces (waved turquois, Figure 9) the molecule from the T_1 to the radical anion state (F^{*-}) and afterwards oxidizes it (waved gray), or *vice versa via* the radical cation state (F^{*+}).[113] These systems also have the advantage that the triplet state is suppressed that leads to reduced blinking of the molecule. Common ROXS chemicals are a combination of ascorbic acid (AA) and methylviologen (MV), or trolox (TX) and trolox quinone (TQ).[114] To synthesize the oxidant trolox quinone from the reductant trolox the reactant has to be irradiated with ultra-violet light (see Figure 10 a)). In the literature the mixture of both is also referred to as aged trolox.

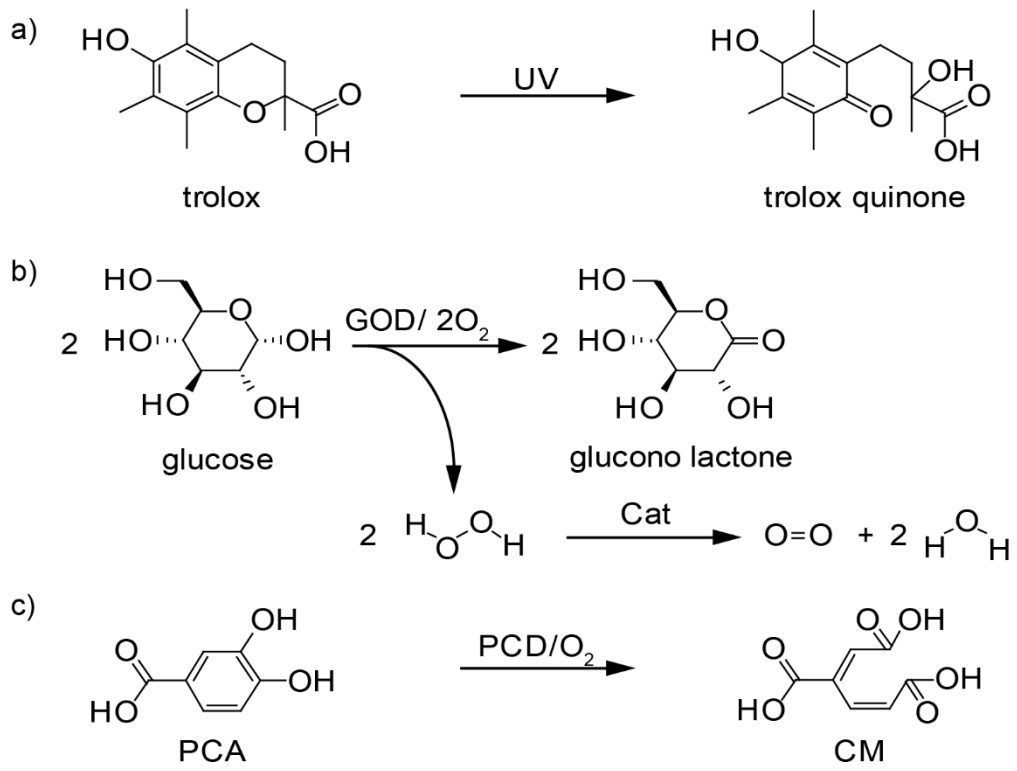

Figure 10: Chemical agents for the stabilization of fluorophores. a) Ageing from trolox to trolox quinone under UV radiation. b) Chemical reaction of the oxygen scavenging system glucose oxidase (GOD), catalase (Cat) and glucose with oxygen. GOD oxidizes glucose to glucono lactone under the production of H_2O_2. The product H_2O_2 is converted to water and oxygen in presence of Cat. c) In the oxygen scavenging system protocatechuic acid (PCA) and protocatechuate decarboxylase the PCA is transformed to beta-carboxy –cis,cis-muconate (CM).

An alternative way to reduce photobleaching is oxygen removal by either a combination of glucose and the enzymes glucose oxidase (GOD) and catalase or with protocatechuic acid (PCA) and the enzyme protocatechuate decarboxylase (PCD). For the first combination the glucose gets oxidized to the glucono lactone in presence of GOD and oxygen under the formation of hydrogen peroxide. The hydrogen peroxide dissociates in presence of catalase to oxygen and water (Figure 10 b)). The other combination oxidizes the PCA with PCD and oxygen to beta-carboxy-cis,cis-muconate (CM) without any intermediate. The latter procedure has the advantage that the intermediate hydrogen peroxide is not synthesized. Hydrogen peroxide is a stronger acid than CM which leads to a faster drop of the pH.[115]

2.6. DNA Origami Technique

The DNA origami technique is based on the composition of the DNA (deoxyribonucleic acid, see Figure 11) itself, which was analyzed and described in 1953.[116] DNA consists of four different nucleotides (nt) adenine (A, orange), thymine (T, blue), guanine (G, green), and cytosine (C, purple), which are linked to a phosphate deoxyribose backbone. Two nucleotides are always complimentary to each other and form base pairs under formation of hydrogen bonds. Adenine forms two hydrogen bonds with thymine and guanine three with cytosine.[116] The structure is additionally stabilized by π-π interaction of stacked base pairs.[117] Double stranded (ds) DNA forms a helix with a diameter of 2 nm. The distance between two nucleotides in a helix is 0.34 nm with a twist of 34.6 °, a whole turn has therefore a height of 3.4 nm.[118] Compared to ds DNA, single stranded (ss) DNA has a larger base distance of 0.63 nm.[116,119]

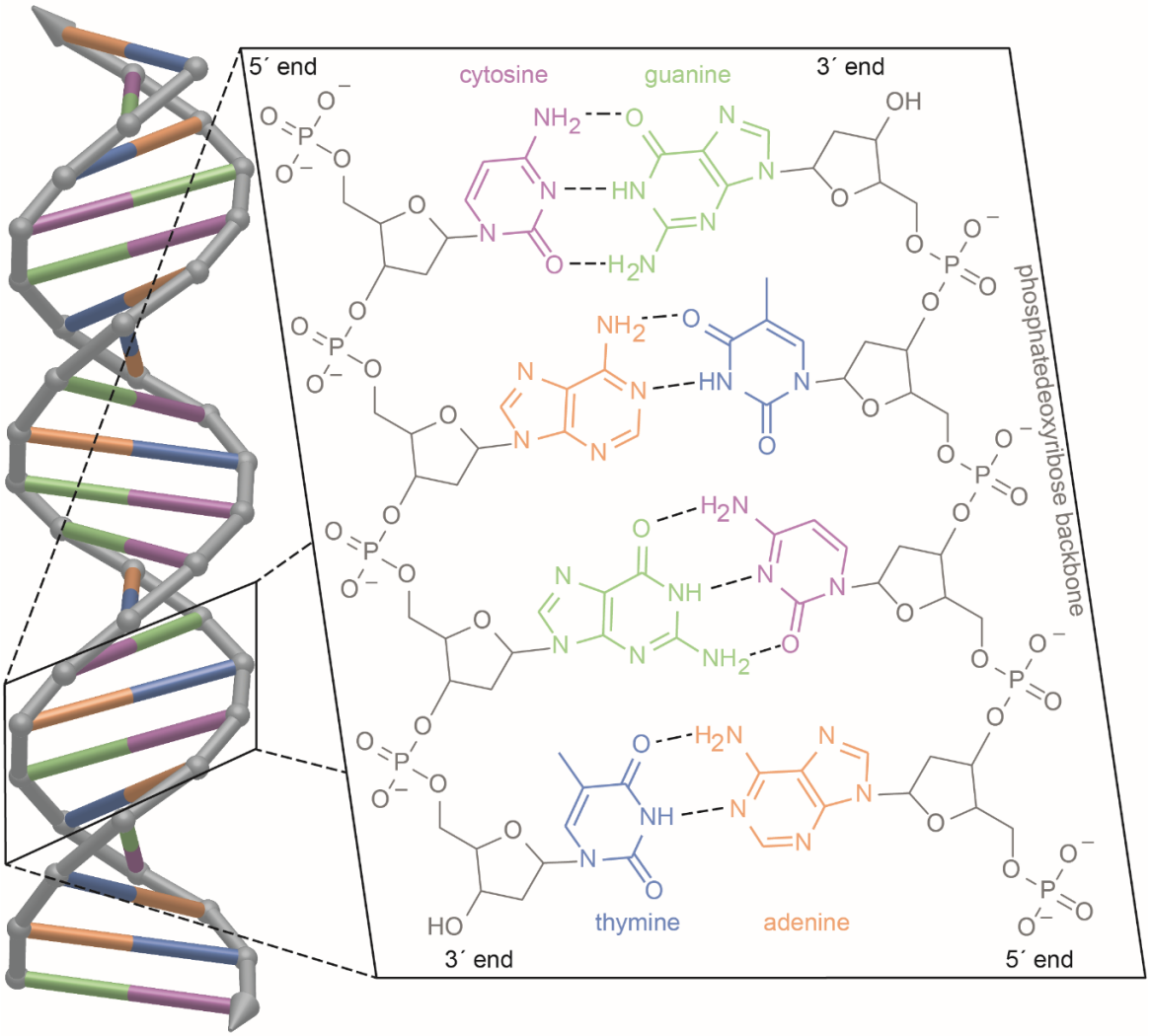

Figure 11: Illustration of the DNA double helix including the gray phosphate deoxyribose backbone with the color coded base pairs. The complimentary oligonucleotides cytosine (purple) and guanine (green) as well as adenine (orange) and thymine (blue) form hydrogen bonds. The inset shows the chemical structures of the base pairs. For a better overview not all valence electrons are shown.

DNA origami structures come in various patterns and forms and were first established in 2006 by Rothemund[22] based on the pioneering work of Seeman.[120] At the beginning the DNA origami structures were only designed as stiff 2D structures but later were further developed to 3D[121–123] and even flexible structures.[124–126] For design the software caDNAno[127] is used and the correct folding of the DNA origami structures can be predicted using simulation programs like Cando[128,129] or oxDNA[130]. The main building block of the DNA origami structure is the roughly 8000 nt circular single stranded scaffold, which is added to an excess of approximately 200 short (~60 nt) single stranded staple strands in a buffered system with salt (either $MgCl_2$ or NaCl). To fold DNA origami structures this mixture is heated (~80 °C) and slowly cooled down to room temperature. A sketch of the folding procedure is illustrated in Figure 12 a). During the folding process staple strands are binding to multiple parts of the scaffold and form the DNA origami structure.[22] To remove unbound staple strands from the DNA origami solution the solution is purified e.g. with filtration, agarose gel, or precipitation. To observe the correct folding, the DNA origami structures can be imaged with AFM (atomic force microscope; Figure 12 b)), TEM (transmission electron microscope), or SEM (scanning electron microscope).[131] The incorporated oligonucleotides can also be extended and hence protrude from the DNA origami structure to bind biomolecules, NPs or dyes to DNA origami structure, as so-called external labels. An internal label is an oligonucleotide which is directly labeled with a dye, biotin or COT (cyclooctatetraene) and incorporated into the DNA origami structure. The biotin label is used to immobilize DNA origami structures *via* neutrAvidin-biotin-BSA (bovine serum albumin) to a glass surface. For the immobilization on graphene oligonucleotides are modified with pyrene,[49] the binding to membranes or vesicles is achieved by a cholesterol modification.[132,133] DNA origami structures are robust, easy to modify, and the high throughput makes it easy to implemented it as a bread board on the single-molecule level.

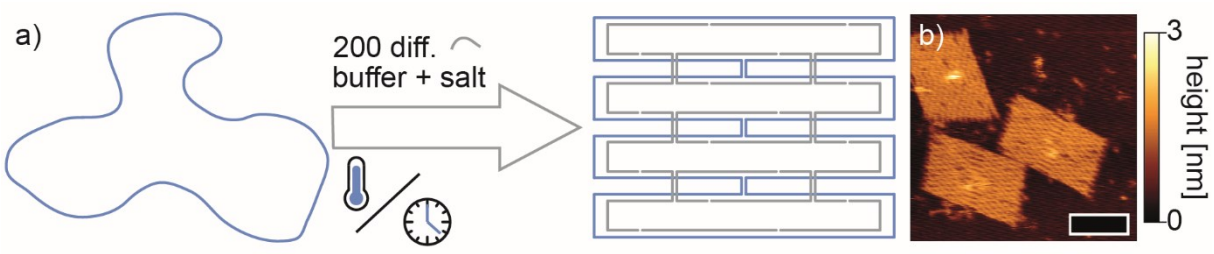

Figure 12:Illustration of the DNA origami structure folding process. To a scaffold (blue) an excess of up to 200 staple strands (gray) is added in a buffered environment, heated up and slowly cooled down (a). The correct folding can be observed with AFM. The DNA origami structure is modified with strands protruding from the DNA origami structure to externally bind a Hfq molecule (from methanocaldococcus jannaschii) which is illustrated as a white dot in the center of the rectangular DNA origami structure (b) (scalebar: 50nm, Reproduced from [134] with permission from the Royal Society of Chemistry).

3. Material and Methods

This chapter gives an overview on the different microscopy techniques used in this work. Microscopy methods like confocal (chapter 3.1) with time correlated single photon counting (TCSPC, chapter 3.1)), wide-field (chapter 3.2) with total internal reflection fluorescence (TIRF, chapter 3.2), and DNA-PAINT (chapter 3.2.1) as well as atomic force microscopy (chapter 3.3) are introduced.

3.1. Confocal Microscopy

An exemplary confocal setup with two laser lines, which can be used for e.g. FRET measurements, is illustrated in Figure 13 a). The red (red) and green light sources (turquoise) are aligned (orange) *via* a dichroic mirror (DC_1). After passing the second dichroic mirror (DC_2) in the microscope body the lasers (orange) are focused through the objective to the sample. The sample is measured point by point which can be realized by either scanning with a laser over the sample (laser scanning) or moving the sample with a piezo stage over the laser (sample scanning). The red-shifted fluorescence emission is passing the dichroic mirror (DC_2) and is focused with the lens L_1 to the pinhole P. Only fluorescence of molecules in the focus can pass through the pinhole, other signals are suppressed. The third dichroic mirror (DC_3) is splitting the fluorescence to different avalanche photo diodes (APD) where the single photons for the red and green channel are detected.

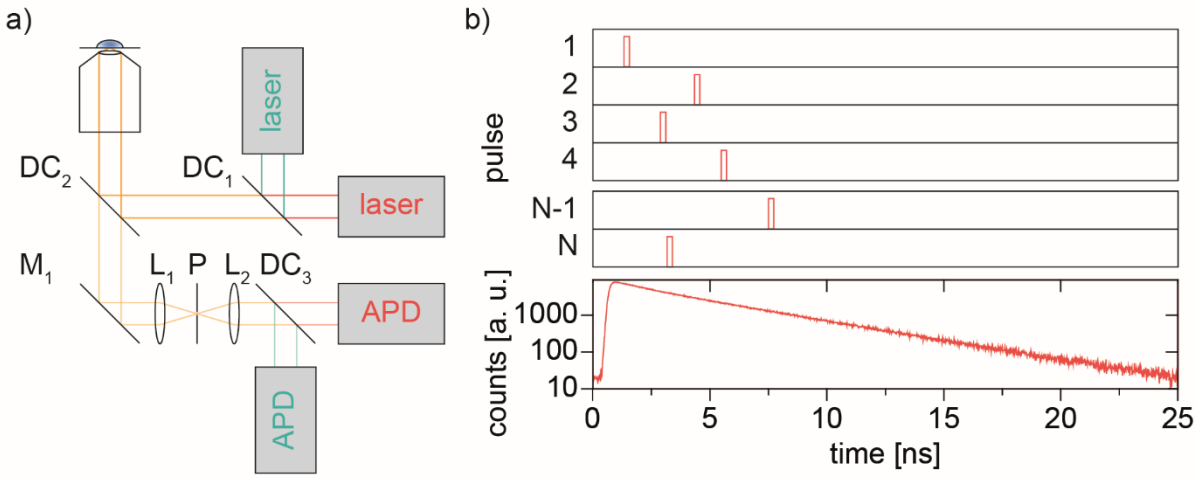

Figure 13: Exemplary two-color confocal microscope (a)) with illustration of time correlation single photon counting (TCSPC) (b)). Every detected arrival time is summed up into a decay (b) lower panel).

To measure the photon arrival time of a molecule a time correlated single photon counting (TCSPC) module and a pulsed laser source are needed. The time between the triggered laser

pulse and the detection of a signal on the APD is measured (see Figure 13 b)). After repetition over multiple pulses a fluorescence lifetime decay (see Figure 13 b)) is gained. This decay has to be de-convoluted from the instrument response function (IRF) to obtain the real fluorescence lifetime. By a pixel-wise fluorescence lifetime measurement during a scan a FLIM is generated. [89]

3.2. Wide-Field Microscopy

An alternative type of fluorescence microscopy is the wide-field microscopy, which is illustrated in Figure 14 a). When the microscope is operated in epi fluorescence the excitation laser is expanded with two lenses L_1 and L_2, an x/y stage, and then passing through the dichroic mirror (DC_1) into the objective illuminating the sample over a large region of interest (ROI, ~20 x 20 µm). The emission of the dye is detected on an EMCCD camera (electron multiplying charged coupled device). In wide-field microscopy multiple molecules can be observed at the same time, but the time resolution is limited by the integration time of the camera, which is around 5 ms. The drawback of wide-field illumination is the increased background signal arising for example from biomolecules and dyes in solution. To only excited molecules close to the glass surface, total internal reflection fluorescence (TIRF) microscopy is used. The difference of the microscopy techniques epi and TIRF is the alignment of the lens system L1 and L2 as the x/y stage is shifted. This changes the pathway of the excitation laser beam (Figure 14 b)) illuminating the sample not directly but at an angle θ to the sample, the so-called TIRF angle. For θ being below the critical angle θ_T, most of the incident light is reflected to the denser medium (glass) and an evanescent field is created (see Figure 14 c)). The critical angle θ_T is given by the diffraction indices of the sample n_2 and the glass slide n_1 (see Eq. 3.1),

$$\theta_T = \arcsin\left(\frac{n_2}{n_1}\right) \qquad (Eq. 3.1)$$

The decay of the intensity $I(d)$ of the evanescent field is given by Eq. 3.2 and includes the distance in the solution d and penetration depth z, which is given in Eq. 3.3 with the excitation wavelength λ.

$$I\,(d) = I_0\, e^{-\frac{d}{z}} \qquad (Eq. 3.2)$$

$$z = \frac{\lambda}{4\pi\sqrt{n_1^2\,\sin^2\theta\, - n_2^2}} \qquad (Eq. 3.3)$$

After a few hundred nanometer no significant excitation intensity is observed and therefore no molecule can be excited. The decay of the intensity can also be used to measure the z position of the fluorophore.[82] Besides in TIRF microscopy, evanescent fields can also be created using zero mode waveguides (ZWM)[135,136] or prisms.[89,137,138]

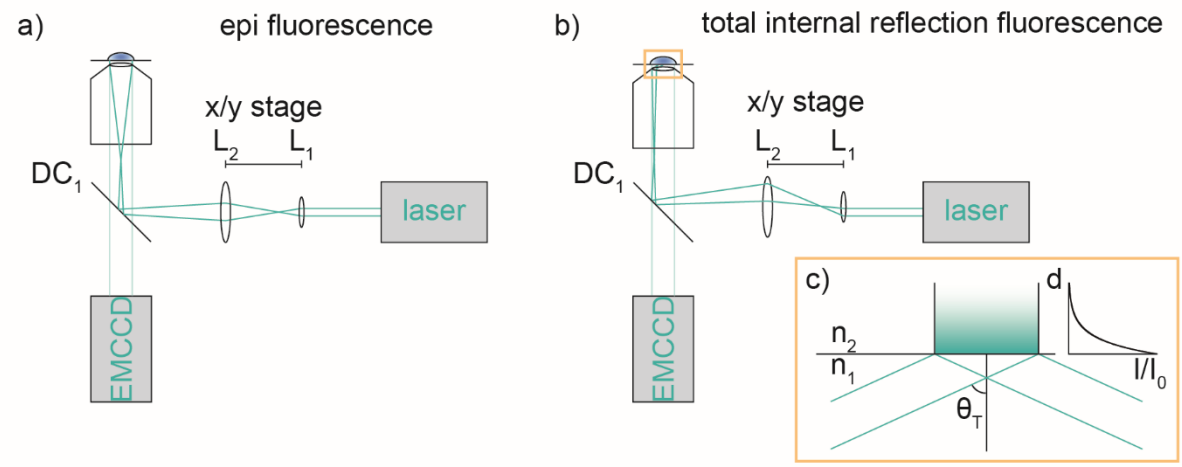

Figure 14: Laser path of a wide-field microscope operating in epi fluorescence (a)) and TIRF (b)) with detailed illustration of TIRF in c). Furthermore, the decaying fluorescence intensity ratio (I/I_0) along the distance d is shown in c), calculated from Eq. 3.2. Epi fluorescence is penetrating the whole sample while the evanescence field of TIRF decays after a few hundred nanometers.

3.2.1. Super-Resolution and DNA-PAINT

The resolution of a microscope or differentiability of two emitting dyes is limited by the Abbé criterion,[139] which is given in Eq. 3.4 for the x/y plane and in Eq. 3.5 for z. (see Figure 15 a)).

$$d_{x/y} = \frac{\lambda}{2\,NA} = FWHM_{x/y} \qquad (Eq.3.4)$$

$$d_z = \frac{2\,\lambda}{NA^2} = FWHM_z \qquad (Eq.3.5)$$

The minimum distance *d* between two dyes or full width half maximum (*FWHM*) of the point spread function (PSF) can be calculated from the wavelength of the light λ and the numerical aperture *NA* of the objective. With an objective with a high numerical aperture (NA = ~1) a resolution in the x/y plane of roughly $\lambda/2$ is obtained while the z resolution is only λ. To circumvent the Abbé criterion and receive super-resolved images, two different approaches can be pursued: the deterministic or the stochastic approach. Deterministic super-resolution, like STED (stimulated emission depletion)[140,141] and GSD (ground state depletion)[142,143] are decreasing the diameter of the excitation laser beam which decreases the *FWHM* of the PSFs

and therefore increases the resolution. In stochastic super-resolution like dSTORM (direct stochastical optical reconstruction microscopy),[144] PALM (photoactivated localization microscopy),[72] and DNA-PAINT (points accumulation for imaging in nanoscale topography)[85] the fluorophores are blinking independently from each other (Figure 15 b)). The blinking is adjusted in a way that only one dye per frame in the diffraction limited distance *d* is emitting. By detecting and fitting every single blinking event over time a super-resolved image can be generated (Figure 15 c)). The localization precision *loc* of the measurement is quantified by Eq. 3.6 with the number of photons *N* and the standard deviation of the PSF *σ*.[145]

$$loc = \frac{\sigma}{\sqrt{N}} \qquad (Eq. 3.6)$$

σ can be calculated from the *FWHM* and Eq.3.7.

$$\sigma = \frac{FWHM}{2\sqrt{2\ ln\ 2}} \qquad (Eq. 3.7)$$

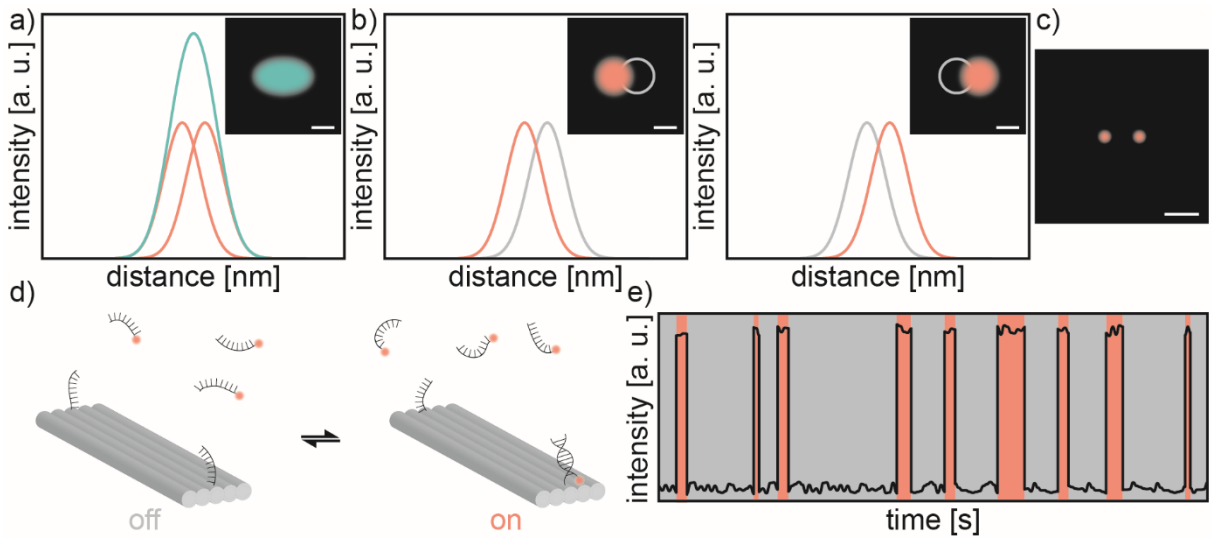

Figure 15: Illustration of the Abbe limit and DNA-PAINT. Two dyes (orange Gaussian) won´t be distinguishable as different light sources when those are limited by the Abbé criterion, leading to the observation of only one elliptical light source (blue Gaussian; (a))). To circumvent the Abbe limitation both dyes have to blink independently from each other (gray: dark fluorophore, b)). Finally, instead of observing one elliptical spot it is possible to detect the single fluorophores. After detecting multiple blinking events and fitting the spots a super-resolution image can be generated (c), scalebar: 30 nm). One way to make the molecules blink is the DNA-PAINT technique. Here oligonucleotides labeled with dyes are transiently binding to the structure of interest (d)). The fluctuation of "off" (unbinding, gray) and "on" (binding, orange) is shown in the intensity transient (e)).

To get a high localization precision, a high number of photons is needed (Eq. 3.6). While other methods like dSTORM and PALM are suffering from photobleaching of the fluorophores, in DNA-PAINT the fluorophores are frequently exchanged through transient binding. To be more precise, biomolecules or DNA origami structures (see chapter 2.6) are labelled with protruding ssDNA to which complimentary ssDNA labels with fluorophores, so-called imager strands, can

temporally bind. This reduces photobleaching in DNA-PAINT and additional the transient binding introduces blinking. An “on” event refers to a binding of the imager to the structure of interest, while at an “off” event no imager binding is observed. (see Figure 15 d)-e)) The “on” time t_{on}, which is the time an “on” event is observed, can easily be adjusted by adapting the length of the complementary ssDNA. In general, more complementary DNA gives a longer t_{on}.[146] Usually, the length of the imager stands is between 6 to 8 nucleotides. By decreasing the concentration of the imager the “off” events and therefore the “off” times t_{off} are increasing. Another advantage of DNA-PAINT is that no other chemical is needed like β-mercaptoethanol (for dSTORM)to introduce blinking to the molecules,[147] which makes this technique more applicable for biological samples.[148] The main drawback of DNA-PAINT is the destruction of the protruding strands from DNA origami structures due to long lasting laser irradiation,[149] which can be decreased by introducing ROXS or oxygen scavenging systems (see chapter 2.5).

3.3. Atomic Force Microscopy

To verify the correct folding of DNA origami structures, atomic force microscopy (AFM) is used.[150] A sketch of an AFM is illustrated in Figure 16 where a laser beam is focused on the backside of a cantilever, which can be described as a leaf spring with a tip of the size of an atom. The laser reflected from the cantilever is detected with a segmented photo diode (SPD). During the measurement the cantilever is moved over the sample and is excited with the eigenfrequency causing the cantilever to oscillate. Depending on the sample,[151] surrounding medium,[152] or modification of the cantilever,[153] the frequency changes, which can be detected on the SPD (illustrated with the lateral deflection in blue and the vertical in green). Besides the oscillating mode, in which the tip and the sample are in the molecular attractive regime, the AFM can also be operated in the contact mode with the tip and sample being in a molecular repulsive regime. The oscillating mode is preferred to the contact mode if “soft” samples like DNA are measured but for surface studies like graphene or SiO_2 the contact mode delivers better results. In general, the AFM is favored to other surface imaging methods like TEM or SEM because AFM allows measurements under physiological conditions without the addition of chemicals like uranyl formate in TEM imaging.[119,154] While the lateral resolution is only a few nanometers (< 2 nm), the axial resolution is limited to cantilever artefacts that make a combination of multiple imaging methods necessary.[150,155]

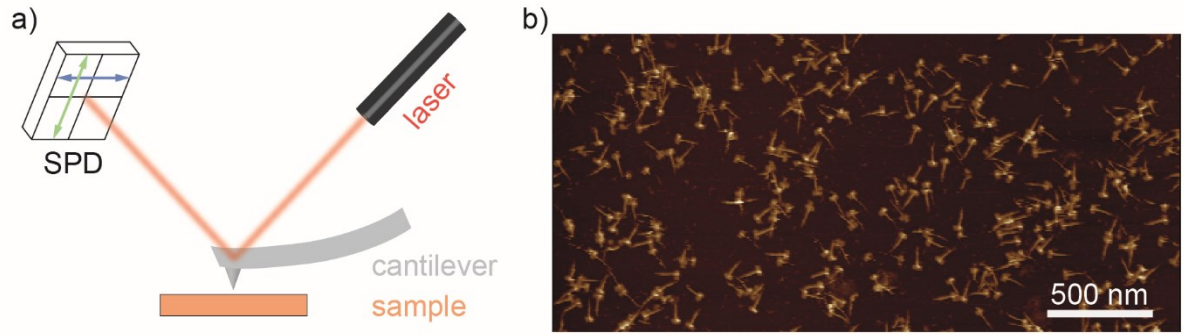

Figure 16: a) Operation principle of an atomic force microscope (AFM) including laser, cantilever and SPD (segmented photo diode)with lateral (blue double headed arrow) and vertical detection (green double headed arrow). b) AFM image of the DNA origami structure.

4. Summary of Publications

4.1. Publication I: Plasmon-assisted Förster resonance energy transfer at the single-molecule level in the moderate quenching regime

J. Bohlen,* Á. Cuartero-González,* E. Pibiri, D. Ruhlandt, A. I. Fernández-Domínguez, P. Tinnefeld, G. P. Acuna (* equal contribution)

The interaction of a donor dye and an acceptor dye (FRET) or the interaction of a donor dye and plasmonic nanoparticles, is well investigated. However, the effect of the proximity of plasmonic nanostructure (NS) on FRET has been controversely discussed with respect to the change of the FRET efficiency E and the FRET rate constant k_{ET}.[40–46] Depending on the study, for E an enhancement[40,41,44] or a reduction[42,43,45,46] is described. Similarly, for k_{ET} different publications show an increasing[41–44] or a constant behavior.[45] The reason for the different outcome originates from variances in the samples and in issues with measurements. The sample variances are caused by different geometrical shapes and materials of the NS as well as FRET pairs with different FRET efficiencies and spectral overlaps between the FRET dyes and the NS. Measurement issues, on the one hand, arise from inconstant distances between the FRET pairs and the NSs, which yield in heterogeneous interaction behaviors between the NS and the FRET pair. On the other hand, the orientation of the FRET-NS assay relative to the incident light, can result in a quenching or enhancement of the fluorophores. Furthermore, the differentiation between completely and partly assembled FRET-NS assay, where the NP, donor, or acceptor is missing, is responsible for heterogenous results.

In our approach, we are tackling the above mentioned measurement issues with the help of an immobilized rectangular DNA origami structure (NRO; Figure 17 a)). The NRO supports a defined spacing between the donor and acceptor as well as between the FRET pair and the NP, which provides homogenous samples. The immobilization of the DNA origami structures ensures similar orientations of the FRET-NP assay to the incident light. Single-molecule experiments guarantee a differentiation between complete and partly assembled FRET-NP assay. Additionally, the acceptor bleaching approach is applied, in which the excitation lasers are alternated on the second time scale (Figure 17 b)). This approach does not require any prior knowledge of the sample and only needs minor corrections, like a deconvolution of the fluorescence lifetime and background corrections of the fluorescence intensity. The alternation between the excitation lasers allows to extract the individual influence of the NP on the donor in absence and presence of the acceptor as well as on the acceptor only. By changing the diameter of the spherical gold NP in close proximity to the FRET pair, a change in fluorescence

intensity and lifetime is observed, from which the FRET efficiency *E* and the FRET rate constant k_{ET} is extracted. The data shows that an increase in NP size results in a decrease of the fluorescence intensity, lifetime, and FRET efficiency *E* while the FRET rate constant k_{ET} stays constant (Figure 17 c)). The fluorescence lifetime and intensity quenching as well as the decrease of *E* is caused by the NP coupling and the resulting change in the rate constants. However, this does not impact k_{ET} as it is independent of the rate constant change. Furthermore, the experimental data are in accordance with numerical simulations from the *Fernández-Domínguez* group. Additionally, a newer publication[156] on FRET close to NP surfaces further underlines the outcome of our single-molecule results.

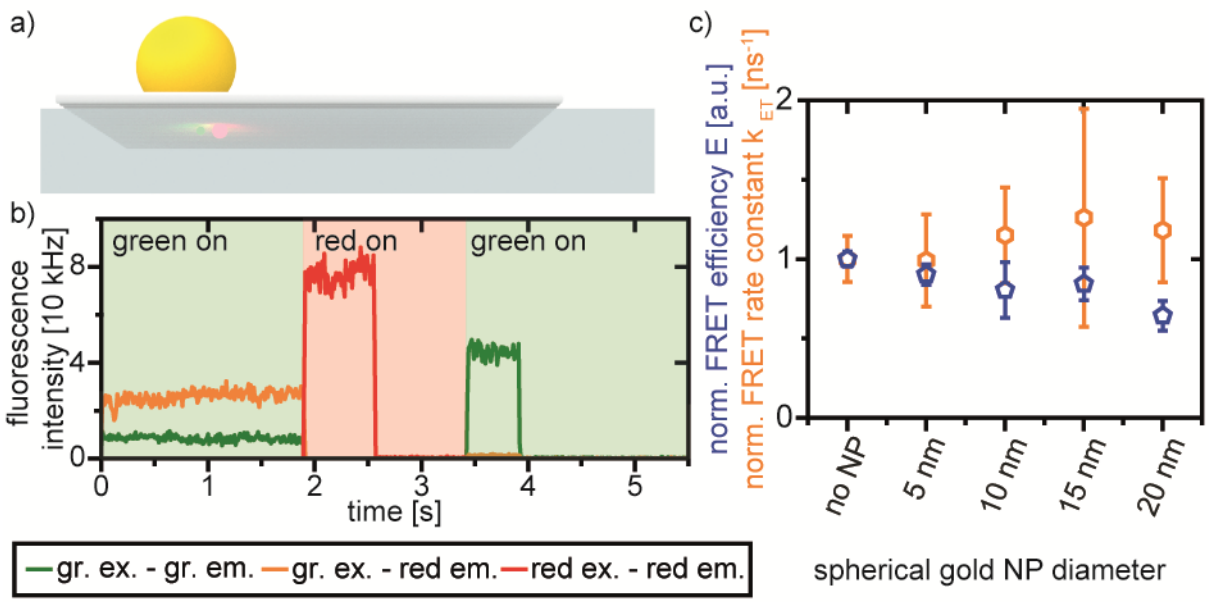

Figure 17: a) Rectangular DNA origami structure immobilized on a glass surface (for a better overview BSA-biotin and neutrAvidin are not illustrated). FRET pair (Atto542/Atto647N) is located underneath the spherical gold NP. b) Illustration of the acceptor bleaching approach: The background colors indicate the excitation laser (green: 532 nm, red: 640 nm). First fluorescence from the green dye (green) and FRET (orange) occurs afterwards the red dye (red) is bleached and in the finale step the green dye is bleached. c) The results demonstrated that with increasing NP diameter the FRET efficiency E decreases while the FRET rate constant k_{ET} stays constant. (both quantities are normalized to corresponding data without any NP).

4.2. Publication II: Distance Dependence of Single-Molecule Energy Transfer to Graphene Measured with DNA Origami Nanopositioners

I. Kaminska, **J. Bohlen**, S. Rocchetti, F. Selbach, G. P. Acuna, P. Tinnefeld

Graphene (see chapter 2.3) can be used as a broad band unbleachable acceptor. Many publications already observed the distance dependent fluorescence change due to graphene. However, all these studies gave different results for the GET distance d_0, where 50% of the energy is transferred to graphene. GET distances d_0 varying between 8 and 20 nm are reported.[51,54–57] The broad range of results is caused by an inaccurate positioning of dyes at defined heights, interactions between neighboring dyes, and dyes with heterogeneous properties. To overcome these problems, DNA origami structures with organic fluorophores are implemented, the DNA origami nanopositioners. DNA origami nanopositioners can be immobilized on a graphene surface *via* π-π stacking of attached pyrene moieties. Via pyrene the DNA origami structure is noninvasively bound to the graphene surface. This interaction is not interfering with the π system of the graphene and therefore is not changing its properties. By using three different DNA origami structures (Figure 18 a)) with a total of six different heights to the graphene surface, we can verify the d^{-4} distance dependence of graphene. Based on fluorescence lifetime and intensity data we can extract the GET distance for different dyes, namely Atto542 ($d_{0,\,Atto542}$ = 17.7 ± 0.5 nm) and Atto647N ($d_{0,\,Atto647N}$ = 18.5 ± 0.7 nm), and further show a good agreement with theoretical calculations (Figure 18 b)). This work is the cornerstone to establish GET in combination with DNA origami structures and organic dyes to observe fluorescence changes up to distance of 40 nm to the graphene surface.

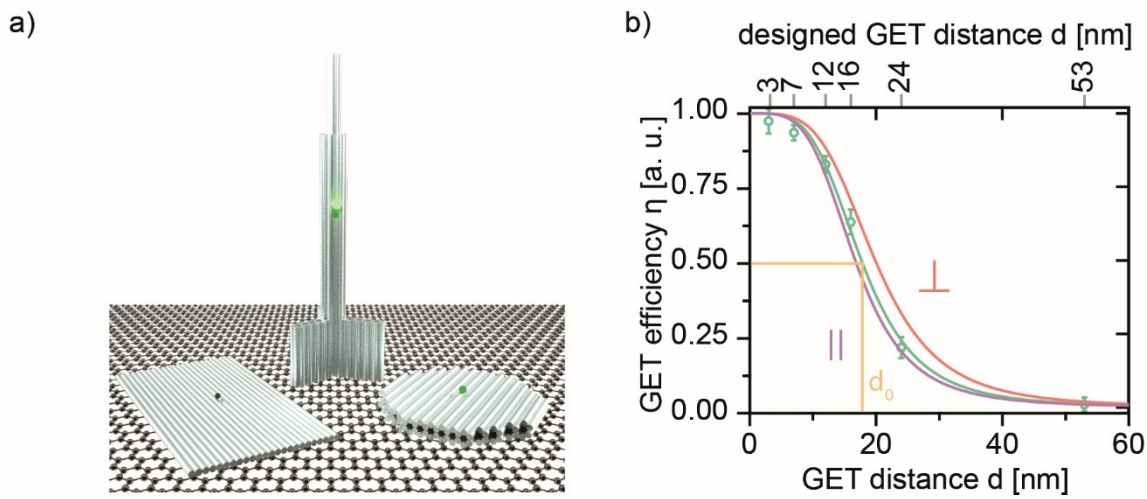

Figure 18: a) Illustration of the three different DNA origami structures investigated in GET studies. b) Distance dependence between graphene and dye with the designed GET distance on top of the graph. The data points from Atto542 (green hollow circle with standard errors) are fitted with the green curve to obtain d_0 (orange). Also the calculated curves for parallel (purple) and perpendicular (purple) oriented dipoles are shown.

4.3. Publication III: Graphene-on-Glass Preparation and Cleaning Methods Characterized by Single-Molecule DNA Origami Fluorescent Probes and Raman Spectroscopy

S. Krause, E. Ploetz, **J. Bohlen**, P. Schüler, R. Yaadav, F. Selbach, F. Steiner, I. Kaminska, P. Tinnefeld

To perform GET experiments on the single-molecule level, graphene-on-glass-coverslips with a high quality are needed. Therefore, we test in total ten different combinations of established methods[59–65] to fabricate graphene-on-glass-coverslips. To control the reproducibility of the protocols, we prepare coverslips according to each method at least three times. The quality is controlled with FLIM (fluorescence lifetime imaging) data of a DNA origami nanopositioner, which is attached *via* pyrene to the graphene surface. The results are correlated with Raman measurements and AFM images. While FLIM and AFM images show similar results, both only show a partial correlation to the Raman results, which is caused by the two orders of magnitude larger probing area of Raman. In this approach the DNA origami nanopositioner can be understood as a probe to verify the graphene quality and further allows the addition of a different DNA origami structure afterwards. As an additional sample we choose an L-shaped DNA origami structure with a dye labeled pointer that can transiently bind to two binding sites on the DNA origami structure itself. As both binding sites are at different heights to the graphene surface the dye experiences different quenching at both positions, which leads to a fluctuation in the fluorescence intensity and lifetime signals. We are confident that these results will increase the availability of graphene for single-molecule experiments.

4.4. Publication IV: Graphene Energy Transfer for Single-Molecule Biophysics, Biosensing, and Super-Resolution Microscopy

I. Kamińska,* **J. Bohlen**,* R. Yaadav, P. Schüler, M. Raab, T. Schröder, J. Zähringer, K. Zielonka, S. Krause, P. Tinnefeld (* equal contribution)

The work of verifying the distance dependence between graphene and organic dyes by the use of nanopositioners (chapter 4.2)[49], and finding the best method for graphene-on-glass coverslips (chapter 4.3)[50] sets out the basis to bring GET to the next level. In this part of the thesis, the broad application capability of GET is demonstrated.

In first experiments, we study the possibility to study a two color assay at different distances to the graphene surface. Another two-color experiment focusses on the different binding behavior of an L-shaped DNA origami structure to the graphene surface. This is studied in more detail because not only the pyrene labeled oligonucleotides show $\pi - \pi$-stacking to the graphene but also the rigid π system of the DNA helices is interacting with graphene. To quantify these interactions, we introduce two different dyes on the DNA origami structure to resolve the relative orientation of the DNA origami structure with the help of graphene energy transfer (GET) (Figure 19 a)). The results show that an increase of pyrene labeled oligonucleotides increases the amount of correct standing L-shaped DNA origami structures. This part underlines that GET is feasible to measure multicolor samples simultaneously.

To illustrate dynamics with GET, the L-shaped DNA origami structure is functionalized with a dye labeled pointer, which can transiently bind at two binding sites that differ in their distance to graphene. By using different lengths of complimentary nucleotides at the binding sites the dwell times at the binding sites are varying by four orders of magnitude. This strategy can be transferred to biosensing applications by equipping the DNA origami structure with a 44 nt double stranded tether, which besides a dye also is provided with a linker for a biomolecule (Figure 19 b)). The experiments demonstrate that the presence of a target molecule or increase of the viscosity results in a slower diffusion than the tether only. As a second biosensor a DNA origami structure is provided with a dye labeled sensing unit. In the beginning the dye is close to graphene and after the addition of a single stranded target DNA the sensing unit can reach a higher position and the quenching of the dye is reduced (Figure 19 c)). GET as a quencher in biosensor assays has the advantage over FRET and quencher-based methods that graphene is unbleachable and due to the different distance dependence longer target strands can be used.

We combine FRET and GET on a static and dynamic DNA origami sample to obtain the relative orientation of a FRET pair in space and observe the influence of FRET to GET and *vice versa*.

For the static case we use three variations of FRET assemblies in the DNA origami nanopillar, in which the acceptor always stays at the same position and the donor is at different heights to the graphene. The assembly of the dynamic FRET on the other hand is implemented in the L-shaped DNA origami structure. The donor labeled pointer can access two different binding sites with the lower binding site having larger FRET and GET than the upper site (Figure 19 e)). We show that from the combination of both energy transfers the orientation in space of the FRET pair in the static and dynamic case can be resolved. In general, the energy transfers from GET and FRET are independent from each other. We only find a discrepancy for the samples that are nearest to the graphene surface. This might be due to an additional energy transfer from the donor to the acceptor through graphene plasmons, the graphene plasmon energy transfer (GPET). This kind of energy transfer has already been described in theoretical works in the infrared[157–160] but needs further experiments to be proven in the visible wavelength range.

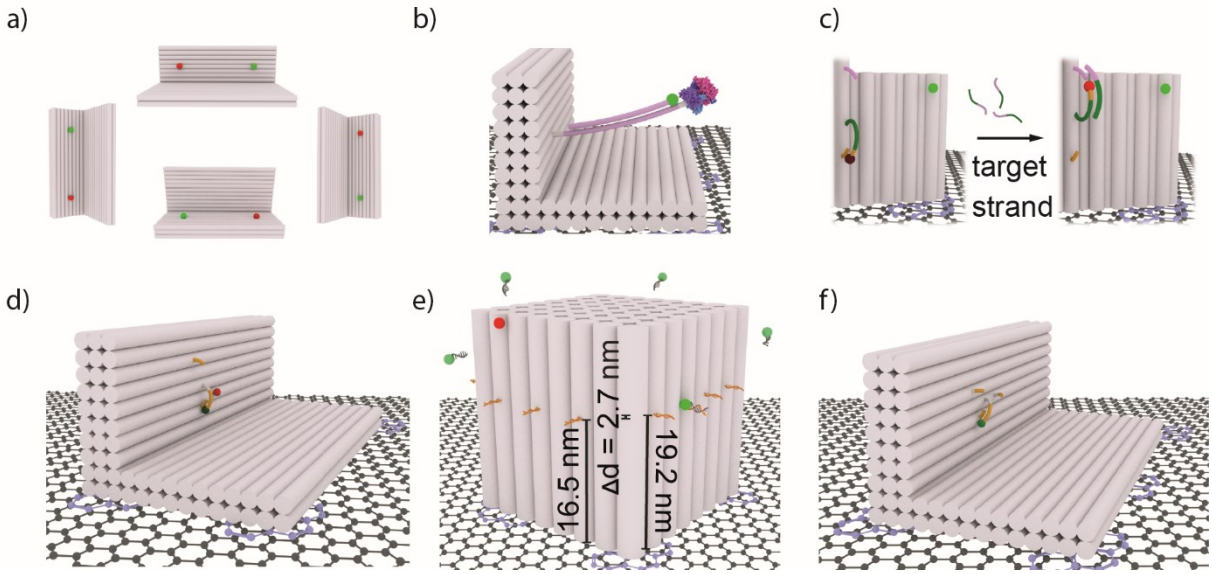

Figure 19: DNA origami structures for GET applications. a) Multiple possible binding geometries of the L-shaped DNA origami structure to graphene due to additional π-π stacking of the helices. b) Dynamic investigations and a bioassay was realized by adding a tether the L-shaped DNA origami structure. c) As a biosensing assay a dye is more quenched by graphene and after binding of the target strand a higher binding site is accessible (right part of c)). d) For FRET measurements a dynamic DNA origami structure which can transiently bind to two binding sites at different heights. e) The cubic DNA origami structure contains different binding sites only 2.7 nm apart for super-resolution imaging of the z-distance with DNA-PAINT. f) Tracking of a dye was realized by equipping the L-shaped DNA origami structure with three different binding sites.

As a final experiment, we use GET to improve super-resolution techniques. With a wide-field setup and the technique of DNA-PAINT a resolution of 6 nm[75–80] can be resolved in the x/y plane. However, a similar isotropic resolution in x/y/z is difficult to obtain.[38,82–84] GET applied in super-resolution microscopy enables a z-resolution of high accuracy by converting the distance dependent fluorescence intensity quenching into the distance between the dye and the graphene surface. The acquired quenched fluorescence intensity is compared to a reference

dye. With the combination of GET and DNA-PAINT we achieve a 3D isotropic resolution on a cubic DNA origami structure, in which opposite sides have DNA-PAINT binding strands at the same height and adjacent sides are 2.7 nm apart (Figure 19 e)). Furthermore, we track a dye labeled pointer that can bind to three different binding sites, which are differing in height to the graphene surface (Figure 19 f)). In comparison to laborious microscopic methods like 3D MIN-FLUX[84] a similar resolution is achieved. The great advantage of combined GET and super-resolution techniques is the suppression of unspecific binding as dyes that bind to the surface will be completely quenched. Furthermore, no sophisticated microscopes like MINFLUX[75,81,84] are needed.

Here we show a plethora of applications for graphene as a broad band unbleachable acceptor. We are confident that this unique material can be easily implemented to complex samples in order to answer questions in many different fields of interest like biology, physics, and material science.

5. Conclusion and Outlook

This thesis focuses on the influence of an NP or a graphene surface to a single dye or FRET pair. In addition to the basic understanding of energy transfers and the dependency of simultaneous energy transfers, a wealth of applications is demonstrated.

In the first part of this thesis, FRET is studied close to a metallic NP. With our single-molecule approach of self-assemble DNA origami structures we can circumvent problems of previous publications.[40–46] These problems contain binding of NP, relative orientations of the FRET pair and NP to the incident light, as well as constant distances between the plasmonic NP and the FRET pair. To answer the question of the individual influences of the NP on the donor and acceptor, the acceptor bleaching approach is applied. Our data shows that the FRET rate constant k_{ET} stays constant with an increasing diameter of the plasmonic gold NP, while the FRET efficiency E is decreasing due to the increasing radiative and non-radiative rate constants induced by the NP. Our data is underlined by numerical simulations from the *Fernández-Domínguez* group. Similar results can also be found in a new publication,[156] in which a cantilever is used as a plamonic antenna. Another interpretation of our results would be that not only E is changed due to the presence of the NP but also the whole distance dependence of FRET is shifted to a shorter donor-acceptor distance (see Figure 20 a)). Based on our results and Eq. 5.1 (derivation see chapter 7) the shifted energy transfer efficiency E_{NP} can be calculated.

$$E_{NP} = \frac{r_0^6}{r^6 + r_0^6 + r^6\,\tau_D\,k_{D,NP}} \qquad (Eq.\,5.1)$$

The FRET energy transfer efficiency E_{NP} is calculated from the fluorescence lifetime of the donor after acceptor bleaching τ_D (3.27 ns) and the rate constant of the energy transfer between donor and NP $k_{D,NP}$ (1.06 ns^{-1}). This hypothesis can be proven by adapting the rectangular DNA origami structure of this project in a way that the acceptor is shifted relative to the donor and NP (see Figure 20 b)). With only four different FRET pairs at distances between 0 and 8 nm the shifted distance dependence can already be illustrated. Finally, FRET in combination with one or even two coupled NPs can be used to study distances in the high FRET regime (< 4 nm), where FRET alone is not sensitive enough. This has the potential to answer biological question for example in the context of protein folding.

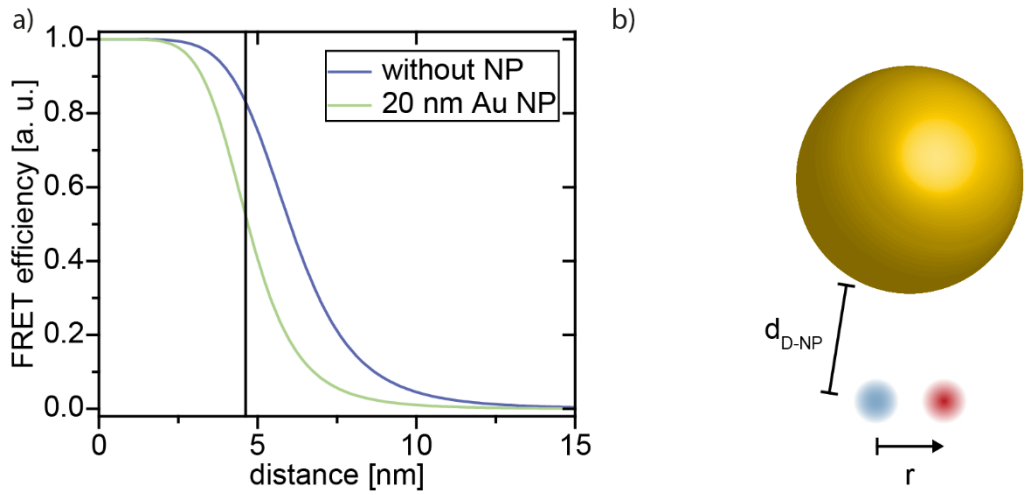

Figure 20: Outlook for FRET samples close to a spherical plasmonic NP. a) Based on the extracted FRET efficiencies the shifted distance dependence in presence of a 20 nm Au NP is calculated. The distance dependence can be proven by designing DNA origami structures with a constant distance between donor and NP surface ($d_{D\text{-}NP}$) and varying the distance between donor and acceptor r (b)).

In the second part of this thesis graphene is introduced as a broadband, unbleachable acceptor to extend the range of FRET above 10 nm. Therefore, the second main part of this thesis is the quantification of the graphene distance dependence and the transfer of graphene to glass coverslips as well as a multitude of GET applications. The distance dependence is tested by positioning organic dyes with DNA origami structures at defined heights above the graphene surface. An immobilization of the DNA origami structures is achieved by pyrene-modifications, which show a π-π stacking interaction to the graphene surface. This immobilization method has the advantage that the DNA origami structure is noninvasively attached to the graphene, which does not change the properties of graphene. Our results show a d^{-4} behavior with regard to the distance between the graphene surface and the fluorophore and is in good agreement with theoretical calculations. Hence, we can extract the specific distance where 50% of the energy is transferred to graphene (d_0) for different organic dyes. Again our approach of controlled dye positioning circumvents the drawbacks from other publications[51,54–57] like positioning dyes at defined heights, avoiding dye-dye interactions, and using emitters with constant properties. To find the best method to fabricate graphene-on-glass-coverslips, we compared in total ten different combinations of established methods,[59–65] and quantified those with FLIM, Raman, and AFM. While FLIM and AFM show similar results, Raman displays only minor correlations because of the two orders of magnitude larger sensing area of Raman. Here, the DNA origami structures serve as a precursor to verify the quality of the graphene sample. Afterwards to the most reliable method a second DNA origami structure is added. This second DNA origami structure has a pointer, which can transiently bind to two different binding sites protruding from the DNA origami structure. Both binding sites differ by the distance to the graphene surface, which yields a different quenching of the dye labeled pointer.

Finally, we establish GET as a tool in biophysics, biosensing, and super-resolution. To this end, we first show that we can resolve spectrally separated fluorophores at different heights. Furthermore, we develop an L-shaped DNA origami, which is based on a bilayer of DNA helices to avoid direct quenching from graphene and a trilayer wall for the attachment of e.g. dyes and binding sites (see Figure 21 a)). In a multicolor assay GET helps to reveal the orientation of the L-shape DNA origami structure on the graphene surface. This DNA origami structure is found to vary in its orientation to the graphene surface. Not only $\pi - \pi$-stacking from the pyrene to the graphene is observed, but also the rigid π-system of the DNA helices itself, which face to the sides of the L-shape, can bind to graphene (see Figure 21 a) light blue). An increase from 8 to 42 pyrene labeled oligonucleotides cannot completely solve this issue. For further investigations a second version of the L-shaped DNA origami structure has to be designed, which is illustrated in Figure 21 b) and c), the so-called L2. To avoid $\pi - \pi$ stacking from the helices the edges of the L2 have an uneven design. Furthermore, at the kink (light red) the helices are facing directly to the graphene surface. This should enable the use of the helical $\pi - \pi$ stacking to our advantage (light blue) to immobilize the DNA origami structure.

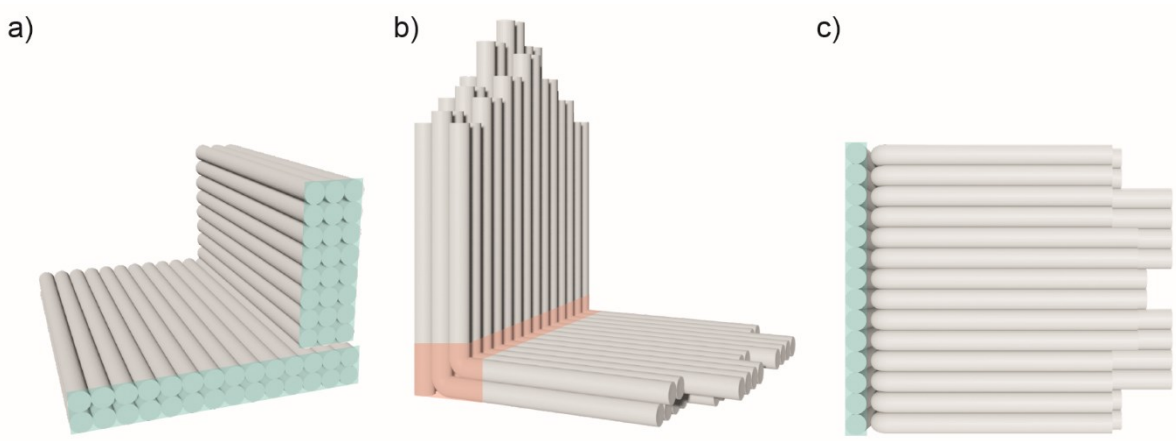

Figure 21: Adapting the L-shaped DNA origami design. a) Illustration of the established L-shaped DNA origami structure with the π-system of the helices highlighted in light blue. b) Improved L-shaped DNA origami structure "L2" with 90° kink (light red), helical π-System (light blue) and uneven helical edges which should enhance the correct standing of the DNA origami structure. The side view and the view from the bottom(c)) are shown. For better overview not all π-systems are highlighted.

For biosensing, we develop a DNA origami structure with a tether as sensing unit for biomolecules and observe the fluctuation in media of different viscosities as well as absence and presence of biomolecules. As a second biosensing concept a DNA origami construct is used, where the dye is close to the graphene surface in the beginning and after the addition of a target strand the dye can bind to a binding site further apart from the graphene surface. Because of the different distance dependence (up to 40 nm) of GET compared to FRET or quencher-based methods (~10 nm) GET permits the possibility to detect larger or even multiple targets at once and it is easier to work with an unbleachable acceptor like graphene.

The third project focusses on the combination of FRET and GET. Here, we can extract the relative orientation of the FRET pair in space and observe an independent behavior of FRET in presence of GET and *vice versa* in most of the samples. For FRET samples, which are nearest to the graphene surface, a discrepancy is revealed, which might be accounted for by an additional energy transfer from the donor through the graphene plasmons to the acceptor (graphene plasmon energy transfer: GPET). To verify this GPET, which was already presented in theoretical works[157–160] further experiments are needed. For a horizontally FRET pair design, we observe this discrepancy starting at a height of 16 nm and lower. For a possible design of GPET investigation horizontally arranged FRET pairs should be placed at a distance between 16 nm and 10 nm to the graphene surface. The lower limit is 10 nm as every dye placed below this height is already quenched by 90% only by GET, and the donor is quenched even more when FRET occurs. To still gain enough fluorescence signal from dyes placed close to the graphene surface, measurements can also be performed at higher laser powers but this usually leads to a fast bleaching of the acceptor under excitation of the donor.

Lastly, for a super-resolution assay, we realize two different samples: a cubic DNA origami structure to resolve a height difference of only 2.7 nm using DNA-PAINT, and a DNA origami structure with a pointer, where we even got a better isotopic resolution than the current best MINFLUX measurement.[84] For DNA-PAINT or biological samples we gain the advantage to not observe any unspecific binding because the fluorescence signal will be quenched when fluorescent entities bind to the graphene surface.

For further experiments like imaging whole cells or arrays of DNA origami structures as biosensors, wide-field measurements are preferred over confocal microscopy as wide-field measurements are recording a larger region of interest (ROI). Wide-field microscopy in general is a fluorescence intensity-based method, which makes it dependent on the excitation laser intensity. Of course fluorescence lifetime methods to be implemented in wide-field microscopy are around[161–163] but these suffer from a low quantum yield of the camera[163] or a low sensitivity,[161,162] which makes it hard to combine those with super-resolution techniques on the single-molecule level. Another drawback of wide-field measurements is the Gaussian profile of the excitation laser. Therefore, molecules close to the center of the laser are excited with a higher laser power and emit more intensity compared to molecules further apart from the laser beam center. To extract the distance from GET data, a reference structure is needed. Reference structures can be dyes without any quenching like on glass or >50 nm away from the graphene surface but also dyes at a defined height in the DNA origami structure. This heterogeneous illumination in a wide-field setup makes it difficult to position reference structures for GET because even a reference structure a few pixels (pixel ≈ 100 nm) away has a different fluorescence intensity. A novel approach to avoid this problem is by extending the microscope either

with FIFI (flat illumination for field independent imaging)[164] or a piShaper,[165] which leads to a homogenous illumination. But placing reference structures to observe biomolecules might still not be straight forward. The first idea for a reference structure is to position DNA origami structures between the biomolecules of interest and refer to those as a reference, but the dye properties might change depending on the environment.[166–170] Therefore, a referencing with the dye itself at the biomolecule of interest seems to be the only possible way to circumvent this problem. This self-referencing can be realized by electrically contacting or doping graphene and make it a switchable acceptor. Compared to undoped graphene (Figure 22 a)), contacting graphene with a negative potential leads to p-doping, which means that electrons are removed from the valence band. When the energy between the valence and conduction band is larger than the energy from the emitting dye no GET takes place and no quenching is observed (Figure 22 b)).[101,171,172] This finally makes it possible to implemented GET beyond DNA origami structures.

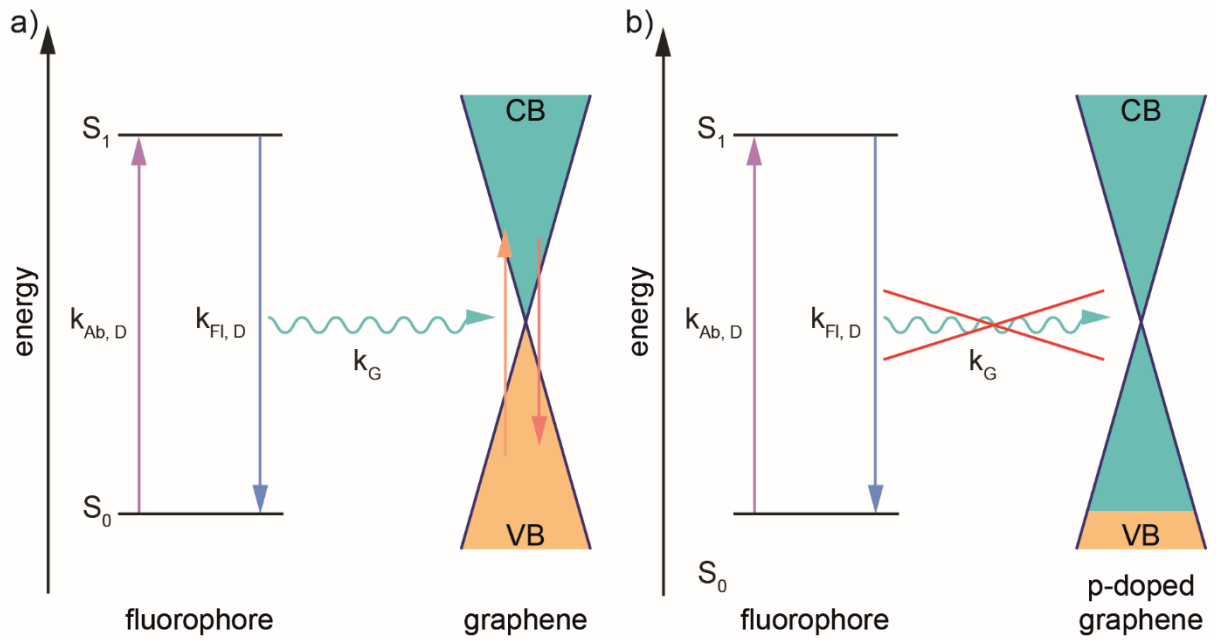

Figure 22: Jablonski diagram of undoped (a)) and p-doped graphene (b)). In case of the undoped graphene an electron from graphene is excited from the VB to the CB (orange arrow) and decays back to the VB (red arrow) after excited from a dye in close proximity (waved torques arrow). The contacting of graphene with a negative voltage yields in a removing of the electron in the VB of graphene. When the applied voltage is large enough the energy transfer from the donor dye is too low to excited an electron from the VB to the CB. Measurements with and without voltage make it possible to implemented graphene as a switchable acceptor.

Another way to make GET more feasible for biomolecules or even cells is to increase the working distance, which is limited at a monolayer of graphene to roughly 40 nm. The sensing limit can be increased by using multilayer graphene. Under the assumption that additional layers show the same quenching behavior Eq. 2.6 can be expanded with the number of layers *n*.

$$\eta = \frac{1}{1 + \frac{d^4}{d_o^4\, n}} \qquad (Eq. 5.2)$$

Figure 23 a) illustrates that together with d_0 also the working range will be increased. When comparing the working range of every layer where η is 4%, the overall impact is only minor: 40 nm for monolayer, 48 nm for bilayer, 53 nm for trilayer, 57 nm for tetralayer, and 60 nm for pentalayer. However, the production of multilayer graphene is still challenging.

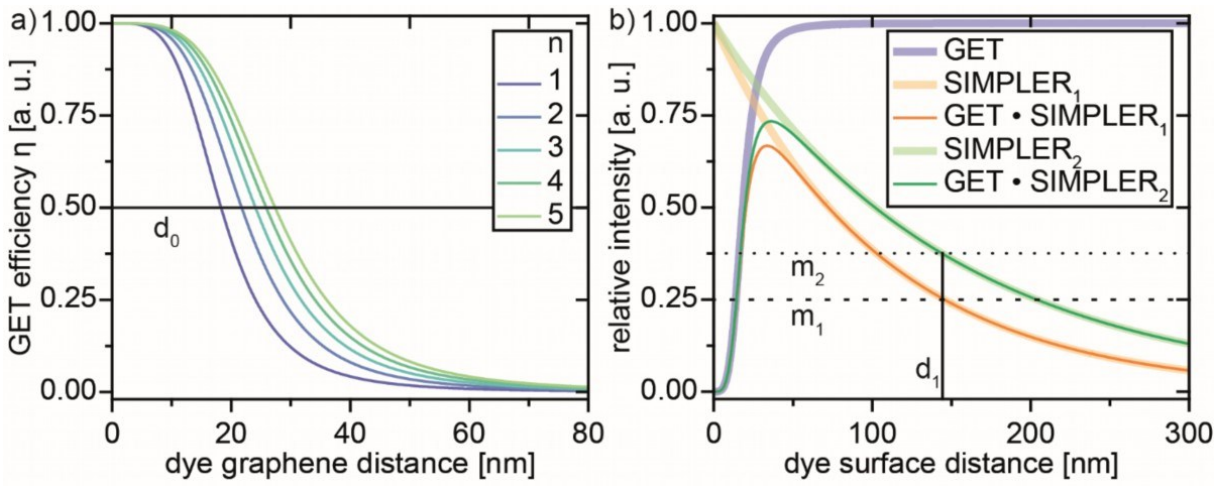

Figure 23: Expanding the distance dependence of GET. a) Calculations of multilayers show a minor increase of d_0 and the working range from monolayer (blue) to pentalayer (green). b) Illustration of GET (blue), SIMPLER (light orange, light green) and the combination of both (orange, green). As both methods are contrary to each other a fluorescence intensity value shows ambiguity in height as it can belong to two different distances. When a measurement m_1 (θ = 69°, light orange, orange) is performed and a fluorescence intensity of 25% relative to the maximum fluorescence intensity is measured this could either be a height of 8 nm or 145 nm. A second measurement m_2 with a different TIRF angle θ (65°, light green, green) delivers a relative fluorescence intensity of 37%, which gives an unambiguous result for distance d_1 of 145 nm.

Another approach to improve the working range of GET is the combination with SIMPLER (Supercritical Illumination Microscopy Photometric z-Localization with Enhanced Resolution). SIMPLER uses the decaying evanescent field of TIRF to estimate the axial position of a dye.[82] Thereby the fluorescence intensity of a dye further apart from the surface decreases with the distance (see Figure 23 b), light orange or light green). GET shows the contrary effect where a dye, which is further apart from the surface, is emitting more fluorescence intensity (see Figure 23 b), light blue). A combination of both techniques would result in a fluorescence intensity that can be attributed to two potentially different heights for a molecule. A solution to circumvent this problem is to perform measurements with different TIRF angles θ. To clarify this point, when combined SIMPLER and GET is measured (m_1) a relative fluorescence intensity of 25% at a TIRF angle θ of 69° is detected. This could be a distance of either 8 nm or 145 nm to the graphene surface. A second measurement (m_2) with an angle of 65° and a relative fluorescence intensity of 37% clarifies the unambiguity to the distance (d_1) of 145 nm.

When fluorescence lifetime-based cameras are improved in their quantum yield in the future, they can also be feasible for the implementation of GET and SIMPLER. For those cameras the information of the fluorescence lifetime is showing the influence of GET only to the dye, while the fluorescence intensity contains combined information of SIMPLER and GET.

A noteworthy observation during the GET measurements is the degradation of graphene in presence of H_2O_2 as a byproduct of the oxygen scavenging system glucose oxidase-catalase-glucose, the triplet quencher cyclooctatetraene (COT), and longtime laser exposure. To circumvent the byproduct H_2O_2, the oxygen scavenging system is exchanged to protocatechuic acid (PCA) and the enzyme protocatechuate decarboxylase (PCD). While the longtime laser exposure[173,174] and H_2O_2[175,176] is already investigated, only simulated data for COT on graphene is published.[177,178] Nevertheless, this underlines the possible use of graphene as a sensor for the detection of chemicals like COT or H_2O_2 and biomolecules.[179,180] The laser induced destruction of graphene can be used to cut defined patterns into the surface. This facilitates a patterning at distances above the diffraction limit. The uncovered glass surface is then accessible for biomolecules enabling high throughput measurements without the stochastic limitations of single-molecule measurements.[181] Patterning with a laser has the advantage over other methods[182–186] that no additional chemical working steps need to be applied, like etching, which can harm the graphene.

To sum up the work of this thesis, the combination of NPs and FRET reports a possible shift of the distance dependence in FRET that potentially helps to resolve distances or dynamics below the sensitive FRET regime. Proceeding on the energy transfer between fluorescent dyes and NPs, GET shows a large variety of possibilities. A problem that occurred from DNA origami immobilization on graphene is an additional $\pi - \pi$-stacking of DNA that complicates correct standing of the L-shaped DNA origami structure. To increase the correct standing fraction of the L-shaped DNA origami structure, a second L-shaped DNA origami structure, which uses the previous knowledge of binding characteristics of DNA and pyrene to the graphene surface has to be developed. Based on the advantages of nanopositioners several assays can be designed using GET. A FRET pair close to the graphene surface (< 16 nm) shows indications of GPET,[157–160] which has to be accurately investigated. Besides further investigations on newly designed samples also microscope assemblies need to be improved. For experiments on the wide-field microscope, for example, the illumination of the ROI has to be more homogeneous, which could be realized by the introduction of either FIFI or a piShaper to the microscope.[164,165] Furthermore, applying a potential to graphene could facilitate to implement graphene as a switchable acceptor, which represents a novel referencing approach.[101,171,172] While the working range of graphene is only minor advanced by the addition of multiple layers

of graphene the combination of SIMPLER[82] and GET shows an increase of up to a few hundred nanometers. A homogeneous illumination, switchable graphene, and a larger working range are crucial for the investigation of biological samples. Also the influence of chemicals[175–178] or laser radiation[173,174] to graphene shows an application potential of graphene as a sensor. Laser patterning in graphene could make it feasible for high throughput measurements.

This work underlines the potential to extend the well-studied energy transfer of FRET with NPs or graphene. Besides quantitative investigations of those energy transfers also a plethora of GET applications is shown. In addition, future experiments will further expand the implementation of the presented energy transfers to broader scientific fields.

6. References

[1] G. D. Scholes, G. R. Fleming, A. Olaya-Castro, R. van Grondelle. Lessons from nature about solar light harvesting, *Nature chemistry* **2011**, *3* (10), 763–774.

[2] H. van Amerongen, R. Croce. Light harvesting in photosystem II, *Photosynth Res* **2013**, *116* (2-3), 251–263.

[3] R. Croce, H. van Amerongen. Natural strategies for photosynthetic light harvesting, *Nature chemical biology* **2014**, *10* (7), 492–501.

[4] X. Hu, A. Damjanović, T. Ritz, K. Schulten. Architecture and mechanism of the light-harvesting apparatus of purple bacteria, *Proceedings of the National Academy of Sciences of the United States of America* **1998**, *95* (11), 5935–5941.

[5] T. Forster. Energiewanderung und Fluoreszenz, *Naturwissenschaften* **1946**, *33* (6), 166–175.

[6] L. Stryer, R. P. Haugland. Energy transfer: a spectroscopic ruler, *Proceedings of the National Academy of Sciences of the United States of America* **1967**, *58* (2), 719–726.

[7] E. Sobakinskaya, M. Am Schmidt Busch, T. Renger. Theory of FRET "Spectroscopic Ruler" for Short Distances: Application to Polyproline, *The journal of physical chemistry. B* **2018**, *122* (1), 54–67.

[8] B. Hellenkamp, S. Schmid, O. Doroshenko, O. Opanasyuk, R. Kühnemuth, S. Rezaei Adariani, B. Ambrose, M. Aznauryan, A. Barth, V. Birkedal, M. E. Bowen, H. Chen, T. Cordes, T. Eilert, C. Fijen, C. Gebhardt, M. Götz, G. Gouridis, E. Gratton, T. Ha, P. Hao, C. A. Hanke, A. Hartmann, J. Hendrix, L. L. Hildebrandt, V. Hirschfeld, J. Hohlbein, B. Hua, C. G. Hübner, E. Kallis, A. N. Kapanidis, J.-Y. Kim, G. Krainer, D. C. Lamb, N. K. Lee, E. A. Lemke, B. Levesque, M. Levitus, J. J. McCann, N. Naredi-Rainer, D. Nettels, T. Ngo, R. Qiu, N. C. Robb, C. Röcker, H. Sanabria, M. Schlierf, T. Schröder, B. Schuler, H. Seidel, L. Streit, J. Thurn, P. Tinnefeld, S. Tyagi, N. Vandenberk, A. M. Vera, K. R. Weninger, B. Wünsch, I. S. Yanez-Orozco, J. Michaelis, C. A. M. Seidel, T. D. Craggs, T. Hugel. Precision and accuracy of single-molecule FRET measurements-a multi-laboratory benchmark study, *Nature methods* **2018**, *15* (9), 669–676.

[9] I. Kamińska, J. Bohlen, R. Yaadav, P. Schüler, M. Raab, T. Schröder, J. Zähringer, K. Zielonka, S. Krause, P. Tinnefeld. Graphene Energy Transfer for Single-Molecule Biophysics, Biosensing, and Super-Resolution Microscopy, *Advanced materials (Deerfield Beach, Fla.)* **2021**, *33* (24), e2101099.

[10] A. Hillisch, M. Lorenz, S. Diekmann. Recent advances in FRET: distance determination in protein–DNA complexes, *Current Opinion in Structural Biology* **2001**, *11* (2), 201–207.

[11] E. Lerner, T. Cordes, A. Ingargiola, Y. Alhadid, S. Chung, X. Michalet, S. Weiss. Toward dynamic structural biology: Two decades of single-molecule Förster resonance energy transfer, *Science (New York, N.Y.)* **2018**, *359* (6373).

[12] R. Roy, S. Hohng, T. Ha. A practical guide to single-molecule FRET, *Nature methods* **2008**, *5* (6), 507–516.

[13] S. Schulz, A. Gietl, K. Smollett, P. Tinnefeld, F. Werner, D. Grohmann. TFE and Spt4/5 open and close the RNA polymerase clamp during the transcription cycle, *Proceedings of the National Academy of Sciences of the United States of America* **2016**, *113* (13), E1816-25.

[14] E. Lerner, A. Barth, J. Hendrix, B. Ambrose, V. Birkedal, S. C. Blanchard, R. Börner, H. Sung Chung, T. Cordes, T. D. Craggs, A. A. Deniz, J. Diao, J. Fei, R. L. Gonzalez, I. V. Gopich, T. Ha, C. A. Hanke, G. Haran, N. S. Hatzakis, S. Hohng, S.-C. Hong, T. Hugel, A. Ingargiola, C. Joo, A. N. Kapanidis, H. D. Kim, T. Laurence, N. K. Lee, T.-H. Lee, E. A. Lemke, E. Margeat, J. Michaelis, X. Michalet, S. Myong, D. Nettels, T.-O. Peulen, E. Ploetz, Y. Razvag, N. C. Robb, B. Schuler, H. Soleimaninejad, C. Tang, R. Vafabakhsh, D. C. Lamb, C. am Seidel, S. Weiss. FRET-based dynamic structural biology: Challenges, perspectives and an appeal for open-science practices, *eLife* **2021**, *10*.

[15] I. H. Stein, C. Steinhauer, P. Tinnefeld. Single-molecule four-color FRET visualizes energy-transfer paths on DNA origami, *Journal of the American Chemical Society* **2011**, *133* (12), 4193–4195.

[16] S. Buckhout-White, C. M. Spillmann, W. R. Algar, A. Khachatrian, J. S. Melinger, E. R. Goldman, M. G. Ancona, I. L. Medintz. Assembling programmable FRET-based photonic networks using designer DNA scaffolds, *Nature communications* **2014**, *5*, 5615.

[17] P. K. Dutta, R. Varghese, J. Nangreave, S. Lin, H. Yan, Y. Liu. DNA-directed artificial light-harvesting antenna, *Journal of the American Chemical Society* **2011**, *133* (31), 11985–11993.

[18] L. Olejko, I. Bald. FRET efficiency and antenna effect in multi-color DNA origami-based light harvesting systems, *RSC Adv.* **2017**, *7* (39), 23924–23934.

[19] E. A. Hemmig, C. Creatore, B. Wünsch, L. Hecker, P. Mair, M. A. Parker, S. Emmott, P. Tinnefeld, U. F. Keyser, A. W. Chin. Programming Light-Harvesting Efficiency Using DNA Origami, *Nano letters* **2016**, *16* (4), 2369–2374.

[20] K. Trofymchuk, A. Reisch, P. Didier, F. Fras, P. Gilliot, Y. Mely, A. S. Klymchenko. Giant light-harvesting nanoantenna for single-molecule detection in ambient light, *Nat. Photonics* **2017**, *11* (10), 657–663.

[21] D. Mathur, A. Samanta, M. G. Ancona, S. A. Díaz, Y. Kim, J. S. Melinger, E. R. Goldman, J. P. Sadowski, L. L. Ong, P. Yin, I. L. Medintz, *ACS nano* **2021**.

[22] P. W. K. Rothemund. Folding DNA to create nanoscale shapes and patterns, *Nature* **2006**, *440* (7082), 297–302.

[23] J. J. Schmied, C. Forthmann, E. Pibiri, B. Lalkens, P. Nickels, T. Liedl, P. Tinnefeld. DNA origami nanopillars as standards for three-dimensional superresolution microscopy, *Nano letters* **2013**, *13* (2), 781–785.

[24] J. J. Schmied, M. Raab, C. Forthmann, E. Pibiri, B. Wünsch, T. Dammeyer, P. Tinnefeld. DNA origami-based standards for quantitative fluorescence microscopy, *Nature protocols* **2014**, *9* (6), 1367–1391.

[25] J. J. Schmied, A. Gietl, P. Holzmeister, C. Forthmann, C. Steinhauer, T. Dammeyer, P. Tinnefeld. Fluorescence and super-resolution standards based on DNA origami, *Nature methods* **2012**, *9* (12), 1133–1134.

[26] M. Raab, I. Jusuk, J. Molle, E. Buhr, B. Bodermann, D. Bergmann, H. Bosse, P. Tinnefeld. Using DNA origami nanorulers as traceable distance measurement standards and nanoscopic benchmark structures, *Scientific reports* **2018**, *8* (1), 1780.

[27] Z. Liang, J. Sun, Y. Jiang, L. Jiang, X. Chen. Plasmonic Enhanced Optoelectronic Devices, *Plasmonics* **2014**, *9* (4), 859–866.

[28] Y. Hu, G. Liu, Z. Liu, X. Liu, X. Zhang, Z. Cai, M. Liu, H. Gao, G. Gu. Extraordinary Optical Transmission in Metallic Nanostructures with a Plasmonic Nanohole Array of Two Connected Slot Antennas, *Plasmonics* **2015**, *10* (2), 483–488.

[29] E. A. Coronado, E. R. Encina, F. D. Stefani. Optical properties of metallic nanoparticles: manipulating light, heat and forces at the nanoscale, *Nanoscale* **2011**, *3* (10), 4042–4059.

[30] M. L. Juan, M. Righini, R. Quidant. Plasmon nano-optical tweezers, *Nat. Photonics* **2011**, *5* (6), 349–356.

[31] L. Grabenhorst, K. Trofymchuk, F. Steiner, V. Glembockyte, P. Tinnefeld. Fluorophore photostability and saturation in the hotspot of DNA origami nanoantennas, *Methods and applications in fluorescence* **2020**, *8* (2), 24003.

[32] I. Kaminska, J. Bohlen, S. Mackowski, P. Tinnefeld, G. P. Acuna. Strong Plasmonic Enhancement of a Single Peridinin-Chlorophyll a-Protein Complex on DNA Origami-Based Optical Antennas, *ACS nano* **2018**, *12* (2), 1650–1655.

[33] M. Pfeiffer, K. Trofymchuk, S. Ranallo, F. Ricci, F. Steiner, F. Cole, V. Glembockyte, P. Tinnefeld. Single antibody detection in a DNA origami nanoantenna, *iScience* **2021**, *24* (9), 103072.

[34] G. P. Acuna, F. M. Möller, P. Holzmeister, S. Beater, B. Lalkens, P. Tinnefeld. Fluorescence enhancement at docking sites of DNA-directed self-assembled nanoantennas, *Science (New York, N.Y.)* **2012**, *338* (6106), 506–510.

[35] Trofymchuk Kateryna, Glembockyte Viktorija, Grabenhorst Lennart, Steiner Florian, Vietz Carolin, Close Cindy, Pfeiffer Martina, Richter Lars, Schütte Max L., Selbach Florian, Yaadav Renukka, Zähringer Jonas, Wei Qingshan, Ozcan Aydogan, Lalkens Birka, Acuna

Guillermo P., Tinnefeld Philip, *Addressable Nanoantennas with Cleared Hotspots for Single-Molecule Detection on a Portable Smartphone Microscope*, Zenodo **2020**.

[36] G. P. Acuna, M. Bucher, I. H. Stein, C. Steinhauer, A. Kuzyk, P. Holzmeister, R. Schreiber, A. Moroz, F. D. Stefani, T. Liedl, F. C. Simmel, P. Tinnefeld. Distance dependence of single-fluorophore quenching by gold nanoparticles studied on DNA origami, *ACS nano* **2012**, *6* (4), 3189–3195.

[37] J. Bohlen, Á. Cuartero-González, E. Pibiri, D. Ruhlandt, A. I. Fernández-Domínguez, P. Tinnefeld, G. P. Acuna. Plasmon-assisted Förster resonance energy transfer at the single-molecule level in the moderate quenching regime, *Nanoscale* **2019**, *11* (16), 7674–7681.

[38] S. Isbaner, N. Karedla, I. Kaminska, D. Ruhlandt, M. Raab, J. Bohlen, A. Chizhik, I. Gregor, P. Tinnefeld, J. Enderlein, R. Tsukanov. Axial Colocalization of Single Molecules with Nanometer Accuracy Using Metal-Induced Energy Transfer, *Nano letters* **2018**, *18* (4), 2616–2622.

[39] R. Carminati, J.-J. Greffet, C. Henkel, J. M. Vigoureux. Radiative and non-radiative decay of a single molecule close to a metallic nanoparticle, *Optics Communications* **2006**, *261* (2), 368–375.

[40] J. Zhang, Y. Fu, M. H. Chowdhury, J. R. Lakowicz. Enhanced Förster Resonance Energy Transfer on Single Metal Particle. 2. Dependence on Donor-Acceptor Separation Distance, Particle Size, and Distance from Metal Surface, *The journal of physical chemistry. C, Nanomaterials and interfaces* **2007**, *111* (32), 11784–11792.

[41] P. Ghenuche, J. de Torres, S. B. Moparthi, V. Grigoriev, J. Wenger. Nanophotonic enhancement of the Förster resonance energy-transfer rate with single nanoapertures, *Nano letters* **2014**, *14* (8), 4707–4714.

[42] S. Bidault, A. Devilez, P. Ghenuche, B. Stout, N. Bonod, J. Wenger. Competition between Förster Resonance Energy Transfer and Donor Photodynamics in Plasmonic Dimer Nanoantennas, *ACS Photonics* **2016**, *3* (5), 895–903.

[43] J. de Torres, M. Mivelle, S. B. Moparthi, H. Rigneault, N. F. van Hulst, M. F. García-Parajó, E. Margeat, J. Wenger. Plasmonic Nanoantennas Enable Forbidden Förster Dipole-Dipole Energy Transfer and Enhance the FRET Efficiency, *Nano letters* **2016**, *16* (10), 6222–6230.

[44] N. Aissaoui, K. Moth-Poulsen, M. Käll, P. Johansson, L. M. Wilhelmsson, B. Albinsson. FRET enhancement close to gold nanoparticles positioned in DNA origami constructs, *Nanoscale* **2017**, *9* (2), 673–683.

[45] C. Blum, N. Zijlstra, A. Lagendijk, M. Wubs, A. P. Mosk, V. Subramaniam, W. L. Vos. Nanophotonic control of the Förster resonance energy transfer efficiency, *Phys. Rev. Lett.* **2012**, *109* (20), 203601.

[46] J. Hu, M. Wu, L. Jiang, Z. Zhong, Z. Zhou, T. Rujiralai, J. Ma. Combining gold nanoparticle antennas with single-molecule fluorescence resonance energy transfer (smFRET) to study DNA hairpin dynamics, *Nanoscale* **2018**, *10* (14), 6611–6619.

[47] K. S. Novoselov, A. K. Geim, S. V. Morozov, D. Jiang, Y. Zhang, S. V. Dubonos, I. V. Grigorieva, A. A. Firsov. Electric field effect in atomically thin carbon films, *Science (New York, N.Y.)* **2004**, *306* (5696), 666–669.

[48] R. R. Nair, P. Blake, A. N. Grigorenko, K. S. Novoselov, T. J. Booth, T. Stauber, N. M. R. Peres, A. K. Geim. Fine structure constant defines visual transparency of graphene, *Science (New York, N.Y.)* **2008**, *320* (5881), 1308.

[49] I. Kaminska, J. Bohlen, S. Rocchetti, F. Selbach, G. P. Acuna, P. Tinnefeld. Distance Dependence of Single-Molecule Energy Transfer to Graphene Measured with DNA Origami Nanopositioners, *Nano letters* **2019**, *19* (7), 4257–4262.

[50] S. Krause, E. Ploetz, J. Bohlen, P. Schüler, R. Yaadav, F. Selbach, F. Steiner, I. Kamińska, P. Tinnefeld. Graphene-on-Glass Preparation and Cleaning Methods Characterized by Single-Molecule DNA Origami Fluorescent Probes and Raman Spectroscopy, *ACS nano* **2021**, *15* (4), 6430–6438.

[51] F. Federspiel, G. Froehlicher, M. Nasilowski, S. Pedetti, A. Mahmood, B. Doudin, S. Park, J.-O. Lee, D. Halley, B. Dubertret, P. Gilliot, S. Berciaud. Distance dependence of the energy transfer rate from a single semiconductor nanostructure to graphene, *Nano letters* **2015**, *15* (2), 1252–1258.

[52] R. S. Swathi, K. L. Sebastian. Resonance energy transfer from a dye molecule to graphene, *The Journal of chemical physics* **2008**, *129* (5), 54703.

[53] L. Gaudreau, K. J. Tielrooij, G. E. D. K. Prawiroatmodjo, J. Osmond, F. J. García de Abajo, F. H. L. Koppens. Universal distance-scaling of nonradiative energy transfer to graphene, *Nano letters* **2013**, *13* (5), 2030–2035.

[54] Z. Chen, S. Berciaud, C. Nuckolls, T. F. Heinz, L. E. Brus. Energy transfer from individual semiconductor nanocrystals to graphene, *ACS nano* **2010**, *4* (5), 2964–2968.

[55] G. Mazzamuto, A. Tabani, S. Pazzagli, S. Rizvi, A. Reserbat-Plantey, K. Schädler, G. Navickaite, L. Gaudreau, F. S. Cataliotti, F. Koppens, C. Toninelli. Single-molecule study for a graphene-based nano-position sensor, *New Journal of Physics* **2014**, *16* (11), 113007.

[56] A. Brenneis, L. Gaudreau, M. Seifert, H. Karl, M. S. Brandt, H. Huebl, J. A. Garrido, F. H. L. Koppens, A. W. Holleitner. Ultrafast electronic readout of diamond nitrogen-vacancy centres coupled to graphene, *Nature nanotechnology* **2015**, *10* (2), 135–139.

[57] H. Gonçalves, C. Bernardo, C. Moura, R. A. S. Ferreira, P. S. André, T. Stauber, M. Belsley, P. Schellenberg. Long range energy transfer in graphene hybrid structures, *Journal of Physics D: Applied Physics* **2016**, *49* (31), 315102.

[58] J. Kang, D. Shin, S. Bae, B. H. Hong. Graphene transfer: key for applications, *Nanoscale* **2012**, *4* (18), 5527–5537.

[59] S. Gorantla, A. Bachmatiuk, J. Hwang, H. A. Alsalman, J. Y. Kwak, T. Seyller, J. Eckert, M. G. Spencer, M. H. Rümmeli. A universal transfer route for graphene, *Nanoscale* **2014**, *6* (2), 889–896.

[60] X. Li, Y. Zhu, W. Cai, M. Borysiak, B. Han, D. Chen, R. D. Piner, L. Colombo, R. S. Ruoff. Transfer of large-area graphene films for high-performance transparent conductive electrodes, *Nano letters* **2009**, *9* (12), 4359–4363.

[61] S. Bae, H. Kim, Y. Lee, X. Xu, J.-S. Park, Y. Zheng, J. Balakrishnan, T. Lei, H. R. Kim, Y. I. Song, Y.-J. Kim, K. S. Kim, B. Ozyilmaz, J.-H. Ahn, B. H. Hong, S. Iijima. Roll-to-roll production of 30-inch graphene films for transparent electrodes, *Nature nanotechnology* **2010**, *5* (8), 574–578.

[62] J. Song, F.-Y. Kam, R.-Q. Png, W.-L. Seah, J.-M. Zhuo, G.-K. Lim, P. K. H. Ho, L.-L. Chua. A general method for transferring graphene onto soft surfaces, *Nature nanotechnology* **2013**, *8* (5), 356–362.

[63] Y.-C. Lin, C.-C. Lu, C.-H. Yeh, C. Jin, K. Suenaga, P.-W. Chiu. Graphene annealing: how clean can it be?, *Nano letters* **2012**, *12* (1), 414–419.

[64] G. Algara-Siller, O. Lehtinen, A. Turchanin, U. Kaiser. Dry-cleaning of graphene, *Appl. Phys. Lett.* **2014**, *104* (15), 153115.

[65] C. J. An, S. J. Kim, H. O. Choi, D. W. Kim, S. W. Jang, M. L. Jin, J.-M. Park, J. K. Choi, H.-T. Jung. Ultraclean transfer of CVD-grown graphene and its application to flexible organic photovoltaic cells, *J. Mater. Chem. A* **2014**, *2* (48), 20474–20480.

[66] P. Tinnefeld, V. Buschmann, D.-P. Herten, K.-T. Han, M. Sauer. Confocal Fluorescence Lifetime Imaging Microscopy (FLIM) at the Single Molecule Level, *Single Mol.* **2000**, *1* (3), 215–223.

[67] N. Akkilic, S. Geschwindner, F. Höök. Single-molecule biosensors: Recent advances and applications, *Biosensors and Bioelectronics* **2020**, *151*, 111944.

[68] F.-G. Banica, *Chemical Sensors and Biosensors: Fundamentals and Applications*, John Wiley & Sons Incorporated, Hoboken **2012**.

[69] C. Dincer, R. Bruch, E. Costa-Rama, M. T. Fernández-Abedul, A. Merkoçi, A. Manz, G. A. Urban, F. Güder. Disposable Sensors in Diagnostics, Food, and Environmental Monitoring, *Adv. Mater.* **2019**, *31* (30), e1806739.

[70] S. E. Ochmann, C. Vietz, K. Trofymchuk, G. P. Acuna, B. Lalkens, P. Tinnefeld. Optical Nanoantenna for Single Molecule-Based Detection of Zika Virus Nucleic Acids without Molecular Multiplication, *Analytical chemistry* **2017**, *89* (23), 13000–13007.

[71] C. Vietz, B. Lalkens, G. P. Acuna, P. Tinnefeld. Synergistic Combination of Unquenching and Plasmonic Fluorescence Enhancement in Fluorogenic Nucleic Acid Hybridization Probes, *Nano letters* **2017**, *17* (10), 6496–6500.

[72] E. Betzig, G. H. Patterson, R. Sougrat, O. W. Lindwasser, S. Olenych, J. S. Bonifacino, M. W. Davidson, J. Lippincott-Schwartz, H. F. Hess. Imaging intracellular fluorescent proteins at nanometer resolution, *Science (New York, N.Y.)* **2006**, *313* (5793), 1642–1645.

[73] M. J. Rust, M. Bates, X. Zhuang. Sub-diffraction-limit imaging by stochastic optical reconstruction microscopy (STORM), *Nature methods* **2006**, *3* (10), 793–795.

[74] S. T. Hess, T. P. Girirajan, M. D. Mason. Ultra-High Resolution Imaging by Fluorescence Photoactivation Localization Microscopy, *Biophysical journal* **2006**, *91* (11), 4258–4272.

[75] F. Balzarotti, Y. Eilers, K. C. Gwosch, A. H. Gynnå, V. Westphal, F. D. Stefani, J. Elf, S. W. Hell. Nanometer resolution imaging and tracking of fluorescent molecules with minimal photon fluxes, *Science (New York, N.Y.)* **2017**, *355* (6325), 606–612.

[76] M. Raab, J. J. Schmied, I. Jusuk, C. Forthmann, P. Tinnefeld. Fluorescence microscopy with 6 nm resolution on DNA origami, *Chemphyschem a European journal of chemical physics and physical chemistry* **2014**, *15* (12), 2431–2435.

[77] M. Dai, R. Jungmann, P. Yin. Optical imaging of individual biomolecules in densely packed clusters, *Nature nanotechnology* **2016**, *11* (9), 798–807.

[78] E. Rittweger, K. Y. Han, S. E. Irvine, C. Eggeling, S. W. Hell. STED microscopy reveals crystal colour centres with nanometric resolution, *Nat. Photonics* **2009**, *3* (3), 144–147.

[79] S. Strauss, R. Jungmann. Up to 100-fold speed-up and multiplexing in optimized DNA-PAINT, *Nature methods* **2020**, *17* (8), 789–791.

[80] F. Schueder, J. Stein, F. Stehr, A. Auer, B. Sperl, M. T. Strauss, P. Schwille, R. Jungmann. An order of magnitude faster DNA-PAINT imaging by optimized sequence design and buffer conditions, *Nature methods* **2019**, *16* (11), 1101–1104.

[81] L. A. Masullo, F. Steiner, J. Zähringer, L. F. Lopez, J. Bohlen, L. Richter, F. Cole, P. Tinnefeld, F. D. Stefani. Pulsed Interleaved MINFLUX, *Nano letters* **2021**, *21* (1), 840–846.

[82] A. M. Szalai, B. Siarry, J. Lukin, D. J. Williamson, N. Unsain, A. Cáceres, M. Pilo-Pais, G. Acuna, D. Refojo, D. M. Owen, S. Simoncelli, F. D. Stefani. Three-dimensional total-internal reflection fluorescence nanoscopy with nanometric axial resolution by photometric localization of single molecules, *Nature communications* **2021**, *12* (1), 517.

[83] B. Huang, W. Wang, M. Bates, X. Zhuang. Three-dimensional super-resolution imaging by stochastic optical reconstruction microscopy, *Science (New York, N.Y.)* **2008**, *319* (5864), 810–813.

[84] R. Schmidt, T. Weihs, C. A. Wurm, I. Jansen, J. Rehman, S. J. Sahl, S. W. Hell. MINFLUX nanometer-scale 3D imaging and microsecond-range tracking on a common fluorescence microscope, *Nature communications* **2021**, *12* (1), 1478.

[85] R. Jungmann, C. Steinhauer, M. Scheible, A. Kuzyk, P. Tinnefeld, F. C. Simmel. Single-molecule kinetics and super-resolution microscopy by fluorescence imaging of transient binding on DNA origami, *Nano letters* **2010**, *10* (11), 4756–4761.

[86] P. MAX. Zur Theorie des Gesetzes der Energieverteilung in Normalspectrum, *Verh. Deutsch. Phys. Gesell.* **1900**, *2*, 237–245.

[87] P. J. Walla, *Modern biophysical chemistry: Detection and analysis of biomolecules*, Wiley-VCH, Weinheim, Germany **2014**.

[88] M. Kasha. Characterization of electronic transitions in complex molecules, *Discuss. Faraday Soc.* **1950**, *9*, 14.

[89] J. R. Lakowicz, *Principles of fluorescence spectroscopy*, Springer, New York, NY **2006**.

[90] J. Franck, E. G. Dymond. Elementary processes of photochemical reactions, *Trans. Faraday Soc.* **1926**, *21* (February), 536.

[91] E. U. Condon, in *Selected scientific papers of e.u. condon* (Ed.: E. U. Condon), Springer **2012**, p. 1.

[92] M. Born, R. Oppenheimer. Zur Quantentheorie der Molekeln, *Ann. Phys.* **1927**, *389* (20), 457–484.

[93] R. Plessow, *Entwicklung und Charakterisierung einer Methode zur Untersuchung von Makromolekülen mit Hilfe zeitaufgelöster laserinduzierter Fluoreszenz und Anregungs-Emissionsspektroskopie*, Cuvillier Verlag, Göttingen **2004**.

[94] R. E. Dale, J. Eisinger, W. E. Blumberg. The orientational freedom of molecular probes. The orientation factor in intramolecular energy transfer, *Biophysical journal* **1979**, *26* (2), 161–193.

[95] D. Patra, I. Gregor, J. Enderlein. Image Analysis of Defocused Single-Molecule Images for Three-Dimensional Molecule Orientation Studies, *J. Phys. Chem. A* **2004**, *108* (33), 6836–6841.

[96] K. Hübner, H. Joshi, A. Aksimentiev, F. D. Stefani, P. Tinnefeld, G. P. Acuna. Determining the In-Plane Orientation and Binding Mode of Single Fluorescent Dyes in DNA Origami Structures, *ACS nano* **2021**, *15* (3), 5109–5117.

[97] A. N. Bader, S. Hoetzl, E. G. Hofman, J. Voortman, P. M. P. van Bergen en Henegouwen, G. van Meer, H. C. Gerritsen. Homo-FRET imaging as a tool to quantify protein and lipid clustering, *Chemphyschem a European journal of chemical physics and physical chemistry* **2011**, *12* (3), 475–483.

[98] D. L. Dexter. A Theory of Sensitized Luminescence in Solids, *The Journal of chemical physics* **1953**, *21* (5), 836–850.

[99] S. S. Skourtis, C. Liu, P. Antoniou, A. M. Virshup, D. N. Beratan. Dexter energy transfer pathways, *Proceedings of the National Academy of Sciences of the United States of America* **2016**, *113* (29), 8115–8120.

[100] A. C. Ferrari, F. Bonaccorso, V. Fal'ko, K. S. Novoselov, S. Roche, P. Bøggild, S. Borini, F. H. L. Koppens, V. Palermo, N. Pugno, J. A. Garrido, R. Sordan, A. Bianco, L. Ballerini, M. Prato, E. Lidorikis, J. Kivioja, C. Marinelli, T. Ryhänen, A. Morpurgo, J. N. Coleman, V. Nicolosi, L. Colombo, A. Fert, M. Garcia-Hernandez, A. Bachtold, G. F. Schneider, F. Guinea, C. Dekker, M. Barbone, Z. Sun, C. Galiotis, A. N. Grigorenko, G. Konstantatos, A. Kis, M. Katsnelson, L. Vandersypen, A. Loiseau, V. Morandi, D. Neumaier, E. Treossi, V. Pellegrini, M. Polini, A. Tredicucci, G. M. Williams, B. H. Hong, J.-H. Ahn, J. M. Kim, H. Zirath, B. J. van Wees, H. van der Zant, L. Occhipinti, A. Di Matteo, I. A. Kinloch, T. Seyller, E. Quesnel, X. Feng, K. Teo, N. Rupesinghe, P. Hakonen, S. R. T. Neil, Q. Tannock, T. Löfwander, J. Kinaret. Science and technology roadmap for graphene, related two-dimensional crystals, and hybrid systems, *Nanoscale* **2015**, *7* (11), 4598–4810.

[101] A. K. Geim, K. S. Novoselov. The rise of graphene, *Nature materials* **2007**, *6* (3), 183–191.

[102] H. Döscher, T. Schmaltz, C. Neef, A. Thielmann, T. Reiss. Graphene Roadmap Briefs (No. 2): industrialization status and prospects 2020, *2D Mater.* **2021**, *8* (2), 22005.

[103] N. Füllbrunn, Z. Li, L. Jorde, C. P. Richter, R. Kurre, L. Langemeyer, C. Yu, C. Meyer, J. Enderlein, C. Ungermann, J. Piehler, C. You. Nanoscopic anatomy of dynamic multiprotein complexes at membranes resolved by graphene-induced energy transfer, *eLife* **2021**, *10*.

[104] A. Ghosh, A. Sharma, A. I. Chizhik, S. Isbaner, D. Ruhlandt, R. Tsukanov, I. Gregor, N. Karedla, J. Enderlein. Graphene-based metal-induced energy transfer for sub-nanometre optical localization, *Nat. Photonics* **2019**, *13* (12), 860–865.

[105] J. C. Johannsen, S. Ulstrup, F. Cilento, A. Crepaldi, M. Zacchigna, C. Cacho, I. C. E. Turcu, E. Springate, F. Fromm, C. Raidel, T. Seyller, F. Parmigiani, M. Grioni, P. Hofmann. Direct view of hot carrier dynamics in graphene, *Physical review letters* **2013**, *111* (2), 27403.

[106] I. Gierz, J. C. Petersen, M. Mitrano, C. Cacho, I. C. E. Turcu, E. Springate, A. Stöhr, A. Köhler, U. Starke, A. Cavalleri. Snapshots of non-equilibrium Dirac carrier distributions in graphene, *Nature materials* **2013**, *12* (12), 1119–1124.

[107] A. Bostwick, T. Ohta, J. L. McChesney, T. Seyller, K. Horn, E. Rotenberg. Band structure and many body effects in graphene, *Eur. Phys. J. Spec. Top.* **2007**, *148* (1), 5–13.

[108] S. K. Murthy. Nanoparticles in modern medicine: state of the art and future challenges, *International Journal of Nanomedicine* **2007**, *2* (2), 129–141.

[109] E. J. Cho, H. Holback, K. C. Liu, S. A. Abouelmagd, J. Park, Y. Yeo. Nanoparticle characterization: state of the art, challenges, and emerging technologies, *Mol. Pharmaceutics* **2013**, *10* (6), 2093–2110.

[110] L. Kool, F. Dekker, A. Bunschoten, G. J. Smales, B. R. Pauw, A. H. Velders, V. Saggiomo. Gold and silver dichroic nanocomposite in the quest for 3D printing the Lycurgus cup, *Beilstein J. Nanotechnol.* **2020**, *11*, 16–23.

[111] P. Holzmeister, *Tackling the limits of single-molecule spectroscopy with brighter and more stable fluorescence from organic dyes*, Braunschweig **2014**.

[112] P. K. Jain. Gold Nanoparticles for Physics, Chemistry, and Biology. Edited by Catherine Louis and Olivier Pluchery, *Angew. Chem. Int. Ed.* **2014**, *53* (5), 1197.

[113] J. Vogelsang, R. Kasper, C. Steinhauer, B. Person, M. Heilemann, M. Sauer, P. Tinnefeld. A reducing and oxidizing system minimizes photobleaching and blinking of fluorescent dyes, *Angewandte Chemie (International ed. in English)* **2008**, *47* (29), 5465–5469.

[114] T. Cordes, J. Vogelsang, P. Tinnefeld. On the mechanism of Trolox as antiblinking and antibleaching reagent, *Journal of the American Chemical Society* **2009**, *131* (14), 5018–5019.

[115] C. E. Aitken, R. A. Marshall, J. D. Puglisi. An oxygen scavenging system for improvement of dye stability in single-molecule fluorescence experiments, *Biophysical journal* **2008**, *94* (5), 1826–1835.

[116] J. D. WATSON, F. H. CRICK. Molecular structure of nucleic acids; a structure for deoxyribose nucleic acid, *Nature* **1953**, *171* (4356), 737–738.

[117] F. Kilchherr, C. Wachauf, B. Pelz, M. Rief, M. Zacharias, H. Dietz. Single-molecule dissection of stacking forces in DNA, *Science (New York, N.Y.)* **2016**, *353* (6304).

[118] R. E. Dickerson, H. R. Drew, B. N. Conner, R. M. Wing, A. V. Fratini, M. L. Kopka. The anatomy of A-, B-, and Z-DNA, *Science* **1982**, *216* (4545), 475–485.

[119] P. C. Nickels, B. Wünsch, P. Holzmeister, W. Bae, L. M. Kneer, D. Grohmann, P. Tinnefeld, T. Liedl. Molecular force spectroscopy with a DNA origami-based nanoscopic force clamp, *Science (New York, N.Y.)* **2016**, *354* (6310), 305–307.

[120] N. C. Seeman. Nucleic acid junctions and lattices, *Journal of Theoretical Biology* **1982**, *99* (2), 237–247.

[121] S. M. Douglas, H. Dietz, T. Liedl, B. Högberg, F. Graf, W. M. Shih. Self-assembly of DNA into nanoscale three-dimensional shapes, *Nature* **2009**, *459* (7245), 414–418.

[122] R. M. Zadegan, M. D. E. Jepsen, K. E. Thomsen, A. H. Okholm, D. H. Schaffert, E. S. Andersen, V. Birkedal, J. Kjems. Construction of a 4 zeptoliters switchable 3D DNA box origami, *ACS nano* **2012**, *6* (11), 10050–10053.

[123] E. Benson, A. Mohammed, J. Gardell, S. Masich, E. Czeizler, P. Orponen, B. Högberg. DNA rendering of polyhedral meshes at the nanoscale, *Nature* **2015**, *523* (7561), 441–444.

[124] A. E. Marras, L. Zhou, H.-J. Su, C. E. Castro. Programmable motion of DNA origami mechanisms, *Proceedings of the National Academy of Sciences of the United States of America* **2015**, *112* (3), 713–718.

[125] F. N. Gür, S. Kempter, F. Schueder, C. Sikeler, M. J. Urban, R. Jungmann, P. C. Nickels, T. Liedl, *Adv. Mater.* **2021**.

[126] E. Kopperger, J. List, S. Madhira, F. Rothfischer, D. C. Lamb, F. C. Simmel. A self-assembled nanoscale robotic arm controlled by electric fields, *Science (New York, N.Y.)* **2018**, *359* (6373), 296–301.

[127] S. M. Douglas, A. H. Marblestone, S. Teerapittayanon, A. Vazquez, G. M. Church, W. M. Shih. Rapid prototyping of 3D DNA-origami shapes with caDNAno, *Nucleic acids research* **2009**, *37* (15), 5001–5006.

[128] C. E. Castro, F. Kilchherr, D.-N. Kim, E. L. Shiao, T. Wauer, P. Wortmann, M. Bathe, H. Dietz. A primer to scaffolded DNA origami, *Nature methods* **2011**, *8* (3), 221–229.

[129] D.-N. Kim, F. Kilchherr, H. Dietz, M. Bathe. Quantitative prediction of 3D solution shape and flexibility of nucleic acid nanostructures, *Nucleic acids research* **2012**, *40* (7), 2862–2868.

[130] J. P. K. Doye, H. Fowler, D. Prešern, J. Bohlin, L. Rovigatti, F. Romano, P. Šulc, C. K. Wong, A. A. Louis, J. S. Schreck, M. C. Engel, M. Matthies, E. Benson, E. Poppleton, B. E. K. Snodin, *The oxDNA coarse-grained model as a tool to simulate DNA origami* **2020**.

[131] K. F. Wagenbauer, F. A. S. Engelhardt, E. Stahl, V. K. Hechtl, P. Stömmer, F. Seebacher, L. Meregalli, P. Ketterer, T. Gerling, H. Dietz. How We Make DNA Origami, *Chembiochem a European journal of chemical biology* **2017**, *18* (19), 1873–1885.

[132] K. Göpfrich, C.-Y. Li, M. Ricci, S. P. Bhamidimarri, J. Yoo, B. Gyenes, A. Ohmann, M. Winterhalter, A. Aksimentiev, U. F. Keyser. Large-Conductance Transmembrane Porin Made from DNA Origami, *ACS nano* **2016**, *10* (9), 8207–8214.

[133] A. Johnson-Buck, S. Jiang, H. Yan, N. G. Walter. DNA-cholesterol barges as programmable membrane-exploring agents, *ACS nano* **2014**, *8* (6), 5641–5649.

[134] J. Molle, L. Jakob, J. Bohlen, M. Raab, P. Tinnefeld, D. Grohmann. Towards structural biology with super-resolution microscopy, *Nanoscale* **2018**, *10* (35), 16416–16424.

[135] M. Sarkar, A. J. H. Wachters, H. P. Urbach, J. J. H. B. Schleipen, P. J. van der Zaag, R. Wimberger-Friedl. Waveguide structures for efficient evanescent field coupling to zero mode waveguides, *JEOS:RP* **2014**, *9*.

[136] J. M. Moran-Mirabal, H. G. Craighead. Zero-mode waveguides: Sub-wavelength nanostructures for single molecule studies at high concentrations, *Methods* **2008**, *46* (1), 11–17.

[137] M. S. Fairlamb, A. M. Whitaker, F. E. Bain, M. Spies, B. D. Freudenthal. Construction of a Three-Color Prism-Based TIRF Microscope to Study the Interactions and Dynamics of Macromolecules, *Biology* **2021**, *10* (7), 571.

[138] M. Celebre, C. Domenici, R. Francesconi, A. Ahluwalia, A. Schirone. A comparative study of efficiencies of fibre optic and prism TIRF sensors, *Meas. Sci. Technol.* **1992**, *3* (12), 1166–1173.

[139] E. Abbe. Beiträge zur Theorie des Mikroskops und der mikroskopischen Wahrnehmung, *Archiv f. mikrosk. Anatomie* **1873**, *9* (1), 413–468.

[140] S. W. Hell, J. Wichmann. Breaking the diffraction resolution limit by stimulated emission: stimulated-emission-depletion fluorescence microscopy, *Optics letters* **1994**, *19* (11), 780–782.

[141] T. A. Klar, S. Jakobs, M. Dyba, A. Egner, S. W. Hell. Fluorescence microscopy with diffraction resolution barrier broken by stimulated emission, *Proceedings of the National Academy of Sciences of the United States of America* **2000**, *97* (15), 8206–8210.

[142] S. W. Hell, M. Kroug. Ground-state-depletion fluorscence microscopy: A concept for breaking the diffraction resolution limit, *Appl. Phys. B* **1995**, *60* (5), 495–497.

[143] S. Bretschneider, C. Eggeling, S. W. Hell. Breaking the diffraction barrier in fluorescence microscopy by optical shelving, *Phys. Rev. Lett.* **2007**, *98* (21), 218103.

[144] S. van de Linde, A. Löschberger, T. Klein, M. Heidbreder, S. Wolter, M. Heilemann, M. Sauer. Direct stochastic optical reconstruction microscopy with standard fluorescent probes, *Nature protocols* **2011**, *6* (7), 991–1009.

[145] R. E. Thompson, D. R. Larson, W. W. Webb. Precise Nanometer Localization Analysis for Individual Fluorescent Probes, *Biophysical journal* **2002**, *82* (5), 2775–2783.

[146] J. SantaLucia, D. Hicks. The thermodynamics of DNA structural motifs, *Annual review of biophysics and biomolecular structure* **2004**, *33*, 415–440.

[147] J. Xu, H. Ma, Y. Liu. Stochastic Optical Reconstruction Microscopy (STORM), *Current protocols in cytometry* **2017**, *81*, 12.46.1-12.46.27.

[148] J. Schnitzbauer, M. T. Strauss, T. Schlichthaerle, F. Schueder, R. Jungmann. Super-resolution microscopy with DNA-PAINT, *Nature protocols* **2017**, *12* (6), 1198–1228.

[149] P. Blumhardt, J. Stein, J. Mücksch, F. Stehr, J. Bauer, R. Jungmann, P. Schwille. Photo-Induced Depletion of Binding Sites in DNA-PAINT Microscopy, *Molecules (Basel, Switzerland)* **2018**, *23* (12).

[150] Binnig, Quate, Gerber. Atomic force microscope, *Physical review letters* **1986**, *56* (9), 930–933.

[151] A. Gannepalli, D. G. Yablon, A. H. Tsou, R. Proksch. Mapping nanoscale elasticity and dissipation using dual frequency contact resonance AFM, *Nanotechnology* **2011**, *22* (35), 355705.

[152] M. Habibnejad Korayem, H. Jiryaei Sharahi, A. Habibnejad Korayem. Comparison of frequency response of atomic force microscopy cantilevers under tip-sample interaction in air and liquids, *Scientia Iranica* **2012**, *19* (1), 106–112.

[153] M. Schneider, M. Zhu, G. Papastavrou, S. Akari, H. Möhwald. Chemical Pulsed-Force Microscopy of Single Polyethyleneimine Molecules in Aqueous Solution, *Langmuir* **2002**, *18* (3), 602–606.

[154] Z. Zhao, E. L. Jacovetty, Y. Liu, H. Yan. Encapsulation of Gold Nanoparticles in a DNA Origami Cage, *Angew. Chem.* **2011**, *123* (9), 2089–2092.

[155] F. Ohnesorge, G. Binnig. True atomic resolution by atomic force microscopy through repulsive and attractive forces, *Science (New York, N.Y.)* **1993**, *260* (5113), 1451–1456.

[156] M. Sanz-Paz, J. Wenger, N. F. van Hulst, M. Mivelle, M. F. Garcia-Parajo. Nanoscale control of single molecule Förster resonance energy transfer by a scanning photonic nanoantenna, *Nanophotonics* **2020**, *9* (12), 4021–4031.

[157] T. Bian, R. Chang, P. T. Leung. Förster Resonance Energy Transfer Between Molecules in the Vicinity of Graphene-Coated Nanoparticles, *Plasmonics* **2016**, *11* (5), 1239–1246.

[158] S.-A. Biehs, G. S. Agarwal. Large enhancement of Förster resonance energy transfer on graphene platforms, *Appl. Phys. Lett.* **2013**, *103* (24), 243112.

[159] V. D. Karanikolas, C. A. Marocico, A. L. Bradley. Dynamical tuning of energy transfer efficiency on a graphene monolayer, *Phys. Rev. B* **2015**, *91* (12).

[160] K. A. Velizhanin, T. V. Shahbazyan. Long-range plasmon-assisted energy transfer over doped graphene, *Phys. Rev. B* **2012**, *86* (24).

[161] C. Y. Dong, T. French, P. T. So, C. Buehler, K. M. Berland, E. Gratton, Vol. 72, Elsevier **2003**, p. 431.

[162] H. Chen, G. Holst, E. Gratton. Modulated CMOS camera for fluorescence lifetime microscopy, *Microscopy research and technique* **2015**, *78* (12), 1075–1081.

[163] N. Oleksiievets, J. C. Thiele, A. Weber, I. Gregor, O. Nevskyi, S. Isbaner, R. Tsukanov, J. Enderlein. Wide-Field Fluorescence Lifetime Imaging of Single Molecules, *The journal of physical chemistry. A* **2020**, *124* (17), 3494–3500.

[164] K. M. Douglass, C. Sieben, A. Archetti, A. Lambert, S. Manley. Super-resolution imaging of multiple cells by optimised flat-field epi-illumination, *Nat. Photonics* **2016**, *10* (11), 705–708.

[165] F. Stehr, J. Stein, F. Schueder, P. Schwille, R. Jungmann. Flat-top TIRF illumination boosts DNA-PAINT imaging and quantification, *Nature communications* **2019**, *10* (1), 1268.

[166] H. Chen, S. S. Ahsan, M. B. Santiago-Berrios, H. D. Abruña, W. W. Webb. Mechanisms of quenching of Alexa fluorophores by natural amino acids, *Journal of the American Chemical Society* **2010**, *132* (21), 7244–7245.

[167] N. Marmé, J.-P. Knemeyer, M. Sauer, J. Wolfrum. Inter- and intramolecular fluorescence quenching of organic dyes by tryptophan, *Bioconjugate chemistry* **2003**, *14* (6), 1133–1139.

[168] R. Zhu, X. Li, X. S. Zhao, A. Yu. Photophysical properties of Atto655 dye in the presence of guanosine and tryptophan in aqueous solution, *The journal of physical chemistry. B* **2011**, *115* (17), 5001–5007.

[169] H. Hwang, H. Kim, S. Myong. Protein induced fluorescence enhancement as a single molecule assay with short distance sensitivity, *Proceedings of the National Academy of Sciences of the United States of America* **2011**, *108* (18), 7414–7418.

[170] H. Hwang, S. Myong. Protein induced fluorescence enhancement (PIFE) for probing protein-nucleic acid interactions, *Chemical Society reviews* **2014**, *43* (4), 1221–1229.

[171] D. van Pham, S. Ghosh, F. Joucken, M. Pelaez-Fernandez, V. Repain, C. Chacon, A. Bellec, Y. Girard, R. Sporken, S. Rousset, Y. J. Dappe, S. Narasimhan, J. Lagoute. Selective control of molecule charge state on graphene using tip-induced electric field and nitrogen doping, *npj 2D Mater Appl* **2019**, *3* (1).

[172] H. Liu, Y. Liu, D. Zhu. Chemical doping of graphene, *J. Mater. Chem.* **2011**, *21* (10), 3335–3345.

[173] C. Li, X. Kang, Q. Zhu, W. Zheng. Effects of ultraviolet nanosecond laser irradiation on structural modification and optical transmission of single layer graphene, *Applied Surface Science* **2017**, *398*, 89–96.

[174] B. Krauss, T. Lohmann, D.-H. Chae, M. Haluska, K. von Klitzing, J. H. Smet. Laser-induced disassembly of a graphene single crystal into a nanocrystalline network, *Phys. Rev. B* **2009**, *79* (16).

[175] Y. Feng, W. Li, J. An, Q. Zhao, X. Wang, J. Liu, W. He, N. Li. Graphene family for hydrogen peroxide production in electrochemical system, *Science of The Total Environment* **2021**, *769*, 144491.

[176] W. Xing, G. Lalwani, I. Rusakova, B. Sitharaman. Degradation of Graphene by Hydrogen Peroxide, *Part. Part. Syst. Charact.* **2014**, *31* (7), 745–750.

[177] A. A. Kroeger, A. Karton. π-π Catalysis in Carbon Flatland-Flipping 8Annulene on Graphene, *Chemistry (Weinheim an der Bergstrasse, Germany)* **2021**, *27* (10), 3420–3426.

[178] S. Oh, M. F. Crommie, M. L. Cohen. Simulating the Nanomechanical Response of Cyclooctatetraene Molecules on a Graphene Device, *ACS nano* **2019**, *13* (2), 1713–1718.

[179] Y. Shao, J. Wang, H. Wu, J. Liu, I. A. Aksay, Y. Lin. Graphene Based Electrochemical Sensors and Biosensors: A Review, *Electroanalysis* **2010**, *22* (10), 1027–1036.

[180] P. Suvarnaphaet, S. Pechprasarn. Graphene-Based Materials for Biosensors: A Review, *Sensors (Basel, Switzerland)* **2017**, *17* (10).

[181] R. M. Shetty, S. R. Brady, P. W. K. Rothemund, R. F. Hariadi, A. Gopinath. Bench-Top Fabrication of Single-Molecule Nanoarrays by DNA Origami Placement, *ACS nano* **2021**, *15* (7), 11441–11450.

[182] T. Choi, S. J. Kim, S. Park, T. Y. Hwang, Y. Jeon, B. H. Hong. Roll-to-roll continuous patterning and transfer of graphene via dispersive adhesion, *Nanoscale* **2015**, *7* (16), 7138–7142.

[183] A. Dimiev, D. V. Kosynkin, A. Sinitskii, A. Slesarev, Z. Sun, J. M. Tour. Layer-by-layer removal of graphene for device patterning, *Science* **2011**, *331* (6021), 1168–1172.

[184] J. Feng, W. Li, X. Qian, J. Qi, L. Qi, J. Li. Patterning of graphene, *Nanoscale* **2012**, *4* (16), 4883–4899.

[185] W. J. Hyun, E. B. Secor, M. C. Hersam, C. D. Frisbie, L. F. Francis. High-resolution patterning of graphene by screen printing with a silicon stencil for highly flexible printed electronics, *Adv. Mater.* **2015**, *27* (1), 109–115.

[186] K. Yong, A. Ashraf, P. Kang, S. Nam. Rapid Stencil Mask Fabrication Enabled One-Step Polymer-Free Graphene Patterning and Direct Transfer for Flexible Graphene Devices, *Scientific reports* **2016**, *6*, 24890.

7. Calculation of the Shifted FRET Distance in Presence of a NP

The FRET efficiency *E* is given by the FRET rate constant k_{ET} and the sum of other rate constants depopulating the S_1 of the donor k_X.

$$E = \frac{k_{ET}}{k_{ET} + k_X} \qquad (Eq. 7.1)$$

When an NP is in close proximity of the FRET pair an additional rate constant $k_{D,NP}$ is added, which decreases *E*.

$$E_{NP} = \frac{k_{ET}}{k_{ET} + k_X + k_{D,NP}} \qquad (Eq. 7.2)$$

By combing both previous equation Eq. 7.3 is generated.

$$E_{NP} = \frac{1}{\frac{1}{E} + \frac{k_{D,NP}}{k_{ET}}} \qquad (Eq. 7.3)$$

E can also be expressed through the distance between donor and acceptor *r* as well as FRET distance r_0.

$$E = \frac{1}{1 + \left(\frac{r}{r_0}\right)^6} \qquad (Eq. 7.4)$$

Now Eq. 7.3 and 7.4 are combined in Eq. 7.5.

$$E_{NP} = \frac{1}{1 + \left(\frac{r}{r_0}\right)^6 + \frac{k_{D,NP}}{k_{ET}}} \qquad (Eq. 7.5)$$

While k_{ET} also depends on the distance between donor and acceptor, it is replaced in Eq. 7.5 by expression of Eq. 7. 6. Eq. 7.6 also includes the fluorescence lifetime of the donor after acceptor bleaching τ_D.

$$k_{ET} = \frac{r_0^6}{r^6\,\tau_D} \qquad (Eq. 7.6)$$

Finally, the distance dependence in presence of an NP is given is Eq. 7.7.

$$E_{NP} = \frac{r_0^6}{r^6 + r_0^6 + r^6 \tau_D k_{D,NP}} \qquad (Eq. 7.7)$$

This equation is only valid for a sample with a constant distance between the donor and the NP surface. Otherwise the distance dependence for $k_{D,NP}$ has to be taken into account.

8. Publication

8.1. List of Publications

1. J. Molle, L. Jakob, J. Bohlen, M. Raab, P. Tinnefeld, D. Grohmann. Towards structural biology with super-resolution microscopy, *Nanoscale* **2018**, *10* (35), 16416–16424.

2. I. Kaminska, J. Bohlen, S. Mackowski, P. Tinnefeld, G. P. Acuna. Strong Plasmonic Enhancement of a Single Peridinin-Chlorophyll a-Protein Complex on DNA Origami-Based Optical Antennas, *ACS nano* **2018**, *12* (2), 1650–1655.

3. S. Isbaner, N. Karedla, I. Kaminska, D. Ruhlandt, M. Raab, J. Bohlen, A. Chizhik, I. Gregor, P. Tinnefeld, J. Enderlein, R. Tsukanov. Axial Colocalization of Single Molecules with Nanometer Accuracy Using Metal-Induced Energy Transfer, *Nano letters* **2018**, *18* (4), 2616–2622.

4. J. Bohlen, Á. Cuartero-González, E. Pibiri, D. Ruhlandt, A. I. Fernández-Domínguez, P. Tinnefeld, G. P. Acuna. Plasmon-assisted Förster resonance energy transfer at the single-molecule level in the moderate quenching regime, *Nanoscale* **2019**, *11* (16), 7674–7681.

5. I. Kaminska, J. Bohlen, S. Rocchetti, F. Selbach, G. P. Acuna, P. Tinnefeld. Distance Dependence of Single-Molecule Energy Transfer to Graphene Measured with DNA Origami Nanopositioners, *Nano letters* **2019**, *19* (7), 4257–4262.

6. L. A. Masullo, F. Steiner, J. Zähringer, L. F. Lopez, J. Bohlen, L. Richter, F. Cole, P. Tinnefeld, F. D. Stefani. Pulsed Interleaved MINFLUX, *Nano letters* **2021**, *21* (1), 840–846.

7. S. Krause, E. Ploetz, J. Bohlen, P. Schüler, R. Yaadav, F. Selbach, F. Steiner, I. Kamińska, P. Tinnefeld. Graphene-on-Glass Preparation and Cleaning Methods Characterized by Single-Molecule DNA Origami Fluorescent Probes and Raman Spectroscopy, *ACS nano* **2021**, *15* (4), 6430–6438.

8. I. Kamińska, J. Bohlen, R. Yaadav, P. Schüler, M. Raab, T. Schröder, J. Zähringer, K. Zielonka, S. Krause, P. Tinnefeld. Graphene Energy Transfer for Single-Molecule Biophysics, Biosensing, and Super-Resolution Microscopy, *Advanced materials* **2021**, *33* (24), e2101099.

9. K. Hübner, M. Raab, **J. Bohlen,** P. Tinnefeld. Salt-Induced Conformational Switching of a Flat Rectangular DNA Origami Structure, *Nanoscale* **submitted**.

10. T. Schröder, **J. Bohlen**, S. Ochmann, P. Schüler, S.Krause, Don C. Lamb, P. Tinnefeld. Shrinking gate fluorescence correlation spectroscopy yields equilibrium constants and distinguishes photophysics from structural dynamics, **in preparation**.

11. F. Heimbach, **J. Bohlen**, H. Rabus, W. Y. Baek P. Tinnefeld. Dielectrophoretic Trapping and Electrical Characterization of DNA Origami Structures, *arXiv.*

8.2. List of Conference Contribution

1. **J. Bohlen**, E. Pibiri, D. Ruhlandt, P. Tinnefeld, G. P. Acuna. Plasmon-assisted Förster resonance energy transfer (FRET) at the single-molecule level using DNA origami, *International Workshop "Future Trends in DNA-based Nanotechnology"*, Dresden, **2017**, poster.

2. **J. Bohlen**, E. Pibiri, D. Ruhlandt, P. Tinnefeld, G. P. Acuna. Single-molecule observation of plasmon-assisted Förster resonance energy transfer on DNA-origami, *Gold 2018*, Paris, **2018**, oral presentation.

3. **J. Bohlen**, I Kaminska, S. Rocchetti, F. Selbach, R. Yaadav, G. P. Acuna, P. Tinnefeld. Single-molecule experiments of graphene fluorescence quenching enabled by DNA origami nanopositioners, *25. International Workshop on "Single Molecule Spectroscopy and Super-resolution Microscopy in Life Sciences*, Berlin, **2019**, oral presentation.

4. **J. Bohlen**, Á. Cuartero-González, E. Pibiri, D. Ruhlandt, A. I. Fernández-Domínguez, P. Tinnefeld, G. P. Acuna. DNA Origami based single-molecule investigation of plasmon-assisted Förster resonance energy transfer in the moderate quencheing regime, *CeNS/CRC235 Workshop "Evolving Nanoscience",* Venedig, **2019**, poster.

8.3. Publication I

Plasmon-assisted Förster resonance energy transfer at the single-molecule level in the moderate quenching regime

by

J. Bohlen,* Á. Cuartero-González,* E. Pibiri, D. Ruhlandt, A. I. Fernández-Domínguez, P. Tinnefeld, G. P. Acuna (* equal contribution)

published in

Nanoscale **2019**, *11* (16), 7674–7681

Author contribution:

J. B designed, planned and executed all experiments, prepared samples, analyzed and interpreted data and wrote parts of the manuscript.

Nanoscale

PAPER

View Article Online
View Journal | View Issue

Check for updates

Cite this: *Nanoscale*, 2019, **11**, 7674

Plasmon-assisted Förster resonance energy transfer at the single-molecule level in the moderate quenching regime†

J. Bohlen, ‡[a,b] Á. Cuartero-González,‡[c] E. Pibiri,[a] D. Ruhlandt,[d] A. I. Fernández-Domínguez,[c] P. Tinnefeld *[b] and G. P. Acuna *[a,e]

Received 7th February 2019,
Accepted 26th March 2019

DOI: 10.1039/c9nr01204d

rsc.li/nanoscale

Metallic nanoparticles were shown to affect Förster energy transfer between fluorophore pairs. However, to date, the net plasmonic effect on FRET is still under dispute, with experiments showing efficiency enhancement and reduction. This controversy is due to the challenges involved in the precise positioning of FRET pairs in the near field of a metallic nanostructure, as well as in the accurate characterization of the plasmonic impact on the FRET mechanism. Here, we use the DNA origami technique to place a FRET pair 10 nm away from the surface of gold nanoparticles with sizes ranging from 5 to 20 nm. In this configuration, the fluorophores experience only moderate plasmonic quenching. We use the acceptor bleaching approach to extract the FRET rate constant and efficiency on immobilized single FRET pairs based solely on the donor lifetime. This technique does not require *a posteriori* correction factors neither *a priori* knowledge of the acceptor quantum yield, and importantly, it is performed in a single spectral channel. Our results allow us to conclude that, despite the plasmon-assisted Purcell enhancement experienced by donor and acceptor partners, the gold nanoparticles in our samples have a negligible effect on the FRET rate, which in turns yields a reduction of the transfer efficiency.

1. Introduction

Surface plasmons supported by metal nanostructures can affect the photophysical properties of fluorophores in multiple ways.[1,2] First, they can alter the excitation rate by changing the intensity of the incident electric field at the fluorophore's position.[3] Second, they can modify the radiative and non-radiative decay rates of molecules through the photonic local density of states, thus affecting their overall quantum efficiency and fluorescence lifetime.[4] Finally, surface plasmons can also shape the fluorophore emission pattern into the far-field.[5,6] Over the last decades, these abilities of metal nanoparticles (NPs) were exploited for the development of optical antennas,[7–9] which have enabled nanophotonic applications ranging from fluorescence enhancement[3,10,11] or photostability[12,13] increment to the detection of single molecules at elevated concentrations[14–17] or the sequencing of DNA in real time.[18]

Förster (or fluorescence) resonance energy transfer (FRET) is the non-radiative dipole–dipole energy exchange between two (donor and acceptor) fluorophores. The extreme sensitivity of this mechanism to the inter-molecular distances (in the few nanometer range) is currently being exploited in a wide range of biophysical and cell biological[19,20] tools, which make it possible to monitor the change in conformation and structure of biological complexes. Moreover, FRET also plays a fundamental role in light harvesting processes[21,22] in plants and photosynthetic bacteria. Apart from its fundamental interest, a profound understanding of FRET and its photonic implications is expected to be instrumental for the development of highly efficient organic photovoltaic devices.[23,24]

Recent theoretical[25,26] and experimental[27] studies indicate that metal structures can alter the energy transfer between donor–acceptor fluorophore pairs, enlarging the energy-transfer distance,[28] and improving fluorescence image resolution.[29] However, the net effect of surface plasmons on FRET remains

[a]*Institute for Physical and Theoretical Chemistry – NanoBioScience and Braunschweig Integrated Centre of Systems Biology (BRICS), and Laboratory for Emerging Nanometrology (LENA), Braunschweig University of Technology, Braunschweig, Germany. E-mail: guillermo.acuna@unifr.ch*
[b]*Faculty of Chemistry and Pharmacy, NanoBioScience, Ludwig-Maximilians-Universität München, München, Germany. E-mail: philip.tinnefeld@cup.lmu.de*
[c]*Departamento de Física Teórica de la Materia Condensada and Condensed Matter Physics Center (IFIMAC), Universidad Autónoma de Madrid, E-28049 Madrid, Spain*
[d]*Third Institute of Physics – Biophysics, Georg-August-Universität Göttingen, Göttingen, Germany*
[e]*Department of Physics, University of Fribourg, Chemin du Musée 3, Fribourg CH-1700, Switzerland*
†Electronic supplementary information (ESI) available. See DOI: 10.1039/c9nr01204d
‡Contributed equally

controversial.[30] Contradictory phenomena have been reported ranging from FRET efficiency reduction[31–33] and enhancement,[27,28] together with a linear and non-linear dependence of the FRET rate on the photonic local density of states.[30,34,35] This lack of conclusive results and overall agreement can be attributed mainly to two factors. First, it is challenging to position a FRET pair in the near field of a metallic nanostructure with nanometer precision. Second, it is also extremely demanding to isolate the effect of the surface plasmons supported by metal NPs on FRET. Indeed, most studies were performed at the ensemble level based on an analysis of both the donor and acceptor intensities. Thus, the FRET rate and efficiency were extracted from averaged populations and not for each single fluorophore pair. Furthermore, these approaches required correction factors and previous knowledge of the NPs effect on the donor and acceptor quantum yield. Note that the fluorophore-NP interaction is characterized by a strong spectral dispersion, as extensively reported in the literature for the fluorescence intensity[11,36] and lifetime[37] enhancement and quenching. This is due, among other factors, to its dependence on the NP size and shape and on the relative orientation of the fluorophore and its distance to the NP. Therefore, conclusive results can only be drawn if FRET is studied at the single NP-fluorophore pair level. These limitations call for a thorough alternative strategy to settle the plasmon-assisted FRET controversy.

In this work, we use the DNA origami technique to position single FRET pairs 10 nm away from single Au NPs of different sizes. These NPs exhibit an extinction cross section that overlaps with the absorption and emission spectral ranges of the donor (strongly) and acceptor (moderately) fluorophores. Experimental reports indicate that 10 nm is the distance where fluorescence quenching of molecules by metal particles is roughly 50% and therefore this is a very relevant and sensitive distance range.[38–40] We determine, at the single molecule level and on immobilized fluorophore pairs, how the NP size affects the FRET rate and efficiency. Our results, obtained following the so-called "acceptor bleaching" approach, allow us to conclude that for sizes between 5 and 20 nm, despite the significant Purcell enhancement experienced by donor and acceptor, there is no significant change in the FRET rate between them. Therefore, the FRET efficiency is reduced due to the increment of the total decay rates of fluorophores in the vicinity of Au NPs. Our findings are supported by electromagnetic calculations implementing a semi-classical model for FRET, parameterized according to the experimental samples and yielding excellent agreement with measured results.

2. Sample preparation and FRET characterization

The study of plasmon-assisted FRET proves to be significantly challenging. The first difficulty comprises sample fabrication. Although the first pioneering experiments were performed on an undetermined number of FRET pairs in the near field of NP dimers,[41] a detailed understanding of the plasmon-assisted FRET effect demands the fabrication of single donor–acceptor pairs with a controlled intermolecular distance, as well as their precise positioning nearby a metal nanostructure. DNA as a scaffold has been extensively employed to self-assemble FRET pairs with nanometer precision,[42] through the hybridization of two complimentary single DNA strands labeled with a donor and acceptor fluorophore respectively. In fact, Wenger and coworkers have exploited this approach to reveal how zero-mode waveguides[32] (also termed nano-apertures) and dimer optical antennas fabricated within nano-apertures[43] modify the FRET of diffusing donor–acceptor pairs based on double-stranded DNA sequences in solution. This approach was also employed to fix the relative orientation between donor and acceptor.[27,31,33] These pioneering works were only able to account for the spatially averaged effect of the metallic structures on FRET because the donor–acceptor pair was allowed to freely diffuse within the nano-apertures. Recently, double-stranded DNA was also employed to place a FRET pair at the hotspot of an optical antenna based on one and two Au NPs.[31,33] The introduction of the DNA origami technique[44] enables the self-assembly of complex hybrid structures, in three dimensions, where different species such as dye molecules, quantum dots, and metal NPs can be positioned with nanometric precision and stoichiometric control.[45] Thus, it has been exploited for nanophotonic applications in recent years[46–48] including the study of FRET in the vicinity of Au NPs.[34]

The second obstacle for FRET assessment originates from the far-field measurement method itself, and the indirect extraction of the transfer rate and efficiency near metal NPs. Note that the FRET efficiency E is defined as[49]

$$E = 1 - I_{DA}/I_D = \frac{I_{AD}/\phi_A}{I_{AD}/\phi_A + I_{DA}/\phi_D} \quad (1)$$

where I_D and I_{DA} are the fluorescence intensities of the donor fluorophore in the absence and presence of the acceptor respectively, I_{AD} the acceptor's fluorescence intensity upon donor excitation and ϕ_A (ϕ_D) the quantum yield of the acceptor (donor). The central and right hand side of eqn (1) enable the calculation of E with different experimental approaches. In the central expression, only the fluorescence intensity of the donor needs to be measured in a single spectral channel. However, it is necessary to determine it in the presence and absence of the acceptor. In experiments with single immobilized molecules, this is typically achieved by waiting until the acceptor bleaches (acceptor bleaching approach). In contrast, the expression on the right side requires the measurement of the fluorescence signal of both donor and acceptor, and therefore in two different spectral channels.

Similarly to eqn (1), the FRET rate constant k_{ET} can be estimated from the donor's fluorescence lifetime in the presence τ_{DA} and absence of the acceptor τ_D as

$$k_{ET} = \frac{1}{\tau_{DA}} - \frac{1}{\tau_D} \quad (2)$$

It is worth noticing that for a particular FRET pair, and under the same excitation and detection conditions, I_{DA}/I_D =

τ_{DA}/τ_D and therefore the FRET efficiency can also be determined based on fluorescence lifetime measurements as[39]

$$E = 1 - \frac{\tau_{DA}}{\tau_D} \quad (3)$$

Note that fluorescence lifetime measurements are typically more reliable than intensity measurements since they do not depend on the analyte concentration and instrument alignment, neither they are sensitive to saturation effects.

As discussed above, to date, the acceptor bleaching approach has not been employed to study plasmon-assisted FRET at the single-molecule level. Instead, most experiments were performed at the ensemble level and on freely diffusing FRET pairs in solution. Ensemble measurements have the inherent disadvantage that only averages over populations can be studied. This is particularly relevant for FRET measurements in which factors like the presence of impurities (including for instance colloidal NP aggregates), or defective plasmonic NP-FRET-pair structures (such as, for example, those where only donor or acceptor are present, where the acceptor is bleached, or the NP is missing) can severely affect the overall results. Furthermore, within ensemble measurements of freely diffusing FRET pairs, the photophysics of a single donor in the presence and absence of its acceptor counterpart cannot be monitored, and therefore the right part of eqn (1) has to be employed. For plasmon-assisted FRET measurements, this approach has the additional shortcoming that the plasmonic nanoparticles affect the donor and acceptor quantum yields ϕ_D and ϕ_A, respectively, thus greatly complicating the reliable determination of E. Finally, a few studies were performed on immobilized samples, but the FRET efficiency was obtained from the intensities of the donor and acceptor channels.[33] In another experiment, FRET rate constants and efficiencies were extracted by comparing the average donor's lifetime on two samples with and without acceptor[30] at the ensemble level.

In order to overcome the aforementioned limitations, we here employ the DNA origami technique to position both the metal NP and the FRET pair and perform single-molecule fluorescence measurements on the resulting surface-immobilized samples. Fig. 1 includes a sketch of these samples, based on a rectangular DNA origami structure with dimensions of 70 nm × 85 nm (the thickness of a DNA double-helix is approximately 2 nm). The FRET pair consists of ATTO532 (donor) and ATTO647N (acceptor) molecules.[38] It is attached to the DNA origami structure through internal labelling on the same double helix,[50] see Fig. 1(a), resulting in a gap of approximately 3.4 nm between the fluorophores. Six biotin-functionalized oligonucleotides are used to immobilize the DNA origami structure on a glass coverslip, which is functionalized with BSA-biotin and neutrAvidin. Following surface immobilization, a single metal NP is bound at a predefined position on the upper side of the DNA origami structure through DNA hybridization,[41] see Fig. 1(b). We employed 5, 10, 15 and 20 nm Au NPs. The FRET pair is located at the bottom side to avoid physical contact of dyes and nanoparticle. The distance between the NP surface and the FRET pair is approx. 10 nm

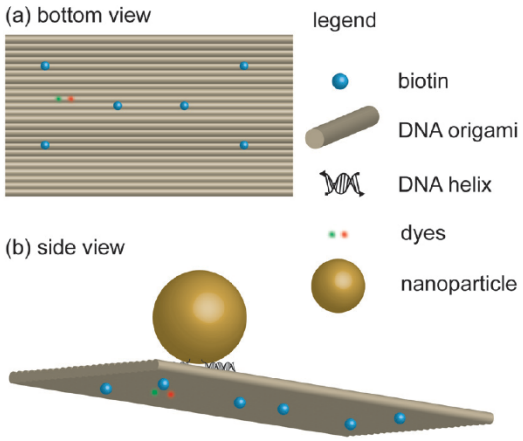

Fig. 1 Sketch of the rectangular DNA origami structure. (a) The bottom view shows the FRET pair of dyes and the six biotins for the surface immobilization. (b) Side view depicting the capturing strands employed for the incorporation of a single metal NP.

(based on geometric calculations assuming the length of each nucleotide to be 0.34 nm). For these NPs' sizes and distances to the FRET pair, the fluorescence lifetime reduction can be accurately determined. Further details on sample fabrication can be found in the Methods and Materials section, whereas a table containing the distances between NPs and fluorophores can be found in the ESI.†

Samples were scanned with a home-built confocal fluorescence microscope in order to locate the immobilized structures. For each FRET pair, fluorescence transients were recorded. In order to maximize the amount of information that can be extracted from fluorescence transients, we manually alternated between donor and acceptor excitation. This procedure is illustrated in Fig. 2. Initially, the donor is excited (*I*, donor excitation at 532 nm), this allows us to extract I_{DA} (green transient, donor intensity upon donor excitation), I_{AD} (orange transient, acceptor intensity upon donor excitation) and the fluorescence lifetime τ_{DA}. Afterwards, the sample is excited in the red spectral range (*II*, acceptor excitation, 640 nm) to determine I_A (red transient, acceptor intensity upon acceptor excitation) and its corresponding fluorescence lifetime τ_A, until the acceptor is bleached in *III*. Finally, the sample is excited again in the green spectral range, *IV*, now to record τ_D and I_D until the donor bleaches (*V*). Importantly, this technique enables the determination of the background signal in each channel and the verification (through the single bleaching steps) that the fluorescence measured arises from single FRET pairs. The presence of single Au NPs can be independently inferred by the reduction of τ_D and τ_A as Au NPs quench both the acceptor and the donor.[51] This procedure was repeated for DNA origami structures with no NPs for referencing. In order to rationalize our experimental results, we perform numerical electromagnetic simulations modelling our system. We use measured values for all geometric parameters (NP radii, DNA origami thickness, and dye-NP and intermolecular distances). Au permittivity is taken from experi-

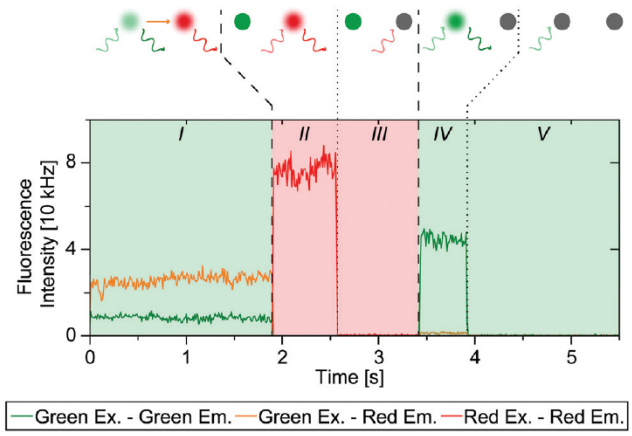

Fig. 2 Example of a fluorescence transient obtained through laser alternation for single-molecule FRET determination using the "acceptor bleaching" approach. In *I*, only the green laser is on to monitor τ_{DA}, I_{DA} (green excitation–green detection) and I_{AD} (green excitation–red detection). In II and III, only the red laser is switched on to measure I_A and τ_A (red excitation–red detection) until the acceptor bleaches (III). In IV and V, only the green laser is exciting to determine τ_D and I_D until the donor bleaches (V).

mental data[52] and the refractive index of DNA origami structure is set to 2.1.[53] We carry out three different numerical studies. In the first two, only one molecule (donor or acceptor) is included as a point-dipole-like electromagnetic source. By averaging over three perpendicular dye orientations, we compute the total Purcell spectrum for all the experimental geometries. Performing the spectral average within the dye emission window and taking into account its intrinsic quantum yield $\phi_{D,A}$, we obtain the fluorescence lifetimes τ_D and τ_A and investigate their sensitivity to the Au NP size (see ESI†). In the third study, the donor is treated again as a dipole source, but the acceptor is modelled as a dielectric sphere whose randomly oriented polarizability matches the one corresponding to a quantum two-level system[44] (see the Methods and materials for further details). These simulations yield the donor Purcell factor in the presence of the acceptor, from which we determine τ_{DA}. Combining these results with those in the absence of the acceptor, we obtain the FRET efficiency E from eqn (3). In addition, we also calculate the FRET rate constant k_{ET} using eqn (2) or directly by computing the spatial average of the electric field intensity within the dielectric sphere modelling the acceptor molecule,[54,55] $k_{ET} \propto V^{-1} \int |E_{DA}|^2 dV$.

3. Results and discussion

Fig. 3(a), (d) and (g) shows the sample-averaged fluorescence intensities I_A, I_D and I_{DA} for different NP diameters. All values were normalized to the intensity obtained without NPs (the measured distributions can be found in the ESI†).

It is worth mentioning that the distance between the NP surface and the donor (acceptor) decreases slightly with the NP size, from 10.48 (11.39) nm for 5 nm NPs to 8.76 (9.41) nm for the 20 nm NPs (all distances can be found in the ESI†). As previously observed, for fluorophores located under the "polar" plane of the NP as defined by the incident light polarization, the overall reduction of the quantum yield due to an increment of the non-radiative rate prevails over the increment of the excitation rate.[4,40] As a result, a reduction of the fluorescence intensity is measured. This effect is stronger in I_D than in I_A due to the spectral overlap between the donor emission and the Au NPs resonance[11] in the green spectral range. In the case of I_{DA}, FRET to the acceptor in close proximity prevails, and the effect of the plasmonic NP on the intensity at the donor channel is significantly less pronounced. Fig. 3(b), (e) and (h) plot measured (empty dots) and simulated (solid dots) fluorescence lifetimes τ_{DA}, τ_D and τ_A. Remarkably, both are in very good agreement, with theoretical predictions lying within the experimental error bars in all cases. The data sets are normalized to the samples without NPs and are also presented in absolute scale (see right axis), revealing up to a two-fold (four-fold) total Purcell enhancement for the acceptor (donor) molecules. These results show a similar trend as the intensities in Fig. 3((a), (d) and (g)), which is in accordance with previous reports.[40] Note again the quenching visible in τ_D, which takes place in the green region of the electromagnetic spectrum. The presence of the metal NPs accelerates the decay of both dyes, with a stronger effect on the non-radiative channel. Therefore, the overall effect on the fluorescence lifetime is comparable to the one on the quantum yield. As the increment in the excitation rate (electric field enhancement at the dyes position) is negligible, similar reductions of the fluorescence lifetime and of the intensity are observed as previously reported. As in Fig. 3(a), (d) and (g), the comparison between τ_{DA} and τ_D in Fig. 3(b), (e) and (h) demonstrates that the presence of the acceptor diminishes the effect of the Au NPs in the donor fluorescence characteristics.

Introducing the measured donor lifetimes τ_{DA} and τ_D into eqn (2) and (3), we can extract the FRET rate constant k_{ET} and FRET efficiency E for each single donor–acceptor pair in the presence of Au NPs. The experimental results obtained this way and normalized to the results of samples without NPs are shown as empty dots in Fig. 3(c) and (f). Electromagnetic calculations for these two magnitudes are plotted in solid dots. Similar to the experiments, the numerical FRET efficiencies are computed by evaluating eqn (3) using the theoretical predictions for τ_{DA} and τ_D. On the contrary, as discussed above, the FRET rates in Fig. 3(c) and (f) are calculated directly from simulations through the spatial averaging of the electric field intensity within the acceptor volume. The agreement between this direct estimation for k_{ET} and an indirect one, consisting in the evaluation of eqn (2) through numerical data, is shown in the ESI.† Both numerical and experimental results indicate that the presence of the metal nanostructure does not have a significant impact on the FRET rate constant. We can observe that Au NPs decrease the FRET efficiency, being the reduction in E of 25% for the largest structure (20 nm diameter). Note that, according to eqn (2) and (3), $E = k_{ET}\ \tau_{DA}$, which reveals

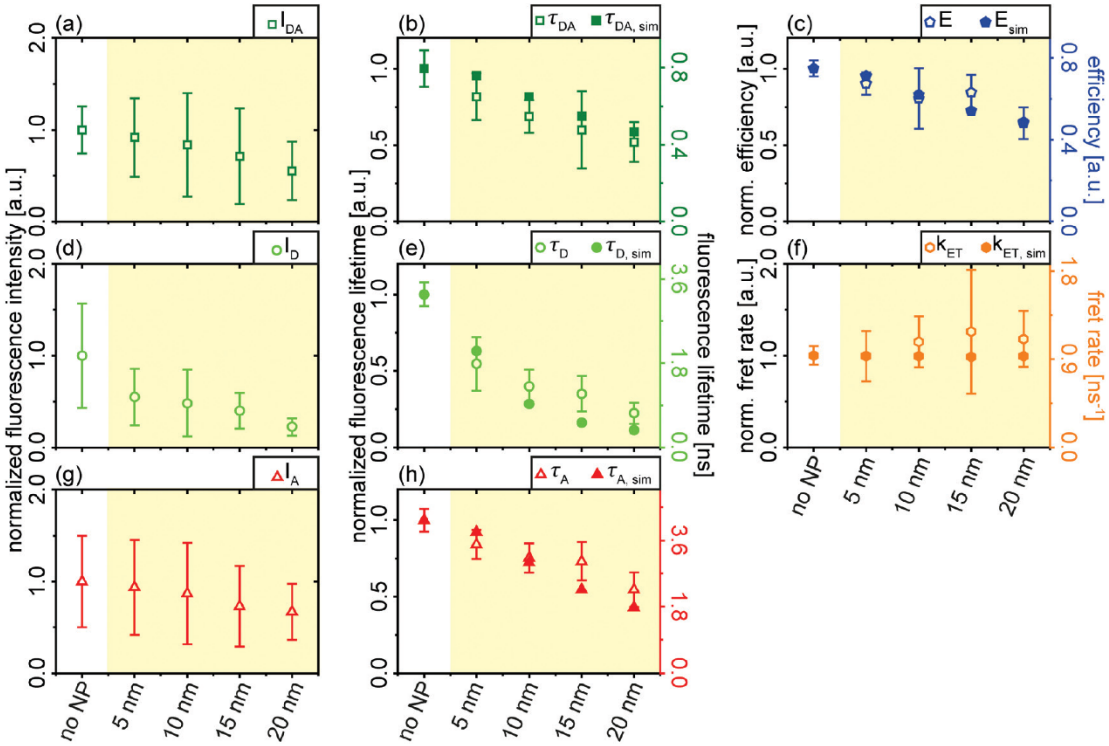

Fig. 3 Summarized results of the measurements with standard deviation and simulation: the normalized averaged fluorescence intensity against the nanoparticle diameter for the donor in presence (I_{DA}; (a)) and absence of the acceptor (I_D; (d)) and the acceptor only (I_A; (g)). The fluorescence lifetime measurements are shown in hollows symbols with error bars compared to the simulated results (filled symbols and indicated by the index sim) for the donor with acceptor (τ_{DA}, $\tau_{DA,\ sim}$; (b)), after photobleaching of the acceptor (τ_D, $\tau_{D,\ sim}$; (d)) and acceptor only (τ_A, $\tau_{A,\ sim}$; (h)). The calculated and simulated FRET efficiency (E, E_{sim}) and FRET rate (k_{ET}, $k_{ET,\ sim}$) are diagrammed in (c) and (f). The difficult differentiation between simulated and experimental results shows a good agreement between both data sets.

that the decrease of the FRET efficiency in Fig. 3(c) is a direct consequence of the reduction of the donor lifetime in presence of the metal NP and acceptor molecule in Fig. 3(b). Importantly, the simple expression above also clarifies why E is not significantly modified due to the metal NP, despite the Purcell lifetime reduction experienced by the donor molecule. It shows that τ_{DA} is the time scale that sets the transfer efficiency, and it is less sensitive to the plasmon field than τ_A.

4. Conclusion

In summary, we have exploited the DNA origami technique to self-assemble structures where a single Au NP and a fluorescent donor–acceptor pair were positioned with stoichiometric control and nanometer precision. These structures were used to analyze the effect on the FRET induced by Au NPs of different diameters (ranging from 5 to 20 nm) placed 10 nm away from the fluorescent pair, which is separated by 3.4 nm. Our measurements were performed at the single-molecule level on surface immobilized structures using the "acceptor bleaching" technique. This approach enabled the reliable determination of the plasmon-assisted FRET rate and efficiency based solely on the measurement of the donor's fluorescence lifetime in the presence/absence of the acceptor. The experimental results are supported by electromagnetic calculations implementing a semiclassical model for FRET. Our findings contradict previous works using colloidal NPs and DNA, in which an enhancement of the FRET rate with the LDOS was reported.[31,34] The presented measurements, performed at the single molecule level following the "acceptor bleaching" technique, reveal that, despite the significant plasmon-assisted fluorescence lifetime reduction and quenching experienced by both donor and acceptor molecules, the Au NPs have a minor effect on the FRET rate in our experimental samples. In contrast, the FRET efficiency decreases with increasing NP size through the fluorescence lifetime reduction undergone by the donor fluorophore in presence of the NP and its acceptor counterpart.

5. Material and methods

If no other company is mentioned all chemicals were ordered by Sigma Aldrich.

A. Preparation of DNA origami structures

The rectangular DNA origami structures were produced by adding the unmodified, modified staples (including the oligonucleotides with Biotin, Atto647N, Atto532 and capturing

strands for the nanoparticle), the folding buffer (final concentration: 1 × TAE, 12 mM $MgCl_2$) and the scaffold p7249 (final concentration: 27.2 nM). The modified and unmodified staples had a tenfold concentration compared to the scaffold. To fold the DNA origami structures the following program was used: heating up to 70 °C for 5 min and then cooling down with a temperature gradient of −1 °C min^{-1} to a final temperature of 24 °C.

Gel purification was used to separate the oligonucleotides from the DNA origami structures. The gel consists of 1.5% vol agarose (Biozym LE Agarose) and 50 mL TAE (1 × TAE with 12 mM $MgCl_2 \cdot 6H_2O$). Also 2 μL peqGreen (VWR) were added to the Gel and 1 × BlueJuice (Thermo Fisher Scientific) as a loading buffer for the sample. As the gel buffer 1 × TAE with 12 mM $MgCl_2$ is used. The total run time for the cooled gel was 2 hours with a voltage of 80 V. An example of a gel is shown in Fig. S4 in the ESI.†

The correct folding of the DNA origami structures was characterized with atomic force microscopy (AFM, Nanowizard 3 ultra, JPK Instruments) in solution. On a freshly cleaved mica surface (Qualty V1, Plano GmbH) 10 μL of a 10 mM $NiCl_2 \cdot 6H_2O$ solution were incubated for 5 min. After three times washing with 300 μL miliQ-water (Merck Milli-Q) and drying with compressed air, 10 μL 1 nM DNA origami structure solution (diluted in AFM buffer (40 mM TRIS, 2 mM EDTA disodium salt dihydrate and 12.5 mM $Mg(OAc)_2 \cdot 6H_2O$) were added and incubated for 5 min. Afterwards 300 μL AFM buffer were added after purging three times with 300 μL AFM buffer. The solution measurements were performed with cantilevers USC-F0.3-k0.3-10 from Nano World. AFM images of the DNA origami structures with and Au NPs are included in Fig. S4 and S5 respectively.†

B. Functionalization of nanoparticles

Au NPs were ordered from BBI solutions and functionalized with 25 T single-stranded DNA oligonucleotides (Ella Biotech GmbH) labelled with a thiol group at 3′-end. After cleaning the coated stir bars, glass and snap on lid with ultra-pure water (Merck Milli-Q), a 2 mL NP solution was added. To the stirred solution (550 rpm), 20 μL Tween20 (10%, Polysorbate20, Alfa Aesar), 20 μL of a potassium phosphate buffer (4 : 5 mixture of 1 M monobasic (P8709) and dibasic potassium phosphate (P8584)) and an excess of 50 nM oligo (for the volume see ESI†) were added. After heating the solution for one hour at 40 °C, the solution was salted every 3 minutes with a PBS solution containing 3.3 M NaCl to a final concentration of 750 mM NaCl. For the followed salting steps see ESI.†

C. Sample preparation

Lab-Tek chambers (Thermo Scientific) were incubated for 2 min with 200 μL 0.1 M hydrofluoric acid (AppliChem), washed three times with 300 μL NP buffer (1 × TAE, 12.5 mM $MgCl_2$, 300 mM NaCl) and incubated again with 200 μL 0.1 M hydrofluoric acid. The hydrofluoric acid provides a clean surface. After cleaning three times with 300 μL NP buffer 100 μL BSA-Biotin (1 mg mL^{-1}) is added and incubated overnight at 4 °C. The BSA-Biotin passivates the surface against unspecific binding. The next day the surface is washed three times with 300 μL NP buffer. Afterwards 100 μL neutrAvidin (1 mg mL^{-1}) is added and incubated for 10 min, the surface is washed three times with 300 μL NP buffer. 200 μL DNA origami structures solution (~80 pM) is added, the surface density is monitored with the confocal setup. After cleaning the surface three times with 300 μL NP buffer, 200 μL SuperBlock (PBS) blocking buffer (Thermo Scientific) is added for 10 min to achieve additional surface passivation. Following the purging of the surface with three times 300 μL NP buffer the nanoparticle solution is added and incubated for 48 h at 4 °C. The NP absorption was set to 0.05 and monitored at a UV-vis spectrometer (Nanodrop 2000, Thermo Scientific). Finally, after washing three times with 300 μL NP buffer to get rid of the nanoparticles in solution, a trolox/trolox quinone solution is added to increase photostability.[56]

D. Imaging

Single molecule fluorescence measurements were performed at a custom-build confocal setup based on an Olympus IX-71 inverted microscope. As power sources a 637 nm (LDH-D-C-640, Picoquant) and a 532 nm (LDH-P-FA530B) pulsed laser are used with an intensity for the FRET samples of 9 μW and 2 μW respectively. Both lasers beams were modified by an AOTF filter (AOTFnc-VIS, AA optoelectronic), cleaned up and expanded by an optical fiber, before entering a $\lambda/2$ (LPVISE100-A, Thorlabs) and a $\lambda/4$ (AQWP05M-600, Thorlabs) plate to achieved circularly polarized light. A dichroic mirror (Dualband z532/633, AHF) was employed to direct the beam to an oil-immersion objective (UPLSA-PO100XO, NA 1.40, Olympus). A piezo stage (P-517.3CL, Physik Instrumente GmbH & co. KG) scans the sample by moving the Lab-Tek over the objective. In this scan every molecule can be selected to perform a time-resolved analysis. The emitted fluorescence is collected by the objective and separated from the excitation light through the dichroic mirror. To minimize the detection volume the beam is focused through a pinhole (Linos 50 μm). The fluorescence light is divided by a dichroic mirror (640DCXR, AHF) and the red and green emission is purified with different filter, Bandpass ET 700/75 m, AHF; RazorEdge LP 647, Semrock (red) and Brightline HC582/75, AHF; RazorEdge LP 532, Semrock (green). Both signals are detected at different Diodes (τ-SPAD-100, Picoquant) and the time-resolved analysis is done by a single-photon counting card (SPC-830, Becker&Hickl). The raw data analysis is performed by a home written LabView software (National instruments).

E. Theoretical model and calculations

In order to verify the experimental results, we have performed numerical simulations using the finite-element solver of Maxwell's Equations in the commercial software COMSOL MULTIPHYSICS™. First, conventional Purcell factor, *Pf*, calculations for the donor and acceptor molecules were carried out for all the relevant orientations. In these simulations, the power radiated through a small box including only the dipole

source was computed within a frequency window matching the experimental emission spectra. The dye lifetime τ_i with $i = D, A$ was then extracted through spectral averaging, and taking into account the inherent quantum yield ϕ_i

$$\tau_i = \frac{\tau_i^{(0)}}{\phi_i P f_i - (1 - \phi_i)} \tag{4}$$

where $\tau_i^{(0)}$ is the lifetime in vacuum (absence of the Au NP).

Simulations describing the emission of the donor in the presence of the acceptor were also performed. In these calculations, a semiclassical model for FRET was implemented, in which the donor is treated as dipole-like electromagnetic source and the acceptor is effectively described as an absorbing dielectric sphere. This is similar to a model recently proposed in the context of plasmon-assisted exciton transport[54] and strong coupling.[55] The randomly oriented polarizability of this sphere is set to match the polarizability of a quantum two-level system. The resulting effective dielectric function has the form

$$\varepsilon_{\mathrm{A,eff}}(\omega) = \frac{1 - 2\eta_{\mathrm{A}}(\omega)}{1 + \eta_{\mathrm{A}}(\omega)} \tag{5}$$

with

$$\eta_{\mathrm{A}}(\omega) = \frac{{\mu_{\mathrm{A}}}^2 \omega_{\mathrm{A}}}{3\varepsilon_0 V \hbar\omega\left(\omega - \left(\omega_{\mathrm{A}} - \frac{i\gamma_{\mathrm{A}}}{2}\right)\right)} \tag{6}$$

where ε_0 is the vacuum permittivity and V the sphere volume. Three parameters, set in accordance with experiments, were required to describe the acceptor molecules: dipole moment (μ_{A} = 14.5 D), natural frequency (ω_{A} = 1.9 eV), and linewidth (γ_{A} = 0.1 eV). The convergence of results against V was checked (the radius of the sphere was finally set to 0.25 nm). Note that this simplified model does not account for the stoke shift of ATTO647N, and that the absorption spectrum resulting is purely Lorentzian while the actual profile presents a well-defined vibronic sideband.

Funding

Deutsche Forschungsgesellschaft (DFG) (AC 279/2-1, TI 329/9-1); Spanish MINECO (FIS2015-64951-R and MDM-2014-0377-16-4), European 7th Framework programme (CIG-630996), European Research Council (ERC) (SiMBA, EU 26116), ChipScope and excellent cluster of Ludwig-Maximilians-Universität München Center for Integrated Protein Science Munich (CIPSM) and Nanosystems Iniative Munich (NIM). This work was supported by the Swiss National Science Foundation through the National Center of Competence in Research Bio-Inspired Materials.

Conflicts of interest

There are no conflicts to declare.

Acknowledgements

We thank Kristina Hübner and Johannes Feist for fruitful discussions, and Tim Schröder for the setup support.

Notes and references

1 E. A. Coronado, E. R. Encina and F. D. Stefani, *Nanoscale*, 2011, **3**(10), 4042.
2 V. Giannini, A. I. Fernández-Domínguez, S. C. Heck and S. A. Maier, *Chem. Rev.*, 2011, **111**(6), 3888.
3 A. Kinkhabwala, Z. Yu, S. Fan, Y. Avlasevich, K. Müllen and W. E. Moerner, *Nat. Photonics*, 2009, **3**(11), 654.
4 P. Holzmeister, E. Pibiri, J. J. Schmied, T. Sen, G. P. Acuna and P. Tinnefeld, *Nat. Commun.*, 2014, **5**, 5356.
5 H. Aouani, O. Mahboub, N. Bonod, E. Devaux, E. Popov, H. Rigneault, T. W. Ebbesen and J. Wenger, *Nano Lett.*, 2011, **11**(2), 637.
6 A. G. Curto, G. Volpe, T. H. Taminiau, M. P. Kreuzer, R. Quidant and N. F. van Hulst, *Science*, 2010, **329**(5994), 930.
7 P. Biagioni, J.-S. Huang and B. Hecht, *Rep. Prog. Phys.*, 2012, **75**(2), 24402.
8 A. F. Koenderink, *ACS Photonics*, 2017, **4**(4), 710.
9 L. Novotny and N. van Hulst, *Nat. Photonics*, 2011, **5**(2), 83.
10 D. Punj, M. Mivelle, S. B. Moparthi, T. S. van Zanten, H. Rigneault, N. F. van Hulst, M. F. García-Parajó and J. Wenger, *Nat. Nanotechnol.*, 2013, **8**(7), 512.
11 C. Vietz, I. Kaminska, M. Sanz Paz, P. Tinnefeld and G. P. Acuna, *ACS Nano*, 2017, **11**(5), 4969.
12 I. Kaminska, C. Vietz, Á. Cuartero-González, P. Tinnefeld, A. I. Fernández-Domínguez and G. P. Acuna, *Nanophotonics*, 2018, **7**(3), 643.
13 J. V. Pellegrotti, G. P. Acuna, A. Puchkova, P. Holzmeister, A. Gietl, B. Lalkens, F. D. Stefani and P. Tinnefeld, *Nano Lett.*, 2014, **14**(5), 2831.
14 G. Acuna, D. Grohmann and P. Tinnefeld, *FEBS Lett.*, 2014, **588**(19), 3547.
15 G. P. Acuna, P. Holzmeister, F. M. Möller, S. Beater, B. Lalkens and P. Tinnefeld, *J. Biomed. Opt.*, 2013, **18**(6), 65001.
16 E. Di Fabrizio, S. Schlücker, J. Wenger, R. Regmi, H. Rigneault, G. Calafiore, M. West, S. Cabrini, M. Fleischer, N. F. van Hulst, M. F. Garcia-Parajo, A. Pucci, D. Cojoc, C. A. E. Hauser and M. Ni, *J. Opt.*, 2016, **18**(6), 63003.
17 V. Flauraud, R. Regmi, P. M. Winkler, D. T. L. Alexander, H. Rigneault, N. F. van Hulst, M. F. García-Parajo, J. Wenger and J. Brugger, *Nano Lett.*, 2017, **17**(3), 1703.
18 J. Eid, A. Fehr, J. Gray, K. Luong, J. Lyle, G. Otto, P. Peluso, D. Rank, P. Baybayan, B. Bettman, A. Bibillo, K. Bjornson, B. Chaudhuri, F. Christians, R. Cicero, S. Clark, R. Dalal, A. Dewinter, J. Dixon, M. Foquet, A. Gaertner, P. Hardenbol, C. Heiner, K. Hester, D. Holden, G. Kearns, X. Kong, R. Kuse, Y. Lacroix, S. Lin, P. Lundquist, C. Ma,

P. Marks, M. Maxham, D. Murphy, I. Park, T. Pham, M. Phillips, J. Roy, R. Sebra, G. Shen, J. Sorenson, A. Tomaney, K. Travers, M. Trulson, J. Vieceli, J. Wegener, D. Wu, A. Yang, D. Zaccarin, P. Zhao, F. Zhong, J. Korlach and S. Turner, *Science*, 2009, **323**(5910), 133.

19 D. W. Piston and G.-J. Kremers, *Trends Biochem. Sci.*, 2007, **32**(9), 407.

20 R. Roy, S. Hohng and T. Ha, *Nat. Methods*, 2008, **5**(6), 507.

21 B. E. Hardin, E. T. Hoke, P. B. Armstrong, J.-H. Yum, P. Comte, T. Torres, J. M. J. Fréchet, M. K. Nazeeruddin, M. Grätzel and M. D. McGehee, *Nat. Photonics*, 2009, **3**, 406–411.

22 W. Kühlbrandt and D. N. Wang, *Nature*, 1991, **350**(6314), 130.

23 H. A. Atwater and A. Polman, *Nat. Mater.*, 2010, **9**, 205–213.

24 K. R. Catchpole and A. Polman, *Opt. Express*, 2008, **16**(26), 21793.

25 J. A. Gonzaga-Galeana and J. R. Zurita-Sánchez, *J. Chem. Phys.*, 2013, **139**(24), 244302.

26 C. L. Cortes and Z. Jacob, *Opt. Express*, 2018, **26**(15), 19371.

27 J. de Torres, M. Mivelle, S. B. Moparthi, H. Rigneault, N. F. van Hulst, M. F. García-Parajó, E. Margeat and J. Wenger, *Nano Lett.*, 2016, **16**(10), 6222.

28 J. Zhang, Y. Fu, M. H. Chowdhury and J. R. Lakowicz, *J. Phys. Chem. C*, 2007, **111**(32), 11784.

29 T. Zhao, T. Li and Y. Liu, *Nanoscale*, 2017, **9**(28), 9841.

30 C. Blum, N. Zijlstra, A. Lagendijk, M. Wubs, A. P. Mosk, V. Subramaniam and W. L. Vos, *Phys. Rev. Lett.*, 2012, **109**(20), 203601.

31 S. Bidault, A. Devilez, P. Ghenuche, B. Stout, N. Bonod and J. Wenger, *ACS Photonics*, 2016, **3**(5), 895.

32 P. Ghenuche, J. de Torres, S. B. Moparthi, V. Grigoriev and J. Wenger, *Nano Lett.*, 2014, **14**(8), 4707.

33 J. Hu, M. Wu, L. Jiang, Z. Zhong, Z. Zhou, T. Rujiralai and J. Ma, *Nanoscale*, 2018, **10**(14), 6611.

34 N. Aissaoui, K. Moth-Poulsen, M. Käll, P. Johansson, L. M. Wilhelmsson and B. Albinsson, *Nanoscale*, 2017, **9**(2), 673.

35 P. Andrew and W. L. Barnes, *Science*, 2000, (290), 785.

36 A. Puchkova, C. Vietz, E. Pibiri, B. Wünsch, M. Sanz Paz, G. P. Acuna and P. Tinnefeld, *Nano Lett.*, 2015, **15**(12), 8354.

37 C. Vietz, B. Lalkens, G. P. Acuna and P. Tinnefeld, *New J. Phys.*, 2016, **18**(4), 45012.

38 G. P. Acuna, M. Bucher, I. H. Stein, C. Steinhauer, A. Kuzyk, P. Holzmeister, R. Schreiber, A. Moroz, F. D. Stefani, T. Liedl, F. C. Simmel and P. Tinnefeld, *ACS Nano*, 2012, **6**(4), 3189.

39 P. Anger, P. Bharadwaj and L. Novotny, *Phys. Rev. Lett.*, 2006, **96**(11), 113002.

40 E. Dulkeith, M. Ringler, T. A. Klar, J. Feldmann, A. Muñoz Javier and W. J. Parak, *Nano Lett.*, 2005, **5**(4), 585.

41 V. Faessler, C. Hrelescu, A. A. Lutich, L. Osinkina, S. Mayilo, F. Jäckel and J. Feldmann, *Chem. Phys. Lett.*, 2011, **508**(1–3), 67.

42 A. A. Deniz, M. Dahan, J. R. Grunwell, T. Ha, A. E. Faulhaber, D. S. Chemla, S. Weiss and P. G. Schultz, *Proc. Natl. Acad. Sci. U. S. A.*, 1999, **96**(7), 3670.

43 P. Ghenuche, M. Mivelle, J. de Torres, S. B. Moparthi, H. Rigneault, N. F. van Hulst, M. F. García-Parajó and J. Wenger, *Nano Lett.*, 2015, **15**(9), 6193.

44 P. W. K. Rothemund, *Nature*, 2006, **440**(7082), 297.

45 M. Pilo-Pais, G. P. Acuna, P. Tinnefeld and T. Liedl, *MRS Bull.*, 2017, **42**(12), 936.

46 G. P. Acuna, F. M. Möller, P. Holzmeister, S. Beater, B. Lalkens and P. Tinnefeld, *Science*, 2012, **338**(6106), 506.

47 A. Kuzyk, R. Jungmann, G. P. Acuna and N. Liu, *ACS Photonics*, 2018, **5**(4), 1151.

48 A. Kuzyk, R. Schreiber, Z. Fan, G. Pardatscher, E.-M. Roller, A. Högele, F. C. Simmel, A. O. Govorov and T. Liedl, *Nature*, 2012, **483**(7389), 311.

49 J. Enderlein, *Int. J. Mol. Sci.*, 2012, **13**(12), 15227.

50 J. J. Schmied, A. Gietl, P. Holzmeister, C. Forthmann, C. Steinhauer, T. Dammeyer and P. Tinnefeld, *Nat. Methods*, 2012, **9**(12), 1133.

51 E. Dulkeith, A. C. Morteani, T. Niedereichholz, T. A. Klar, J. Feldmann, S. A. Levi, F. C. J. M. van Veggel, D. N. Reinhoudt, M. Möller and D. I. Gittins, *Phys. Rev. Lett.*, 2002, **89**(20), 947.

52 A. D. Rakić, A. B. Djurišić, J. M. Elazar and M. L. Majewski, *Appl. Opt.*, 1998, **37**(22), 5271.

53 V. V. Thacker, L. O. Herrmann, D. O. Sigle, T. Zhang, T. Liedl, J. J. Baumberg and U. F. Keyser, *Nat. Commun.*, 2014, **5**(1), 3448.

54 C. Gonzalez-Ballestero, J. Feist, E. Moreno and F. J. Garcia-Vidal, *Phys. Rev. B: Condens. Matter Mater. Phys.*, 2015, **92**(12), 121402(5).

55 G. Kewes, F. Binkowski, S. Burger, L. Zschiedrich and O. Benson, *ACS Photonics*, 2018, **5**(10), 4089.

56 T. Cordes, J. Vogelsang and P. Tinnefeld, *J. Am. Chem. Soc.*, 2009, **131**(14), 5018.

Plasmon-assisted Förster resonance energy transfer at the single-molecule level in the moderate quenching regime

J. Bohlen[a,b,†], Á. Cuartero-González[c,†], E. Pibiri[a], D. Ruhlandt[d], A. I. Fernández-Domínguez[c], P. Tinnefeld[a,b,*], G. P. Acuna[1,5,*]

[a]Institute for Physical and Theoretical Chemistry – NanoBioScience and Braunschweig Integrated Centre of Systems Biology (BRICS), and Laboratory for Emerging Nanometrology (LENA), Braunschweig University of Technology, Braunschweig, Germany
[b]Faculty of Chemistry and Pharmacy, NanoBioScience, Ludwig-Maximilians-Universität München, München, Germany
[c]Departamento de Física Teórica de la Materia Condensada and Condensed Matter Physics Center (IFIMAC), Universidad Autónoma de Madrid, E-28049 Madrid, Spain
[d]Third Institute of Physics – Biophysics, Georg-August-Universität Göttingen, Göttingen, Germany.
[e]Department of Physics, University of Fribourg, Chemin du Musée 3, Fribourg CH-1700, Switzerland.
[†]Contributed equally
*Corresponding author: philip.tinnefeld@cup.lmu.de, guillermo.acuna@unifr.ch

1. Spectra

An overview of all spectra, including scattering and absorption of the monomer nanoparticle and absorption and emission of the FRET pair are shown in figure S1. The data for the nanoparticles are computed with the Mie Theory Calculator from Nanocomposix and the dye spectra are from the Atto tec website.

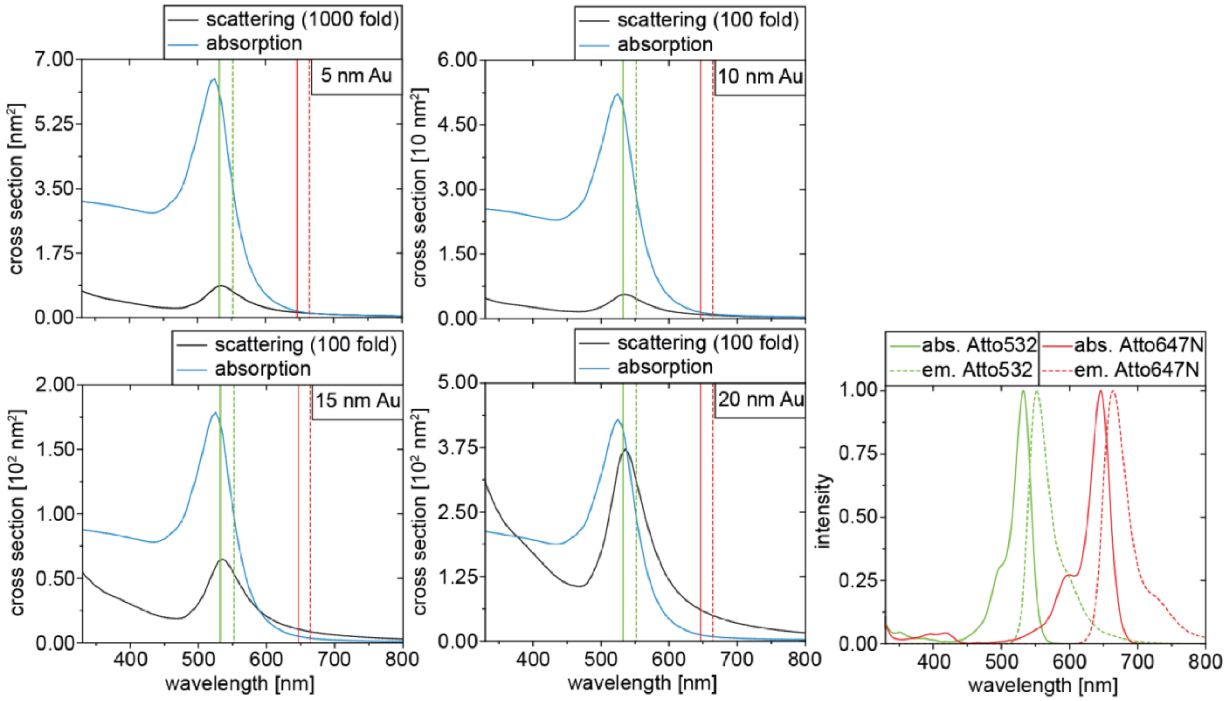

Figure S1: Scattering (black) and absorption spectra (blue) of the employed nanoparticles with the absorption (continuous) and emission maxima (dashed) of the Atto532 (green) and Atto647N (red). In addition, the whole spectra of the FRET pair is diagrammed.

2. Raw Data

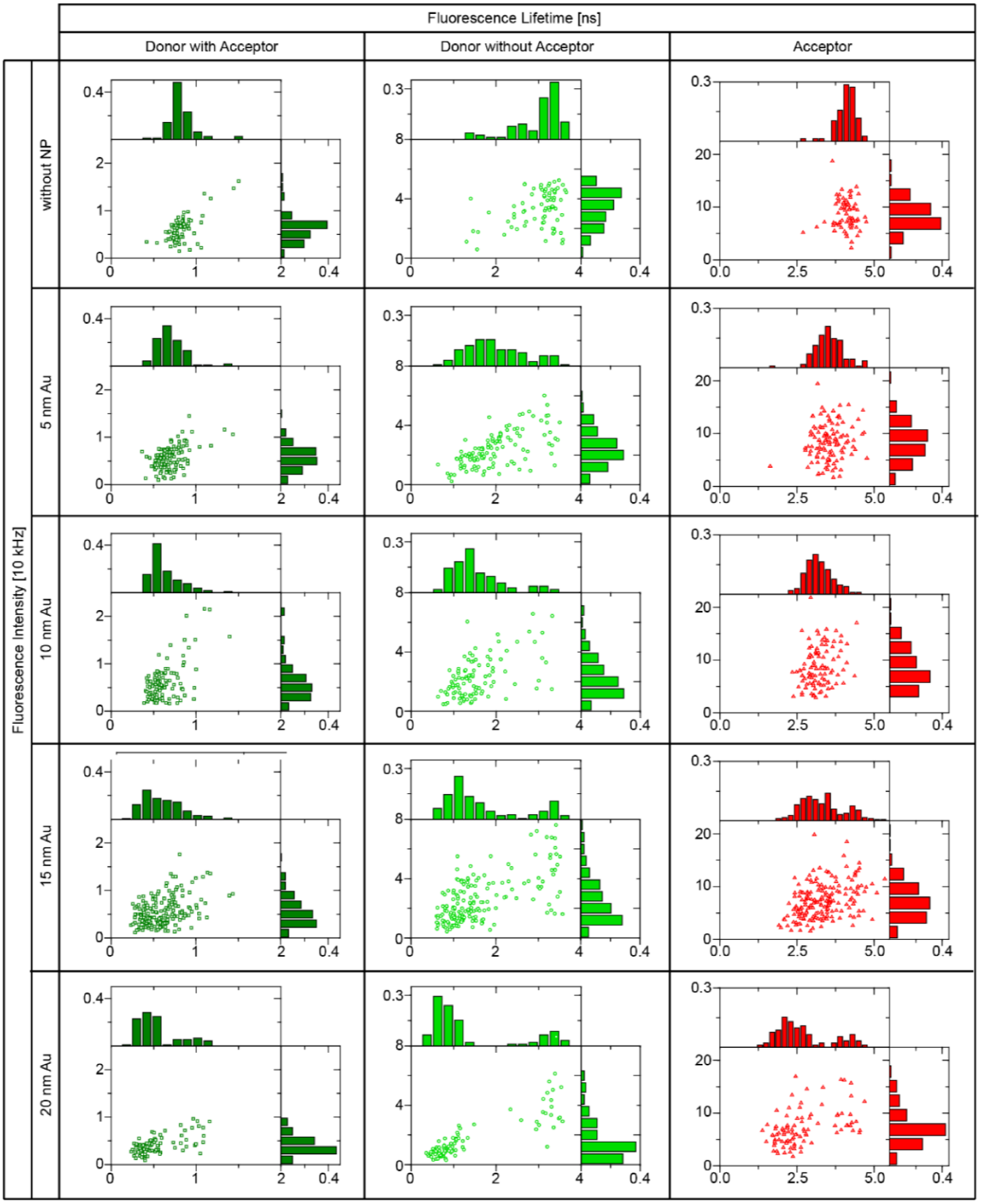

Figure S2: Raw data of the fluorescence lifetime and intensity of all three channels (donor in the presence of the acceptor and after photobleaching of the acceptor and acceptor only) from the measured with and without nanoparticle.

3. Distance calculation between dyes and nanoparticle surface

For the distance between dyes and nanoparticle a, the centroid (S) of the fictive triangle between all possible capturing strands (P_1, P_2, P_3) has to be calculated (see Figure S3).

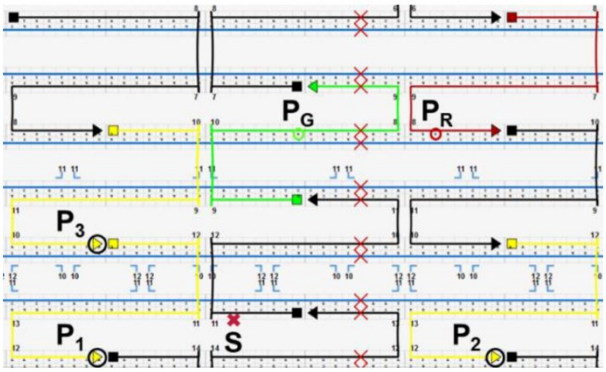

Figure S3: Section from the caDNano images with positions of Atto647N (PR), Atto532 (PG), all capturing strands (P1, P2, P3) and centroid of the capturing strands (S).

With the equations (S1) and coordinates (see table S 1) the centroid S (x_S, y_S) can be calculated.

$$x_S = \frac{x_{P_1} + x_{P_2} + x_{P_3}}{3};\ y_S = \frac{y_{P_1} + y_{P_2} + y_{P_3}}{3} \qquad (1)$$

Table S1: coordinates of Atto647N (P_R), Atto532 (P_G), all capturing strands (P_1, P_2, P_3) and centroid of the capturing strands (S) (the n in the index Indicates a Position, e.g. x_{P_1} stands for the x coordinate of P_1.

	P_1	P_2	P_3	S	P_R	P_G
Helix (x_n)	13	13	11	12.3	9	9
Base (y_n)	63	94	63	73.3	89	79

Distances between S and P_R or P_G is calculated by the Pythagoras´ theorem (eq. S2, F indicates the different dyes) with the distance between two oligonucleotides o (0.34 nm), the diameter of a helix d (2 nm) and the crossover between two helix c (1 nm).

$$d_F = \sqrt{((x_S - x_{P_F}) \cdot d + 3c)^2 + ((y_S - y_{P_F}) \cdot o)^2} \quad (S2)$$

The distances are 10.98 nm for S-P_R (d_R) and 9.79 nm for S-P_G (d_G). The height difference, h, is the sum of linker between dye and DNA origami structure (0.5 nm), the diameter of the DNA origami structure (2 nm), the crossover between DNA origami structure and formed linking helix (1 nm), the diameter of the linking helix (2 nm) and linker between linking helix and NP (0.5 nm), so overall 6 nm. By using the Pythagoras´ theorem a second time and subtract the radius r of the NP, a is calculated by Equation (S3).

$$a_{F,r} = \sqrt{((h + r)^2 + {d_F}^2)} - r \qquad (S3)$$

The overall distances are shown in table S2.

Table S2: Distances calulations between NP surfaces and both dyes (Atto647N and Atto532).

r [nm]	$a_{G,r}$ [nm]	$A_{R,r}$ [nm]
5	10.8	11.7
10	10.0	10.8
15	9.4	10.1
20	9.0	9.6

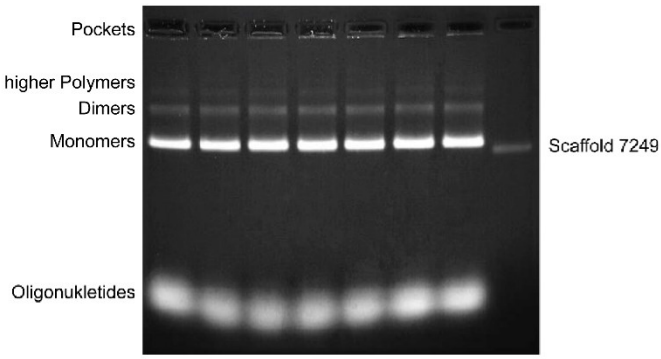

Figure S4: Gel images for the purified rectangular DNA origami structures with monomers, polymers, oligonucleotide and the scaffold as a reference.

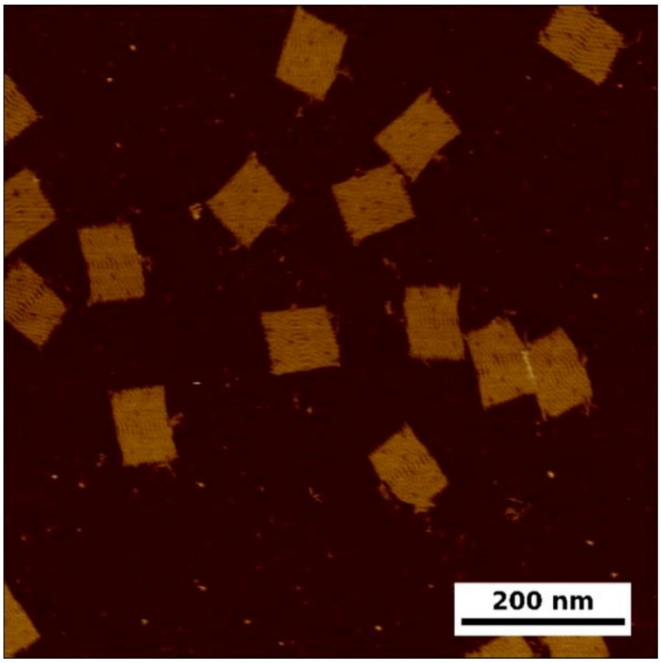

Figure S5: 800×800 µm images of the rectangular DNA origami structure. The holes in the edges and on the left and right side from sprout like center are showing the eight missing oligonucleotides from biotin.

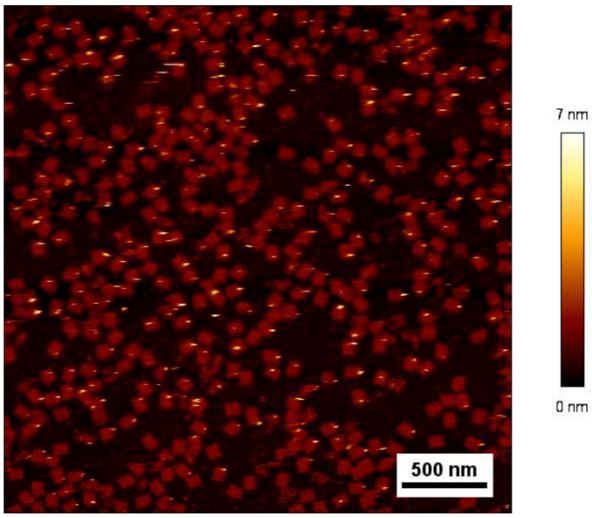

Figure S6: Rectangular DNA origami structure with 5 nm gold nanoparticle with a scale bar ranging from 0 to 7 nm. This DNA origami structure has an height with NP of 2 nm (one helix).

Table S3: Volume of the oligonucleotides with a thiol group at the 3` for nanoparticle with different sizes and materials.

d [nm]	5 Au	10 Au	15 Au	20 Au
V [µL/mL]	95.4	49.5	31.7	24

Table S4: Salting steps.

Step	1	2	3	4	5	6	7
V [µL]	10	10	20	20	20	20	50
Step	8	9	10	11	12	13	
V [µL]	50	50	50	100	100	100	

4. Design of DNA origami structure

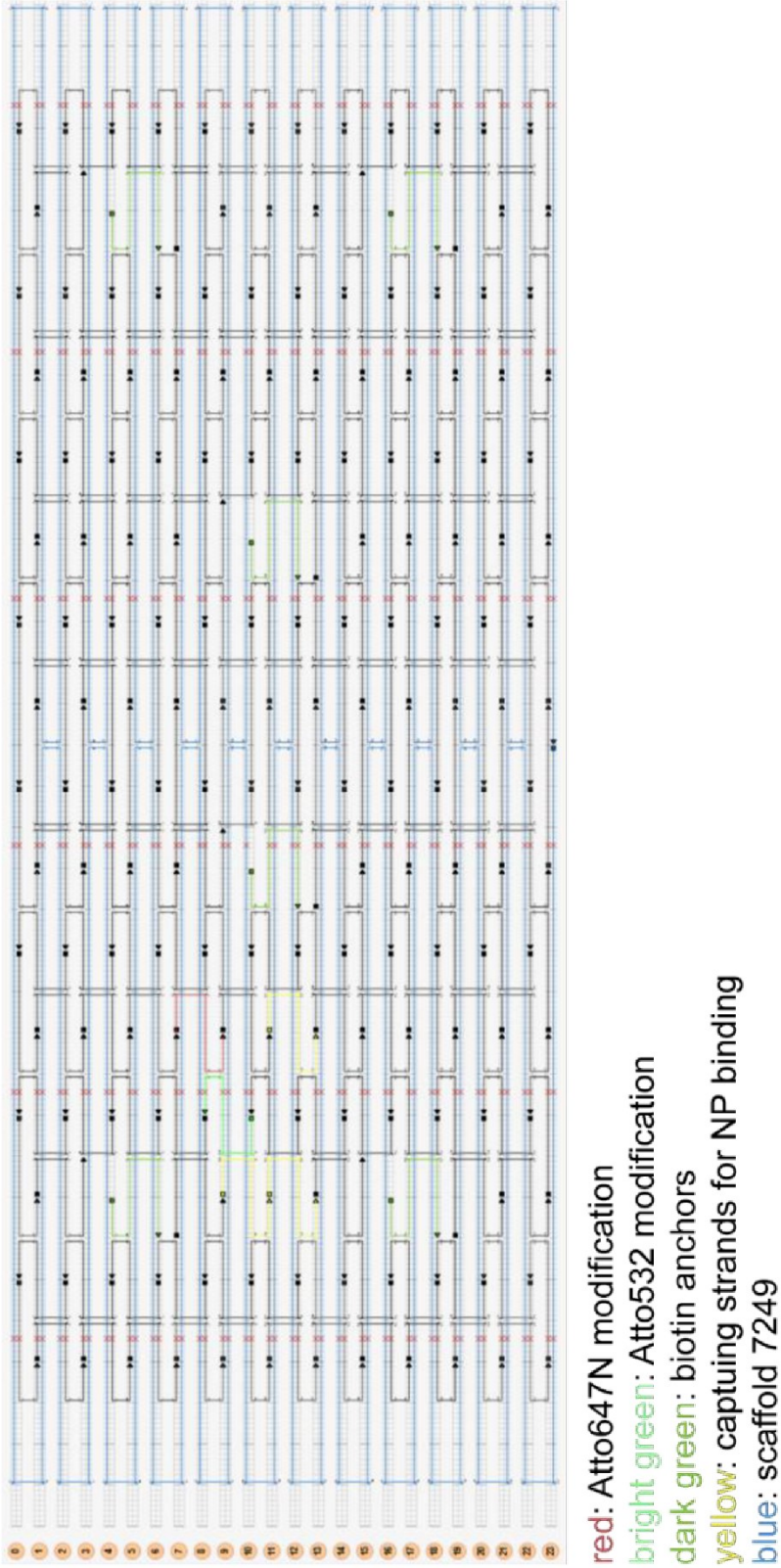

Figure S7: caDNAno image of rectangular DNA origami structure.

Tab. S 5. sequences of unmodified staples.

Sequence (5‘->3‘)	Length [nt]
TGACAACTCGCTGAGGCTTGCATTATACCA	30
AGAAAACAAAGAAGATGATGAAACAGGCTGCG	32
CTGTAGCTTGACTATTATAGTCAGTTCATTGA	32
TATATTTTGTCATTGCCTGAGAGTGGAAGATTGTATAAGC	40
CTTTAGGGCCTGCAACAGTGCCAATACGTG	30
TTAATGAACTAGAGGATCCCCGGGGGGTAACG	32
TCATCGCCAACAAAGTACAACGGACGCCAGCA	32
TCTTCGCTGCACCGCTTCTGGTGCGGCCTTCC	32
CTACCATAGTTTGAGTAACATTTAAAATAT	30
CGAAAGACTTTGATAAGAGGTCATATTTCGCA	32
ATTTTAAAATCAAAATTATTTGCACGGATTCG	32
GCGAAAAATCCCTTATAAATCAAGCCGGCG	30
CTGTGTGATTGCGTTGCGCTCACTAGAGTTGC	32
AGCGCGATGATAAATTGTGTCGTGACGAGA	30
GATGGTTTGAACGAGTAGTAAATTTACCATTA	32
GATGTGCTTCAGGAAGATCGCACAATGTGA	30
TAAATCAAAATAATTCGCGTCTCGGAAACC	30
GACAAAAGGTAAAGTAATCGCCATATTTAACAAAACTTTT	40
CCAGGGTTGCCAGTTTGAGGGGACCCGTGGGA	32
CTTATCATTCCCGACTTGCGGGAGCCTAATTT	32
CAGAAGATTAGATAATACATTTGTCGACAA	30
CGTAAAACAGAAATAAAAATCCTTTGCCCGAAAGATTAGA	40
AATACTGCCCAAAAGGAATTACGTGGCTCA	30
ATATTCGGAACCATCGCCCACGCAGAGAAGGA	32
ATACATACCGAGGAAACGCAATAAGAAGCGCATTAGACGG	40
CATCAAGTAAAACGAACTAACGAGTTGAGA	30
TTTCGGAAGTGCCGTCGAGAGGGTGAGTTTCG	32
AATAGTAAACACTATCATAACCCTCATTGTGA	32
GACCTGCTCTTTGACCCCCAGCGAGGGAGTTA	32
AACACCAAATTTCAACTTTAATCGTTTACC	30
CTCGTATTAGAAATTGCGTAGATACAGTAC	30
ATTACCTTTGAATAAGGCTTGCCCAAATCCGC	32
GCCGTCAAAAAACAGAGGTGAGGCCTATTAGT	32
AGTATAAAGTTCAGCTAATGCAGATGTCTTTC	32
TGTAGCCATTAAAATTCGCATTAAATGCCGGA	32
CAGCGAAACTTGCTTTCGAGGTGTTGCTAA	30
TACCGAGCTCGAATTCGGGAAACCTGTCGTGCAGCTGATT	40
GCGGATAACCTATTATTCTGAAACAGACGATT	32
AGCAAGCGTAGGGTTGAGTGTTGTAGGGAGCC	32
TTAAAGCCAGAGCCGCCACCCTCGACAGAA	30
TTCCAGTCGTAATCATGGTCATAAAAGGGG	30
CACAACAGGTGCCTAATGAGTGCCCAGCAG	30
TCAAGTTTCATTAAAGGTGAATATAAAAGA	30
GCTTTCCGATTACGCCAGCTGGCGGCTGTTTC	32
CCACCCTCTATTCACAAACAAATACCTGCCTA	32
TCAAATATAACCTCCGGCTTAGGTAACAATTT	32
AAAGGCCGGAGACAGCTAGCTGATAAATTAATTTTTGT	38
CTGAGCAAAAATTAATTACATTTTGGGTTA	30
GCGGAACATCTGAATAATGGAAGGTACAAAAT	32
CACCAGAAAGGTTGAGGCAGGTCATGAAAG	30

Sequence (5‘->3‘)	Length [nt]
GAAATTATTGCCTTTAGCGTCAGACCGGAACC	32
GAATTTATTTAATGGTTTGAAATATTCTTACC	32
GTACCGCAATTCTAAGAACGCGAGTATTATTT	32
GTTTATCAATATGCGTTATACAAACCGACCGTGTGATAAA	40
CAACTGTTGCGCCATTCGCCATTCAAACATCA	32
AAAGTCACAAAATAAACAGCCAGCGTTTTA	30
CAGGAGGTGGGGTCAGTGCCTTGAGTCTCTGAATTTACCG	40
GTAATAAGTTAGGCAGAGGCATTTATGATATT	32
ATTATACTAAGAAACCACCAGAAGTCAACAGT	32
GAGGGTAGGATTCAAAAGGGTGAGACATCCAA	32
AAGGAAACATAAAGGTGGCAACATTATCACCG	32
TTTTATTTAAGCAAATCAGATATTTTTTGT	30
TAGGTAAACTATTTTTGAGAGATCAAACGTTA	32
ACAAACGGAAAAGCCCCAAAAACACTGGAGCA	32
ATACCCAACAGTATGTTAGCAAATTAGAGC	30
ACCGATTGTCGGCATTTTCGGTCATAATCA	30
CATAAATCTTTGAATACCAAGTGTTAGAAC	30
TATAACTAACAAAGAACGCGAGAACGCCAA	30
ACGGCTACAAAAGGAGCCTTTAATGTGAGAAT	32
TTAGGATTGGCTGAGACTCCTCAATAACCGAT	32
AATTGAGAATTCTGTCCAGACGACTAAACCAA	32
AATAGCTATCAATAGAAAATTCAACATTCA	30
ACCTTGCTTGGTCAGTTGGCAAAGAGCGGA	30
ATATTTTGGCTTTCATCAACATTATCCAGCCA	32
AGGCTCCAGAGGCTTTGAGGACACGGGTAA	30
GCAAGGCCTCACCAGTAGCACCATGGGCTTGA	32
TTAACACCAGCACTAACAACTAATCGTTATTA	32
GCCAGTTAGAGGGTAATTGAGCGCTTTAAGAA	32
TTTATCAGGACAGCATCGGAACGACACCAACCTAAAACGA	40
TTGACAGGCCACCACCAGAGCCGCGATTTGTA	32
AGACGACAAAGAAGTTTTGCCATAATTCGAGCTTCAA	37
CGATAGCATTGAGCCATTTGGGAACGTAGAAA	32
ACACTCATCCATGTTACTTAGCCGAAAGCTGC	32
TGGAACAACCGCCTGGCCCTGAGGCCCGCT	30
TTATACCACCAAATCAACGTAACGAACGAG	30
TAATCAGCGGATTGACCGTAATCGTAACCG	30
CGCGCAGATTACCTTTTTTAATGGGAGAGACT	32
GTTTATTTTGTCACAATCTTACCGAAGCCCTTTAATATCA	40
AAATCACCTTCCAGTAAGCGTCAGTAATAA	30
TGAAAGGAGCAAATGAAAAATCTAGAGATAGA	32
CCTGATTGCAATATATGTGAGTGATCAATAGT	32
CTTAGATTTAAGGCGTTAAATAAAGCCTGT	30
AAGTAAGCAGACACCACGGAATAATATTGACG	32
TTATTACGAAGAACTGGCATGATTGCGAGAGG	32
GGCCTTGAAGAGCCACCACCCTCAGAAACCAT	32
GCCATCAAGCTCATTTTTTAACCACAAATCCA	32
TTGCTCCTTTCAAATATCGCGTTTGAGGGGGT	32
TTAACGTCTAACATAAAAACAGGTAACGGA	30
AGGCAAAGGGAAGGGCGATCGGCAATTCCA	30
ATCCCAATGAGAATTAACTGAACAGTTACCAG	32
AAAGCACTAAATCGGAACCCTAATCCAGTT	30

Sequence (5‘->3‘)	Length [nt]
ATCCCCCTATACCACATTCAACTAGAAAAATC	32
TCATTCAGATGCGATTTTAAGAACAGGCATAG	32
GCGAACCTCCAAGAACGGGTATGACAATAA	30
TAAATGAATTTTCTGTATGGGATTAATTTCTT	32
TCACCGACGCACCGTAATCAGTAGCAGAACCG	32
CATTTGAAGGCGAATTATTCATTTTTGTTTGG	32
ACAACATGCCAACGCTCAACAGTCTTCTGA	30
TCACCAGTACAAACTACAACGCCTAGTACCAG	32
GCCCGAGAGTCCACGCTGGTTTGCAGCTAACT	32
GCGCAGACAAGAGGCAAAAGAATCCCTCAG	30
ATTATCATTCAATATAATCCTGACAATTAC	30
AAACAGCTTTTTGCGGGATCGTCAACACTAAA	32
ACCCTTCTGACCTGAAAGCGTAAGACGCTGAG	32
GTATAGCAAACAGTTAATGCCCAATCCTCA	30
AAGGCCGCTGATACCGATAGTTGCGACGTTAG	32
CCTAAATCAAAATCATAGGTCTAAACAGTA	30
CTTTTGCAGATAAAAACCAAAATAAAGACTCC	32
CTTTTACAAAATCGTCGCTATTAGCGATAG	30
CATGTAATAGAATATAAAGTACCAAGCCGT	30
GACCAACTAATGCCACTACGAAGGGGGTAGCA	32
CAGCAAAAGGAAACGTCACCAATGAGCCGC	30
TAAATCGGGATTCCCAATTCTGCGATATAATG	32
AACGCAAAGATAGCCGAACAAACCCTGAAC	30
TAAATCATATAACCTGTTTAGCTAACCTTTAA	32
ATCGCAAGTATGTAAATGCTGATGATAGGAAC	32
AGCCAGCAATTGAGGAAGGTTATCATCATTTT	32
GCCCTTCAGAGTCCACTATTAAAGGGTGCCGT	32
GCTATCAGAAATGCAATGCCTGAATTAGCA	30
GCGAGTAAAAATATTTAAATTGTTACAAAG	30
TATTAAGAAGCGGGGTTTTGCTCGTAGCAT	30
AATACGTTTGAAAGAGGACAGACTGACCTT	30
AAATTAAGTTGACCATTAGATACTTTTGCG	30
TGCATCTTTCCCAGTCACGACGGCCTGCAG	30
TACGTTAAAGTAATCTTGACAAGAACCGAACT	32
ATGCAGATACATAACGGGAATCGTCATAAATAAAGCAAAG	40
CCCGATTTAGAGCTTGACGGGGAAAAAGAATA	32
ACCTTTTTATTTTAGTTAATTTCATAGGGCTT	32
CACATTAAAATTGTTATCCGCTCATGCGGGCC	32
GCCTCCCTCAGAATGGAAAGCGCAGTAACAGT	32
ACAACTTTCAACAGTTTCAGCGGATGTATCGG	32
CTTTAATGCGCGAACTGATAGCCCCACCAG	30
GCACAGACAATATTTTTGAATGGGGTCAGTA	31
AGAAAGGAACAACTAAAGGAATTCAAAAAAA	31
AACAGTTTTGTACCAAAAACATTTTATTTC	30
AGGAACCCATGTACCGTAACACTTGATATAA	31
CCAACAGGAGCGAACCAGACCGGAGCCTTTAC	32
AACGCAAAATCGATGAACGGTACCGGTTGA	30
CAACCGTTTCAAATCACCATCAATTCGAGCCA	32
TTCTACTACGCGAGCTGAAAAGGTTACCGCGC	32
GCCTTAAACCAATCAATAATCGGCACGCGCCT	32
GCCCGTATCCGGAATAGGTGTATCAGCCCAAT	32

Sequence (5‘->3‘)	Length [nt]
TCCACAGACAGCCCTCATAGTTAGCGTAACGA	32
TCTAAAGTTTTGTCGTCTTTCCAGCCGACAA	31
AACAAGAGGGATAAAAATTTTTAGCATAAAGC	32
AGAGAGAAAAAAATGAAAATAGCAAGCAAACT	32
TCAATATCGAACCTCAAATATCAATTCCGAAA	32
CCACCCTCATTTTCAGGGATAGCAACCGTACT	32
GTCGACTTCGGCCAACGCGCGGGGTTTTTC	30
GTTTTAACTTAGTACCGCCACCCAGAGCCA	30
TTAGTATCACAATAGATAAGTCCACGAGCA	30
GCAATTCACATATTCCTGATTATCAAAGTGTA	32
TAAAAGGGACATTCTGGCCAACAAAGCATC	30
AAGCCTGGTACGAGCCGGAAGCATAGATGATG	32
AACGTGGCGAGAAAGGAAGGGAAACCAGTAA	31
CCAATAGCTCATCGTAGGAATCATGGCATCAA	32
ACGCTAACACCCACAAGAATTGAAAATAGC	30
TGTAGAAATCAAGATTAGTTGCTCTTACCA	30
CAAATCAAGTTTTTTGGGGTCGAAACGTGGA	31
TCGGCAAATCCTGTTTGATGGTGGACCCTCAA	32
TTTTCACTCAAAGGGCGAAAAACCATCACC	30
CTCCAACGCAGTGAGACGGGCAACCAGCTGCA	32
TTTACCCCAACATGTTTTAAATTTCCATAT	30
GAGAGATAGAGCGTCTTTCCAGAGGTTTTGAA	32
TTTAGGACAAATGCTTTAAACAATCAGGTC	30

Tab. S 6: Modified staples with dyes, biotin and capturing strands for NP.

Sequence (5‘->3‘)	Length [nt]
TAAGAGCAAATGTTTAGACTGGATAG-Atto647N-AAGCC	32
GATGGCTTATCAAAA-Atto532-GATTAAGAGCGTCC	30
Biotin-CGGATTCTGACGACAGTATCGGCCGCAAGGCGATTAAGTT	40
Biotin-AGCCACCACTGTAGCGCGTTTTCAAGGGAGGGAAGGTAAA	40
Biotin-ATAAGGGAACCGGATATTCATTACGTCAGGACGTTGGGAA	40
Biotin-GAGAAGAGATAACCTTGCTTCTGTTCGGGAGAAACAATAA	40
Biotin-TAGAGAGTTATTTTCATTTGGGGATAGTAGTAGCATTA	38
Biotin-GAAACGATAGAAGGCTTATCCGGTCTCATCGAGAACAAGC	40
AATGGTCAACAGGCAAGGCAAAGAGTAATGTGAAAAAAAAAAAAAAAAAAAA	52
GATTTAGTCAATAAAGCCTCAGAGAACCCTCAAAAAAAAAAAAAAAAAAAAA	52
CGGATTGCAGAGCTTAATTGCTGAAACGAGTAAAAAAAAAAAAAAAAAAAAA	52

Oligonucleotide sequence for nanoparticle from 5’ to 3’:
TTTTTTTTTTTTTTTTTTTTTTTTT-Thiol

5. Numerical calculations

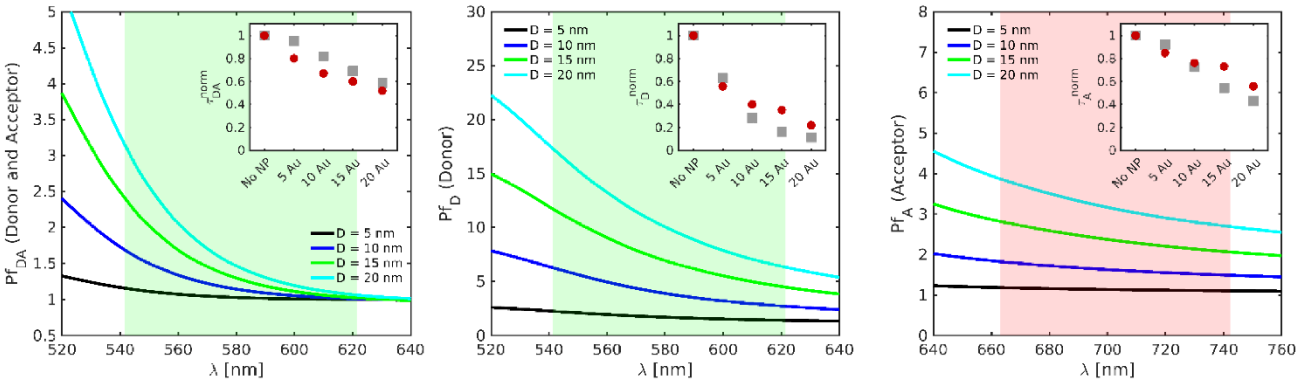

Figure S8: Numerical Purcell factor, Pf, spectra for the donor in presence (left) and absence (center) of the acceptor, and for the acceptor in isolation (right). Calculations for the four Au NP sizes considered in the experiments are shown (D indicates the NP diameter). The insets show normalized lifetimes calculated from the spectral averaging (taken within the colored range in the main panels) of the Pf spectra and using Equation (4). Experimental and theoretical results are plotted in red circles and grey squares, respectively.

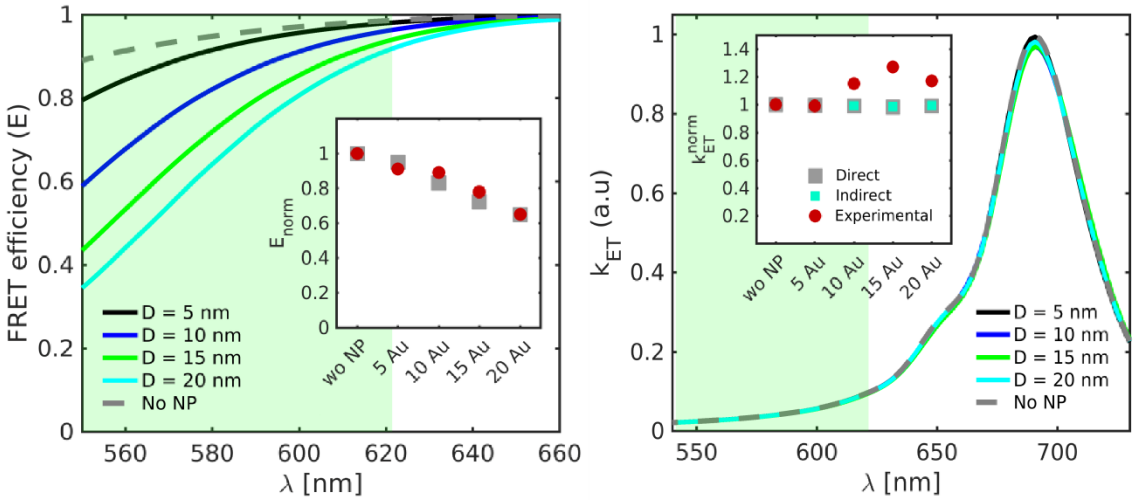

Figure S9: Theoretical predictions for the FRET efficiency and rate. Right: $E = 1 - Pf_D/Pf_{DA}$ (note the equivalence with Equation (3)) as a function of the donor emission wavelength. The inset (grey squares) plots the efficiency obtained from the spectral averaging within the green window. Left: $k_{ET} \propto V^{-1} \int |E_{DA}|^2 dV$ as a function of the donor emission wavelength. The inset (grey squares) shows the rate obtained from the spectral averaging within the green window. For comparison, the indirect prediction obtained from the evaluation of Equation (2) with numerical results in the insets of Figure S8 is shown in cyan squares. In both panels, red circles correspond to experimental data.

8.4. Publication II

Distance Dependence of Single-Molecule Energy Transfer to Graphene Measured with DNA Origami Nanopositioners

by

I. Kaminska, **J. Bohlen**, S. Rocchetti, F. Selbach, G. P. Acuna, P. Tinnefeld

published in

Nano letters **2019**, *19* (7), 4257–4262

Author contribution:

J. B. prepared parts of the DNA origami structures as well as graphene samples, analyzed DNA origami structure with AFM and helped writing the manuscript.

NANO LETTERS

Letter

Cite This: Nano Lett. 2019, 19, 4257−4262

pubs.acs.org/NanoLett

Distance Dependence of Single-Molecule Energy Transfer to Graphene Measured with DNA Origami Nanopositioners

I. Kaminska,*,† J. Bohlen,‡ S. Rocchetti,‡ F. Selbach,‡ G. P. Acuna,§ and P. Tinnefeld*,‡

†Institute of Physical Chemistry of the Polish Academy of Sciences, 01-224 Warsaw, Poland

‡Department of Chemistry and Center for NanoScience, Ludwig-Maximilians-Universität München, 80539 München, Germany

§Department of Physics, Université de Fribourg, Ch. du Musée 3, CH-1700 Fribourg, Switzerland

Supporting Information

ABSTRACT: Despite the thorough investigation of graphene since 2004, altering its surface chemistry and reproducible functionalization remain challenging. This hinders fabrication of more complex hybrid materials with controlled architectures, and as a consequence the development of sensitive and reliable sensors and biological assays. In this contribution, we introduce DNA origami structures as nanopositioners for placing single dye molecules at controlled distances from graphene. The measurements of fluorescence intensity and lifetime of single emitters carried out for distances ranging from 3 to 58 nm confirmed the d^{-4} dependence of the excitation energy transfer to graphene. Moreover, we determined the characteristic distance for 50% efficiency of the energy transfer from single dyes to graphene to be 17.7 nm. Using pyrene molecules as a glue to immobilize DNA origami nanostructures of various shape on graphene opens new possibilities to develop graphene-based biophysics and biosensing.

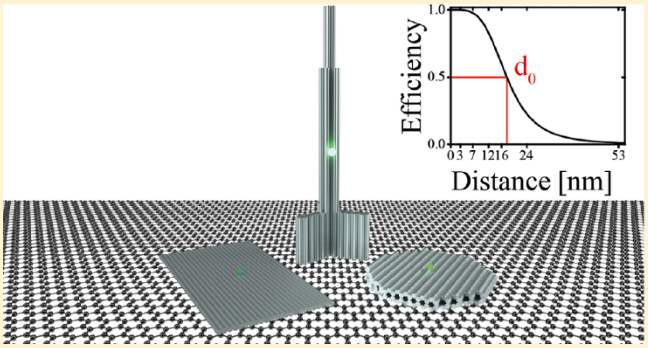

KEYWORDS: *DNA origami, graphene, single molecules, fluorescence quenching, energy transfer*

Graphene is a two-dimensional carbon lattice resembling a honeycomb, which has attracted great attention since 2004, when it was experimentally isolated for the first time. Due to its unique electronic, optical, and mechanical properties, it has been intensively explored worldwide and found applications probably in every branch of science.[1] Its gapless energy band structure and linear dispersion relation near the corners of the Brillouin zone result in a frequency-independent light absorption, governed solely by the fine-structure constant, $\alpha \approx 1/137$. As a result, this only one-atom thick material absorbs as much as $\pi\alpha \approx 2.3\%$ of light, over the visible and near-infrared spectral regions.[2] As a consequence, graphene behaves as an extraordinary energy sink and a unique acceptor system, which is one of the key characteristics of graphene and graphene-related two-dimensional materials exploited in the field of optical biosensors and distance rulers.[3,4] Fluorescent dyes placed close to graphene are strongly quenched and their displacement from graphene can restore fluorescence.[5−8] It has been demonstrated both theoretically and experimentally that the energy transfer from a molecule (a single dipole) to graphene ("2D array of dipoles") strongly depends on the distance d between both and scales proportional to d^{-4}.[8−11] Whereas the distance dependence is well understood, reports vary with respect to the d_0 value, which states the distance of 50% quenching efficiency. This variation is related to the different emitters used (e.g., quantum dots, nitrogen-vacancy centers, or dyes embedded in crystals) and how the distance to the graphene layer was controlled, with reported values range from d_0 = 8 to 20 nm.[5−7,11,12] In one work quenching up to 60 nm was reported.[12]

Hitherto, gold surfaces and not graphene surfaces are commonly used in fluorescence quenching biosensing because, besides the quenching, a well-developed surface chemistry exists. Gold has thus been the material of choice for biosensing[13−15] as well as for MIET[16,17] (metal induced energy transfer) super-resolution imaging. Compared to gold, graphene offers the outstanding advantage of good optical transparency in the far-field and less background fluorescence. So far, however, graphene and other related 2D materials lack the chemical flexibility to carry out complex biomolecular assays. Main problems include missing control over surface chemistry, construct composition and fabrication, and low reproducibility of graphene-based hybrid structures.

In this work, we used DNA origami[18] as nanopositioners to generally overcome the problem of chemical functionalization of graphene for optical biosensing assays. The DNA origami technique enables the formation of custom-designed DNA nanostructures with a volume of ∼21.000 nm^3, and the rich

Received: January 14, 2019
Revised: June 3, 2019
Published: June 19, 2019

DOI: 10.1021/acs.nanolett.9b00172
Nano Lett. 2019, 19, 4257−4262

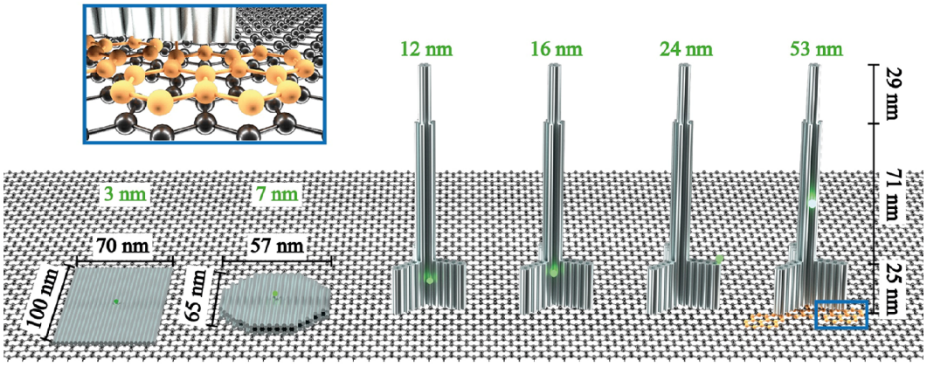

Figure 1. Sketches of rectangular-, disc-, and pillar-shaped DNA origami structures. A single ATTO542 fluorophore (green sphere) is positioned at a height of 3 nm (NR), 7 nm (ND), 12 nm (NP1), 16 nm (NP2), 24 nm (NP3), and 53 nm (NP4). Blue frame: zoom-in of pyrene-modified (orange) DNA strand protruding from DNA origami and interacting with graphene via $\pi-\pi$ interactions. Gray bars represent double-stranded DNA.

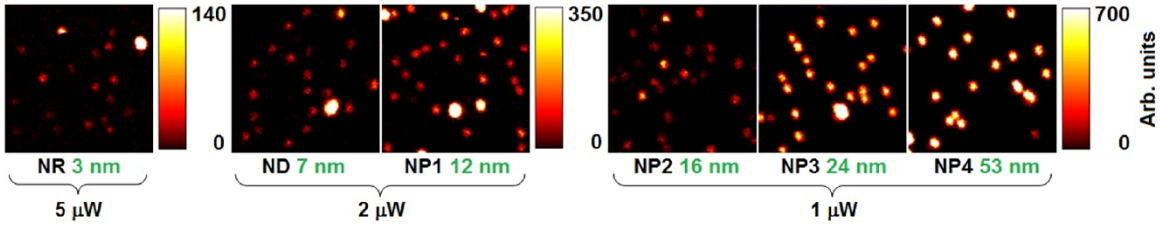

Figure 2. Fluorescence intensity images (5×5 μm) obtained for DNA origami structures with a single dye (ATTO542) immobilized on graphene, for 532 nm excitation wavelength, and laser power ranging from 1 to 5 μW (NR, 5 μW; ND and NP1, 2 μW; NP2, NP3, and NP4, 1 μW).

DNA chemistry available allows placing of arbitrary objects and complex biomolecular assays[19−21] at programmed positions on the DNA nanostructure.[18,22−24] For biomolecular assays, DNA origami can act as a biocompatible surface.[25] In previous works, DNA origami structures were coupled to pristine graphene either to increase their stability[26] or as a template for metallized DNA nanolithography.[27] However, it was demonstrated with TEM imaging that DNA origami nanoplates were denatured due to hydrophobic interactions of the DNA bases with graphene upon adsorption.[28,29] As a universal glue to connect the DNA origami constructs to the graphene layer, we used several pyrene-modified DNA strands that are hybridized to the DNA origami on the one hand and interact with the graphene lattice via $\pi-\pi$ stacking interactions on the other hand. We show that this immobilization scheme provides stable DNA origami structures for different geometries and enables placing of single, freely rotating fluorescent molecules at defined distances to the graphene layer. We exploit the exquisite distance control of single fluorescent dyes to graphene in order to revisit the distance dependence of energy transfer to graphene. Our narrow intensity−fluorescence lifetime distributions confirm the d^{-4} law with a precise value of d_0 of 17.7 nm in aqueous buffer solution and present the basis for a broad range of applications in biosensing and optoelectronics.

Results and Discussion. The selection of DNA origami shapes was guided by the possibility to position a single dye molecule at a designed height from the bottom (distance from graphene) and included rectangular- (nanorectangle = NR), disc- (nanodisc = ND), and pillar-shaped (nanopillar = NP) self-assembled DNA origami structures (see Figure 1). Each DNA origami structure contains one dye molecule (ATTO542) marked as a small green sphere, which is positioned at the height of 3 nm (NR), 7 nm (ND), 12 nm (NP1), 16 nm (NP2), 24 nm (NP3), and 53 nm (NP4) (further details are included in the Materials and Methods). The selected values cover the range of distances for which the energy transfer from a single dye molecule to graphene is expected to vary from 0 to almost 100%.[8] As the dyes are attached to the DNA origami by six-carbon linkers and measurements were carried out in buffer solution, it is expected that the fluorescent dyes are free to rotate on the flexible linker.

Additionally, at the bottom of each structure, we incorporated six to eight staple strands with single-stranded extensions protruding from the DNA origamis. The protrusions are used to label the DNA origami with pyrene-modified complementary oligonucleotides. The pyrene enabled selective binding of the DNA origami with the bottom side to the graphene layer (Figure 1 blue frame). External labeling with extended staple strands allowed modular modifications also for other moieties. For example, in order to measure the same samples on glass, biotin-modified oligonucleotides were used and DNA origami structures were immobilized on neutravidin−biotinylated BSA surfaces.[30] A detailed description of the DNA origami structures and sample preparation can be found in the Materials and Methods, whereas AFM and TEM images of the obtained DNA origami structures are included in the Supporting Information (Figure S1).

Single-molecule fluorescence measurements were carried out with a home-built confocal microscope (further details are included in Imaging and Analysis). Figure 2 depicts ATTO542 fluorescence intensity images for each of the six DNA origami structures using 532 nm excitation. The closer the emitter is to the graphene layer, the more its fluorescence is quenched. Therefore, we adjusted the excitation power to always work with a count rate in a regime that showed linear excitation intensity dependent emission. Laser powers ranged from 1 μW for three nanopillar samples (NP2, NP3, and NP4), 2 μW for

DOI: 10.1021/acs.nanolett.9b00172
Nano Lett. 2019, 19, 4257−4262

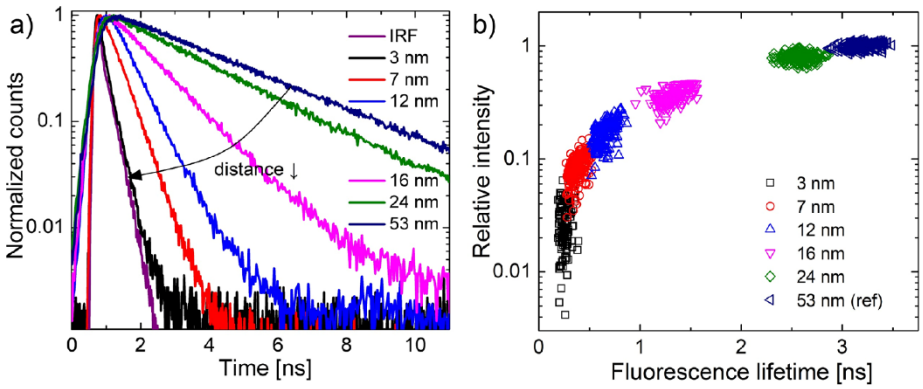

Figure 3. (a) Normalized fluorescence intensity decays of ATTO542 at difference distances to graphene (averaged from 20 decays for each sample). (b) Relative fluorescence intensity as a function of fluorescence lifetime (fluorescence lifetimes were obtained by reconvolution). For better separation of the populations a semilogarithmic presentation is provided.

one nanopillar sample and the nanodisc (NP1 and ND), to 5 μW for the nanorectangle (NR) DNA origami structure. On all images, we observed that the fluorescence intensities of most spots corresponding to dye molecules are very homogeneous with occasional very bright spots.

We also performed control measurements to confirm that the immobilization of the samples on graphene depends on the number of pyrene molecules. The results of the experiments carried out for NP2 DNA origami structure without pyrene molecules, as well as with one or eight pyrene molecules confirm that only in the last case, the samples are successfully immobilized on graphene (Figure S2). Moreover, we compared immobilization of pyrene-modified DNA origami structures on graphene with the immobilization of DNA origami structures with protruding strands on graphene functionalized with complementary pyrene-modified strands. This experiment clearly shows that the reversed immobilization scheme is not efficient, and it is necessary to incorporate pyrene molecules within DNA origami structures beforehand (Figure S3).

In order to characterize interactions between dye molecules and graphene, fluorescence transients were recorded for each spot. This enabled the identification of single DNA origami structures by observing blinking events (fluctuating between "on"/bright and "off"/dark states) and single-step photobleaching (examples of fluorescence transients are depicted in Figure S4). We identified two types of deviations from the typical single-molecule behavior, which is related to the mentioned brighter spots in the images. In cases with multistep photobleaching, we attributed the signal to aggregates of multiple DNA origami structures, also present in analogous measurements carried out on glass coverslips (Figure S5). In other cases, the brighter spots exhibited single-step photobleaching and showed similar intensities and fluorescence lifetimes as molecules of the reference structures measured on glass coverslips. We hence attribute these molecules to DNA origami structures immobilized within small defects/cracks of the graphene layer. Nevertheless, taking into account the small number of such spots (<10%), together with the quality control performed by Graphenea and our additional characterization using Raman spectroscopy (several tens of spectra obtained from Raman measurements, an exemplary spectrum presented in Figure S6), we conclude that graphene samples used in our measurements have little defects and contaminations.

For further analysis, only transients with single bleaching steps were considered and used to determine the fluorescence intensity and fluorescence lifetime of each spot (see Imaging and Analysis for details). As expected, dye molecules incorporated in DNA origami structures bound to graphene exhibit shorter fluorescence lifetimes compared to samples immobilized on glass (see Figure 3a). Only for the largest distance of 53 nm to graphene (NP4), the fluorescence properties are not affected (see Figure S7) and the unperturbed fluorescence lifetime of 3.25 ns for ATTO542 is obtained.

The reduction of fluorescence intensity and fluorescence lifetime is correlated and arises from the strong near-field interactions between the emitter and graphene.[5,8,31] Figure 3b shows the relative fluorescence intensity $\frac{I_G}{\langle I_{ref}\rangle}$ as a function of the fluorescence lifetime, where I_G is fluorescence intensity of a dye molecule within the DNA origami bound to graphene, and $\langle I_{ref}\rangle$ is the average fluorescence intensity obtained for the reference sample, NP4. Due to the differences in the applied laser powers in our measurements, all the obtained values of fluorescence intensities were normalized to the laser power of 1 μW. It is noteworthy that narrow and clearly separated populations of fluorescence intensity and fluorescence lifetime are obtained, indicating the selectivity and robustness of the immobilization strategy. The homogeneity of the data is also fostered by the binding strategy of the dye, which can rotate during the measurement. It is therefore justified to assume that the measured data reflect the interaction of an averaged dipole orientation with the graphene layer. Interestingly, the positioning with the pyrene subunits as selective glue even yields narrow distributions for the nanopillar samples NP1 to NP4, which is remarkable in view of the high aspect ratio of this DNA origami. As measurements were carried out for up to 2 days after sample preparation DNA origamis on graphene are also stable and no degradation was observed.

For a quantitative analysis of the interaction between single dye molecules and graphene and its strong distance dependence, we investigated how the quenching (relative intensity) and the energy transfer efficiency to graphene both depend on the emitter−graphene distance. The energy transfer efficiency η was calculated from fluorescence lifetimes $\left(\eta_L = 1 - \frac{\tau_G}{\langle\tau_{ref}\rangle}\right)$,[5−7] where τ_G is the fluorescence lifetime of a dye molecule within DNA origami bound to graphene, and

DOI: 10.1021/acs.nanolett.9b00172
Nano Lett. 2019, 19, 4257−4262

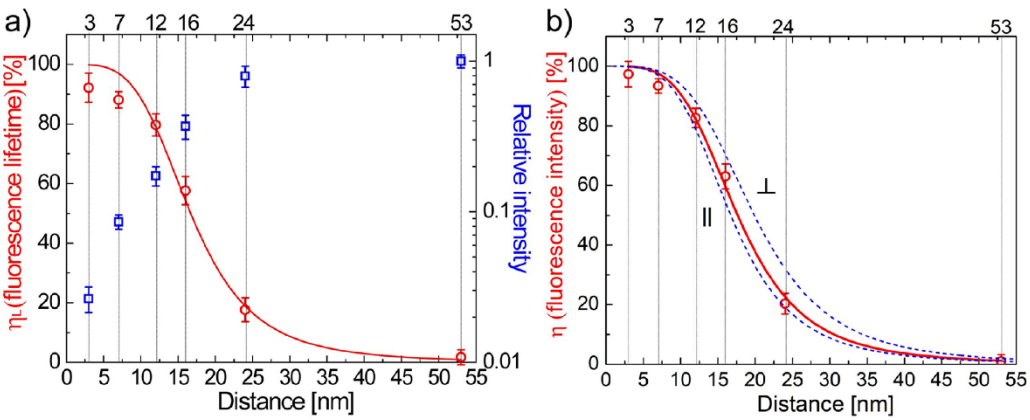

Figure 4. (a) Mean values of the energy transfer efficiency calculated from fluorescence lifetime values (red circles) and relative intensity values (blue squares); (b) mean values of the excitation energy transfer efficiency calculated from fluorescence intensity values, all plotted as a function of the distance between ATTO542 and graphene. Standard errors calculated from the fitted normal distribution (not shown) for N = 140−250 molecules are shown. Fitted curve (red line) of the energy transfer efficiency as the function of the distance d between graphene and emitter, $\left(\frac{1}{1+\left(\frac{d}{d_0}\right)^4}\right)\cdot 100\%$, where d_0 states the distance of 50% quenching efficiency, and from the fit equals 17.7 ± 0.5 nm. Blue dashed lines: calculated curves based on semiclassical model, for point-dipole emitters parallel (||) and perpendicular (⊥) to graphene.

$\langle\tau_{ref}\rangle$ is the average fluorescence lifetime obtained for the reference sample, as well as from fluorescence intensities $\left(\eta_I = 1 - \frac{I_G}{\langle I_{ref}\rangle}\right)$. Figure 4 show the distance dependent energy transfer efficiency calculated by both methods. While the shapes of the graphs are similar, lower energy transfer efficiencies were obtained from the fluorescence lifetime graph for the shortest distances (Figure 4a), which we attribute to uncertainty induced by the limited time resolution of the setup (see decays and instrument response function (IRF) in Figure 3a). The energy transfer efficiency obtained from intensities reaches up to 97% quenching for the smallest distance. We fitted the experimental data (Figure 4b) with the expected d^{-4} dependence (red line) and obtained a d_0 value (the distance of 50% energy transfer efficiency) of 17.7 ± 0.5 nm. Additionally, in Figure 4b we compare experimental data with results calculated from the semiclassical model, which describes the near-field interactions between an emitter and graphene $\left(\frac{\langle\tau_{ref}\rangle}{\tau_G} = 1 + \frac{9\nu\alpha}{256\pi^3(\epsilon+1)^2}\left(\frac{\lambda_0}{d}\right)^4\right)$.[8,11] In this approximation, the emitters (energy donors) are considered as classical dipoles (placed in vacuum) coupled to neighboring semi-infinite media (graphene), which acts as an energy acceptor. In the equation, λ_0 states the emission wavelength (562 nm, peak emission of ATTO542), ϵ is the permittivity of the glass substrate (2.25), and α is the fine-structure constant. In Figure 4b, we show how the intensity of the emitter decreases with distance from graphene when the dipole is oriented either parallel (||, ν = 1) or perpendicular (⊥, ν = 2) to graphene (blue dashed lines). We obtained d_0 equals 16.8 nm for ν = 1 and 20.0 nm for ν = 2, which is in excellent agreement with our measurement. With geometric averaging implying that the probability of parallel orientation of dye dipole and graphene is twice as high as that of perpendicular orientation, the distance dependence should be more similar to the graph for the parallel orientation as is well reflected in our data. Analogous results were found for a dye in the red spectral region (ATTO647N), as shown in Figure S8.

Conclusions. We immobilized DNA origami structures on graphene using pyrene modifications of DNA oligonucleotides. The specificity and robustness of the immobilization without denaturation enabled placing fluorescent dyes at defined distances to the graphene layer. We confirmed the d^{-4} dependence of energy transfer from the dye to graphene and determined the distance of 50% energy transfer: d_0 = 17.7 nm. The homogeneity of the population indicates that distances to graphene can be determined with very high precision in a range of 5−30 nm. Together with its good transparency in the far-field graphene might become the substrate of choice for superresolution microscopy involving fluorescence lifetime measurement for determining the z-position of dyes.[16,17] Beyond that, DNA origami as nanopositioners will enable placing biomolecular assays on the graphene with the optimized distance to the surface for optimized sensitivity. Placing assays at a height around d_0 of 17−20 nm will yield an extremely sensitive method of detecting small distance changes to the surface while avoiding direct contact to the interfering hydrophobic graphene surface. DNA origami as a chemical converting and placement platform could be used to incorporate further functionalities for electronic, nanophotonic, and energy conversion devices with graphene and other 2D materials opening a myriad of new possibilities.

Materials and Methods. Samples of single-layer CVD (chemical vapor deposition) graphene on glass coverslips was purchased from Graphenea. DNA origami Nanorectangles, Nanodiscs, and Nanopillars were prepared as described elsewhere.[32,33] The details on DNA origami design and DNA sequences can be found in Tables S1−S8. All unmodified (Table S1−S6) and modified (Table S7 and S8) staple strands used for DNA origami folding are commercially available and were purchased from Eurofins Genomics, except two modified staple strands, with ATTO542 and pyrene, which were purchased from biomers.net GmbH. The DNA origami structures were incubated with pyrene-modified (for graphene samples) or biotin-modified (for glass samples) staple strands, complementary to the oligonucleotides protruding from DNA origami structures, for 2 h in 37 °C. Such prepared structures

DOI: 10.1021/acs.nanolett.9b00172
Nano Lett. 2019, 19, 4257−4262

were immobilized on the glass surface of a Lab-Tek chamber (Thermo Fisher Scientific) coated with BSA-biotin/neutravidin (Sigma-Aldrich) or directly on a single layer of CVD graphene, in a buffer 1 × TE containing 12 mM $MgCl_2$, at room temperature. Finally, after several minutes of incubation (which is a time necessary to record a control fluorescence intensity map to check the appropriate density of the sample coverage) the sample was washed with 1 × TE containing 12 mM $MgCl_2$ and further single-molecule fluorescence measurements were performed.

The designed height values of 3 nm (NR), 7 nm (ND), 12 nm (NP1), 16 nm (NP2), 24 nm (NP3), and 53 nm (NP4) were calculated using the size parameter of a double helix, namely, its diameter of 2.2 nm and length of 0.34 nm per base pair. Taking into account a previous report about the overestimation of the calculated values (the measured values smaller of about 10% compared to the designed values), these numbers were corrected.[17] Additionally, a thickness of 1 nm for the pyrene-modified protruding strands was added.

Imaging and Analysis. Single-molecule fluorescence measurements were performed on a custom built confocal microscope based on an Olympus IX71 inverted microscope. The green laser beams (532 nm LDH-P-FA-530B, Picoquant) is controlled by a PDL 828 "SepiaII" (Picoquant). The green fiber laser is decoupled by a collimator (F2220APC-532, Thorlabs). After passing through cleanup filters (532/2) and a dichroic mirror (640DCXR, AHF), the laser beam is coupled into a fiber (P3-488PM-FC, Thorlabs) with a collimator (PAF2-2A, Thorlabs) and decoupled with a collimator (G169015000, Qioptics). A combination of a linear polarizer (WP12L-Vis, Thorlabs) and a quarter wave plate (AQWP05M-600, Thorlabs) is used to obtain circularly polarized light. After passing a dual band dichroic beam splitter (z532/633, AHF), the light beam is focused by an oil-immersion objective (UPLSAPO 100XO, NA 1.40, Olympus) on the measurement chamber, which can be positioned accurately by a piezo-stage (P-527.3CD, PhysikInstrumente) which is driven by a E-727 controller (PhysikInstrumente). The emission of the fluorophores is collected by the same objective, focused on a 50 μm pinhole (Linos), collimated with a lens (AC050-150-A-ML, Thorlabs) and split spectrally by another dichroic beam splitter (640DCXR, AHF). The green laser beams were cleaned with a filter set (HC582/75, AHF and LP 532, both Semrock) and focused with a lens (AC080-020-A-ML, Thorlabs) on the APD (SPCM-AQRH-TR-14, Excelitas). The signals of the APD are detected by a HydraHarp 400 (Picoquant) and the whole system is operated with SymPhoTime 64 (PicoQuant).

■ ASSOCIATED CONTENT

Supporting Information

The Supporting Information is available free of charge on the ACS Publications website at DOI: 10.1021/acs.nanolett.9b00172.

Detailed information on DNA origami design, DNA origami folding, and immobilization; TEM, AFM, and fluorescence intensity images, Raman spectrum of a single-layer graphene, fluorescence intensity decays, mean values of the excitation energy transfer efficiency; tables of unmodified staples, pyrene-modified staples, and Atto542-modified staples (PDF)

■ AUTHOR INFORMATION

Corresponding Authors

*E-mail: ikaminska@ichf.edu.pl (I.K.).
*E-mail: philip.tinnefeld@cup.uni-muenchen.de (P.T.).

ORCID

I. Kaminska: 0000-0002-9435-8198
G. P. Acuna: 0000-0001-8066-2677

Author Contributions

The manuscript was written through contributions of all authors. All authors have given approval to the final version of the manuscript.

Notes

The authors declare no competing financial interest.

■ ACKNOWLEDGMENTS

Many thanks to Tim Schröder for help with a setup. I.K. is grateful for the support by the Foundation for Polish Science, within the program HOMING/2017-4/32 (POIR.04.04.00-00-42E8/17-00) and Polish National Science Center (MAESTRO, UMO-2016/22/A/ST4/00029). P.T. and G.P.A. acknowledge support by the DFG (AC 279/2-1 and TI 329/9-1, INST 86/1904-1 FUGG, excellence clusters e-conversion, and NIM). This work was supported by the Swiss National Science Foundation through the National Center of Competence in Research Bio-Inspired Materials.

■ REFERENCES

(1) Ferrari, A. C.; Bonaccorso, F.; Falko, V.; Novoselov, K. S.; Roche, S.; Bøggild, P.; Borini, S.; Koppens, F.; Palermo, V.; Pugno, N.; et al. Science and Technology Roadmap for Graphene, Related Two-Dimensional Crystals, and Hybrid Systems. *Nanoscale* **2015**, *7*, 4598−4810.

(2) Nair, R. R.; Blake, P.; Grigorenko, A. N.; Novoselov, K. S.; Booth, T. J.; Stauber, T.; Peres, N. M. R.; Geim, A. K. Fine Structure Constant Defines. *Science* **2008**, *320*, 1308.

(3) Zhu, C.; Du, D.; Lin, Y. Graphene and Graphene-like 2D Materials for Optical Biosensing and Bioimaging: A Review. *2D Mater.* **2015**, *2*, 032004.

(4) Anichini, C.; Czepa, W.; Pakulski, D.; Aliprandi, A.; Ciesielski, A.; Samorì, P. Chemical Sensing with 2D Materials. *Chem. Soc. Rev.* **2018**, *47*, 4860−4908.

(5) Chen, Z.; Berciaud, S.; Nuckolls, C.; Heinz, T. F.; Brus, L. E. Energy Transfer from Individual Semiconductor Nanocrystals to Graphene. *ACS Nano* **2010**, *4*, 2964−2968.

(6) Federspiel, F.; Froehlicher, G.; Nasilowski, M.; Pedetti, S.; Mahmood, A.; Doudin, B.; Serin, P.; Lee, J.; Halley, D.; Dubertret, B.; et al. Distance Dependence of the Energy Transfer Rate from a Single Semiconductor Nanostructure to Graphene. *Nano Lett.* **2015**, *15*, 1252−1258.

(7) Mazzamuto, G.; Tabani, A.; Pazzagli, S.; Rizvi, S.; Reserbat-Plantey, A.; Schädler, K.; Navickaite, G.; Gaudreau, L.; Cataliotti, F. S.; Koppens, F.; et al. Single-Molecule Study for a Graphene-Based Nano-Position Sensor. *New J. Phys.* **2014**, *16*, 113007.

(8) Gaudreau, L.; Tielrooij, K. J.; Prawiroatmodjo, G. E. D. K.; Osmond, J.; García de Abajo, F. J.; Koppens, F. H. L. Universal Distance-Scaling of Nonradiative Energy Transfer to Graphene. *Nano Lett.* **2013**, *13*, 2030−2035.

(9) Swathi, R. S.; Sebastian, K. L. Resonance Energy Transfer from a Dye Molecule to Graphene. *J. Chem. Phys.* **2008**, *129*, 054703.

(10) Swathi, R. S.; Sebastian, K. L. Long Range Resonance Energy Transfer from a Dye Molecule to Graphene Has (Distance)(−4) Dependence. *J. Chem. Phys.* **2009**, *130*, 086101.

(11) Brenneis, A.; Gaudreau, L.; Seifert, M.; Karl, H.; Brandt, M. S.; Huebl, H.; Garrido, J. A.; Koppens, F. H. L.; Holleitner, A. W.

DOI: 10.1021/acs.nanolett.9b00172
Nano Lett. 2019, 19, 4257−4262

Ultrafast Electronic Readout of Diamond Nitrogen-Vacancy Centres Coupled to Graphene. *Nat. Nanotechnol.* **2015**, *10*, 135−139.
(12) Gonçalves, H.; Bernardo, C.; Moura, C.; Ferreira, R. A. S.; André, P. S.; Stauber, T.; Belsley, M.; Schellenberg, P. Long Range Energy Transfer in Graphene Hybrid Structures. *J. Phys. D: Appl. Phys.* **2016**, *49*, 315102.
(13) Langer, A.; Schräml, M.; Strasser, R.; Daub, H.; Myers, T.; Heindl, D.; Rant, U. Polymerase/DNA Interactions and Enzymatic Activity: Multi-Parameter Analysis with Electro-Switchable Biosurfaces. *Sci. Rep.* **2015**, *5*, 1−15.
(14) Schlichtiger, A.; Baier, C.; Yin, M. X.; Holmes, A. B.; Maruyama, M.; Strasser, R.; Rant, U.; Thaler, M.; Luppa, P. B. Covalent Attachment of Functionalized Cardiolipin on a Biosensor Gold Surface Allows Repetitive Measurements of Anticardiolipin Antibodies in Serum. *Anal. Bioanal. Chem.* **2013**, *405*, 275−285.
(15) Langer, A.; Hampel, P. A.; Kaiser, W.; Knezevic, J.; Welte, T.; Villa, V.; Maruyama, M.; Svejda, M.; Jähner, S.; Fischer, F.; et al. Protein Analysis by Time-Resolved Measurements with an Electro-Switchable DNA Chip. *Nat. Commun.* **2013**, *4*, 2099.
(16) Chizhik, A. I.; Rother, J.; Gregor, I.; Janshoff, A.; Enderlein, J. Metal-Induced Energy Transfer for Live Cell Nanoscopy. *Nat. Photonics* **2014**, *8*, 124−127.
(17) Isbaner, S.; Karedla, N.; Kaminska, I.; Ruhlandt, D.; Raab, M.; Bohlen, J.; Chizhik, A.; Gregor, I.; Tinnefeld, P.; Enderlein, J.; et al. Axial Colocalization of Single Molecules with Nanometer Accuracy Using Metal-Induced Energy Transfer. *Nano Lett.* **2018**, *18*, 2616−2622.
(18) Rothemund, P. W. K. Folding DNA to Create Nanoscale Shapes and Patterns. *Nature* **2006**, *440*, 297−302.
(19) Acuna, G. P.; Bucher, M.; Stein, I. H.; Steinhauer, C.; Kuzyk, A.; Holzmeister, P.; Schreiber, R.; Moroz, A.; Stefani, F. D.; Liedl, T.; et al. Distance Dependence of Single-Fluorophore Quenching by Gold Nanoparticles Studied on DNA Origami. *ACS Nano* **2012**, *6*, 3189−3195.
(20) Vietz, C.; Lalkens, B.; Acuna, G. P.; Tinnefeld, P. Synergistic Combination of Unquenching and Plasmonic Fluorescence Enhancement in Fluorogenic Nucleic Acid Hybridization Probes. *Nano Lett.* **2017**, *17*, 6496−6500.
(21) Ochmann, S. E.; Vietz, C.; Trofymchuk, K.; Acuna, G. P.; Lalkens, B.; Tinnefeld, P. Optical Nanoantenna for Single Molecule-Based Detection of Zika Virus Nucleic Acids without Molecular Multiplication. *Anal. Chem.* **2017**, *89*, 13000−13007.
(22) Douglas, S. M.; Dietz, H.; Liedl, T.; Högberg, B.; Graf, F.; Shih, W. M. Self-Assembly of DNA into Nanoscale Three-Dimensional Shapes. *Nature* **2009**, *459*, 414−418.
(23) Hong, F.; Zhang, F.; Liu, Y.; Yan, H. DNA Origami : Scaffolds for Creating Higher Order Structures. *Chem. Rev.* **2017**, *117*, 12584−12640.
(24) Ke, Y.; Lindsay, S.; Chang, Y.; Liu, Y.; Yan, H. Self-Assembled Water-Soluble Nucleic Acid Probe Tiles for Laber-Free RNA Hybridization Assays. *Science* **2008**, *319* (2008), 180−183.
(25) Gietl, A.; Holzmeister, P.; Grohmann, D.; Tinnefeld, P. DNA Origami as Biocompatible Surface to Match Single-Molecule and Ensemble Experiments. *Nucleic Acids Res.* **2012**, *40*, e110.
(26) Matković, A.; Vasić, B.; Pesić, J.; Prinz, J.; Bald, I.; Milosavljević, A. R.; Gajić, R. Enhanced Structural Stability of DNA Origami Nanostructures by Graphene Encapsulation. *New J. Phys.* **2016**, *18*, 025016.
(27) Jin, Z.; Sun, W.; Ke, Y.; Shih, C.-J.; Paulus, G. L. C.; Hua Wang, Q.; Mu, B.; Yin, P.; Strano, M. S. Metallized DNA Nanolithography for Encoding and Transferring Spatial Information for Graphene Patterning. *Nat. Commun.* **2013**, *4*, 1663.
(28) Kabiri, Y.; Ananth, A. N.; van der Torre, J.; Katan, A.; Hong, J. Y.; Malladi, S.; Kong, J.; Zandbergen, H.; Dekker, C. Distortion of DNA Origami on Graphene Imaged with Advanced TEM Techniques. *Small* **2017**, *13*, 1700876.
(29) Green, N. S.; Pham, P. H. Q.; Crow, D. T.; Burke, P. J.; Norton, M. L. Layered Graphene-Mica Substrates Induce Melting of DNA Origami. *Mater. Res. Express* **2018**, *5*, 045035.
(30) Pibiri, E.; Holzmeister, P.; Lalkens, B.; Acuna, G. P.; Tinnefeld, P. Single-Molecule Positioning in Zeromode Waveguides by DNA Origami Nanoadapters. *Nano Lett.* **2014**, *14*, 3499−3503.
(31) Kaminska, I.; Wiwatowski, K.; Mackowski, S. Efficiency of Energy Transfer Decreases with the Number of Graphene Layers. *RSC Adv.* **2016**, *6*, 102791−102796.
(32) Puchkova, A.; Vietz, C.; Pibiri, E.; Wünsch, B.; Sanz Paz, M.; Acuna, G. P.; Tinnefeld, P. DNA Origami Nanoantennas with over 5000-Fold Fluorescence Enhancement and Single-Molecule Detection at 25 Mm. *Nano Lett.* **2015**, *15*, 8354−8359.
(33) Vietz, C.; Lalkens, B.; Acuna, G. P.; Tinnefeld, P. Functionalizing Large Nanoparticles for Small Gaps in Dimer Nanoantennas. *New J. Phys.* **2016**, *18*, 045012.

DOI: 10.1021/acs.nanolett.9b00172
Nano Lett. 2019, 19, 4257−4262

Supporting Information

Distance Dependence of Single-Molecule Energy Transfer to Graphene Measured with DNA Origami Nanopositioners

I. Kaminska,[†*] *J. Bohlen,*[‡] *S. Rocchetti,*[‡] *F. Selbach,*[‡] *G. P. Acuna,*[§] *P. Tinnefeld*[‡*]

[†] Institute of Physical Chemistry of the Polish Academy of Sciences, 01-224 Warsaw, Poland

[‡] Department of Chemistry and Center for NanoScience, Ludwig-Maximilians-Universität München, 80539 München, Germany

[§] Department of Physics, Université de Fribourg, Ch. du Musée 3, CH-1700 Fribourg, Switzerland

Corresponding Authors

* E-mail: ikaminska@ichf.edu.pl (I.K.).

* E-mail: philip.tinnefeld@cup.uni-muenchen.de (P. T.).

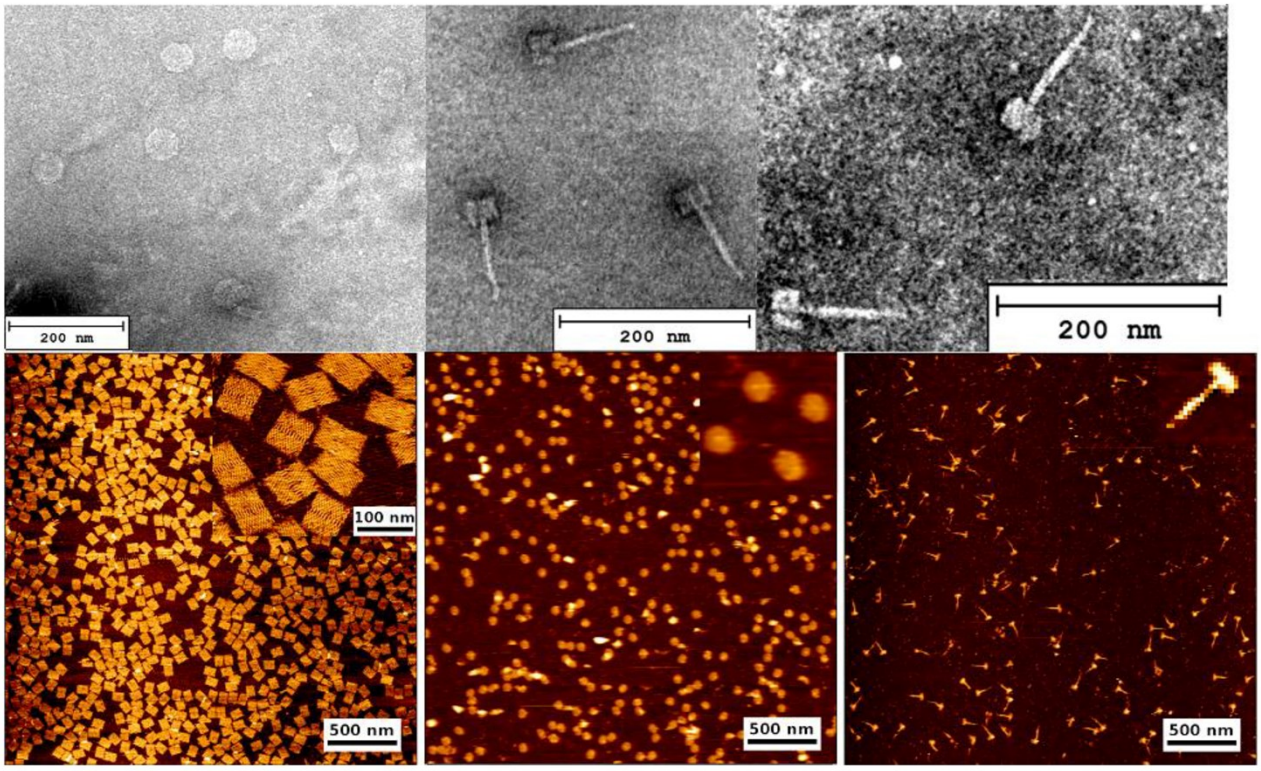

Figure S1. (Top) TEM images of: (from left) nanodisc and nanopillar. (Bottom) AFM images of: (from left) nanorectangle, nanodisc and nanopillar.

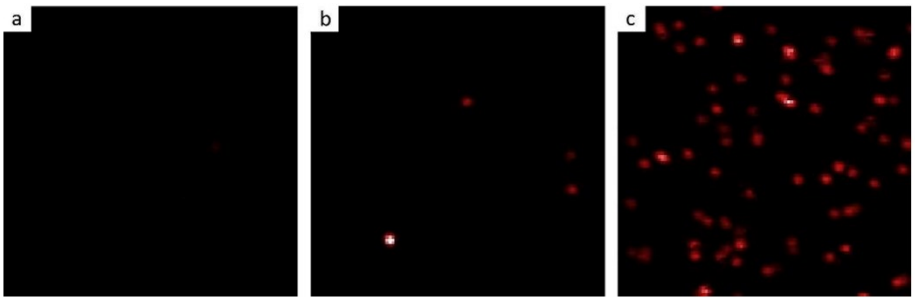

Figure S2. Fluorescence intensity images (10 × 10 μm) obtained for DNA origami structure NP2 with a single dye (ATTO647N) containing (a) zero, (b) one or (c) eight pyrene molecules, incubated on graphene, for 640 nm excitation wavelength, and laser power 1 μW.

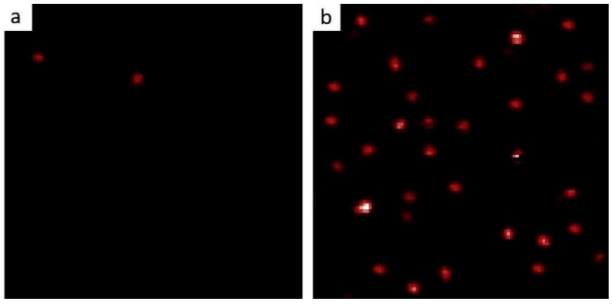

Figure S3. Fluorescence intensity images (10 × 10 μm) obtained for DNA origami structure NP2 with a single dye (ATTO647N) immobilized on (a) graphene covered with a monolayer of pyrene-modified staple strands *via* hybridization of complementary strands protruding from DNA origamis, (b) graphene *via* eight pyrene molecules incorporated beforehand within DNA origamis, for 640 nm excitation wavelength, and laser power 1 μW.

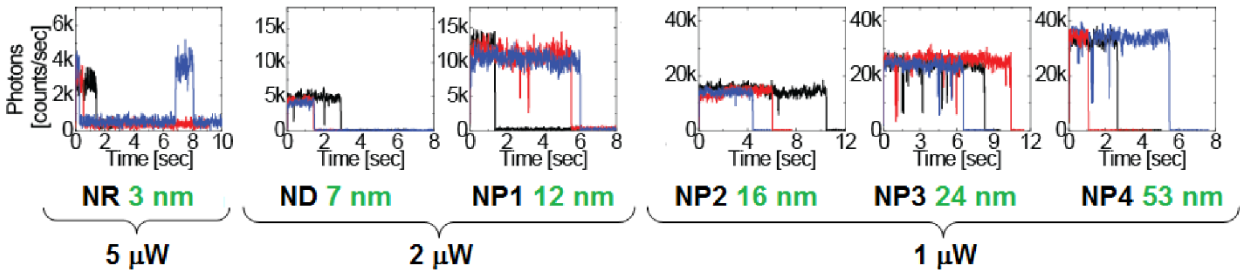

Figure S4. Examples of fluorescence transients obtained for DNA origami structures with a single dye (ATTO542) immobilized on graphene, for 532 nm excitation wavelength, and laser power ranging from 1 to 5 μW (NR, 5 μW; ND and NP1, 2 μW; NP2, NP3 and NP4, 1 μW).

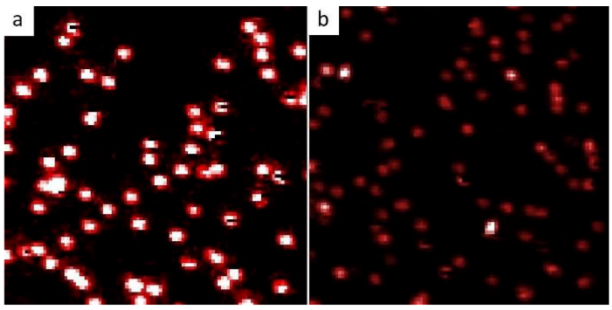

Figure S5. Fluorescence intensity images (10 × 10 μm) obtained for DNA origami structure NP2 with a single dye (ATTO647N) immobilized on (a) glass and (b) graphene, for 640 nm excitation wavelength, and laser power 1 μW.

Raman spectra measured for single spots as well as maps confirm the presence of high quality single layer graphene, $\frac{I_{2D}}{I_G} > 2$ and $\frac{I_D}{I_G} \rightarrow 0$.

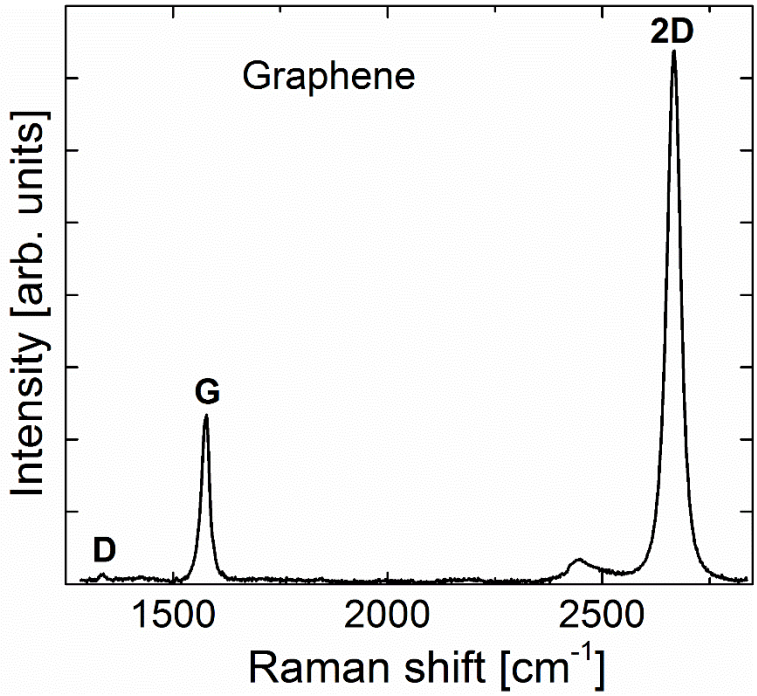

Figure S6. Raman spectrum of a single graphene layer, averaged from a map of 30 measured spots.

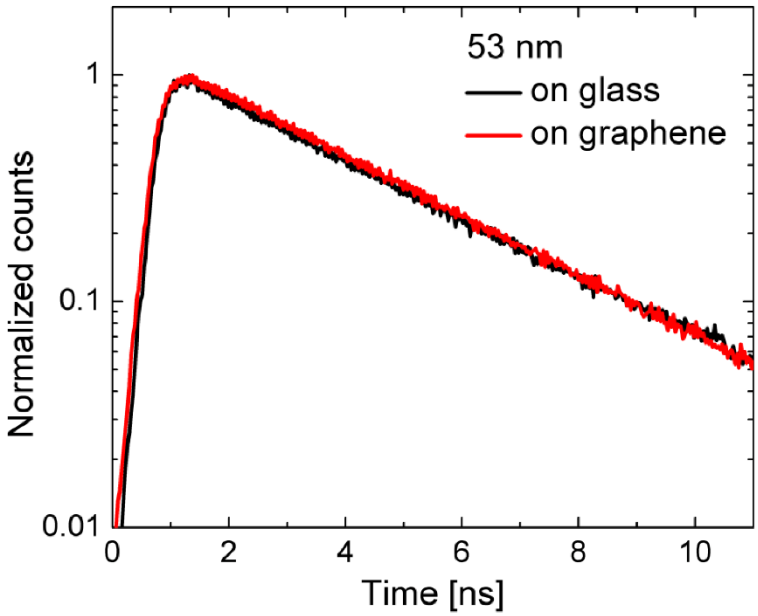

Figure S7. Normalized fluorescence intensity decays of ATTO542 within DNA origami structure NP4 (a dye placed at the height of 53 nm) immobilized on glass (■) or graphene (●).

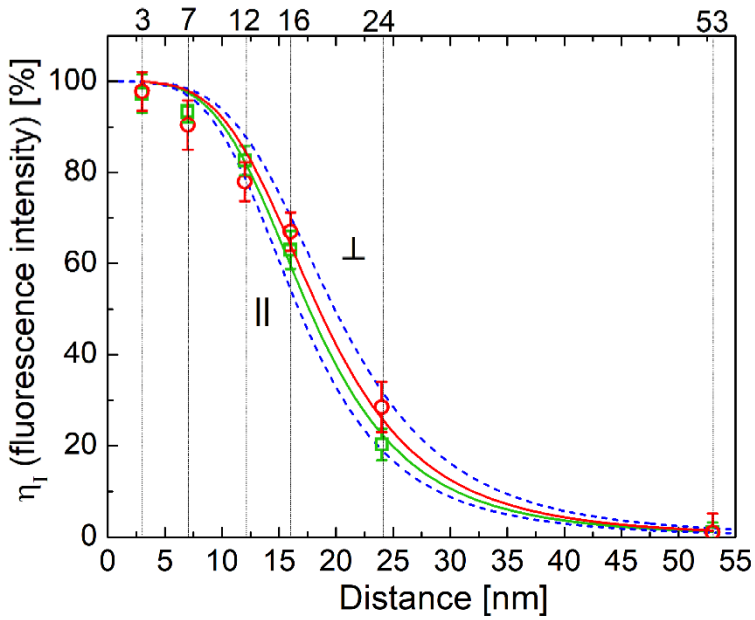

Figure S8. Mean values of the excitation energy transfer efficiency calculated from fluorescence intensity values, all plotted as a function of the distance between ATTO542 (□) or ATTO647N (○) and graphene. Standard errors calculated from the fitted normal distribution (not shown) for N =

140 – 250 molecules are shown. Fitted curve (green/red line) of the energy transfer efficiency as the function of the distance d between graphene and emitter, $\left(\frac{1}{1+\left(\frac{d}{d_0}\right)^4}\right) \cdot 100\%$, where d_0 states the distance of 50% quenching efficiency, and from the fit equals to 17.7 ± 0.5 nm (ATTO542) and 18.5 ± 0.7 nm (ATTO647N). Blue dashed lines: calculated curves based on semiclassical model, for point-dipole emitters parallel (||) and perpendicular (⊥) to graphene.

DNA sequences

Table S1. Unmodified staples from the 5' to the 3' end for the DNA origami nanopillar.

Sequence (5' to 3')	Length
CTAGTCAGTTGGCAAATCAACAGTCTTTAGGTAGATAACAAA	42
CCTCATCACCCCAGCAGGCCTCTTCGCTATTACGCCAGTGCC	42
TAAGTTGGCATGATTAAAGAA	21
CAAACGGAATAGGAAACCGAGGAATAAGAAATTACAAG	38
ACCGCCACCCTCAGAACCCGTACTCTAGGGA	31
AATTTCTTAAACCCGCTTAATTGTATCGTTGCGGGCGATATA	42
GCGAATCAGTGAGGCCACCGAGTAGTAGCAACTGAGAGTTGA	42
GAATTCGTCTCGTCGCTGGGTCTGCAATCCATTGCAACACGG	42
CCCGGTTGATAAAGCATGTCAATC	24
TCACAGCGTACTCCGTGGTGAAGGGATAGCTAAGAGACGAGG	42
GGCAACACCAGGGTCTAATGAGTGAGCTCACAACAATAGGGT	42
AATAGAAAAAAATAAACGTCTGAGAGGAATATAAGAGCAACACTATGAT	49
TAGCCCGGAATAGGTGTAAGGATAAGTGCCGTCGA	35
AATAAAACGAACTATGACCCCACCAAGC	28
TGCTAAATCGGGGAGCCCCCGATTTAGAGCTAGCAGAACATT	42
AAGAAAGCGCTGAACCTCAAATATTCTAAAGGAAAGCGTTCA	42
AAATGCGGAAACATCGGTTTTCAGGTTTAACGTCAGATTAAC	42
CACGGCAACAATCCTGATATACTT	24
CGAGGGTACTTTTTCATGAACGGGGTCATAATGCCGAGCCACCACC	46
TATTTAAATTGCAGGAAGATTG	22
TTCGGTCCCATCGCATAGTTGCGCCGACATGCTTTCGAGGTG	42
TAACGACATTTTTACCAGCGCCAAAGAAAGTTACCAGAACCCAAA	45
CAAATTATTCATTTCAATTACCTGAGTA	28
GCTGTAGTTAGAGCTTAATTG	21
GAGTTAAAAGGGTAATTGAGCGCTAATATCAGAGGAACTGAACACC	46

TTAGTTTGAGTGCCCGAGAAATAAAGAAATTGCGTAGAGATA	42
GAACCGCCACCCTCCATATCATACC	25
TGCTGATTGCCGTTGTCATAAACATCGGGCGG	32
TAGCCAGCTTTCATCCAAAAATAAACGT	28
TAAAGCCTCCAGTACCTCATAGTTAGCG	28
AGAATTTTAGAGGAAAACAATATTACCGCCAGCTGCTCATTT	42
CTCATCGGGATTGAGTGAGCGAGTAACAACCCGTC	35
GGGATATTGACGTAGCAATAGCTAAGATAGC	31
AATTGTGTCGAAATCCGCGGCACACAACGGAGATTTGTATCA	42
CCTCGTTTACCAGAAACCAAA	21
ACCAACAAACCAAAATTAACAATTTCATTTGAATTACCGAGG	42
CTGGCATTAGGAGAATAAAATGAAGAAACGATTTTTTGAGTA	42
ACCTGACGGGGAAAGCCGGCGAACCAAGTGTCTGCGCGTTGC	42
AACCGTGTCATTGCAACGGTAATATATTTTAAATGAAAGGGT	42
GAACTGGCTCATTACAACTTTAATCATTCTTGAGATTACTTA	42
AGAAATCGTTAGACTACCTTTTTAAGGCGTTCTGACCTTTTTGCA	45
CAAAATCACCGGAACCAGAGCCAGATTTTGTCACAATCACAC	42
TGCGTGTTCAGGTTGTGTACATCG	24
GAGGCCAAGCTTTGAATACCAAGTACGGATTACCTTTTCAAA	42
TAATATCAAAGGCACCGCTTCTGGCACT	28
GGCGAAGCACCGTAATAACGCCAGGGTTTTCCCAGTCATGGG	42
TATGACTTTATACATTTTTTTTTAATGGAAACAGTACACCGT	42
TTGGGCGGCTGATTTCGGCAAAATCCCT	28
CCTCGTCTTTCCACCACCGGAACCGCCTCCCTCA	34
CGTACAGGCCCCCTAACCGTCCCCGGGTACCGAGCGTTC	39
CCTAATTTAACAAACCCTCAATCAATATCTGATTCGCTAATC	42
ATTACGAGATAAATGCCAGCTTTGAGGGGACGACGACAG	39
CAGCAGCGCCGCTTGTTTATCAGCTTCACGAAAAA	35
AATATTCATTGAATCCATGCTGGATAGCGTCCAAT	35
GAGTCTGGATTTGTTATAATTACTACATACACCAC	35
AGTTTCCAACATTATTACATTATAC	25
TTGCGAATAATATTTACAGCGGAGTGAGGTAAAATTTTGAGG	42
GTCGCAGAAAAACTTAAATTTGCC	24
GCTGGCATAGCCACATTATTC	21
AGTCGCCTGATACTTGCATAACAGAATACGTGGCACAGCTGA	42
AATATCGTTAAGAGAGCAAAGCGGATTGTGAAAAATCAGGTCTTT	45
AATACCCCAACATTCATCAAAAATAATTCGCGTCT	35
AGGACAGATGAACGGTGTAACATAAGGGAACCGAAGAAT	39
ACGTAAGAATTCGTTCTTAGAAGAACTCAAACTATCGGATAA	42
GCGAAACAAAGTGTAAAACACATGGCCTCGATTGAACCA	39

ATTGCGTTGCTGTTATCCGCTCACAATTCCAAACTCACTTGCGTA	45
CAAGCCGCCCAATAGCAAGTAAACAGCCATATTATTTTGCCATAAC	46
GCCCGAGTACGAGCCGGAAGC	21
AAAGATTACAGAACGGGAGAAGGAAACGTCACCAATGAAACCA	43
TAAAACCGTTAAAGAGTCTGTCCATCCAGAAACCACACAATC	42
CAAAGCACTAGATAGCTCCATTCAGGCTGCGCAACTGTCTTG	42
AAGGCCTGTTTAGTATCATGTTAGCTACCTC	31
TATTGAAAGGAATTGAGGTAG	21
TTTAGATTCACCAGTCACACGACCGGCGCGTGCTTTCCCAGA	42
TAACATCCAATAAATGCAAAGGTGGCATCAACATTATGAAAG	42
TTAACTCGGAATTAGAGTAAATCAATATATGTGAGTGATTCT	42
TTTTCCAGCATCAGCGGGGCTAAAGAACCTCGTAGCACGCCA	42
CCGTAATCAGTAGCGACAGAATCTAATTATTCATTAAAAAGG	42
CTGTATGGGATTACCGTTAGTATCA	25
ACTAATGCCACTACGAATAAA	21
TTTTTGCGGATGCTCCTAAAATGTTTAGATGAATTTTGCAAAAGAAGTT	49
AGTACCGCATTCCACAACATGTTCAGCCTTAAGGTAAAGTAATTC	45
CTTACGGAACAGTCAGGACGTTGGGAAGAAA	31
ACGCGAGAGAAGGCCATGTAATTTAGGCCAGGCTTAATTGAGAATCGC	48
AAGGCTCCAAAAGGAGCCTTTATATTTTTTCACGTGCTACAGTCACCCT	49
CCCCGCTAGGGCAACAGCTGGCGAAAGGGGGATGTGCTTATT	42
CCTGCGCTGGGTGGCGAGAAAGGAAGGGAAGGAGCGGGGCCG	42
TGAGTAAAGGATAAGTTTAGCTATATCATAGACCATTAGATA	42
TGAGCAAATTTATACAGGAATAACATCACTTGCCTGAGTCTT	42
CCAATGTTTAAGTACGGTGTCCAAC	25
TGAAAATCCGGTCAATAACCTAAATTTTAGCCTTT	35
CCCAGCTACAATGACAGCATTTGAGGCAAGTTGAGAAATGAA	42
CGGAATAGAAAGGAATGCCTTGCTAAACAACTTTCAAC	38
TTATAAGGGTATGGAATAATTCATCAATATA	31
CCATAATGCCAGGCTATCAAGGCCGGAGACATCTA	35
CCGACTTGTTGCTAAAATTTATTTAGTTCGCGAGAGTCGTCTTTCCAGA	49
ACGCGGTCCGTTTTTGGGTAAGTGA	25
AGCTCTTACCGAAGCCCAATA	21
AGTTTATTGTCCATATAACAGTTGATTC	28
TTACCATTAGCAAGGCCTTGAATTAGAGCCAGCCCGACTTGAGC	44
GGCGCAGACGGTCAATCATCGAGACCTGCTCCATGTGGT	39
AAATCAGCTCATTTTTTAACCATTTTGTTAAAATTCGCATTA	42
AGGCTTGCGAGACTCCTCAAGAGAAAAGTATTCGGAAC	38
GAGAACAATATACAAAATCGCGCAGAGGCGATTCGACAAATCCTTTAAC	49
TTTAGCGATACCAACGCGTTA	21

AGGGAGCCGCCACGGGAACGGATAGGCGAAAGCATCAGCACTCTG	45
ACGAGCGGCGCGGTCAGGCAAGGCGATTAAGTTGGGTAAAAC	42
TCATACATTTAATACCGATAGCCCTAAAACATCGAACGTAAC	42
GTTAAAGGAAAGACAGCATCTGCCTATTTAAGAGGCAGGAGGTTTA	46
TAGCCTCAGAGCATACCCTGT	21
CATCGAGATAACGTCAAACATAAAAGAGCAAAAGAATT	38
GAGAAGGCATCTGCAATGGGATAGGTCAAAAC	32
TTGGTAGAACATTTAATTAAGCAAC	25
ATTTGGAAGTTTCATGCCTCAACATGTTTTA	31
AAATGACGCTAAATGGATTATTTACATTGGCGAATACCTGGA	42
TTCGGGGTTTCTGCCAGGCCTGTGACGATCC	31
AAACTCACAGGAACGGTACGCCAGTAAAGGGGGTGAGGAACC	42
GAGCATTTATCCTGAATCAAACGTGACTCCT	31
AGTAGGTATATGCGTTATACA	21
GACAATTACGCAGAGGCATTTTCGAG	26
ACTAAAGAGCAACGTGAAAATCTCCACCCACAACTAAAGGAA	42
ACATAAGTAGAAAAATCAAGAAGCAAAAGAAGATGTCAT	39
ATTTCAACCAAAAATTCTACTAATAGTTAGTTTCATTTGGGGCGCGAGC	49
TAAGTTTACACTGAGTTTCGT	21
TTTCCATGGCACCAACCTACGTCATACA	28
GTAATTAATTTAGAATCTGGGAAGGGCGATCGGTGCGGCAAA	42
ACCAGACCGGATTAATTCGAGC	22
ATAGCGAGAGGCTATCATAACCAAATCCCAAAGAAAATTTCATCCTCAT	49
AGAACTTAGCCTAATTATCCCAAGCCCCCTTATTAGCGTTTGCCA	45
GGCTAAAACTTCAGAAAAGTTTTGCGGGAGATAGAACC	38
TGACCGCGCCTTAATTTACAATATTTTTGAATGGCTATCACA	42
CATTTCGCAAATGTCATCTGCGAACGAGAGATTCACAATGCC	42
CAAGCCCAATAGGAACCACCCTCACCCGGAA	31
GGAACCATACAGGCAAGGCAAATCAAAAAGACGTAGTAGCAT	42
AACAAGAGCCTAATGCAGAACGCGC	25
CGCGCTACAGAGTAATAAAAGGGACATTCTGATAGAACTTAG	42
CGTGTCAAATCACCATCTAGGTAATAGATTT	31
ATTGTTATCTGAGAAGAAACCAGGCAAAGCGCCATTCGTAGA	42
TGGCTTTTTACCGTAGAATGGAAAGCG	27
TCGTGCCGGAGTCAATAGTGAATTTGCAGAT	31
ATCGATGCTGAGAGTCTACAAGGAGAGGGAACGCCAAAAGGA	42
ATGAAGGGTAAAGTTCACGGTGCGGCCATGCCGGTCGCCATG	42
TTAGCCCTGACGAGAAACACCAGAAATTGGGGTGAATTATTTTAA	45
CCGTGTGATAAATAACCTCCGGCTGATG	28
TATCAGCAACCGCAAGAATGCCAATGAGCCTGAGGATCTATC	42

TATTACGAATAATAAACAAATCAGATATGCGT	32
GTAAAACGACGGCCCATCACCCAAATCAGCGC	32
CATTTGAGATAACCCACGAAACAATG	26
CTAAATCGGTCAGAATTAGCAAAATTAAGCAATAAAATAATA	42
ATTTCCTGATTATCAGATGATGGCTTTAAAAAGACGCTAAAA	42
CCAGCCTCCGATCCTCATGCCGGA	24
ATCGGTCAGATGATATTCACAAACCAAAAGA	31
CGAACACCAAATAAAATAGCAGCCAAGTTTGCCTTTAGCGTCAGA	45
ACAACGCCTGTAGCATTTACCGTATAGGAAG	31
AGCTTTCAGAGGTGGCGATGGCCAGCGGGAAT	32
TTTACCAGTCCCGGCCTGCAGCCCACTACGGGCGCACCAGCT	42
GTCGCGTGCCTTCGAATTGTCAAAG	25
AAGAAAGCTTGATACCGCCACGCATACAGACCAGGCGCTGAC	42
AAGACAAATCAGCTGCTCATTCAGTCTGACCA	32
AGCAACAAAGTCAGAAATAATATCCAATAATCGGCTCAGGGA	42
ATAAAGTCTTTCCTTATCACT	21
GAAGGAGCGGAATTATCATCATATATCATTTACATAGCACAA	42
CTGAATATAGAACCAAATTATTTGCACGTAAAACAACGT	39
CGTACTATGGTAACCACTAGTCTTTAATGCGCGAACTGAATC	42
TGAGTGTTCCGAAAGCCCTTCACCGCCTAGGCGGTATTA	39
GCGAAAATCCCGTAAAAAAAGCCGTGGTGCTCATACCGGCGTCCG	45
AACAACAGGAAGCACGTCCTTGCTGGTAATATCCAGAAACGC	42
CGCGCCGCCACCAGAACAGAGCCATAAAGGTGGAA	35
TTCATCGGCATTTTCGGTCATATCAAAA	28
TGCAGCAAATCGGCCAACGCGCGGGGAGGGCCCTGAGAGAGT	42
GCCAGCAGTTGGGCGCAAATCAGGTTTCTTGCCCTGCGTGGT	42
GAGAGATAGACTTTACGGCATCAGA	25
TGCCATCCCACGCAGGCAGTTCCTCATTGCCGTTTTAAACGA	42
ACATAAAGCCCTTACACTGGTCGGGTTAAATTTGT	35
GCTGGTCTGGTCAGGAGCCGGAATCCGCCGTGAACAGTGCCA	42
TACGGCTGGAGGTGCGCACTCGTCACTGTTTGCTCCCGGCAA	42
CTTGTAGAACGTCAGCGGCTGATTGCAGAGTTTTTCGACGTT	42

Table S2. Unmodified staples from the 5’ to the 3’ end for the DNA origami nanodisc.

Sequence (5’ to 3’)	Length
TTAATGGAATACCACCGAACGAACCATAATGGACAT	36
TCCCCATTCTGCAACAAAACATGGCAACTATTACG	35

CATTAATGGGCAACCTTACCAAGCGAAC	28
CCATATCACCAAGGATTCCCTGCCGTACTGGGGAA	35
AAAAGCGCCAGGCGATCACAGTTCTTCAGCAGGATCT	37
GGAATTATTTTGCAAGTAGATATGCAAC	28
GCGAACGAAAGAAGGACTGGATAGCGTCATGCTTTTGGC	39
TTTAGCGTCAGACTCATCTTTTTACATAGGTTGAG	35
AATAGACGTTCGATCTAACCCTCATAGTACCGAGG	35
CCGTTTCACGAACTTTCACGCCTGAGGGATAAAGT	35
ACATACATTGCTGATACCG	19
TGAAGCCACCGCACACTCCAACGTCATTTTAGTTGCAGCAAG	42
GGGCAAAGAATACTTTTGTAATGTAGAGGGT	31
GGAAAAAATCGTCTCTTAGAAAAGAAAA	28
GTTAAATAGGTTGGGAAGAACTCAAATTATAAAGGGATTTTA	42
GAGCCGTCAATAGTTTACAACGAACGTTATTA	32
CCCTTCTGACCTGATAGCCCTCGAATTATACAGTA	35
GGGGATTCACTTCCAAGTTACGCCCAAT	28
AATAAGAAATTAACTAACTCACCAGCTG	28
CATGAAGTTATGTAGATGAAGGTATAGA	28
CAATAATTAAACAACGGCGAAGCAAGTG	28
CATTTCTTTGAAGTGTTTGCTTTCCACGCTGTTGA	35
TTCGCAATGCAGATAGAGGGGTGATTCCTGGAAGT	35
AGAGGGACCAGCAGAGAGGTTCGAAGTGCAAGTTAACTACAAACAGTT	48
CCTGTAATTAGCAATAGAAAGTAGTAAG	28
CGGTGAACCAAGTTTGGGAAAATCGTGAGACGAAT	35
CATCAATATATGATTATTCTAAAAATT	27
ATCACGAAGGTGTGTTTATACGGAAATAAAGGGC	34
AGCGGTTGAGCTCAGAGACCGGAACCGCCTCCCTCA	36
GAATTTTGCTCCAAGCCAGTGATGTGCT	28
TAATGTTTAGGAGCCAGACGACAACGGCTGTGAACAAGCTTG	42
TCTGGCCAACAGAAAAAATAAGTTACAATCGGGA	34
GAAATGACTGATACACGATACCAAAGACACTGGCA	35
CAATAGGCAGTACAGCCAGGATCAGAAA	28
AGCTATTTTTGAGAAATGCAATGGTTTAGCGATTT	35
TTAGATCTACAGCAAACTTCGCATCAATAGG	31
CCCCCTTATTAGGAACCAGAGCCACCCCACCACATGCTGATGTCTGA	47
GCTAAACTTGAAAATCGCATTACGCCAG	28
GATAAAAGTAGCATCTCTGATTGCTTTGAAACAGT	35
AGAATAGAACCGCCAAGTTTTGTGGCGAATATCTG	35
GTACTCAAACATCGAACATTGCAAGGAGTTTATAA	35
CTGAAAAGGTGGCACAATAAATATTTCATATT	32

CGAAATCTTGAAAGACTAGCATAAATTA	28
CCTGTCAATAAAAAAAACAAAAAGGGTAGCTGATGTC	37
GCAAAGCGACTATTCCCTCAACAATACTGAGA	32
GGCCGAGGCAATTCATCTGGCTCAAATTGGGGGAT	35
AGCACCAATATTGAAGTCTAATGAAGTCTTGCAGAC	36
AGAAGATAAAACAGAACCTCAATATCAATTGTTTG	35
AACGGGTCTAAAACTCAACATACAGGAA	28
AATAAGACGAGCGTTTCACCACTGTTTG	28
GTGCATTAATTCATAGCAGGAGAAATCCTCGCTCTGTATGTGCGA	45
TTTTAACAAACAGTGAAAGCAAGTAGGG	28
AATATTACATAACATGGATCCAAGTAAGACAATGA	35
GCACTGCACTGGTGGGATGGGGAACCTAAGACTCC	35
AGCAACAAAAACCAAGATACAGTAGCTCAACATGTATTGCTGTGAATCC	49
AATAGCAGGGAAGCCGCTCACTGCCCTTGTCTCGA	35
ATTCACCCTCATTACAGGACTTGTGAGCGAATGAA	35
ACATCATTGAAGGGATTCAACTAACAC	27
CGACACGAGGGTAGAAGCGCGTTTTAACTAAATTT	35
AGAGTGAAATCGAAGCGAAAATACATACAACCGAT	35
TAAAGTATTGCGGAAAACAGTCAGGTCT	28
ACATATTGTGAATTCATTCAATAACATCTCAATTC	35
ATCAGGTTTAGAACCAAATCAATATATGGACTACC	35
TTCATTCCCTTTTGTGCCACCAGAAGGACTTCTGAATAATAA	42
GCAGCAAATGAAAACACCGCCGAACTGAAAGCGTAATTATTTCAGC	46
CCTATATAAAAAAGACATATTCATGCAAAATATCGATA	38
GACGGAAGAACGAGGATATTGGAAAGAATTGATATGCAAGCC	42
AATCAAATTATCTCACCTGGACGTTAGTATTCGCATAACGCT	42
GTTTTATGGAAACGAACCCAC	21
CGGCCTAATGAATTGTTATAAATGTATTTTAGGTGGAACGTGCAAAATT	49
TCAGCGGGCGAATATTAACCAGGTGCGG	28
CATTTTCTATCATAGAATCAGGCCAGAA	28
CCAATCACCGCGTTTGCGTAGCGCGTTTTCATCGG	35
AAGAACCCTTGAGATGCCTGAGCGGGAG	28
TCGCATCGCCAGGAATTAGTGAGATCGTCACAACCCATGTA	41
TGTGAAACCTCAGACAGCATTGACAGGAGCAGTCTGACATCA	42
CGCTGGCAACTATCCTGAATTGATGATA	28
CTGAGGTGAGCGCCATTGATAGAA	24
ACCAGTCTATCCAGCACTTGCACGGTACAGCGGGAGGCG	39
TCAAGAGGTACTCACACCATCGAAGCGG	28
CGGCGCTAACACGAAGTGCCATCCTTGGA	29
TACTAATTAACAGTGTGGAAGGGTTAGATAACGGA	35

ACAGTACTGCACGTGCATCACATCAACAGTTG	32
ACTGGGGTGTGAGTGTTAGTTGCTATTTTACAGAG	35
CGATAGTAGGCCGCACCGCTTATAGGTC	28
CAAAATTCAATTACAATGCGCTGCAACAGTG	31
ATGCCGGGTAGGTAAGTAGTATTATACC	28
ACGACGATACTATCATAACATTAACGTTGGGAAACACACGTAACACCA	48
GCATACAGAATTATGGTTTACCAGCGCCAGAAACGTTGCCCTCACTCGC	49
AGTCAGGTTACAGGAATTAAGTTAGCTA	28
AGGGATTAAGGTTGTAACCAGGCTTCCGATAGGCAATGCCATGAA	45
CGACCGTTGTAAATATAACATAACAATA	28
TCTGAGATGAGTGACAGTAATAAAAGTTCACTATC	35
TTACCCTGGATTGCCGAGCTTCAAAGCG	28
GCTATTAGACAATACGCTCACGCTCATAATT	31
GAAACAAACCTACCAATATCAAACCCTAAGCCAGC	35
AGCCATATTAATTTGCCGGCGCCAATCGGCAAAATC	36
AGCTTGAACGCGTCATCTTAGCCAACTATTTAATTTA	37
CTGCGTGGCGTCAGGGCATTAAAGCGCTGGTTGCCCTTTGTC	42
CAGTATGTTAAGAACCGGGTACCGAGGAAGAACCC	35
ATTATGAACGCTGATAACTCATCTGGACTAAGGAT	35
ACCGTTCTGAGAAACTGACGAGAAGAAAAATC	32
CCTGGTCACTGCGTGATTGTGGTGTTGAGTATTGCTTATCAA	42
AATCAGTAGCGACAGAATCAATCACCAATCTTGTC	35
ATGAGTATGTTTCTTCAGGCCGGAAACGGTTTGCC	35
TATTTTCGACCATTAAATAGCGCGGAATCG	30
CATTTTCTAGCATTGTTGTCGCGCAACA	28
TTGTTGTTCCCGTGAAAACAGTGAGTACCAGGCGGA	36
CGTAAACAGCAAAAAAGCTGTATGCAGCCCTAGAG	35
TTCAAATATCGCGTGGATTAGGTCATTTCGGTGTCCAATTCT	42
ACTCCTGTAAACTGTAATGCCAGGATTA	28
AATCGCCAGCTCAACATGGTTGGAGTAA	28
TCTTAAAGTATTAAGCCACCCACCTTTTCATGACG	35
TCAATAGAAAAAATAAGTCGAGTACTCTGAACTCGCTAC	39
ACTCGCGACCGCAAAAGGGAAGTTGAGTTAATGCG	35
CTGTTATTCTGGCTTTTTACCGTTCCGCCGCGCCG	35
TCAATCCCATCGCGCCCCCGGTATGAGCCTATTTATCCATTGAG	44
AAATTTAAATCGCAGCAATACTGCAACA	28
TAGCAATAATCAAACCAGAACTAAAAGATCAAAGG	35
TGTTGGGAAGTTCGCCAGATATATGTAA	28
ATCGCGTTTTACGCTAAAACGATTCCTGAACGAGT	35
GAGTCTGTAGTGTCGTCTCGCCACCGCAGGTC	32

GCTAAGGGGGCCAAGCTAAAAATGCGCCGCC	31
TGTTACTAGGGAACACCCCGGATATTCA	28
TATTATCGGTTTTGCAGAGGGAAGGTAATTACCAT	35
CAGAGCAGATGAACAGCGTAAAGTAAAT	28
AGTTAATTAGAAAACTCACGCAGG	24
CCAGTCGGGAAACCCACCGCCAGCTACAGAGGTTT	35
GGCCTTGCTGGTAAACACGACATAACCTACCTTTT	35
GCCATTTGGGAATTAGAGCCATAAAGGTAATATTC	35
TTACGCACATATGAATTTCGCGTCAGATGATGACC	35
AACGGAATACCAAACCGAGGAGATGATCCGCT	32
CAGGAGTTATTTCGAGTAAGCGCTTGAAACAGCAA	35
AAATAAAATGAATATTCATTTAATTACATTAATTAAGAA	39
GCGGGGATTTTCTTCTTTCCATCTAAGA	28
TAGTAAAACGAGAAATAAGAGAGAGTACCTTTAATCGAAGAC	42
ATTTTGCCTTTGCCACAATTCGACAACTTGAGATTA	36
TGATTAACCGAACAGAGTCACTGTTTCC	28
TTTTTCCTTCATCACTTTAATCCTCATAACGCAAG	35
CTCAGGCGTTCAGGCCACAGAGGATTTT	28
GAGTTATACCCAACGGCAAAGACATGCTTTCCTTT	35
AGAACTCACAGCCAGGTGAGTATCTGTCGCTATCCAGAATTAATAAG	47
GAGCAAATCCATGGTTTTACAAATAATTTAGAGCTAATATGTAGATTTC	49
AAGGCTTATAATAGCAAGCCCGAGGGTCGAGGTGC	35
AACGCCACCAGCGAATTTGTATCATCGCGTGTACATCGATGA	42
ACGTAGTCATACATGAAACATGAAGGTGACTCAAC	35
TTACCGCACATTGGGTCGCTATTTAACA	28
AACACACAAAGTACGCTGGCTAGTCTGGAAAGGCT	35
AACGGCCACCCTTTGACACCCGCCAGGGAGCTTTT	35
TCTCCGTGGGAGCGAGACGAAGGAAC	26
CCAACCTTATATTTCAAAGAGTAACGCATAGAACG	35
TGAGGCCACCAGAGCCAGTAACAAGACCAGAGTTT	35
AGTAAATATTCCATCCTGAAATTATTCTTT	30
AACGTCAGGAAATTGCGTA	19
CACAATTTAAAGCCGAGGGTACAATCCA	28
ATTCGTAATCATGGTGCGTTGGCATTAGAAAATAG	35
AGATTAACAAAAATTCAGAAAATGTTTATTTTGCCACATAACAATA	46
TACGAGCGCAGAACTTAGAGCCGCGTAA	28
GATTATAGCGGAATCTAACAACTAATCTCATCAAT	35
TCCATACTCAATGAGTTAGAGTCTGAGCTCCGGTGTGAAACCCACCAGT	49
AAGCCTTTCATACAATTTAGGGCCAAAA	28
CGGATTTTATAAAAATGACGGGAGGCAAGAACAGATAGGACT	42

TAACAGAAGGCAAAAGAACCACGGTTCATATCACCGTC	38
AAATAATACAATAGACCCTAAGCGCTTAATGC	32
ATATTTGCTCCCCGTATGGGGTCAAATCCTCTGGCCTTGAT	41
AACATGTTCTTACCTATAACGTTTATAA	28
TTAACTCCAACAGGTCATTTAATTATCAAAA	31
TTCATGAAATACACCCTTCCTATATTTA	28
CTTGCCGGCCGGAAAATCGGTTGTACCGCCTCAGACGGAACAAC	44
AGTATTAGACATAATACTATCTTTTTGGCAACTTG	35
CAATATCTGGTCAGAGGAGCATATCATCCATTATC	35
GACATTCATAAAGGTATAGATGATTATTGAACAAA	35
ACGGTAAAACGTTATAATTCGTGTAGATGCCA	32
CAGCCTTTGCACCCTGGCCCTGAGAGGTATGCTTT	35
GAGCAGCGACGCAGTCAACATAAAAACAATAGCTA	35
GTGGCACAGTCTTTCTGAGCAAAAGAAGAAACATCTCCTT	40
GCATAAAGTGCCACACAACA	20
TACAAATCGCTTGAATTTGCTTCTATCAAAAAACTATAGTGA	42
AGACGATATTAAAGTACGGGGTGGGAAG	28
GTCAATCATATAGCCGGCACCAACAAAATACTCGG	35
GTTGTGCAGAAAAAAGATTG	20
TTGGATAGGGTTCCGAAGGGTGGTGAGGCGGTTT	34
GACAGTCCAATATGTTGATAACCCAAAATAAATGTGAAC	39
CTGCGGCGTATTACGACCGAAGCCCTTTTTAGCAA	35
GAAGCAAGAGCTTATTTAAATTTAGTTTATTT	32
ATTTCATGCAGAGGAAAACATGCGGTCAGTATTAAATCTAAAAAAACAG	49
AATTAAGCAAGTAGCCATAATGGGCTGGTGCCGCT	35
CCCGATATTAAATCGGAACAAAGAAAACCATAAATGAGGAAG	42
TAAGAACAGTTGAGGGCAAGGGCGCGAG	28
CAACAACCTGAGGCCAGGCAACGGCGGA	28
TTGGTAAGGAGGTTGAACCGCCACCCTCCATAGTTGAAGACG	42
ACGCGAGGTAGGAATTGTTCCTCACCCA	28
CTCCCGACAAGCCGGTCCACTGATGGCC	28
CCACCACGAGCACGAGTATAACTGACCT	28
CAGCAATTTATTATTCTCCAATTGATAC	28
TAGAAGAATGCGTAATAATTTACAATGA	28
TAGCGGTCTCGTTATGCGTTAGAAATAC	28
AATCAAGCCCCGATGCGCCTGCAACGCC	28
TCGTAACCGTGCATCCTC	18
AATTGTATCGTAAAAGGACAGCATTACC	28
CCGTCTAAGAAAGGCCAGACGTAATAAG	28
TAACGTCCCTGAATAGCTGATTTGCCCC	28

AGCAGGCAACAAGATTTTTATAACCAAT	28
TCCTGAGATTAGTAGCTGATGTCAATAGTGAATTTGTAAATCCAGATTC	49
ATGGTGGTTGAGTGTCATTACCCTAATT	28
CTGGCGATTCCGGCTTTTGCGAGACTTT	28
GCGCTAGGCTAAACAAAAGCCATAAGGC	28
GCAAGGCAAGATCGAGCAGCGTACAGAG	28
TGAACCAAACGACGAAGGAGCGAGGTGA	28
TTGTTAAGCCTGAGGAAACCTCCGGCTTAAGAATA	35
TTGACCGGCTTTCAGAAAGAGTGCTCCA	28
TGTGTGAAGTGAGCTGAACACTTTTGTT	28
ACGTTGGCGTCTGGTAAAACAATTGTGT	28
CCACTCATTCCCAGGTATTAAACCAAGTTTAAATC	35
GTTAAAAAAGAGAAGACCAGGTCTTGAC	28
AAACTGCCTGGAACATAGGTGCCACCCT	28
TCAGTGACGTTGTAAGACAAAAGATTAA	28
CGGTCCAAACGTGGTCATCGACTTTCCT	28
GACAGGACTGAGTAGTTATATTCATAGG	28
CGGGTTTATCAGCTGCATCGGGTATCGGCTGCCAG	35
TTTGAGGGCTCATTAACGGAATCATAATAAAGTAC	35
CACTACGGGAAAGCCATGTTCGCAGAGG	28
GCCTCTTCGGAAACTTGCAGGTCCATTA	28
AAGATCGTCTTTCCTGTATCGTCACGACTTGGGTA	35
GATTGTACATATGTCGAACTGAAAGCTGCTCATT	34

Table S3. Unmodified staples from the 5’ to the 3’ end for the DNA origami nanorectangle.

Sequence (5’ to 3’)	Length
CATGTAATAGAATATAAAGTACCAAGCCGT	30
AGCCAGCAATTGAGGAAGGTTATCATCATTTT	32
GTTTATTTTGTCACAATCTTACCGAAGCCCTTTAATATCA	40
TAAATCATATAACCTGTTTAGCTAACCTTTAA	32
GCCCTTCAGAGTCCACTATTAAAGGGTGCCGT	32
TAAATCAAAATAATTCGCGTCTCGGAAACC	30
CATAAATCTTTGAATACCAAGTGTTAGAAC	30
CGGATTGCAGAGCTTAATTGCTGAAACGAGTA	32
TTTCGGAAGTGCCGTCGAGAGGGTGAGTTTCG	32
ATTATACTAAGAAACCACCAGAAGTCAACAGT	32
AAAGTCACAAAATAAACAGCCAGCGTTTTA	30

AATAGCTATCAATAGAAAATTCAACATTCA	30
TAAATCGGGATTCCCAATTCTGCGATATAATG	32
AACGTGGCGAGAAAGGAAGGGAAACCAGTAA	31
ATTATCATTCAATATAATCCTGACAATTAC	30
GCTTTCCGATTACGCCAGCTGGCGGCTGTTTC	32
GGCCTTGAAGAGCCACCACCCTCAGAAACCAT	32
CAACTGTTGCGCCATTCGCCATTCAAACATCA	32
GCGGAACATCTGAATAATGGAAGGTACAAAAT	32
TATATTTTGTCATTGCCTGAGAGTGGAAGATTGTATAAGC	40
TGGAACAACCGCCTGGCCCTGAGGCCCGCT	30
GAAATTATTGCCTTTAGCGTCAGACCGGAACC	32
CAGAAGATTAGATAATACATTTGTCGACAA	30
CTTTTACAAAATCGTCGCTATTAGCGATAG	30
TTAATGAACTAGAGGATCCCCGGGGGGTAACG	32
ATCGCAAGTATGTAAATGCTGATGATAGGAAC	32
TCACCAGTACAAACTACAACGCCTAGTACCAG	32
GAGGGTAGGATTCAAAAGGGTGAGACATCCAA	32
AAGTAAGCAGACACCACGGAATAATATTGACG	32
GTCGACTTCGGCCAACGCGCGGGGTTTTTC	30
GAGAGATAGAGCGTCTTTCCAGAGGTTTTGAA	32
TTTTCACTCAAAGGGCGAAAAACCATCACC	30
CTTTAATGCGCGAACTGATAGCCCCACCAG	30
TTAGTATCACAATAGATAAGTCCACGAGCA	30
ACGGCTACAAAAGGAGCCTTTAATGTGAGAAT	32
TTGACAGGCCACCACCAGAGCCGCGATTTGTA	32
GCCTTAAACCAATCAATAATCGGCACGCGCCT	32
GCCCGTATCCGGAATAGGTGTATCAGCCCAAT	32
AAAGGCCGGAGACAGCTAGCTGATAAATTAATTTTTGT	38
TTCTACTACGCGAGCTGAAAAGGTTACCGCGC	32
AATACTGCCCAAAAGGAATTACGTGGCTCA	30
TTTTATTTAAGCAAATCAGATATTTTTTGT	30
ATACCCAACAGTATGTTAGCAAATTAGAGC	30
AGGCTCCAGAGGCTTTGAGGACACGGGTAA	30
GCTATCAGAAATGCAATGCCTGAATTAGCA	30
GACCTGCTCTTTGACCCCCAGCGAGGGAGTTA	32
ACCTTGCTTGGTCAGTTGGCAAAGAGCGGA	30
TTAACGTCTAACATAAAAACAGGTAACGGA	30
AACGCAAAATCGATGAACGGTACCGGTTGA	30
CGTAAAACAGAAATAAAAATCCTTTGCCCGAAAGATTAGA	40
CAAATCAAGTTTTTTGGGGTCGAAACGTGGA	31

TCATTCAGATGCGATTTTAAGAACAGGCATAG	32
AGGAACCCATGTACCGTAACACTTGATATAA	31
AGCAAGCGTAGGGTTGAGTGTTGTAGGGAGCC	32
CTGTAGCTTGACTATTATAGTCAGTTCATTGA	32
TTTATCAGGACAGCATCGGAACGACACCAACCTAAAACGA	40
ACAAACGGAAAAGCCCCAAAAACACTGGAGCA	32
GTACCGCAATTCTAAGAACGCGAGTATTATTT	32
CCTAAATCAAAATCATAGGTCTAAACAGTA	30
GCAAGGCCTCACCAGTAGCACCATGGGCTTGA	32
TCAAGTTTCATTAAAGGTGAATATAAAAGA	30
ATATTTTGGCTTTCATCAACATTATCCAGCCA	32
GAATTTATTTAATGGTTTGAAATATTCTTACC	32
TATAACTAACAAAGAACGCGAGAACGCCAA	30
CTTTAGGGCCTGCAACAGTGCCAATACGTG	30
GTTTTAACTTAGTACCGCCACCCAGAGCCA	30
CATCAAGTAAAACGAACTAACGAGTTGAGA	30
TCATCGCCAACAAAGTACAACGGACGCCAGCA	32
TCTAAAGTTTTGTCGTCTTTCCAGCCGACAA	31
CACATTAAAATTGTTATCCGCTCATGCGGGCC	32
ACCTTTTTATTTTAGTTAATTTCATAGGGCTT	32
AGTATAAAGTTCAGCTAATGCAGATGTCTTTC	32
ATACATACCGAGGAAACGCAATAAGAAGCGCATTAGACGG	40
TAGGTAAACTATTTTTGAGAGATCAAACGTTA	32
CAACCGTTTCAAATCACCATCAATTCGAGCCA	32
GCGCAGACAAGAGGCAAAAGAATCCCTCAG	30
TTTACCCCAACATGTTTTAAATTTCCATAT	30
CCAACAGGAGCGAACCAGACCGGAGCCTTTAC	32
AAACAGCTTTTTGCGGGATCGTCAACACTAAA	32
ACGCTAACACCCACAAGAATTGAAAATAGC	30
ATTTTAAAATCAAAATTATTTGCACGGATTCG	32
ATATTCGGAACCATCGCCCACGCAGAGAAGGA	32
GCGAAAAATCCCTTATAAATCAAGCCGGCG	30
AGCGCGATGATAAATTGTGTCGTGACGAGA	30
GCCCGAGAGTCCACGCTGGTTTGCAGCTAACT	32
ACACTCATCCATGTTACTTAGCCGAAAGCTGC	32
CTGAGCAAAAATTAATTACATTTTGGGTTA	30
AGAAAACAAAGAAGATGATGAAACAGGCTGCG	32
TCAAATATAACCTCCGGCTTAGGTAACAATTT	32
AAATCACCTTCCAGTAAGCGTCAGTAATAA	30
TCAATATCGAACCTCAAATATCAATTCCGAAA	32

GCGAGTAAAAATATTTAAATTGTTACAAAG	30
CCACCCTCATTTTCAGGGATAGCAACCGTACT	32
CAGCGAAACTTGCTTTCGAGGTGTTGCTAA	30
AATTGAGAATTCTGTCCAGACGACTAAACCAA	32
TTCCAGTCGTAATCATGGTCATAAAAGGGG	30
CACAACAGGTGCCTAATGAGTGCCCAGCAG	30
GCAATTCACATATTCCTGATTATCAAAGTGTA	32
TTTAGGACAAATGCTTTAAACAATCAGGTC	30
CCAATAGCTCATCGTAGGAATCATGGCATCAA	32
GACCAACTAATGCCACTACGAAGGGGGTAGCA	32
CAGGAGGTGGGGTCAGTGCCTTGAGTCTCTGAATTTACCG	40
TAAATGAATTTTCTGTATGGGATTAATTTCTT	32
AAGGAAACATAAAGGTGGCAACATTATCACCG	32
CCTGATTGCAATATATGTGAGTGATCAATAGT	32
AATAGTAAACACTATCATAACCCTCATTGTGA	32
CGATAGCATTGAGCCATTTGGGAACGTAGAAA	32
ACCCTTCTGACCTGAAAGCGTAAGACGCTGAG	32
GTATAGCAAACAGTTAATGCCCAATCCTCA	30
CTCGTATTAGAAATTGCGTAGATACAGTAC	30
TTAACACCAGCACTAACAACTAATCGTTATTA	32
TCTTCGCTGCACCGCTTCTGGTGCGGCCTTCC	32
AACAGTTTTGTACCAAAAACATTTTATTTC	30
GCGAACCTCCAAGAACGGGTATGACAATAA	30
AGGCAAAGGGAAGGGCGATCGGCAATTCCA	30
AGAAAGGAACAACTAAAGGAATTCAAAAAAA	31
GACAAAAGGTAAAGTAATCGCCATATTTAACAAAACTTTT	40
TAAGAGCAAATGTTTAGACTGGATAGGAAGCC	32
AACAAGAGGGATAAAAATTTTTAGCATAAAGC	32
TACCGAGCTCGAATTCGGGAAACCTGTCGTGCAGCTGATT	40
ACCGATTGTCGGCATTTTCGGTCATAATCA	30
AGACGACAAAGAAGTTTTGCCATAATTCGAGCTTCAA	37
GCACAGACAATATTTTTGAATGGGGTCAGTA	31
TGCATCTTTCCCAGTCACGACGGCCTGCAG	30
TTATTACGAAGAACTGGCATGATTGCGAGAGG	32
AAATTAAGTTGACCATTAGATACTTTTGCG	30
GTAATAAGTTAGGCAGAGGCATTTATGATATT	32
CATTTGAAGGCGAATTATTCATTTTTGTTTGG	32
CTACCATAGTTTGAGTAACATTTAAAATAT	30
AAAGCACTAAATCGGAACCCTAATCCAGTT	30
CGCGCAGATTACCTTTTTTAATGGGAGAGACT	32

ATCCCAATGAGAATTAACTGAACAGTTACCAG	32
CAGCAAAAGGAAACGTCACCAATGAGCCGC	30
AATACGTTTGAAAGAGGACAGACTGACCTT	30
AACACCAAATTTCAACTTTAATCGTTTACC	30
CTTATCATTCCCGACTTGCGGGAGCCTAATTT	32
GATGTGCTTCAGGAAGATCGCACAATGTGA	30
CTTAGATTTAAGGCGTTAAATAAAGCCTGT	30
AACGCAAAGATAGCCGAACAAACCCTGAAC	30
TCACCGACGCACCGTAATCAGTAGCAGAACCG	32
AAGCCTGGTACGAGCCGGAAGCATAGATGATG	32
ACAACTTTCAACAGTTTCAGCGGATGTATCGG	32
GCCATCAAGCTCATTTTTTAACCACAAATCCA	32
GATTTAGTCAATAAAGCCTCAGAGAACCCTCA	32
TTAAAGCCAGAGCCGCCACCCTCGACAGAA	30
TCCACAGACAGCCCTCATAGTTAGCGTAACGA	32
TGAAAGGAGCAAATGAAAAATCTAGAGATAGA	32
TTGCTCCTTTCAAATATCGCGTTTGAGGGGGT	32
AGAGAGAAAAAAATGAAAATAGCAAGCAAACT	32
CCCGATTTAGAGCTTGACGGGGAAAAAGAATA	32
TGACAACTCGCTGAGGCTTGCATTATACCA	30
TAAAAGGGACATTCTGGCCAACAAAGCATC	30
AATGGTCAACAGGCAAGGCAAAGAGTAATGTG	32
ACAACATGCCAACGCTCAACAGTCTTCTGA	30
GCCGTCAAAAAACAGAGGTGAGGCCTATTAGT	32
AAGGCCGCTGATACCGATAGTTGCGACGTTAG	32
TTAGGATTGGCTGAGACTCCTCAATAACCGAT	32
CCAGGGTTGCCAGTTTGAGGGGACCCGTGGGA	32
GATGGTTTGAACGAGTAGTAAATTTACCATTA	32
GCGGATAACCTATTATTCTGAAACAGACGATT	32
GATGGCTTATCAAAAAGATTAAGAGCGTCC	30
TGTAGAAATCAAGATTAGTTGCTCTTACCA	30
ATGCAGATACATAACGGGAATCGTCATAAATAAAGCAAAG	40
TATTAAGAAGCGGGGTTTTGCTCGTAGCAT	30
CTTTTGCAGATAAAAACCAAAATAAAGACTCC	32
CACCAGAAAGGTTGAGGCAGGTCATGAAAG	30
TAATCAGCGGATTGACCGTAATCGTAACCG	30
GCCTCCCTCAGAATGGAAAGCGCAGTAACAGT	32
CCACCCTCTATTCACAAACAAATACCTGCCTA	32
ATCCCCCTATACCACATTCAACTAGAAAAATC	32
ATTACCTTTGAATAAGGCTTGCCCAAATCCGC	32

TACGTTAAAGTAATCTTGACAAGAACCGAACT	32
GCCAGTTAGAGGGTAATTGAGCGCTTTAAGAA	32
CTCCAACGCAGTGAGACGGGCAACCAGCTGCA	32
CTGTGTGATTGCGTTGCGCTCACTAGAGTTGC	32
TGTAGCCATTAAAATTCGCATTAAATGCCGGA	32
TTATACCACCAAATCAACGTAACGAACGAG	30
GTTTATCAATATGCGTTATACAAACCGACCGTGTGATAAA	40
TCGGCAAATCCTGTTTGATGGTGGACCCTCAA	32

Table S4. Unmodified staples from the 5' to the 3' end for the DNA origami nanopillar with extensions for pyrene-modified staples binding.

ATATTTCCTCTACCACCTACATCACTAATTAGCGGGGTTTTGCTCAGTACCAGGCTGACAACAAGCTG	68
ATATTTCCTCTACCACCTACATCACTAAGAAAACGAGAATGACCATAAATCTACGCCCCTCAAATGCTTTA	71
ATATTTCCTCTACCACCTACATCACTAATAACTATATGTAAATGCTTAGGATATAAT	57
ATATTTCCTCTACCACCTACATCACTAGCATGTAGAAACCAATCCATCCTAGTCCTG	57
ATATTTCCTCTACCACCTACATCACTATGCCCGTATAAACAGTGTGCCTTCTGGTAA	57
ATATTTCCTCTACCACCTACATCACTAAGGAATCATTACCGCGTTTTTATAAGTACC	57
ATATTTCCTCTACCACCTACATCACTAGATTAGAGAGTACCTTAACTCCAACAGG	54
ATATTTCCTCTACCACCTACATCACTACCTTAAATCAAGATTAGCGGGAGGCTCAAC	57

Table S5. Unmodified staples from the 5' to the 3' end for the DNA origami nanodisc with extensions for pyrene-modified staples binding.

ATATTTCCTCTACCACCTACATCACTAAGAATATTACTAGAAGGAGGCCGATTCAGGCGAAAGGAGCGG	69
ATATTTCCTCTACCACCTACATCACTAGCTTTGATTGACCCTCAAAAAATATTTT	55
ATATTTCCTCTACCACCTACATCACTAATTTCTTCACCCTCCACTCCAGGGCGCATCGTAACCGTGCATCCTC	72
ATATTTCCTCTACCACCTACATCACTATATCATTATTCTGTAAGGGAAGAAAGACGGAAGGGCGAAAAA	69

ATATTTCCTCTACCACCTACATCACTAAAGAATTAAAGTCATGGGGTGCCAACGC	55
ATATTTCCTCTACCACCTACATCACTAGACGCTGATTTTCCGAAATGGAGAATAC	55
ATATTTCCTCTACCACCTACATCACTAGCGGGGTGCCCGGATGCTGGAATTAACT	55
ATATTTCCTCTACCACCTACATCACTACAAATCACAGAACGAAGATTCTTATGAC	55

Table S6. Unmodified staples from the 5' to the 3' end for the DNA origami nanorectangle with extensions for pyrene-modified staples binding.

ATATTTCCTCTACCACCTACATCACTATAGAGAGTTATTTTCATTTGGGGATAGTAGTAGCATTA	65
ATATTTCCTCTACCACCTACATCACTAGAAACGATAGAAGGCTTATCCGGTCTCATCGAGAACAAGC	67
ATATTTCCTCTACCACCTACATCACTACGGATTCTGACGACAGTATCGGCCGCAAGGCGATTAAGTT	67
ATATTTCCTCTACCACCTACATCACTAAGCCACCACTGTAGCGCGTTTTCAAGGGAGGGAAGGTAAA	67
ATATTTCCTCTACCACCTACATCACTAGAGAAGAGATAACCTTGCTTCTGTTCGGGAGAAACAATAA	67
ATATTTCCTCTACCACCTACATCACTAATAAGGGAACCGGATATTCATTACGTCAGGACGTTGGGAA	67

Table S7. Pyrene-modified staple from the 5' to the 3' end for surface immobilization of DNA origami structures.

GTGATGTAGGTGGTAGAGGAAATAT-**pyrene**	25

Table S8. Atto542-modified staples from the 5' to the 3'.

ATTO542-CGAAAGACTTTGATAAGAGGTCATATTTCGCA (NR)	32
ATTO542-ACGCCAGGACGACAAAAAAGGTAAAGTACCAAGAA (ND)	35
AGACAGCAGAAACGAAAGAGGAAATAAATCGAGGTGACAGTTAAAT-**ATTO542** (NP1)	46
AATATGCAACTACCATCATAGACCGGAACCGC-**ATTO542** (NP2)	32
AAGGGATATTCATTACCGTAATCTATAGGCT-**ATTO542** (NP3)	31
ACGGGCCGATAATCCTGAGAAGTGTTTTTATGGAGCTAACCG-**ATTO542** (NP4)	42

REFERENCES

(1) Puchkova, A.; Vietz, C.; Pibiri, E.; Wünsch, B.; Sanz Paz, M.; Acuna, G. P.; Tinnefeld, P. *Nano Lett.* **2015**, *15* (12), 8354–8359.

(2) Vietz, C.; Lalkens, B.; Acuna, G. P.; Tinnefeld, P. *New J. Phys.* **2016**, *18*, 45012.

8.5. Publication II

Graphene-on-Glass Preparation and Cleaning Methods Characterized by Single-Molecule DNA Origami Fluorescent Probes and Raman Spectroscopy

by

S. Krause, E. Ploetz, **J. Bohlen**, P. Schüler, R. Yaadav, F. Selbach, F. Steiner, I. Kaminska, P. Tinnefeld

published in

ACS nano **2021**, *15* (4), 6430–6438

Author contribution:

J. B. prepared parts of DNA origami structures as well as graphene samples, executed FLIM experiments with P. S., analyzed graphene surfaces with AFM and helped writing the manuscript.

ACSNANO

www.acsnano.org

ARTICLE

Graphene-on-Glass Preparation and Cleaning Methods Characterized by Single-Molecule DNA Origami Fluorescent Probes and Raman Spectroscopy

Stefan Krause,* Evelyn Ploetz, Johann Bohlen, Patrick Schüler, Renukka Yaadav, Florian Selbach, Florian Steiner, Izabela Kamińska, and Philip Tinnefeld*

Cite This: *ACS Nano* 2021, 15, 6430−6438

Read Online

ABSTRACT: Graphene exhibits outstanding fluorescence quenching properties that can become useful for biophysics and biosensing applications, but it remains challenging to harness these advantages due to the complex transfer procedure of chemical vapor deposition-grown graphene to glass coverslips and the low yield of usable samples. Here, we screen 10 graphene-on-glass preparation methods and present an optimized protocol. To obtain the required quality for single-molecule and super-resolution imaging on graphene, we introduce a graphene screening method that avoids consuming the investigated sample. We apply DNA origami nanostructures to place fluorescent probes at a defined distance on top of graphene-on-glass coverslips. Subsequent fluorescence lifetime imaging directly reports on the graphene quality, as deviations from the expected fluorescence lifetime indicate imperfections. We compare the DNA origami probes with conventional techniques for graphene characterization, including light microscopy, atomic force microscopy, and Raman spectroscopy. For the latter, we observe a discrepancy between the graphene quality implied by Raman spectra in comparison to the quality probed by fluorescence lifetime quenching measured at the same position. We attribute this discrepancy to the difference in the effective area that is probed by Raman spectroscopy and fluorescence quenching. Moreover, we demonstrate the applicability of already screened and positively evaluated graphene for studying single-molecule conformational dynamics on a second DNA origami structure. Our results constitute the basis for graphene-based biophysics and super-resolution microscopy.

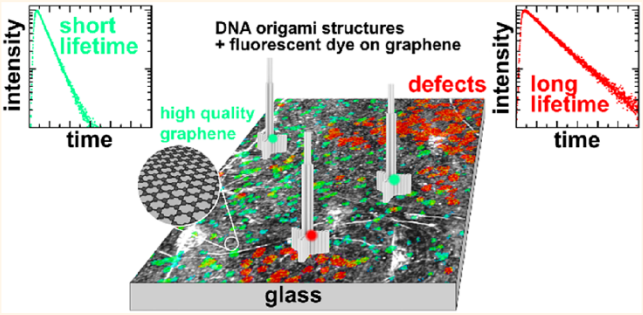

KEYWORDS: *graphene, DNA origami, Raman spectroscopy, fluorescence quenching, single-molecule spectroscopy, fluorescence lifetime imaging microscopy*

Two-dimensional materials, in particular, graphene, have gained enormous attention due to their unusual electronic properties.[1] Graphene is usually investigated with respect to its electronic properties as well as its subsequent utilization. However, in the past decade, the astonishing fluorescence quenching properties, resulting from energy transfer from a fluorophore to graphene (or graphene oxide) have stimulated several studies,[2−5] which turned this fascinating material into a frequently employed quencher for fluorescence-based biosensing, electroporation of cells, and high-resolution methods.[6−9] Only recently, graphene-on-coverslips has been combined with single-molecule biophysics and super-resolution microscopy enabling a myriad of applications if such coverslips are easily available.[7,8,10] Thereby, the advantage of graphene over hitherto utilized quenching materials, for example, metal surfaces or molecular quenchers, is manifold. While metal surfaces quench fluorescence over distances up to 200 nm, graphene shows a steeper, short-range quenching behavior below 50 nm that scales with the inverse

Received: October 6, 2020
Accepted: April 2, 2021
Published: April 9, 2021

https://doi.org/10.1021/acsnano.0c08383
ACS Nano 2021, 15, 6430−6438

distance to the power of four ($\sim 1/d^4$).[7,8,11,12] This steep quenching dependence is the property responsible for resolving subnanometer differences in dye-to-graphene distances.[7,8] One of the main advantages of graphene is the better optical transparency in the far-field and less background fluorescence. Moreover, preparation of thin (up to several nanometers thick) metal surfaces is challenging, and they tend to degrade in a relatively short time, transforming into metal islands, additionally covered with a metal oxide layer. On the other hand, and in contrast to individual commercially available molecular quenchers, graphene quenching can be observed over the entire visible wavelength range.[8] Since graphene is transparent in the UV−vis spectral range (only 2.3% absorption), it can be easily applied as a two-dimensional and atomically flat quencher in fluorescence microscopy which usually employs oil immersion lenses. Furthermore, graphene is, nowadays, cheaply available as it can be produced on large scales with high quality by chemical vapor deposition (CVD).[13,14]

One major hurdle in spreading the application and implementing graphene as a two-dimensional quenching material for single-molecule imaging is the challenging procedure for transferring and cleaning graphene, for example, on a glass substrate. Consequently, an increasing number of studies report on varying techniques to solve this issue.[15−17] In our hands, only a fraction of commercially available graphene-on-glass samples had the required quality for optical single-molecule experiments.[8] Using existing protocols, homogeneity and reproducibility issues as well as batch dependence were frequent causes of frustration, so we decided to revisit and optimize graphene-transfer methods for graphene-on-glass coverslips suitable as robust and routine substrates for optical microscopy with advanced features.

In this article, we screen 10 preparation methods and present an optimized protocol to obtain graphene-on-glass coverslips for single-molecule applications. For improved screening, we apply a fluorescence lifetime imaging microscopy (FLIM) method using DNA origami nanopositioners as probes.[18−22] The DNA origami nanopositioner purpose is two-fold: (i) It specifically binds to graphene *via* pyrene feet in the desired orientation; and (ii) it places a fluorescent dye at a defined distance above graphene, for which a well-defined fluorescence lifetime is expected. The height of the dye, which can be adjusted by the design of the DNA origami structure, is chosen to be close to the height of 50% quenching. This makes it most sensitive to small changes in the energy transfer that could reflect different heights or imperfections of the graphene. This FLIM screening approach also accounts for the fact that the requirements for single-molecule-based applications are different from those typically known for graphene in other applications, for example, electronic devices, catalysis, or biomedical applications, where a certain degree of imperfection or small areas of high-quality graphene are tolerable.[23−26] The transferred graphene should, for example, not show any defects (holes, wrinkles) or protective layer residuals over a large range, as that would hinder single-molecule fluorescence or super-resolution microscopy measurements. A lack of graphene quality typically arises from the transfer process of graphene to a glass substrate and the subsequent removal of the protective layer, for example, poly(methyl-methacrylate) (PMMA). Residuals of the protective layer or disruption of the graphene can cause insufficient quenching or unspecific binding of, for example, pyrene-functionalized DNA origami structures.

To evaluate their potential, we compare the DNA origami probes for graphene characterization with established techniques, including light microscopy, atomic force microscopy (AFM), and Raman spectroscopy. Using correlative imaging, we investigate the very same area of the sample with all four techniques and pinpoint not only how defects are revealed by the different techniques but also how complementary the gained information is, for example, due to the fact that a different area contributes to the observed signals. Moreover, we demonstrate that the dynamics of a single-molecule transitioning between two distinct states on a DNA origami structure can be visualized by fluorescence intensity fluctuations caused by graphene quenching. In contrast to other fluorescence characterization methods,[2,27,28] this is possible on surfaces that were previously evaluated by our approach, as the DNA origami probes do not consume the graphene-on-glass coverslips. Our results constitute the foundation so that graphene-based biophysics and super-resolution microscopy can unlock its full potential.

RESULTS AND DISCUSSION

We investigate 10 different graphene-transfer and cleaning protocols. All of them involve etching of the copper foil, which serves as a substrate for the graphene/PMMA layer, with ammonium persulfate, which is a standard etchant for copper.[29] In comparison, etching with iron(III)chloride delivers worse sample quality (data not shown). The detailed steps for each protocol are described in the Supporting Information. Common to almost all preparations, samples are cured with a chlorobenzene solution of PMMA after transfer to glass following studies from Li *et al.*[17] The techniques differ mainly in how the protective polymer layer, here PMMA, is removed. This last step is crucial for the resulting graphene quality, and very different results are obtained (*vide infra*). In literature, washing with different solvents, including acetone[17] and toluene,[30] as well as solvent vapor cleaning,[16] heating,[31] and active absorber treatment[32] have been proposed, among others, to obtain clean and intact single-layer graphene surfaces.

Figure 1 illustrates the transfer and cleaning procedure, which leads to the best graphene sample quality and reproducibility out of 10 different approaches (described in detail in the Supporting Information sections 2−4 and Figures S3 − S17). After cutting a piece of the desired size from the back etched copper/graphene/PMMA foil, it is placed on the surface of a 0.2 M aqueous solution of ammonium persulfate to dissolve the copper.[29] Afterward, the graphene/PMMA sheet is scooped with a clean microscopy coverslip and washed twice in ultrapure water by repetitive releasing and scooping. After the third scooping step, residual water on the graphene-coated glass slide is removed with a clean nitrogen stream. A drop of PMMA in chlorobenzene (50 mg/mL) is deposited on the sheet to dissolve the initial PMMA and cure the graphene below.[17] The graphene is protected by the PMMA, which should be removed within a couple of days. According to our observations, longer-remaining PMMA coverage (several weeks) can lead to graphene disruption probably due to polymer-aging and reorganization. To remove PMMA, the sample was placed in a bath of clean acetone two times for 5 min each. PMMA residuals are removed by further treatment with clean toluene for about 10 min. The remaining toluene can be removed with a gentle, clean nitrogen flow. In the final step, the sample is placed upside down on active coal and

https://doi.org/10.1021/acsnano.0c08383
ACS Nano 2021, 15, 6430−6438

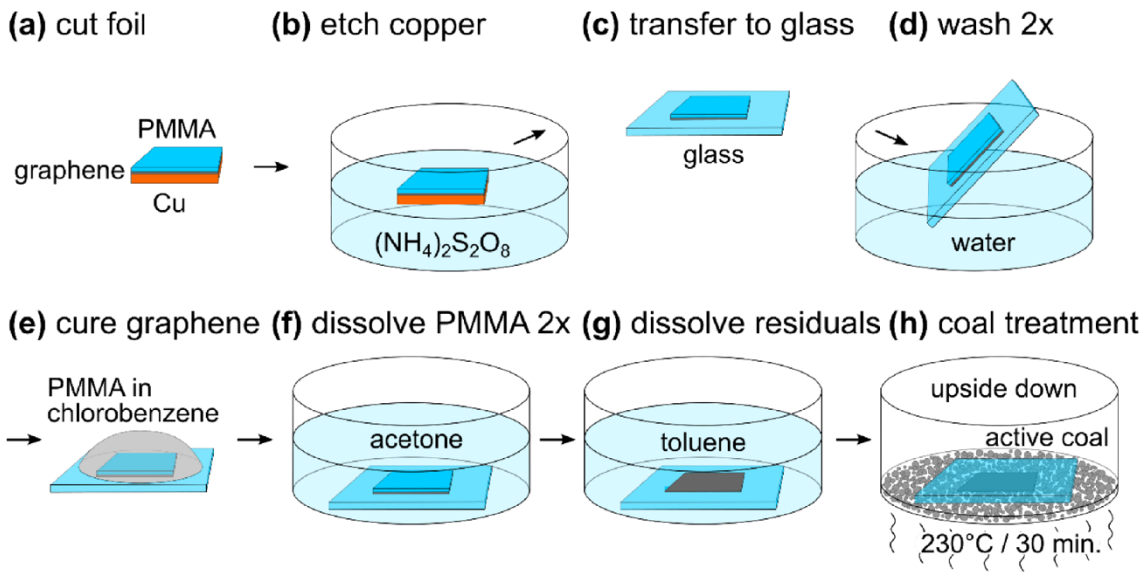

Figure 1. Scheme of the most successful graphene preparation method (ATC, strategy no. 1 see Supporting Information). (a) Cutting off a small rectangle from the PMMA-graphene-copper foil. (b) Copper etching for 4 h in a 0.2 M aqueous solution of ammonium persulfate. (c and d) Transferring to glass and releasing in water for washing two times. (e) Curing of graphene by temporarily dissolving PMMA with a PMMA-chlorobenzene solution (50 mg/mL) and slow evaporation of the solvent. (f) Dissolving PMMA in two consecutive baths of acetone for 5 min each. (g) Dissolving residual polymer through a 10 min toluene treatment. (h) Upside-down dry-cleaning step with heated (230 °C) active coal for about 30 min.

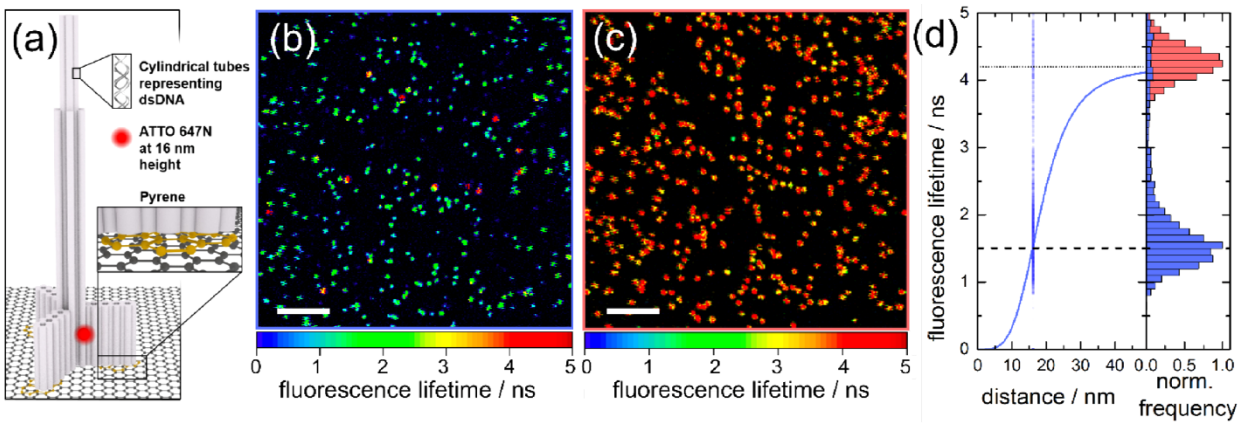

Figure 2. (a) Scheme of a pillar-shaped DNA origami structure (gray rods represent dsDNA) bound to graphene *via* pyrene units (orange). The DNA origami structure ensures a well-defined dye-to-graphene distance of 16 nm. The inset shows pyrene-modified DNA strands protruding from the structure interacting with graphene *via* $\pi-\pi$ stacking. (b, c) Exemplary FLIM images (30 × 30 μm^2) of ATTO647N functionalized DNA origami structures on a (b) successfully and (c) unsuccessfully prepared graphene-coated coverslip. Scale bar 5 μm. (d) Calculated fluorescence lifetime as a function of the distance of ATTO647N from the graphene surface (blue curve) and determined fluorescence lifetime histograms as for both data sets shown in (b and c). The blue scatter plot at a distance of 16 nm represents the fluorescence lifetime histogram for FLIM images taken from the successfully prepared graphene-coated coverslip. The black dashed line marks the theoretically expected fluorescence lifetime for a distance of 16 nm, while the black dotted line marks the initial fluorescence lifetime of ATTO647N.

heated to about 230 °C for 30 min. In case the coal has taken up water over time, preheating of the active coal is necessary to avoid water condensation on graphene. In this last step, molecular contaminants are removed from the graphene surface.[32] Afterward, the graphene samples can be combined with a flow chamber for incubation purposes. We note that, although we observe for the above-described transfer and cleaning procedure a higher quality of graphene on glass in comparison to other methods, defects and polymer residuals still occur. Here, we investigated these imperfections by means of FLIM, Raman spectroscopy, light microscopy, and AFM.

In the following, we describe the applied screening method, which enables a fast survey of the graphene quality. As AFM and Raman measurements are time-consuming, we decide to perform a fast screening of the differently prepared graphene samples using FLIM. Thereby, we apply a fluorescent dye (ATTO647N) implemented into a pillar-shaped DNA origami structure at a fixed height of 16 nm from the bottom, as depicted in Figure 2a.[8] The DNA origami structure itself is attached to the graphene surface *via* $\pi-\pi$ interactions between pyrene-modified staple strands at the bottom (see external labeling process in the Supporting Information) and the graphene sheet. As we could recently show, graphene features a

https://doi.org/10.1021/acsnano.0c08383
ACS Nano 2021, 15, 6430−6438

strong, distance-dependent quenching behavior on a short range that can be described by a $1/d^4$ function.[8] Accordingly, ATTO647N attached to the pillar-shaped DNA origami structure with its pyrene anchors at the bottom serves as a calibration ruler, with a fluorescence lifetime of 1.5 ns for its designed distance of 16 nm above the graphene surface.[8] For a given graphene-transfer method, summarized in detail in the Supporting Information, three individual graphene samples are prepared. The DNA origami structure is incubated on each graphene sample at a concentration of 25 pM in 1× TAE buffer with 12.5 mM $MgCl_2$. The surface density of the DNA origami structures is then checked, and, in case of distinguishable individual fluorescent spots, the sample is washed again three times with the same buffer. Afterward, at least three FLIM images ($30 \times 30\ \mu m^2$) are acquired at three different sample areas. Thus, the fluorescence lifetime for individual ATTO647N molecules attached to a pillar-shaped DNA origami structure can be extracted solely from an image scan *via* pulsed excitation and subsequent time-correlated single-photon counting at each pixel of the image.

To illustrate the utility of this FLIM screening approach without confusing the reader with too many different transfer methods, we limit the discussion to a comparison of the most successful (intact and properly quenching graphene) and an unsuccessful (disrupted and detached graphene) method. An exemplary FLIM image, taken from a properly quenching graphene surface, is given in Figure 2b. The fluorescence lifetime distribution for this transfer method is shown in Figure 2d. The extracted fluorescence lifetimes are in line with theoretical expectations (blue curve) for a dye-to-graphene distance of 16 nm. Furthermore, for this method, all examined sample areas are usable (see Figure S3 in the Supporting Information). In addition, and in agreement with the FLIM image in Figure 2b, a few spots remain unquenched and show fluorescence lifetime values around 4.2 ns. This indicates that either the graphene shows local defects or there are residuals of the protective layer remaining on graphene. Occasionally, small DNA origami aggregates might also be present that prevent fluorescence quenching due to altered dye-to-graphene distances.[8] Nonetheless, about 90% of the found fluorescent spots show fluorescent lifetimes in the expected range.

For comparison, Figure 2c shows an example of a "bad" graphene sample treated with hot acetone and acetone vapor (see details for cleaning procedure A'1*, strategy no. 8 in the Supporting Information). This transfer and cleaning method, highlighted in red, results in an average fluorescence lifetime around the unquenched value of 4.2 ns (see Figure 2d), which can be explained with the removal of the graphene layer, which is probably due to harsh treatment with a hot solvent. Besides, all examined areas show primarily unquenched spots and can therefore not be considered to be good sample areas. As found by Raman spectroscopy and light microscopy (see Supporting Information), the graphene sheets are detached from the substrate for this procedure.

With a reproducible graphene-transfer/cleaning procedure established, we elucidate how our above-described FLIM-based screening approach compares to standard methods, for example, light microscopy, AFM, and Raman spectroscopy, in particular. Thereby, light microscopy and AFM allow for detailed monitoring of the surface topography. They are complementary to the defect-sensitive Raman spectroscopy. The main feature of graphene in a Raman spectrum is the G band near 1580 cm^{-1}, which results from the stretching motion of sp^2 pairs. The position and intensity of this Raman resonance are indicators of the number of transferred graphene layers.[33] The quality of single-layer graphene is reflected by the number of defects, which can be monitored by the appearance of the disorder-induced D band around 1340 cm^{-1}. It is the result of lattice motions and shows an excitation energy dispersion.[34] Defects can be quantified *via* two strategies: an absent or negligible D band ($I_D/I_G \rightarrow 0$) or a large ratio of the peak intensities of the 2D to G band ($I_{2D}/I_G > 2-3$).[35,36] For a better understanding, an example Raman spectrum acquired from high-quality graphene is given in Figure S4. Ideally, fast screening with a light microscope or acquisition of a few representative Raman spectra would be sufficient to tell whether the underlying graphene sample is suitable or not. However, this approach still requires understanding the connection between Raman-detected graphene defects and fluorescence quenching efficiency. Hence, we perform FLIM and single-molecule fluorescence lifetime measurements in combination with subsequent Raman measurements at the very same positions. The overlap of the pulsed laser for time-correlated single-photon counting (TCSPC) and a helium−neon laser for Raman spectroscopy is validated by consecutive sample scans with one or the other excitation light source (see Supporting Information section 1, Figure S1).

Figure 3 shows combined FLIM, AFM, and Raman data from a graphene sample prepared according to the procedure depicted in Figure 1. For this sample area, the light microscopy image (Figure S18a) is not sensitive enough to reveal any defects (Figure S18e gives an example for large defects visible *via* light microscopy). In contrast, the FLIM (Figure 3a and Figure S18b) and AFM (Figure 3d and Figure S18c) images show unquenched spots or wrinkles and impurities, respectively. From the FLIM image, we can extract the fraction of quenched spots to 92.5%, which is in good agreement with the data shown in Figure 2b,d. About 60% of unquenched spots can be related to impurities measured by AFM (see Figure S18c for the full FLIM and AFM data set). In general, the AFM image shows a smooth sample surface with minor height variations stemming from wrinkles and probably a few polymer residuals. To compare fluorescence lifetime data with Raman spectra, we measure time-correlated single-photon statistics of a single-molecule first and change the excitation and detection path for acquiring Raman spectra directly afterward. For the cyan, blue, orange, and red spots marked in Figure 3a, fluorescence decays and Raman spectra are depicted in Figure 3b,c, respectively. The Raman spectra deviate strongly from each other. While the spectrum, taken at the position of the cyan marked spot, shows a minor D peak and a high 2D/G ratio, the spectrum depicted in blue is dominated by the D peak. For the latter spectrum, the G peak shows a sideband at about 1615 cm^{-1}, which we assign to the energy-dependent and defect-related D′ or G_S peak.[34,36,37] From the Raman spectrum plotted in blue, one would expect low-quality graphene and consecutively a reduced quenching efficiency. Surprisingly, the corresponding decay curve with a fluorescence lifetime of 1.8 ns shown in Figure 3b is similar to the decay curve acquired at the cyan-marked spot with a fluorescence lifetime of 1.4 ns. This indicates a small, or even negligible, correlation between the Raman signature and the quenching behavior of a fluorescent emitter at the same sample position. Figure 3e shows the correlation between the peak intensity ratio I_{2D}/I_G, serving as an indicator for graphene quality and the fluorescence lifetime of 235 fluorophores

https://doi.org/10.1021/acsnano.0c08383
ACS Nano 2021, 15, 6430−6438

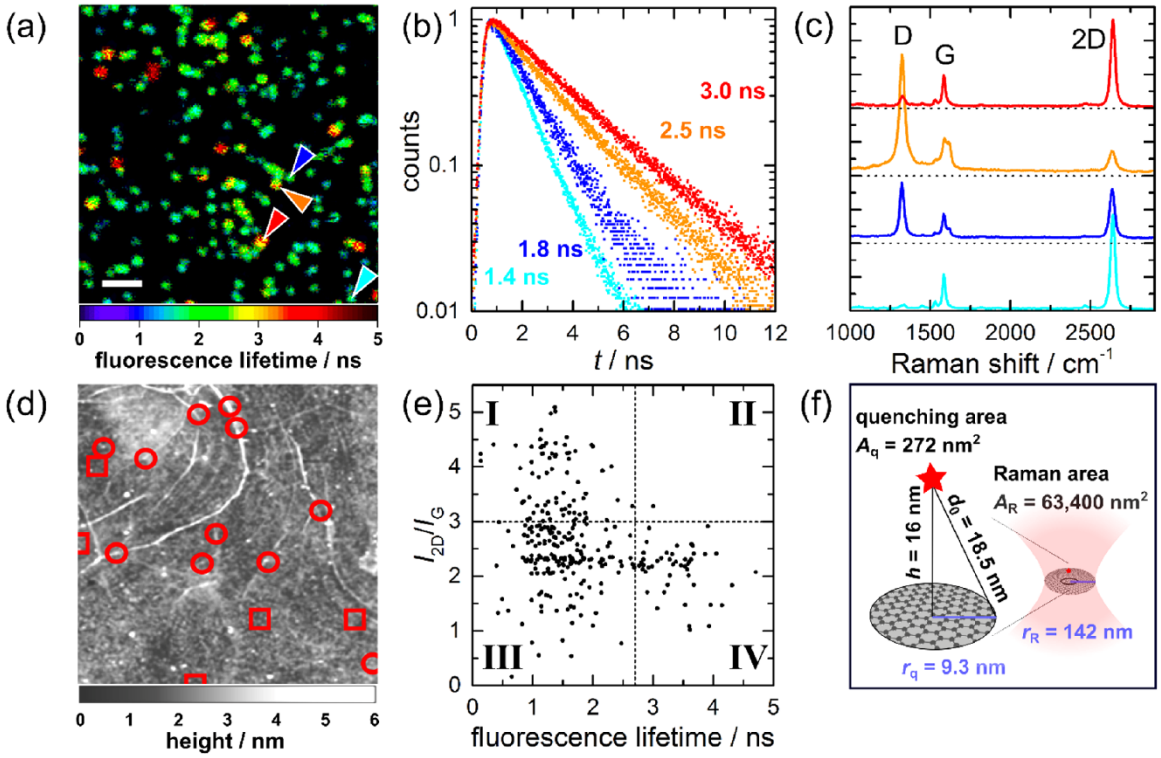

Figure 3. (a) 15 × 15 μm^2 FLIM image of the pillar-shaped DNA origami structure on graphene. Scale bar 2 μm. The cyan, blue, orange, and red triangles mark individual positions, which correspond to the data sets in (b) and (c). (b) Photon histogram of the four fluorescent molecules marked in (a). (c) Raman spectra, taken at the four spots as indicated in the FLIM image in (a). Spectra are shifted vertically for better visibility. Hence, horizontal black dotted lines indicate zero intensity for the respective spectrum above. (d) AFM image of the same area as in a). Red circles indicate defects, which can be associated with unquenched fluorescent molecules in (a). Red squares mark positions of unquenched fluorescence molecules from (a) which cannot be associated with any defects in the AFM image. (e) Ratio of the peak intensities of 2D and G peak within single Raman spectra over fluorescence lifetime measured at the same position. The vertical dashed line at 2.7 ns separates quenched from unquenched fluorescent molecules. The horizontal dashed line can be used as an indicator for high-quality graphene with $I_{2D}/I_G > 3$. (f) Scheme of the effective quenching area and Raman area. While the quenching area of a dye with a height h above graphene is essentially determined by the distance of 50% quenching efficiency, the area, in which the Raman scattering signal is generated and detected, is defined by the diffraction limit of the excitation beam.

measured at the same sample position on graphene.[36] The scatter plot is divided into four sections, which can be attributed to the following cases: (I) quenched fluorescence and high I_{2D}/I_G ratio, both indicating high-quality graphene; (II) unquenched fluorescence indicating low-quality graphene and high I_{2D}/I_G ratio indicating high-quality graphene; (III) quenched fluorescence indicating high-quality graphene and low I_{2D}/I_G ratio indicating low-quality graphene; and (IV) unquenched fluorescence and low I_{2D}/I_G ratio, both indicating low-quality graphene. The broad scatter of data points supports our previous observation that little correlation is observed between Raman spectra and fluorescence lifetime. This is surprising because defects in graphene are well-known to influence the quenching efficiency of the material.[38] The data allow concluding only one explicit correlation: We can assume proper quenching of a fluorophore for $I_{2D}/I_G > 3$ (section I). The counter-conclusion of insufficient quenching upon $I_{2D}/I_G < 3$ (section IV), however, is not justifiable (significant population in section III). The criterion of $I_{2D}/I_G > 3$ for high-quality graphene is in good agreement with previous studies.[35] Nonetheless, we imagine different scenarios where Raman spectra and fluorescence lifetime of a dye molecule might sense different environments despite being acquired at the same diffraction-limited spot. A thin residual layer of the protective polymer, which does not need to cover a large area of graphene, can, for example, give a constant offset to the fluorescence lifetime. As a polymer, such as PMMA, shows only minor, nonresonant Raman scattering compared to graphene, its Raman bands would not be visible, but the quenching efficiency would be reduced following the previously described distance dependence. This case would explain reduced quenching of the dye despite a Raman signal indicating high-quality graphene, which we do not observe for I_{2D}/I_G (but for I_D/I_G and the red section in the Figure S19). We can also imagine an opposite scenario, where a Raman signal indicating low graphene quality is acquired, but the graphene area gives sufficient quenching (blue spot in Figure 3a and section III in Figure 3e). To explain such a behavior, we estimate the area that is probed by the two methods. As illustrated in Figure 3f, Raman spectroscopy carried out on a confocal microscope measures the signal from a diffraction-limited area with a radius of about 142 nm (λ = 632.8 nm and NA = 1.4) corresponding to the area of about 6.3 × 10^4 nm^2. In contrast, if we consider 50% quenching (d_0 = 18.5 nm) to be the threshold for still considering a molecule as sufficiently quenched, the probed area of the dye molecule that is placed at 16 nm height above the graphene layer and attached to the DNA origami structure is only 2.7 × 10^2 nm^2. This enormous discrepancy of more than 2 orders of magnitude in the area probed by the two methods might explain the observed

https://doi.org/10.1021/acsnano.0c08383
ACS Nano 2021, 15, 6430−6438

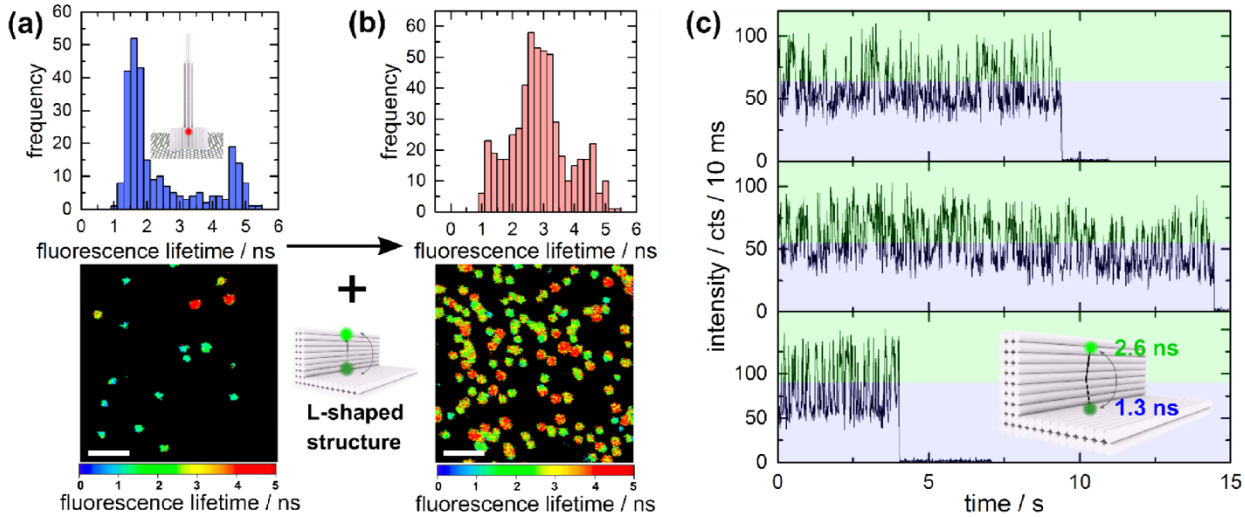

Figure 4. (a) Fluorescence lifetime histogram from three FLIM images, as shown below, of ATTO 647N on a pillar-shaped DNA origami structure (inset) on graphene. Scale bar of the FLIM image 2 μm. (b) Fluorescence lifetime histogram and FLIM image of the same sample as in (a) after incubation with an L-shaped DNA origami structure (shown in the middle) with a vertically moving pointer and ATTO542 at its end position. Scale bar of the FLIM image 2 μm. (c) Example transients of ATTO542 that interconverts between the distal and proximal position along the upright DNA origami structure side and hence between a quenched and nonquenched state as illustrated in the inset scheme.

divergence between Raman spectra and fluorescence quenching efficiency. Within an area dominated by defects visible in the Raman spectrum, sufficient quenching within the small area probed by the DNA origami structure is possible. Despite the previously shown examples, we point out that the acquired Raman spectra and fluorescence quenching efficiencies are not always uncorrelated. This is, of course, especially true for holes and areas where the graphene has been completely removed but sometimes also for defective areas. An example is given in Figure 3b,c by the orange spectrum and fluorescence lifetime curve. In this case, the amplitude of the G peak is as high as the amplitude of the 2D peak, while the disorder-induced D peak is three times higher than G and 2D, which is a clear indicator for graphene defects. The observed fluorescence lifetime of 2.5 ns confirms a reduced quenching efficiency.

In the last section, we demonstrate the power of our screening method, based on the pillar-shaped DNA origami structure shown in Figure 2a, by applying it to a general experimental situation. We choose a second DNA origami structure with a distinguishable green dye molecule (ATTO542), which serves as the object of interest. The L-shaped origami structure has a flexible pointer with an ATTO542 molecule attached to the end (see Figure 4a,b). Above and below this pointer, binding strands are integrated with a seven nucleotides long binding sequence, to which the pointer can bind. Upward binding leads to an energy-transfer efficiency of 15.7% (τ_{high} = 2.6 ns) at a height of 26.5 nm above the graphene surface. For downward binding, an increased transfer efficiency of 59.3% (τ_{low} = 1.3 ns) at a height of 16.1 nm is measured. Although the observed fluorescence intensity fluctuations themselves serve as an indicator for proper quenching by the graphene, the DNA origami structure is more vulnerable to false orientations on the graphene surface. To exclude graphene as a source for insufficient quenching, we first add a low concentration of our pillar-shaped DNA origami structure to a freshly prepared graphene sample. The sample is then confocally scanned to obtain FLIM images, as shown in Figure 4a. From these images, we can readily estimate the quality of the graphene surface. Since the FLIM image and fluorescence lifetime histogram in Figure 4a shows a good quenching-behavior of graphene, we add the L-shaped DNA origami structure afterward. The individual fluorescent spots are then measured without the risk of underlying defective graphene. From correctly oriented DNA origami structures, fluctuations between the two quenching states are observed, as expected. Figure 4c depicts the intensity fluctuations between the two discrete states (upper and lower binding sites as indicated in the inset in Figure 4c). Blinking and photodegradation are negligible for ATTO542. However, for other fluorophores, such effects may necessitate photostabilization. In this case, H_2O_2 should be avoided. We noticed that H_2O_2, as an intermediate of the oxygen-scavenging system glucose oxidase/catalase, oxidizes graphene. This alters the properties of graphene and has already been reported on graphene surfaces and carbon nanotubes.[39,40] DNA origami structures, as exemplarily demonstrated here, have great potential for biosensing applications and will be explored in the near future. Thereby, more complex DNA origami structures with an implemented reference dye, for example, a red-emitting dye beside the green fluorophore in the L-shaped origami structure, will allow evaluating proper graphene quenching. The ability to ensure the necessary graphene quality for these types of experiments will tremendously promote this innovative research field.

However, we are aware that DNA origami structures and FLIM imaging are difficult to realize for many laboratories. To give at least the opportunity for a first estimation of the quality of transferred graphene, we have summarized a step-by-step procedure based on inspection by eye and standard light microscopy (see Figure S20).

CONCLUSION

Recently, the potential of graphene-on-glass coverslips was indicated for super-resolution imaging and single-molecule biophysics and biosensing.[10] We here used DNA nanopositioners for characterizing the quality of graphene-on-glass

https://doi.org/10.1021/acsnano.0c08383
ACS Nano 2021, 15, 6430−6438

and compared the method to the state-of-the-art. The advantage of DNA origami nanopositioners is that the samples are not consumed and can be reused consecutively. In addition, graphene characterization with DNA origami nanopositioners and FLIM is the most effective way of testing the graphene for related fluorescence applications. In this context, we found discrepancies between spatially correlated Raman spectra and fluorescence decay curves, which can be explained by the different sizes of the area probed by the two techniques, while AFM measurements revealed correlations between unquenched fluorescent molecules and residuals on top of graphene. Testing many graphene preparation methods, we worked out a protocol yielding exceptionally high-quality graphene-on-glass in excellent yields for broad applications of graphene-on-glass in optical and fluorescence applications. We envision that graphene-on-glass coverslips might replace conventional coverslips for a multitude of sensing and single-molecule applications, as a FRET acceptor is provided for free and without additional labeling.

METHODS

Chemicals. All chemicals were purchased from Sigma-Aldrich, if not stated otherwise. Agarose, ammonium persulfate, "Blue Juice" gel loading buffer (ThermoFisher Scientific), ethylene-diamine-tetraacetic acid sodium salt dihydrate (EDTA-Na_2 × $2H_2O$), magnesium chloride ($MgCl_2$ × $6H_2O$), peqGREEN 20.000x DNA staining dye (peqLab; VWR), Tris base, Tris HCl, PCA, PCD, Trolox were used as purchased.

The solvents acetic acid, acetone, chlorobenzene, dimethyl sulfoxide (DMSO), ethanol (EtOH, Aldrich, absolute), and toluene were used without further purifications.

All unmodified staple strands (Tables S1−S4) and one staple strand modified with ATTO647N (Table S2) used for DNA origami folding were commercially available and purchased from Eurofins Genomics. Two modified staple strands, with ATTO542 (Table S3) and pyrene (Table S2) were purchased from Biomers.

For stabilization of ATTO542 at the L-shaped origami structure, a combination of ROXS and oxygen scavenging system is used. The first buffer contained aqueous solution of aged 6-hydroxy-2,5,7,8-tetramethylchroman-2-carboxylic acid (Trolox) with protocatechuic acid (PCA) (2 mM Trolox, 25 mM PCA, 12 mM $MgCl_2$ × $6H_2O$, 40 mM Tris base, 20 mM acetic acid, 1 mM EDTA-Na_2 × $2H_2O$), and the second contained a 50× aqueous solution of protocatechuate 3,4-dioxygenase from pseudomonas sp. (PCD) (2.8 mM PCD, 50% glycerol, 50 mM KCl, 100 mM Tris HCl, 1 mM EDTA-Na_2 × $2H_2O$). For measurements, both buffers were diluted in a 50:1 ratio (Trolox/PCA:PCD).

Preparation of the DNA Origami Structures. The pillar-shaped and L-shaped DNA origami structures were folded with a 10-fold excess of unmodified and internally labeled oligonucleotides to the scaffold and a 10-fold excess of pyrene-modified oligonucleotides to the complementary internal oligonucleotides in folding buffer (20 mM $MgCl_2$ × $6H_2O$, 40 mM Tris base, 20 mM acetic acid, 1 mM EDTA-Na_2 × $2H_2O$). For folding, a nonlinear thermal annealing ramp over 16 h was used.[41]

Afterward, the DNA origami solution was cleaned *via* gel electrophoresis. Therefore, 1× "BlueJuice" gel loading buffer was added to the DNA origami solution, and the purification took place in 50 mL 1.5× agarose-gel with 2 μL peqGREEN DNA staining in folding buffer II (12 mM $MgCl_2$ × $6H_2O$, 40 mM Tris base, 20 mM acetic acid, 1 mM EDTA-Na_2 × $2H_2O$). The ice-cooled gel ran for 2 h at 60 V. After cutting of the gel, the DNA origami solution was extracted *via* squeezing. The concentration of the DNA origami solution was measured with a NanoDrop 2000 Spectrophotometer (Thermo Fisher Scientific). Before putting the purified DNA origami solution onto the graphene samples, the concentration was adjusted with folding buffer II to a concentration of 25 pM.

Summary of the Preparation Procedures. Different procedures to produce high-quality, single-layer graphene-coated glass cover slides have been discussed in the literature.[15−17,29,32] We tested 10 different approaches that are experimentally described in section 2 of the Supporting Information. The prepared slides were thoroughly characterized *via* wide-field imaging, fluorescence lifetime imaging, and Raman spectroscopy. The experimental results are presented in section 3 of the Supporting Information.

Fluorescence Lifetime Imaging Microscopy. FLIM was performed on a home-built confocal setup equipped with a 532 nm and a 637 nm pulsed laser (both Picoquant) and a time correlated single-photon counting module (HydraHarp 400, Picoquant). Further details can be found in section 1.2. of the Supporting Information.

Correlative Fluorescence Lifetime and Raman Spectroscopy. Spectroscopy was performed on a second home-built confocal microscope extended by a HeNe CW laser (NEC gas laser) and a spectrograph (Kymera 193i, Oxford Instrument) with EMCCD camera (iXon 897, Oxford Instruments). In addition, the confocal microscope featured again a pulsed laser source at 639 nm (NKT Photonics) and a time correlated single-photon counting module (HydraHarp 400, Picoquant). Further details can be found in section 1.3. of the Supporting Information.

Raman Spectroscopy. Spectroscopy was carried out on a home-built scanning Raman microscope with a wide-field imaging modality. Raman spectra were taken under 633 nm excitation with a spectrograph with a 600 and 1200 lines per mm (Kymera 328i, Oxford Instruments) with an EMCCD camera (iXon 897, Oxford Instruments). Further details can be found in section 1.4. of the Supporting Information.

Atomic Force Microscopy. AFM on graphene on grids with a grid repeat distance of 50 μm (Gridded Glass Coverslips Grid-50, ibidi) was performed using a commercial atomic force microscope (Nanowizard 3 ultra, JPK Instruments). The measurements were performed under ambient conditions with cantilevers from Nanosensors (PPP-NCHAuD) with a scanning speed of 1 Hz and 1024 × 1024 pixels in AC mode.

ASSOCIATED CONTENT

Supporting Information

The Supporting Information is available free of charge at https://pubs.acs.org/doi/10.1021/acsnano.0c08383.

Detailed methods description, light microscopy, Raman and FLIM data for all preparation methods, correlated AFM and FLIM data, and used DNA sequences (PDF)

AUTHOR INFORMATION

Corresponding Authors

Stefan Krause − *Department of Chemistry and Center for NanoScience (CeNS), Ludwig-Maximilians-Universität München, 81377 München, Germany;* orcid.org/0000-0002-7062-8472; Email: stefan.krause@lmu.de

Philip Tinnefeld − *Department of Chemistry and Center for NanoScience (CeNS), Ludwig-Maximilians-Universität München, 81377 München, Germany;* orcid.org/0000-0003-4290-7770; Email: philip.tinnefeld@cup.uni-muenchen.de

Authors

Evelyn Ploetz − *Department of Chemistry and Center for NanoScience (CeNS), Ludwig-Maximilians-Universität München, 81377 München, Germany;* orcid.org/0000-0003-0922-875X

Johann Bohlen − *Department of Chemistry and Center for NanoScience (CeNS), Ludwig-Maximilians-Universität München, 81377 München, Germany;* orcid.org/0000-0001-7826-9147

https://doi.org/10.1021/acsnano.0c08383
ACS Nano 2021, 15, 6430−6438

Patrick Schüler – *Department of Chemistry and Center for NanoScience (CeNS), Ludwig-Maximilians-Universität München, 81377 München, Germany;* orcid.org/0000-0002-3786-0982

Renukka Yaadav – *Department of Chemistry and Center for NanoScience (CeNS), Ludwig-Maximilians-Universität München, 81377 München, Germany;* orcid.org/0000-0002-2633-1639

Florian Selbach – *Department of Chemistry and Center for NanoScience (CeNS), Ludwig-Maximilians-Universität München, 81377 München, Germany;* orcid.org/0000-0003-3870-9069

Florian Steiner – *Department of Chemistry and Center for NanoScience (CeNS), Ludwig-Maximilians-Universität München, 81377 München, Germany;* orcid.org/0000-0002-9148-5837

Izabela Kamińska – *Institute of Physical Chemistry of the Polish Academy of Sciences, 01-224 Warsaw, Poland;* orcid.org/0000-0002-9435-8198

Complete contact information is available at: https://pubs.acs.org/10.1021/acsnano.0c08383

Notes

The authors declare no competing financial interest.

ACKNOWLEDGMENTS

The authors thank Tim Schröder for help with software and fruitful discussions. Financial support by the Deutsche Forschungsgemeinschaft (DFG, grant INST 86/1904-1 FUGG, grant TI 329/14-1, excellence cluster e-conversion under Germany's Excellence Strategy - EXC2089/1-390776260, Project - ID 201269156 - SFB1032) and by the Center for NanoScience (CeNS) is gratefully acknowledged. I.K. acknowledges support by the Foundation for Polish Science, within the program HOMING/2017-4/32 (POIR.04.04.00-00-42E8/17-00) and the National Science Center (Sonata 2019/35/D/ST5/00958).

REFERENCES

(1) Xu, M.; Liang, T.; Shi, M.; Chen, H. Graphene-Like Two-Dimensional Materials. *Chem. Rev.* **2013**, *113* (5), 3766–3798.

(2) Kim, J.; Cote, L. J.; Kim, F.; Huang, J. Visualizing Graphene Based Sheets by Fluorescence Quenching Microscopy. *J. Am. Chem. Soc.* **2010**, *132* (1), 260–267.

(3) Swathi, R.; Sebastian, K. Resonance Energy Transfer from a Dye Molecule to Graphene. *J. Chem. Phys.* **2008**, *129* (5), 054703.

(4) Chang, H.; Tang, L.; Wang, Y.; Jiang, J.; Li, J. Graphene Fluorescence Resonance Energy Transfer Aptasensor for the Thrombin Detection. *Anal. Chem.* **2010**, *82* (6), 2341–2346.

(5) Loh, K. P.; Bao, Q.; Eda, G.; Chhowalla, M. Graphene Oxide as a Chemically Tunable Platform for Optical Applications. *Nat. Chem.* **2010**, *2* (12), 1015.

(6) Liu, J.; Liu, Z.; Barrow, C. J.; Yang, W. Molecularly Engineered Graphene Surfaces for Sensing Applications: A Review. *Anal. Chim. Acta* **2015**, *859*, 1–19.

(7) Ghosh, A.; Sharma, A.; Chizhik, A. I.; Isbaner, S.; Ruhlandt, D.; Tsukanov, R.; Gregor, I.; Karedla, N.; Enderlein, J. Graphene-Based Metal-Induced Energy Transfer for Sub-Nanometre Optical Localization. *Nat. Photonics* **2019**, *13* (12), 860–865.

(8) Kaminska, I.; Bohlen, J.; Rocchetti, S.; Selbach, F.; Acuna, G. P.; Tinnefeld, P. Distance Dependence of Single-Molecule Energy Transfer to Graphene Measured with DNA Origami Nanopositioners. *Nano Lett.* **2019**, *19* (7), 4257–4262.

(9) Moon, S.; Li, W.; Hauser, M.; Xu, K. Graphene-Enabled, Spatially Controlled Electroporation of Adherent Cells for Live-Cell Super-Resolution Microscopy. *ACS Nano* **2020**, *14* (5), 5609–5617.

(10) Kamińska, I.; Bohlen, J.; Yaadav, R.; Schüler, P.; Raab, M.; Schröder, T.; Zähringer, J.; Zielonka, K.; Krause, S.; Tinnefeld, P. Graphene Energy Transfer for Single-Molecule Biophysics, Biosensing & Superresolution Microscopy. *Adv. Mater.* DOI: 10.1002/adma.202101099.

(11) Chizhik, A. I.; Rother, J.; Gregor, I.; Janshoff, A.; Enderlein, J. Metal-Induced Energy Transfer for Live Cell Nanoscopy. *Nat. Photonics* **2014**, *8* (2), 124.

(12) Karedla, N.; Chizhik, A. I.; Gregor, I.; Chizhik, A. M.; Schulz, O.; Enderlein, J. Single-Molecule Metal-Induced Energy Transfer (Smmiet): Resolving Nanometer Distances at the Single-Molecule Level. *ChemPhysChem* **2014**, *15* (4), 705–711.

(13) Kim, K. S.; Zhao, Y.; Jang, H.; Lee, S. Y.; Kim, J. M.; Kim, K. S.; Ahn, J.-H.; Kim, P.; Choi, J.-Y.; Hong, B. H. Large-Scale Pattern Growth of Graphene Films for Stretchable Transparent Electrodes. *Nature* **2009**, *457* (7230), 706–710.

(14) Li, X.; Cai, W.; An, J.; Kim, S.; Nah, J.; Yang, D.; Piner, R.; Velamakanni, A.; Jung, I.; Tutuc, E.; et al. Large-Area Synthesis of High-Quality and Uniform Graphene Films on Copper Foils. *Science* **2009**, *324* (5932), 1312–1314.

(15) Kang, J.; Shin, D.; Bae, S.; Hong, B. H. Graphene Transfer: Key for Applications. *Nanoscale* **2012**, *4* (18), 5527–5537.

(16) Gorantla, S.; Bachmatiuk, A.; Hwang, J.; Alsalman, H. A.; Kwak, J. Y.; Seyller, T.; Eckert, J.; Spencer, M. G.; Rümmeli, M. H. A Universal Transfer Route for Graphene. *Nanoscale* **2014**, *6* (2), 889–896.

(17) Li, X.; Zhu, Y.; Cai, W.; Borysiak, M.; Han, B.; Chen, D.; Piner, R. D.; Colombo, L.; Ruoff, R. S. Transfer of Large-Area Graphene Films for High-Performance Transparent Conductive Electrodes. *Nano Lett.* **2009**, *9* (12), 4359–4363.

(18) Becker, W. Fluorescence Lifetime Imaging–Techniques and Applications. *J. Microsc.* **2012**, *247* (2), 119–136.

(19) Tinnefeld, P.; Buschmann, V.; Herten, D. P.; Han, K. T.; Sauer, M. Confocal Fluorescence Lifetime Imaging Microscopy (Flim) at the Single Molecule Level. *Single Mol.* **2000**, *1* (3), 215–223.

(20) Han, D.; Pal, S.; Nangreave, J.; Deng, Z.; Liu, Y.; Yan, H. DNA Origami with Complex Curvatures in Three-Dimensional Space. *Science* **2011**, *332* (6027), 342–346.

(21) Rothemund, P. W. Folding DNA to Create Nanoscale Shapes and Patterns. *Nature* **2006**, *440* (7082), 297–302.

(22) Saccà, B.; Niemeyer, C. M. DNA Origami: The Art of Folding DNA. *Angew. Chem., Int. Ed.* **2012**, *51* (1), 58–66.

(23) Chung, C.; Kim, Y.-K.; Shin, D.; Ryoo, S.-R.; Hong, B. H.; Min, D.-H. Biomedical Applications of Graphene and Graphene Oxide. *Acc. Chem. Res.* **2013**, *46* (10), 2211–2224.

(24) Huang, X.; Qi, X.; Boey, F.; Zhang, H. Graphene-Based Composites. *Chem. Soc. Rev.* **2012**, *41* (2), 666–686.

(25) Schwierz, F. Graphene Transistors. *Nat. Nanotechnol.* **2010**, *5* (7), 487.

(26) Qu, L.; Liu, Y.; Baek, J.-B.; Dai, L. Nitrogen-Doped Graphene as Efficient Metal-Free Electrocatalyst for Oxygen Reduction in Fuel Cells. *ACS Nano* **2010**, *4* (3), 1321–1326.

(27) Treossi, E.; Melucci, M.; Liscio, A.; Gazzano, M.; Samorì, P.; Palermo, V. , High-Contrast Visualization of Graphene Oxide on Dye-Sensitized Glass, Quartz, and Silicon by Fluorescence Quenching. *J. Am. Chem. Soc.* **2009**, *131* (43), 15576–15577.

(28) Her, M.; Beams, R.; Novotny, L. Graphene Transfer with Reduced Residue. *Phys. Lett. A* **2013**, *377* (21–22), 1455–1458.

(29) Bae, S.; Kim, H.; Lee, Y.; Xu, X.; Park, J.-S.; Zheng, Y.; Balakrishnan, J.; Lei, T.; Kim, H. R.; Song, Y. I.; et al. Roll-to-Roll Production of 30-Inch Graphene Films for Transparent Electrodes. *Nat. Nanotechnol.* **2010**, *5* (8), 574.

(30) Song, J.; Kam, F.-Y.; Png, R.-Q.; Seah, W.-L.; Zhuo, J.-M.; Lim, G.-K.; Ho, P. K.; Chua, L.-L. A General Method for Transferring Graphene onto Soft Surfaces. *Nat. Nanotechnol.* **2013**, *8* (5), 356–362.

(31) Lin, Y.-C.; Lu, C.-C.; Yeh, C.-H.; Jin, C.; Suenaga, K.; Chiu, P.-W. Graphene Annealing: How Clean Can It Be? *Nano Lett.* **2012**, *12* (1), 414−419.
(32) Algara-Siller, G.; Lehtinen, O.; Turchanin, A.; Kaiser, U. Dry-Cleaning of Graphene. *Appl. Phys. Lett.* **2014**, *104* (15), 153115.
(33) Gupta, A.; Chen, G.; Joshi, P.; Tadigadapa, S.; Eklund, P. Raman Scattering from High-Frequency Phonons in Supported *n*-Graphene Layer Films. *Nano Lett.* **2006**, *6* (12), 2667−2673.
(34) Krause, S.; Overgaard, M. H.; Vosch, T. Photon Energy Dependent Micro-Raman Spectroscopy with a Continuum Laser Source. *Sci. Rep.* **2018**, *8* (1), 11621.
(35) Childres, I.; Jauregui, L. A.; Tian, J.; Chen, Y. P. Effect of Oxygen Plasma Etching on Graphene Studied Using Raman Spectroscopy and Electronic Transport Measurements. *New J. Phys.* **2011**, *13* (2), 025008.
(36) Cançado, L. G.; Jorio, A.; Ferreira, E. M.; Stavale, F.; Achete, C. A.; Capaz, R. B.; Moutinho, M. V. d. O.; Lombardo, A.; Kulmala, T.; Ferrari, A. C. Quantifying Defects in Graphene *via* Raman Spectroscopy at Different Excitation Energies. *Nano Lett.* **2011**, *11* (8), 3190−3196.
(37) Heller, E. J.; Yang, Y.; Kocia, L.; Chen, W.; Fang, S.; Borunda, M.; Kaxiras, E. Theory of Graphene Raman Scattering. *ACS Nano* **2016**, *10* (2), 2803−2818.
(38) Guo, X.; Zafar, A.; Nan, H.; Yu, Y.; Zhao, W.; Liang, Z.; Zhang, X.; Ni, Z. Manipulating Fluorescence Quenching Efficiency of Graphene by Defect Engineering. *Appl. Phys. Express* **2016**, *9* (5), 055502.
(39) Xing, W.; Lalwani, G.; Rusakova, I.; Sitharaman, B. Degradation of Graphene by Hydrogen Peroxide. *Part. Part. Syst. Char.* **2014**, *31* (7), 745−750.
(40) Zhao, Y.; Allen, B. L.; Star, A. Enzymatic Degradation of Multiwalled Carbon Nanotubes. *J. Phys. Chem. A* **2011**, *115* (34), 9536−9544.
(41) Nickels, P. C.; Wünsch, B.; Holzmeister, P.; Bae, W.; Kneer, L. M.; Grohmann, D.; Tinnefeld, P.; Liedl, T. Molecular Force Spectroscopy with a DNA Origami−Based Nanoscopic Force Clamp. *Science* **2016**, *354* (6310), 305−307.

https://doi.org/10.1021/acsnano.0c08383
ACS Nano 2021, 15, 6430−6438

Publication

Supporting Information

Graphene-on-Glass Preparation and Cleaning Methods Characterized by Single-Molecule DNA Origami Fluorescent Probes and Raman Spectroscopy

Stefan Krause,[1*] Evelyn Ploetz,[1] Johann Bohlen,[1] Patrick Schüler,[1] Renukka Yaadav,[1] Florian Selbach,[1] Florian Steiner,[1] Izabela Kamińska,[2] Philip Tinnefeld[1*]

(1) Department of Chemistry and Center for NanoScience (CeNS), Ludwig-Maximilians-Universität München, 81377 München, Germany
(2) Institute of Physical Chemistry of the Polish Academy of Sciences, 01-224 Warsaw, Poland

Table of Contents

1. Methods and Characterization ... 3
1.1. pH Measurements ... 3
1.2. Fluorescence lifetime imaging ... 3
1.3. Correlative fluorescence lifetime and Raman spectroscopy ... 3
1.4. Raman spectroscopy ... 4
1.5. Hyperspectral Raman imaging ... 5
1.6. Atomic force microscope (AFM) imaging ... 5

2. Experimental Section ... 5
2.1. Summary of the different preparation procedures ... 5
2.3.1 Wet-transfer method ... 5
2.3.2 Post-transfer treatments ... 5
2.3.3 PMMA curing followed by Acetone ... 6

3. Raman spectroscopy and hyper-spectral imaging to probe the quality of graphene ... 8

4. Correlative microscopy: FLIM and Raman data for different preparation procedures 11

5. Correlative microscopy: Light microscopy, FLIM and AFM data ... 22

6. I_D/I_G ratio versus fluorescence lifetime for the data set in Figure 3e ... 24

7. Quick quality estimation procedure ... 25

8. DNA sequences ... 26

9. References ... 41

1. Methods and Characterization

1.1. pH Measurements

All pH measurements are performed by a SevenEasy pH Meter (Mettler Toledo, Ohio, USA), which is calibrated with buffer solutions of pH 4, 7 and 11.

1.2. Fluorescence lifetime imaging

Measurements are performed on a home built confocal setup with an Olympus IX71 microscope. The red and green laser (LDH-D-C-640 and LDH-P-FA-530B, both Picoquant) are controlled by a PDL 828 "Sepia II" (Picoquant). The green fiber (polarisation maintaining fiber with FC/APC output connector) coupled laser light is decoupled *via* a F220APC-532 collimator (Thorlabs) and cleaned up with a 532/2 (Z532/10 X, Chroma) filter before passing a dichroic mirror (640 LPXR, Chroma) for combination with the already cleaned up (Z640/10 X, Chroma) red laser. Both lasers are overlapped with a fiber (P3-488PM-FC, Thorlabs) which is entered through a collimator (PAF2-2A, Thorlabs) and exited *via* a collimator (G169015000, Qioptics). A linear polarizer (WP12L-Vis, Thorlabs) and a quarter-wave plate (AQWP05M-600, Thorlabs) are combined to obtain circularly polarized light. After passing a second dichroic mirror (zt532/640rpc, Chroma) the beam is focused *via* an oil immersion objective (UPLSAPO 100 XO, NA 1.40, Olympus) onto the samples. The sample is scanned with a piezo-stage (P-527.3CD, Physik Instrumente) which is controlled by an E-727 controller (Physik Instrumente). The emitted light is focused on a 50 µm pinhole (Linos) and collimated with a lens (AC050-150-A-ML, Thorlabs). After passing a dichroic beam splitter (640LPXR, Chroma) and a combination of two filters (red: 731/137 BrightLine HC, Semrock and Razor Edge 647 nm, Semrock; green: 582/75 BrightLine HC, Semrock and Razor Edge 532 nm, Semrock) the beam is focused *via* a lens (AC080-020-B-ML, Thorlabs) on an APD (SPCM-AQRH-TR-14, Excelitas). The APD signal is processed with a HydraHarp 400 (PicoQuant) and controlled with the software SymPhoTime 64 (PicoQuant). The FLIM Images (30 x 30 µm; 256 x 256 pixels, monodirectional) were taken with a laser power of 1 µW.

1.3. Correlative fluorescence lifetime and Raman spectroscopy

The setup for fluorescence lifetime imaging is extended by a HeNe CW laser (NEC gas laser) for Raman spectroscopy using a flip mirror to switch between pulsed and CW excitation source. The overlap of both excitation sources is verified by scanning a single molecule sample consecutively with both sources and superimposing the two images as shown in Figure S1. The false-color image proves an accurate overlap of both excitation spots in the sample plane. Raman backscattered light is separated from Rayleigh scattering at 633 nm (zt532/640/NIR rpc, Chroma and FELH0650, Thorlabs) and recorded *via* a spectrograph (Kymera 193i, Oxford Instruments) with EMCCD camera (iXon 897, Oxford Instruments). Switching between APD-based fluorescence lifetime measurements and spectrometer-based Raman measurement is achieved by an additional flip mirror in the detection path. The spectral resolution at 633 nm amounts to 25.98 cm^{-1} per pixel (Grating with 300 l/mm and blaze at 500 nm). The acquisition time per pixel is set to 20 s at an excitation power of 1.2 to 2 mW at the sample plane. Correlative data acquisition per DNA origami structure is carried out consecutively: (1) FLIM Images (20 x 20 µm 256 x 256 pixels, monodirectional) is taken with a laser power of 1 µW at 639 nm. (2) The position of the molecules are selected within the FLIM image for fluorescence lifetime measurement and Raman spectroscopy. (3) The fluorescence trace of each molecule is recorded until the molecule bleached. (4) A Raman spectrum of the same confocal volume is taken consecutively. Step (3) and (4) are repeated until a sufficient number of spot data is acquired.

Confocal data acquisition is carried out on home written LabVIEW routines while the recording of Raman spectra is realized with the spectrometer accompanying software *Andor SOLIS* (Andor, Oxford Instruments). The data is analyzed with home-written Matlab routines.

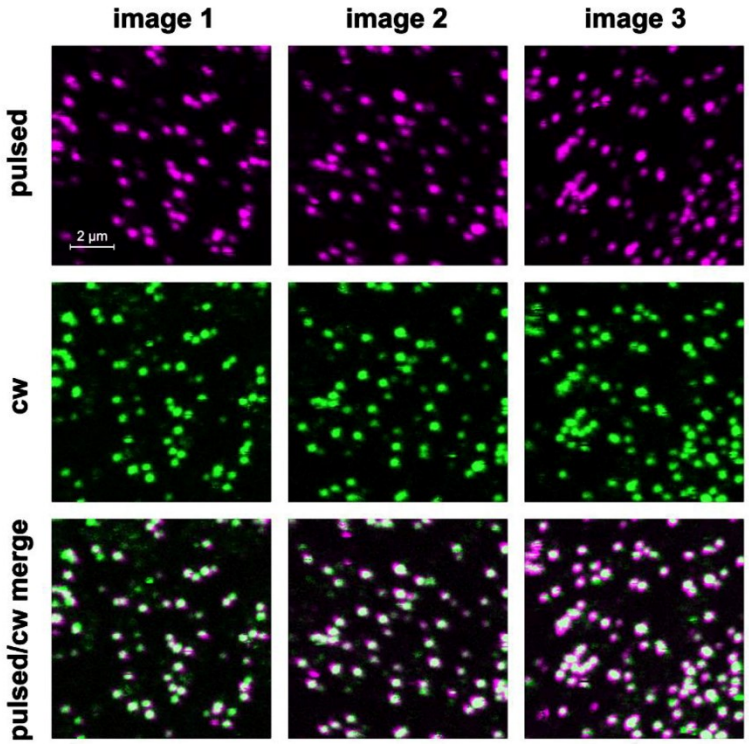

Figure S1: *Example images of individual DNA origami structures labeled with ATTO647N imaged consecutively with pulsed excitation (magenta) and CW excitation (green). The bottom row shows the false color merge of the images above.*

1.4. Raman spectroscopy

Spontaneous Raman spectroscopy is carried out on a home-built scanning Raman microscope with a widefield imaging modality. Using a Mercury lamp for illumination, widefield images of the sample are recorded on a CMOS camera in parallel to spatially resolved Raman spectra for each measurement position. Raman spectra are taken under 633 nm excitation on a Nikon300 microscope equipped with 60 × 1.2 NA water immersion objective (Plan Apo VC 60×, 1.20 NA, Nikon). Excitation and detection paths are decoupled by a dichroic filter (zt405/488/561/633/785 rpc; AHF) in combination with two filters to block shorter wavelengths including Rayleigh scattering at 633 nm (two 633 nm notch filter, OD6, Edmund Optics). Raman backscattered radiation is recorded *via* a spectrograph (Kymera 328i, Oxford Instruments) with an EMCCD camera (iXon 897, Oxford Instruments). The spectral resolution at 633 nm amounts to ~ 5 and 2.8 cm^{-1} per pixel (Grating with 600 and 1200 l/mm and blaze at 500 nm). Data is recorded using the manufacturer's software *Andor Solis for Imaging V4.30* (Oxford Instruments). The acquisition time per pixel is set to 10 times 30 s with an excitation power of 22 mW at the back-focal plane. The recorded spectra are corrected against cosmic rays, Rayleigh scattering and spurious background by spline subtraction.

1.5. Hyperspectral Raman imaging

Hyper-spectral imaging is carried out using an InVia Renishaw Raman spectrometer based on a Leica microscope equipped with a 532 nm CW laser source (CNI, China), cutoff optical filters, and a 1024 × 256 pixel Peltier-cooled RenCam CCD detector. This allows registering the Stokes part of Raman spectra with 5–6 cm^{-1} spectral resolution. The wavenumber accuracy is 2 cm^{-1}, which is calibrated with both Rayleigh laser line and the 520.6 cm^{-1} Raman resonance of a silicon crystal. Raman spectra are collected using Leica N Plan EPI 100× 0.85 NA objective and 1800 $1/mm^{-1}$ grating. For image acquisition, areas with 500 nm step-size are raster-scanned, while full Raman spectra are recorded at each pixel of the image. The acquisition time per pixel is set to 1 s with an excitation power of 2.3 mW at the sample. The hyper-spectral data is acquired with the Renishaw software WiRE 3.2, analyzed with custom-written Matlab software using Octave 5.2.0, and processed using Origin 8.5. The recorded hyper-spectral data cube, *i.e.* data set of Raman spectra as a function of spatial coordinate, is first corrected against cosmic rays, Rayleigh scattering and spurious background.

1.6. Atomic force microscope (AFM) imaging

Graphene on grids with a grid repeat distance of 50 µm (Gridded Glass Coverslips Grid-50, ibidi) is imaged using a commercial atomic force microscope (AFM, Nanowizard 3 ultra, JPK Instruments). The measurements are performed under ambient conditions with cantilevers from Nanosensors (PPP-NCHAuD) with a scanning speed of 1Hz and 1024 × 1024 pixels in AC mode.

2. Experimental Section

2.1. Summary of the different preparation procedures

2.3.1 Wet-transfer method

The wet-transfer-method is essentially the same for all preparation procedures, except the reverse transfer method. Monolayer graphene on a 60 mm × 40 mm back-etched copper substrate covered with poly(methyl methacrylate) (PMMA) is purchased from Graphenea®. Subsequently, a wet-transfer approach is used to transfer the graphene to glass coverslips. All coverslips are treated beforehand in a UV-Ozone cleaner at 100˚C for 30 minutes on each side to remove/destroy any fluorescent contaminants from the surface. Pieces of roughly 0.5 × 0.5 cm^2 are carefully cut from the PMMA/graphene/Cu foil. The copper is wet-etched by letting a piece float with the copper film exposed to 0.2 M ammonium persulfate for ~4 hours. A pre-treated coverslip is dipped vertically while slowly moving towards the PMMA/graphene and scooped gently out of the solution. The PMMA/graphene layer is washed twice in fresh MilliQ water before carefully drying it on the substrate using a gentle nitrogen stream.

2.3.2 Post-transfer treatments

The use of a polymer support for the wet transfer of CVD (Chemical Vapor Deposition) grown graphene is becoming increasingly common. Amongst others, PMMA is widely used. *Via* spin coating, a 60-100 nm thick PMMA layer is typically deposited on top of the CVD grown graphene. After a successful transfer, PMMA can be dissolved in organic solvents like acetone, toluene etc. However, it was found that the harsh conditions of CVD may lead to an increased roughness of the metal substrate that was used to grow graphene. Additional coating with PMMA leads to rigidification during drying. This prevents the underlying graphene from relaxing and thus graphene maintains all the ripples and folds caused during the process.[1] To avoid this, it is proposed to add another layer of liquid PMMA on top

of the first PMMA/graphene layer. With this strategy (see next section), the dried PMMA shall re-dissolve allowing the underlying graphene monolayer to relax and form improved contact with the substrate.[1]

2.3.3 PMMA curing followed by Acetone

We use this method by dissolving PMMA (M_w = 120,000 g/mol, Sigma Aldrich) in chlorobenzene (50 mg/mL) and drop-cast on the dry PMMA/graphene on glass. After 30 minutes, the PMMA is dissolved by keeping it in acetone for 5-10 minutes followed by holding the substrate with PMMA facing towards the acetone vapors for 5-10 minutes as similarly reported in literature.[2] This harsh strategy turns out to not fully remove PMMA in a few cases but even worse, it often results in the complete disruption of the graphene layer. Due to this reason, other treatments are explored for a successful removal of PMMA aiming for the highest quality of graphene possible. These methods are described in the following section sorted according to the graphene quality they yielded. The name of each method indicates the type of applied cleaning step: A – acetone, T – toluene, C – active coal, H – thermal treatment of 350 °C, D – DMSO, prime (') – heated solvent to about 50°C, asterisk (*) – acetone vapor treatment, R – reverse transfer method.[3]

1. **Acetone + Toluene + Active coal treatment (Strategy No1 – ATC1 / ATC2):**[4] The PMMA/graphene on glass is first dipped twice in fresh acetone and then in toluene for 5-10 minutes for each single washing step. The remaining toluene is removed with a gentle, clean nitrogen flow. Afterwards, the sample is kept on active coal (Merck) while slowly heating the coal to 230 ˚C for 30 minutes and allowing it to cool down.
2. **Acetone + Active coal treatment (Strategy No2 – A'C):**[4] The PMMA/graphene on glass is dipped in fresh acetone twice for 5-10 minutes at about 50 °C and kept afterwards upside down on active coal (Merck) while slowly heating the coal to 230 ˚C for 30 minutes and allowing it to cool down.
3. **Acetone + Heating treatment (Strategy No3 – A'H):** The PMMA/graphene on glass is rinsed in acetone for 5-10 minutes at about 50 °C followed by heating at 350 ˚C for 3 hours in an atmosphere of Ar:H_2 in the ratio 950 sccm : 50 sccm.
4. **Acetone + Toluene treatment at RT (Strategy No4 – AT1 / AT2):** The PMMA/graphene on glass is first dipped twice in fresh acetone for 5-10 minutes at room temperature and then in toluene for 5-10 minutes at room temperature followed by drying under nitrogen.
5. **Acetone + Toluene treatment (Strategy No5 – A'T'):** The PMMA/graphene on glass is first dipped twice in fresh acetone for 5-10 minutes at about 50 °C and then in toluene for 5-10 minutes at about 50 °C followed by drying under nitrogen.
6. **Acetone (50 °C) + Toluene (RT) treatment at RT (Strategy No6 – A'T):** The PMMA/graphene on glass is first dipped twice in fresh acetone for 5-10 minutes at about 50 °C and then in toluene for 5-10 minutes at room temperature followed by drying under nitrogen.
7. **Acetone + DMSO treatment (Strategy No7 – A'D'*):** The PMMA/graphene on glass is first cleaned in fresh acetone twice for 5-10 minutes at about 50 °C and then rinsed in DMSO for 5-10 minutes again at 50 °C. Finally, the glass is held upside down for about 2 minutes over acetone vapor.
8. **Acetone treatment (Strategy No8 – A'1*):** The PMMA/graphene on glass is rinsed three times in fresh acetone for 5 minutes at about 50 °C for the successful removal of PMMA before exposing it to acetone vapor for 5-10 minutes and drying under nitrogen.

9. **Overnight acetone treatment (Strategy No9 – A'2*):** The PMMA/graphene on glass is rinsed three times in fresh acetone for 5 minutes at about 50 °C for the successful removal of PMMA before leaving it in acetone overnight, followed by drying under nitrogen.
10. **Reverse Transfer Method (Strategy No10):** In order to find the best way to deal with the leftover polymer residue, we noticed a reverse transfer strategy that promised both - better control over contamination and improved adhesion of graphene onto substrates.[3] With slight modification, the final method involves placing the PMMA/graphene/Cu foil in the etchant (ammonium persulfate) solution with copper facing upwards. After 4 hours of etching, the floating graphene/PMMA is scooped from the solution by using a coverslip and washed twice with MilliQ water followed by drying with nitrogen. This results in layers stacked in the order of graphene/PMMA/Glass compared to the PMMA/graphene/Glass as in the normal wet-transfer method.

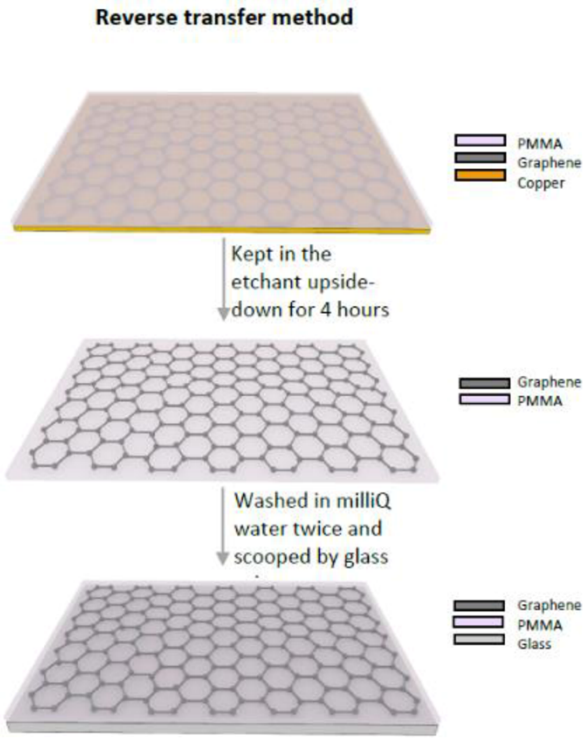

Figure S2: *Scheme of the reverse transfer method. Cutting off a small rectangle from the PMMA-graphene-copper foil. Etching for 4 h in a 0.2 M aqueous solution of ammonium persulfate. Transferring to glass and releasing in water for washing two times. Final scooping onto clean glass cover slide.*

The quality of the method is in the following described by two entities: (i) the mean fluorescence lifetime averaged over all samples which should be close to the theoretical value of 1.5 ns, (ii) the relative amount of good sample areas. The latter can be seen as an indicator of the reliability of the method but also for the homogeneity of the foil. A sample area is considered to be good, if the density of fluorescent spots is sufficient, no dirt can be seen and the majority of fluorescent spots shows a fluorescence lifetime close to the expected 1.5 ns.

The transfer and cleaning strategies are evaluated as described above. The results are shown in Figure S3 giving the relative amount of good sample areas over the average fluorescence lifetime for the 9 different transfer and cleaning methods.

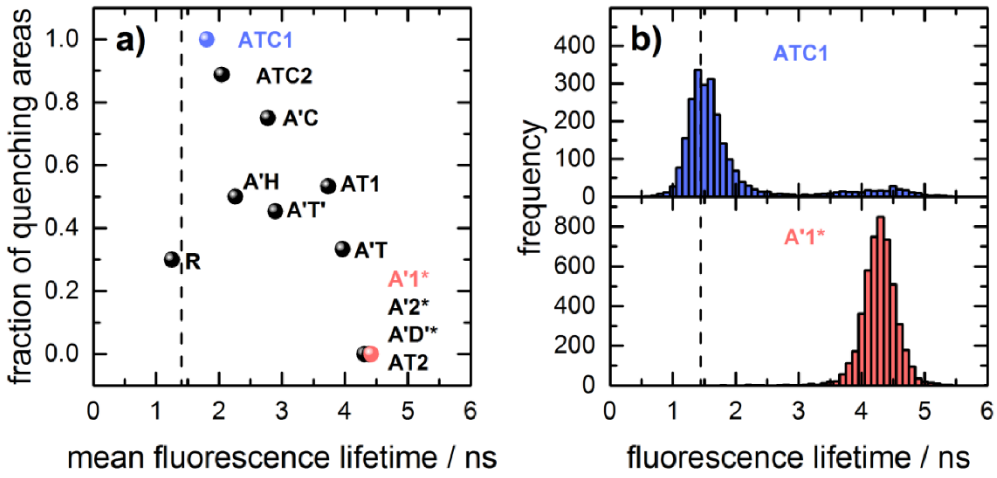

Figure S3. *Comparison of different graphene transfer and cleaning procedures. a) Ratio of good (quenched) to bad (none-quenched, no visible DNA origami structures at all) sample areas as a function of the average fluorescence lifetime of all found spots. The vertical dashed line represents the theoretically expected fluorescence lifetime based on the DNA origami structure design. The name of each method indicates the type of applied cleaning step: A – acetone, T – toluene, C – active coal, H – thermal treatment of 350 °C, D – DMSO, prime (') – heated solvent to about 50°C, asterisk (*) – acetone vapor treatment, R – reverse transfer method.[3] Samples prepared from different PMMA/graphene/Cu foil batches are numbered with 1 or 2, respectively. The vertical dashed line indicates the theoretically expected fluorescence lifetime value of 1.5 ns. The method highlighted in blue (ATC1) shows the best agreement with the theoretical fluorescence lifetime. b) Fluorescence lifetime distribution for the best- (ATC1) and worst-performing (A'1*) cleaning procedure.*

3. Raman spectroscopy and hyper-spectral imaging to probe the quality of graphene

Raman spectroscopy is the state-of-the-art method to characterize graphene materials and in particularly to understand quality and layer structure.[5-10] The main spectral feature of graphene, the G band near 1580 cm^{-1} results from the stretching motion of sp^2 pairs. The position and intensity of this Raman resonance is a good indicator of the number of transferred graphene layers. Similarly, the sheet number can also be determined by the position and shape of the 2D band (2650-2700 cm^{-1}). The quality of single-layer graphene, on the other hand, is reflected by the absence of defects, which can be monitored by the appearance of the disorder-induced D band around 1340 cm^{-1}. It is the result of lattice motions and shows an excitation energy dispersion.[11] Defects can be quantified *via* two strategies: an absent or negligible D band ($\frac{I_D}{I_G} \rightarrow 0$) is the first indicator for high-quality graphene.[12] Another parameter of defect-free graphene is the ratio of the peak intensities of the 2D band to the G band, which should be larger than 2 ($\frac{I_{2D}}{I_G} > 2$).[13] For a better understanding, an example Raman spectrum acquired from high quality graphene is given in Figure S4. Apart from these key parameters, Raman spectroscopy can provide other valuable information about graphene, such as strain effects, interference, charge carriers, thermal effects and stacking.[14-16]

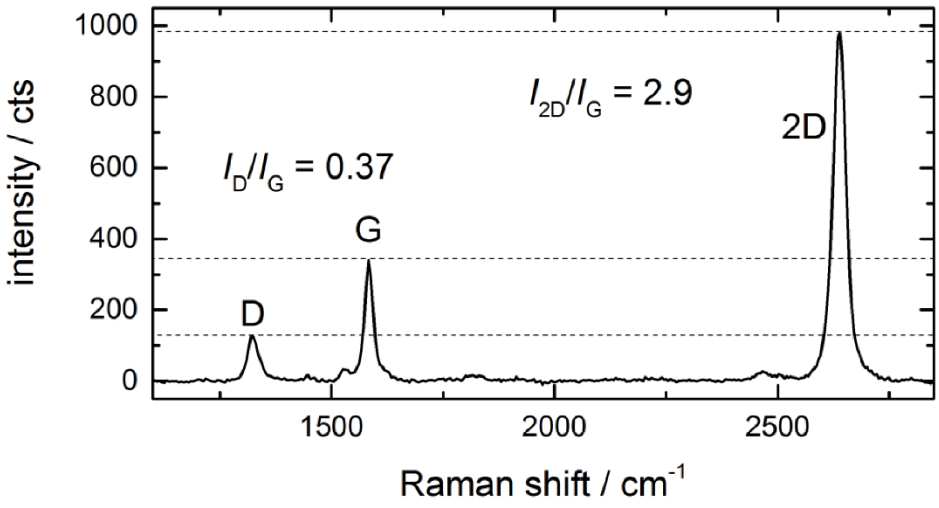

Figure S4: *Representative Raman spectrum of graphene featuring the three Raman peaks typically used for an estimation of the graphene quality. The horizontal dashed lines indicate the peak intensities of D, G and 2D band for comparison. Integration time was 20 s at an excitation power of 1.6 mW.*

Generally, Raman spectroscopy offers detailed insights into defects, flake sizes, layer numbers and tension of graphene sheets and is therefore routinely applied for characterization.[5, 9, 12, 17] As a single Raman spectrum is not sufficient to draw conclusions on the quality of a large graphene sheet we use Raman-based hyper-spectral imaging, *i.e.* mapping to get an impression of the spatial distribution of defects for our transferred graphene samples. Here, the intensity of the D, G and 2D bands were shown as a function of position coordinate. Figure S5 shows Raman images and selected spectra of a high-quality single-layer graphene sample in comparison to a graphene layer with defects. For the high-quality sample, we find an almost constant amplitude for D, G and 2D band thus also a constant height ratio of 2D/G for most of the layer (Figure S5 a-c, g and h). The representative Raman spectrum in Figure S5k (black curve) for these intact graphene areas shows a negligible D band and a 2D/G ratio of more than 2 which implies Raman scatter from high-quality single-layer graphene.[12, 14] For comparison, Figure S5 d-f, i and j show Raman maps (20 × 20 µm^2) of a sample area with defects. These defects become apparent from the increased D band (Fig. S5b) and reduced G and 2D bands (Fig. S5d and f). Closer inspection of the spatial distribution of D and G bands suggest also that different types of defects with different influence on D and G are present. This is even more obvious from the three example Raman spectra (Fig. S5k red, green, blue curve) recorded at point 1, 2 and 3 in Figure S5d-f. Spot 1 is most probably a wrinkle, characterized by a negligible D band (no distortion of graphene), but more intense G than 2D band, which is attributed to >3 layers of graphene. On the other hand, the spectrum recorded at spot 2 represents single-layer graphene, while at spot 3 one can recognize a destroyed graphene lattice confirmed by the very intense D band. Overall, the data in Figure S5 demonstrates that Raman mapping excellently reveals the spatial distribution of defects in graphene. Although time-consuming, Raman mapping therefore is a sensitive and nondestructive tool for characterizing our graphene samples.

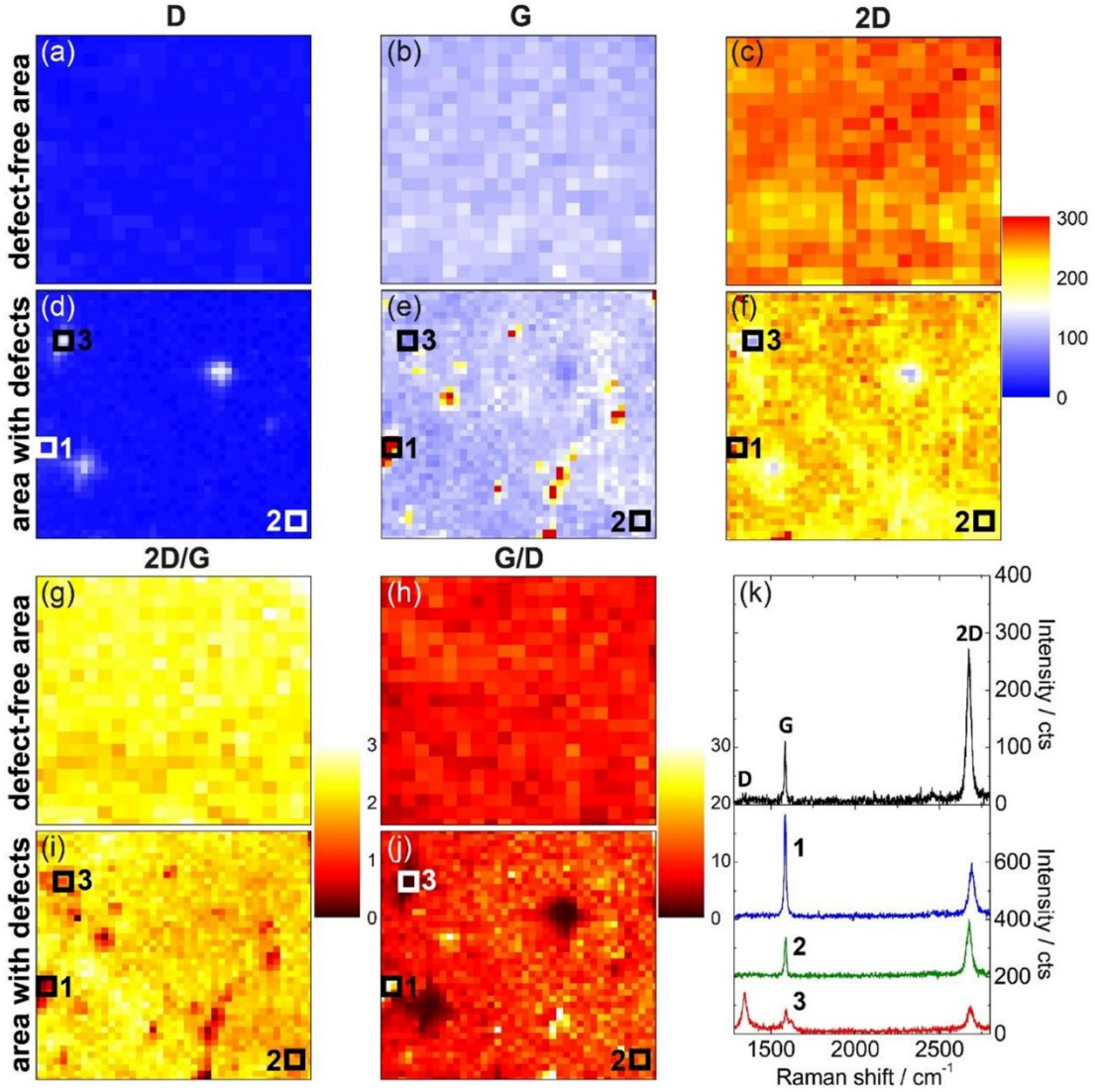

Figure S5. *Comparison of intact and defect-related sample areas of a graphene sample prepared according to the protocol depicted in Figure 1. The Raman maps a) - j) show spatial intensity distributions of the disorder-induced D band (a,d) the G band (b,e) as well as the 2D band (c,f). g) and i) show the 2D/G ratio which serves as an indicator of the graphene quality. A similar quality criterion is shown in h) and j) depicting the G/D ratio. k) Representative Raman spectra taken from the intact sample area (black) and Raman spectra taken at the three defect positions marked in d)-f), i and j. Map sizes are 10 × 10 µm² for image a),b),c),g),h) and 20 × 20 µm² for image d),e),f),i),j). The step size amounted to 500 nm.*

4. Correlative microscopy: FLIM and Raman data for different preparation procedures

Coverslips carrying single-layered graphene are prepared following ten different approaches as described in section 2. Samples of each approach are characterized by three different methods: (1) Widefield microscopy for fast visual inspection of the layer's quality. (2) Fluorescence lifetime imaging microscopy (FLIM) to characterize the homogeneity and quality of the prepared single-layer graphene by measuring the fluorescence lifetime of ATTO647N-labeled DNA origami structures attached to the graphene layer. (3) Raman spectroscopy to monitor defects and/or additional, remaining polymer layers. The following SI figures summarize the experimental findings for each preparation strategy. Each sample is characterized with widefield and FLIM imaging as shown in panel (a) and (b) at three different areas. The corresponding fluorescence lifetime distribution is summarized in panel (c) and quenched ($\tau \leq 2.7$ ns) and unquenched ($\tau > 2.7$ ns) molecules are distinguished according to their fluorescence lifetime. Representative Raman spectra in panel (d) are recorded at the cross hair-marked positions in the widefield images (panel a) that show the graphene environment around the measurement position.

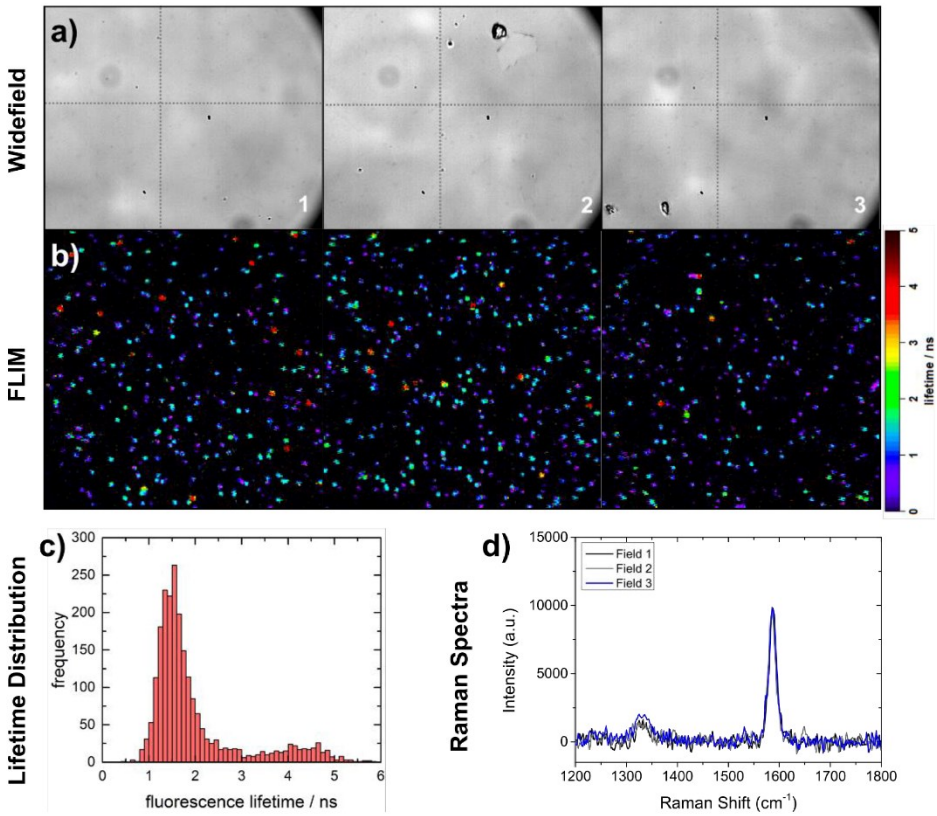

Figure S6. *ATC1 Characterization (Strategy No1). Washing twice with acetone and toluene followed by active coal treatment results in homogeneous single-layer graphene with little to no scratches as seen in the widefield images in a). b) and c) FLIM reveals that about 90 % of the ATTO647N molecules are quenched in all investigated areas with a mean fluorescence lifetime of the distribution of ~ 1. 5 ns (quenched) and 4.2 ns (unquenched). d) Raman spectroscopy confirms an intact and homogeneous layer with little defects. The measurement positions are marked in the widefield images.*

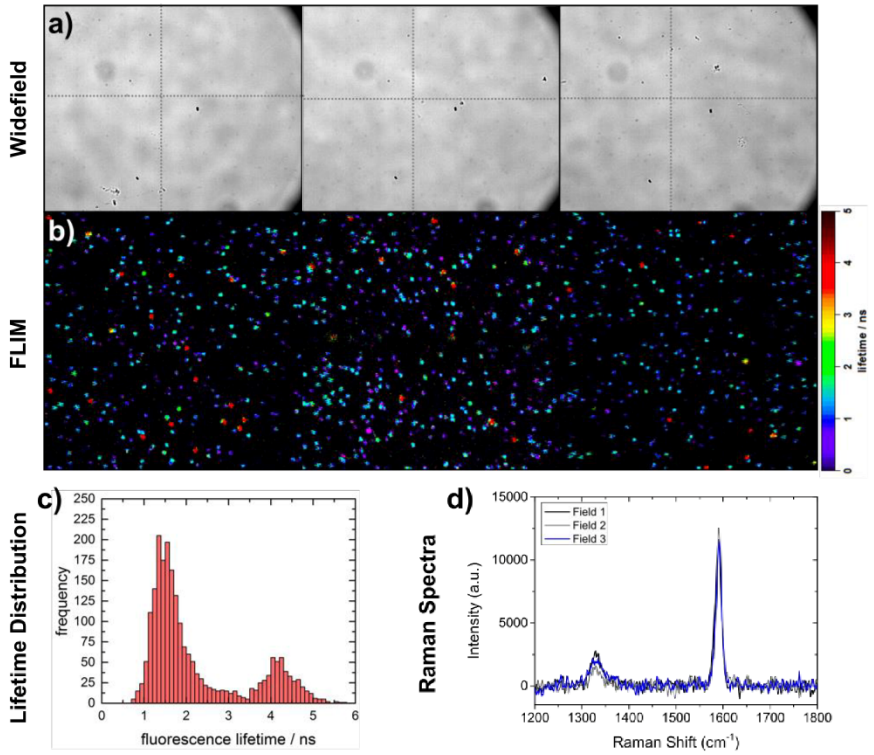

Figure S7. *ATC2 Characterization (Strategy No1, different foil). a) Identical to Figure S6, the ATC strategy leads again to reproducible results with homogeneous, single-layer graphene without scratches and little defects. b) and c) ATTO647N molecules are mainly quenched in a ratio of about 4:1 in all three areas with a mean fluorescence lifetime of the distribution of ~ 1.5 ns (quenched) and 4.2 ns (unquenched). d) The Raman spectra indicate little defects from the small intensity of the D band. The measurement positions are marked in the widefield images.*

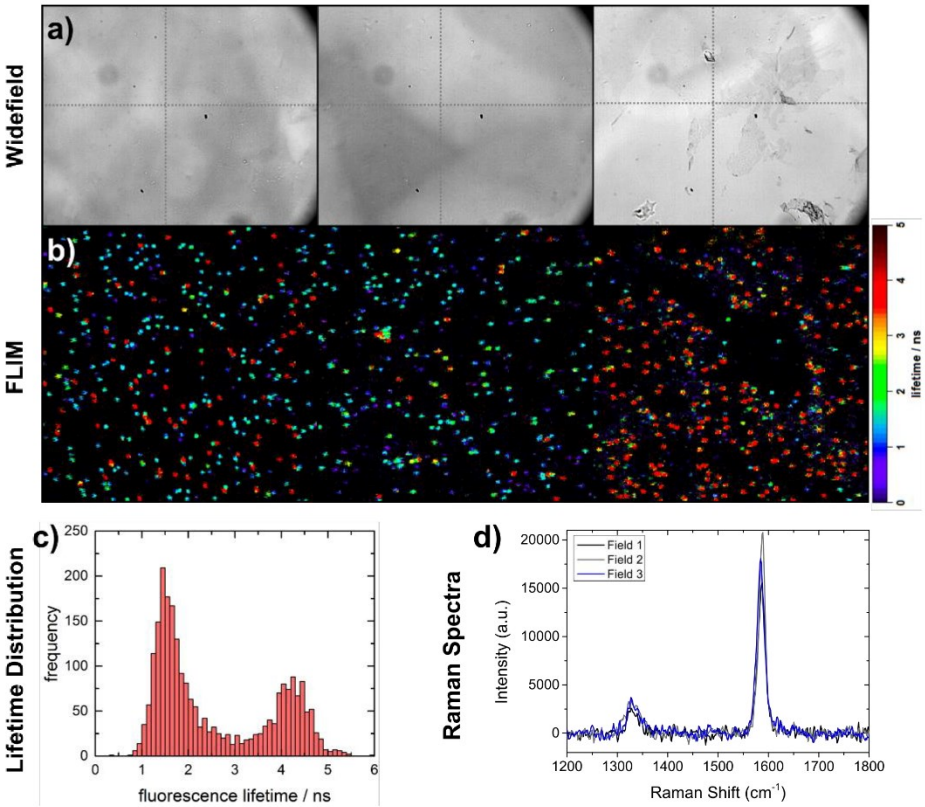

Figure S8. A'C Characterization (Strategy No2). a) Active coal treatment and heating of the sample leads to evenly spread single-layer graphene that show scratches and partial removal from the glass as observed by widefield microscopy. b) and c) FLIM shows a heterogeneous distribution of ATTO647N molecules that are quenched in areas with remaining graphene in a ratio of ~ 2:1 with mean fluorescence lifetimes of ~ 1.6 ns and 4.2 ns. d) Raman spectroscopy reveals a homogeneous single layer with little defects in the remaining areas of the graphene. The measurement positions are marked in the widefield images.

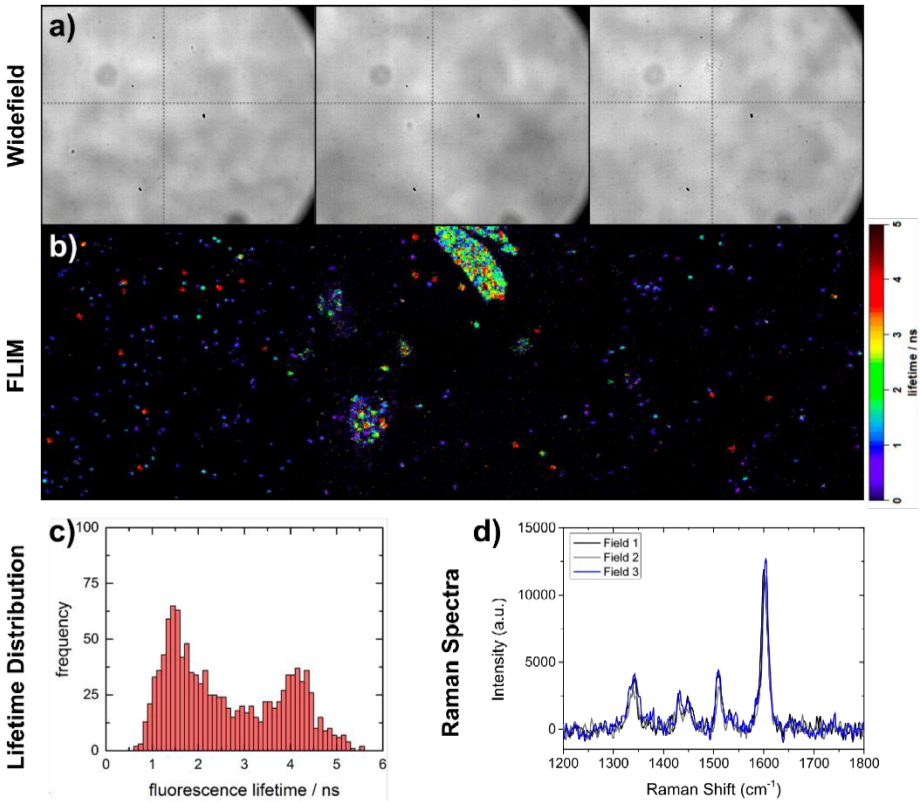

Figure S9. *A'H Characterization (Strategy No3). a) Washing with acetone followed by heating at 350 ˚C in an atmosphere of Ar:H_2 in the ratio 950 sccm : 50 sccm forms homogeneous single-layer graphene, which does not show any scratches in widefield microscopy. b) and c) Surprisingly, ATTO647N molecules are not evenly distributed on the surface and do not show a homogeneous, quenched fluorescence lifetime in all three areas as seen by FLIM imaging. While the majority of molecules is quenched with a fluorescence lifetime of ~ 1.5 ns, a full range of fluorescence lifetimes is found between 1 and 5 ns. This indicates that the molecules have either different distances to the graphene layer or the graphene features defects reducing the quenching efficiency. d) Raman experiments reveal additional resonances at ~ 1430, 1450, 1510 and 1605 cm^{-1}. Acetone pre-cleaning and heating does not remove the polymer layer completely leading to differently spaced sample heights of the DNA origami structures above the graphene layer. The measurement positions are marked in the widefield images.*

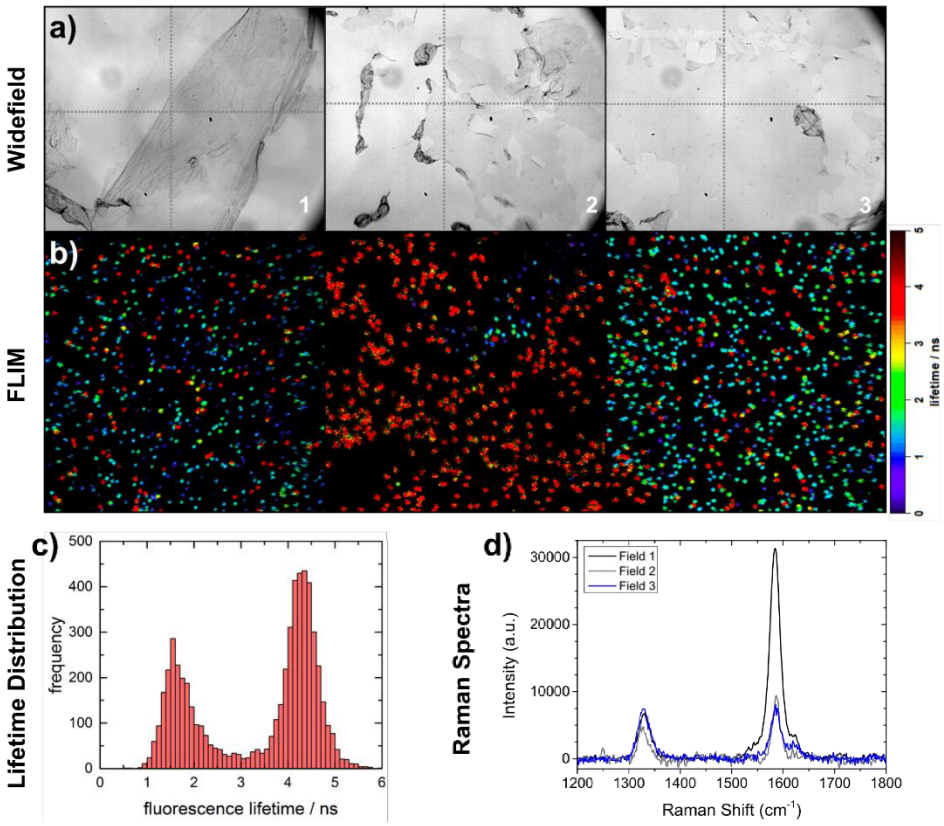

Figure S10. *AT1 Characterization (Strategy No4). a) Dissolving PMMA twice with acetone and once with toluene at room temperature leads to partially disrupted single- and multi-layer graphene surface detachment from the glass. b) and c) FLIM imaging shows that ATTO647N molecules are evenly distributed and quenched in a ratio of ~ 1:2 with a mean fluorescence lifetime of the distribution of ~ 1.6 ns and 4.3 ns. d) The reduced quenching can be explained by a mix of homogeneous single and multi-layer graphene with little defects as seen by Raman spectroscopy. The measurement positions are marked in the widefield images.*

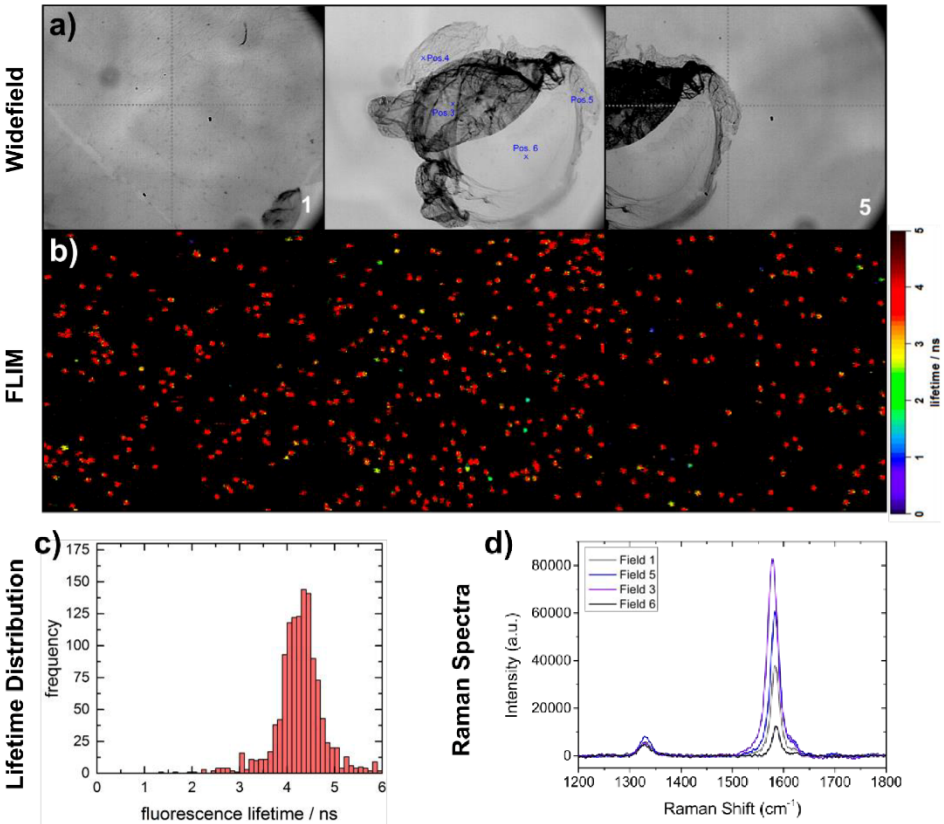

Figure S11. *AT2 – Characterization (Strategy No4). a) Dissolving PMMA twice with acetone and once with toluene at room temperature leads to partially disrupted single- and multi-layer graphene surface detachment from the glass. b) and c) ATTO647N molecules are evenly distributed as shown by FLIM microscopy, however, they are not quenched. The fluorescence lifetime distribution features a mean fluorescence lifetime of about 4.3 ns. d) The lack of quenching is due to the detachment and folding of graphene into multi-layers with defects as revealed by Raman spectroscopy. The measurement positions are marked in the widefield images.*

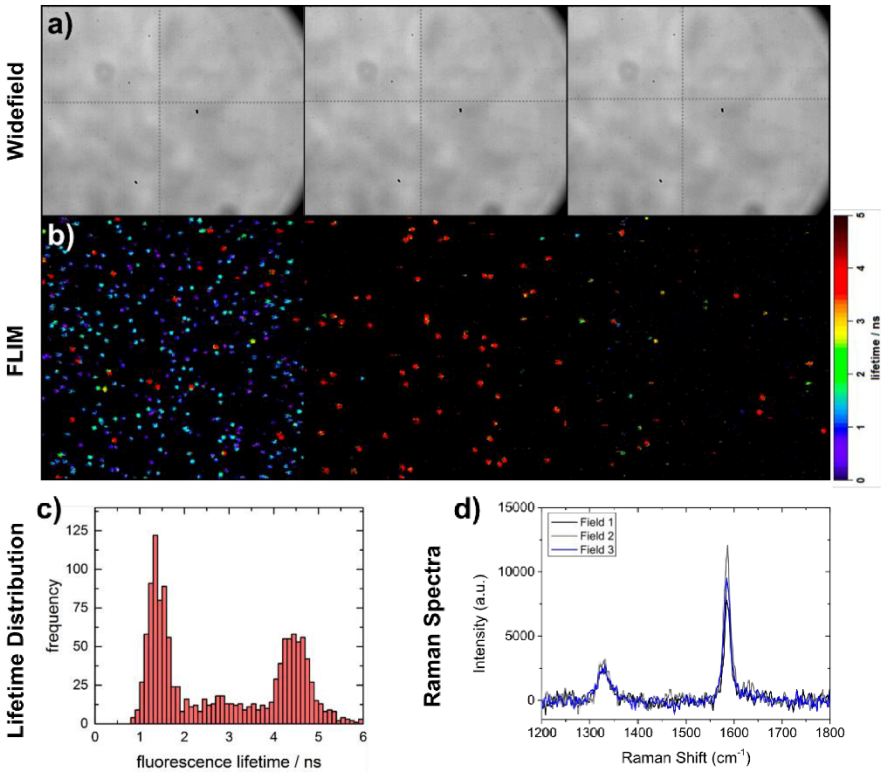

Figure S12. *A'T' Characterization (Strategy No5). a) Washing twice with acetone and once with toluene at about 50 °C forms homogeneous single-layer graphene with little scratches as observed by widefield microscopy. b) and c) Surprisingly, ATTO647N molecules do not show a homogeneous, quenched fluorescence lifetime in all three areas as measured by FLIM imaging. While some areas show homogenous, full quenching, some show no quenching at all. Hence, the fluorescence lifetime distribution is characterized by two populations with fluorescence lifetimes around ~ 1.4 ns and 4.3 ns. d) The variation in fluorescence lifetimes is also reflected in the quality of the graphene. Raman experiments reveal varying intensities of the D and G band, indicating disturbed single-layered graphene. The measurement positions are marked in the widefield images.*

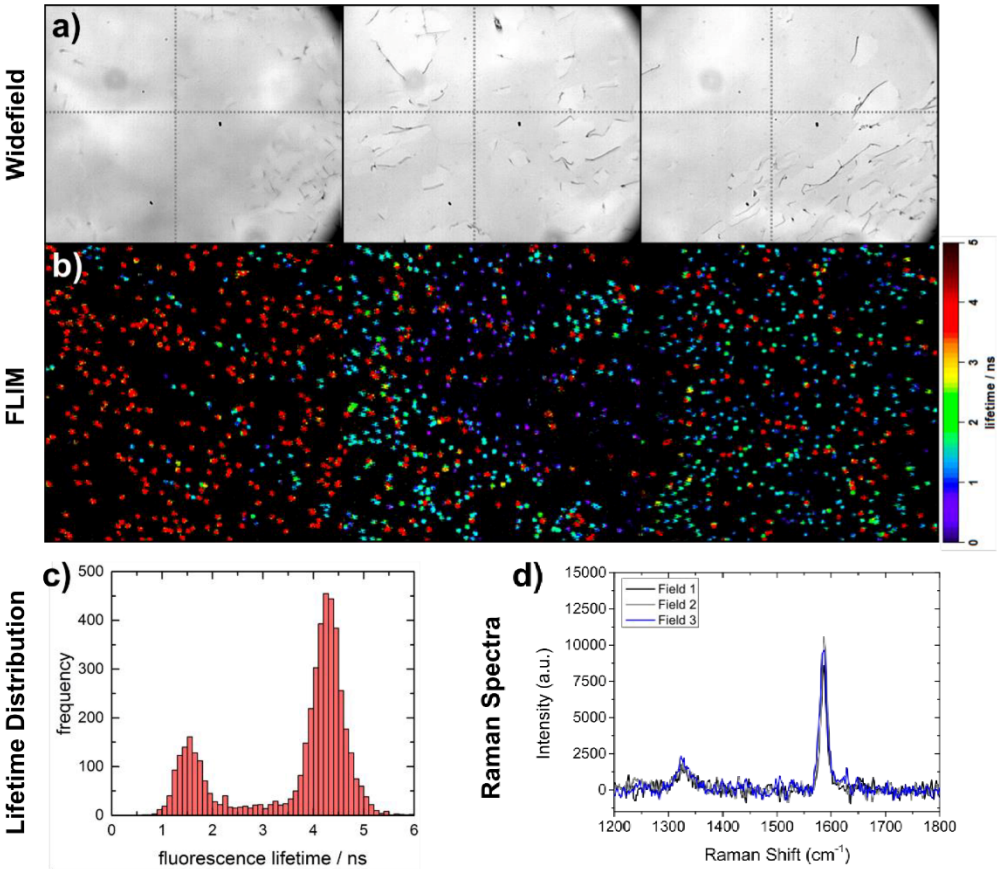

Figure S13. *A'T Characterization (Strategy No6). a) Washing twice with acetone and once with toluene at room temperature forms single-layer graphene partially with micrometer-sized holes. b) and c) Accordingly, ATTO647N molecules do not show a homogeneous, quenched fluorescence lifetime in all areas of the FLIM images. While some areas show homogenous, full quenching, some show partial quenching with compartment sized according to hole sizes seen in the widefield images. Hence two populations with fluorescence lifetimes around ~1.5 ns and 4.3 ns were found in the fluorescence lifetime histogram. d) Raman spectroscopy acquired in the intact areas reveals a homogeneous single layer with little defects. The measurement positions are marked in the widefield images.*

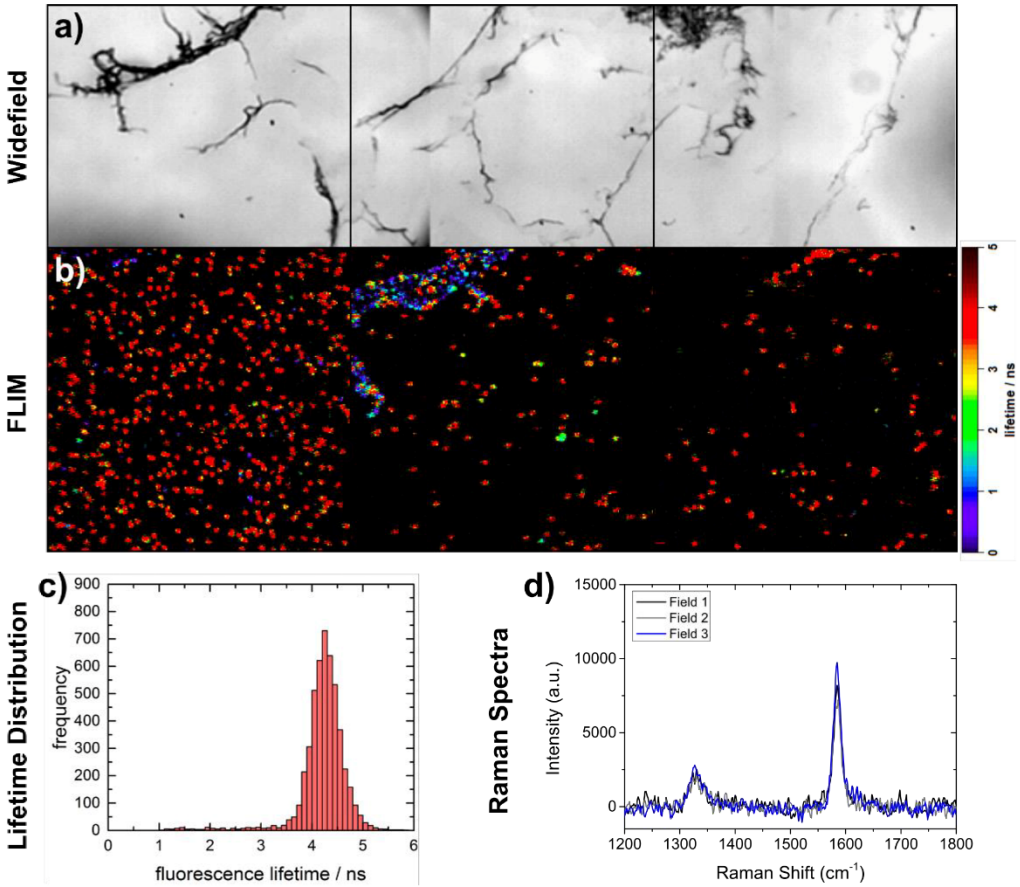

Figure S14. *A'D'* Characterization (Strategy No7). a) Washing with acetone followed by DMSO destroys the graphene layer. If still attached to the glass, graphene forms rolled wraps as seen in widefield. b) and c) The non-intact graphene layer did not quench the fluorescence lifetime of ATTO647N for most of the molecules and show a mean fluorescence lifetime around 4.3 ns. d) Areas that are not made of bare glass or covered by rolled graphene still have single-layer graphene on as shown by Raman spectroscopy.*

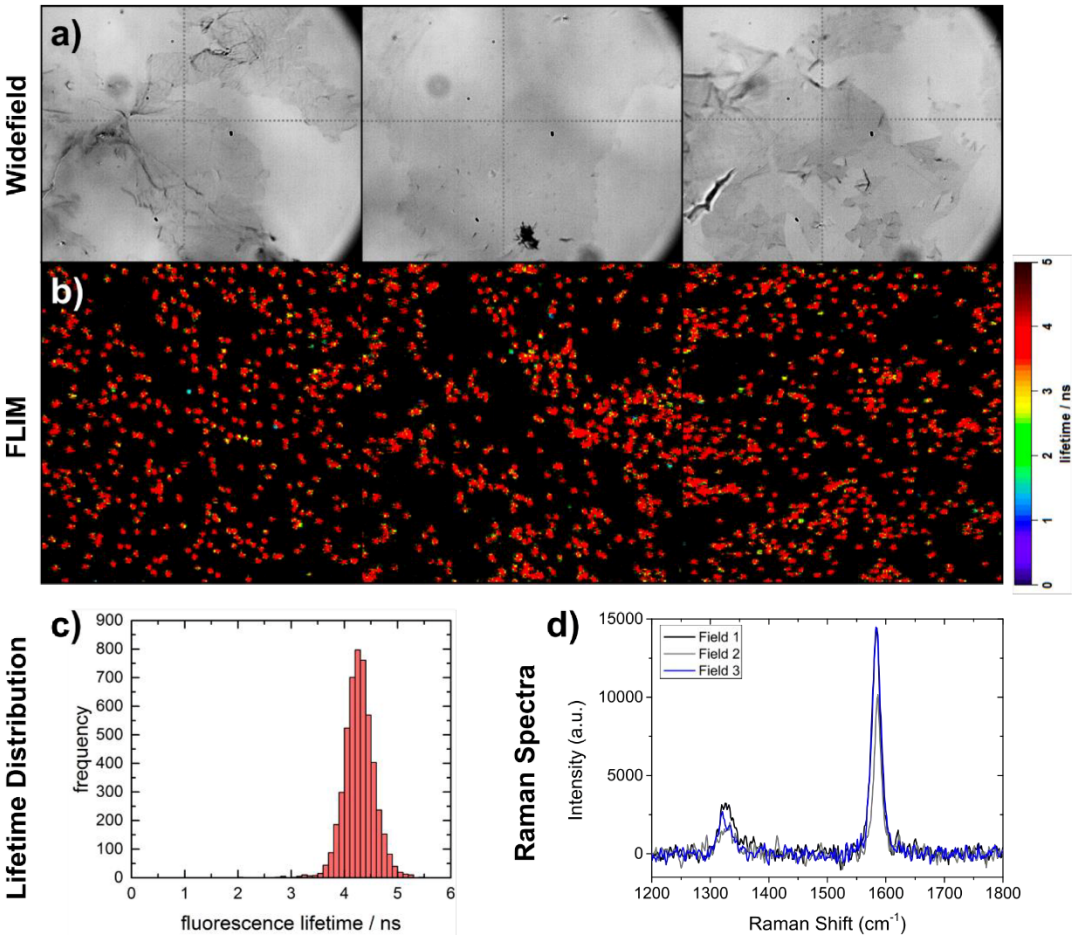

Figure S15. *A'1* Characterization (Strategy No8). a) Washing twice in acetone in combination with acetone vapor exposition and nitrogen drying destroys the single-layer graphene and partially removes it from the glass. b) and c) All areas measured with FL microscopy show an equally spread distribution with homogeneous fluorescence emission without quenching. ATTO647N-labeled DNA origami structures share one fluorescence lifetime of about 4.3 ns. d) Raman spectroscopy revealed single-layered graphene with different D:G ratios in areas where it was not removed from the glass, yet. The measurement positions are marked in the widefield images.*

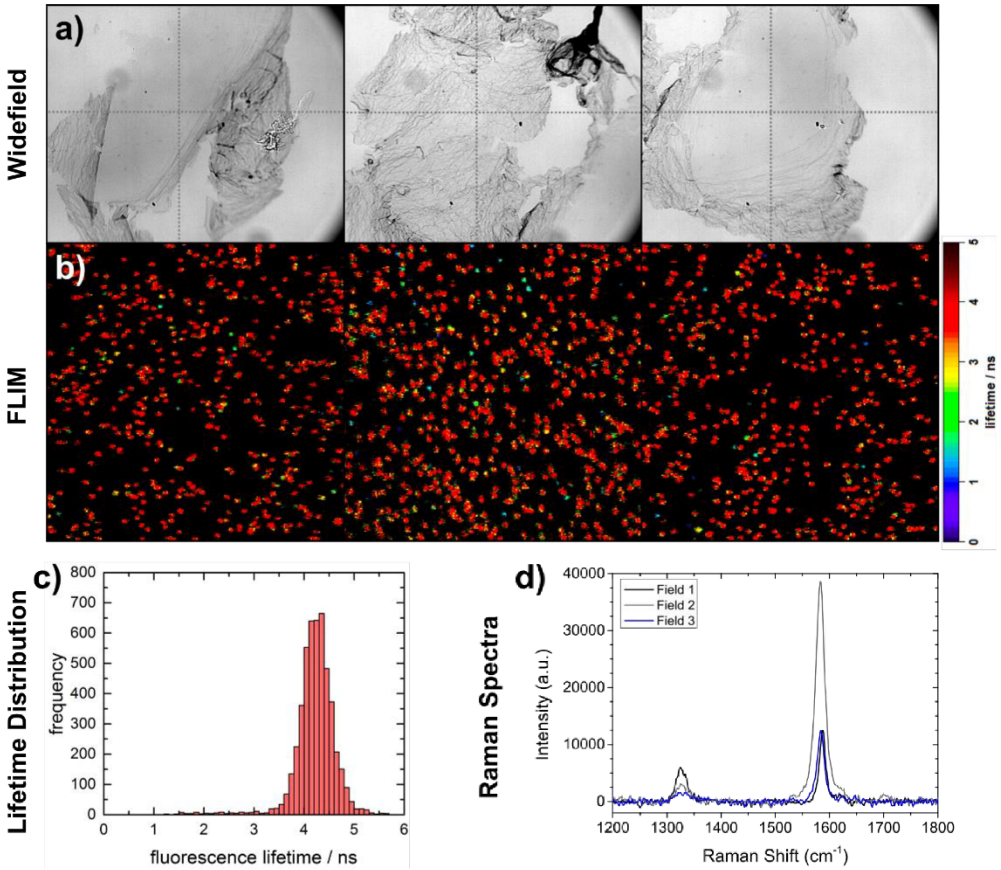

Figure S16. *A'2* Characterization (Strategy No9). a) Similar to strategy 1, washing with acetone only twice before incubation in acetone for 12 hours followed by acetone vapor exposition and nitrogen drying destroys the single-layer graphene and partially removes it from the coverslips. b) and c) All areas measured with FL microscopy reveal no quenching and show homogeneously distributed DNA origami structures. The mean fluorescence lifetime is about 4.3 ns. d) Raman spectroscopy reveals single-and multi-layered graphene with different D:G ratios in areas where it is not removed from the glass, yet (panel d). The measurement positions are marked in the widefield images.*

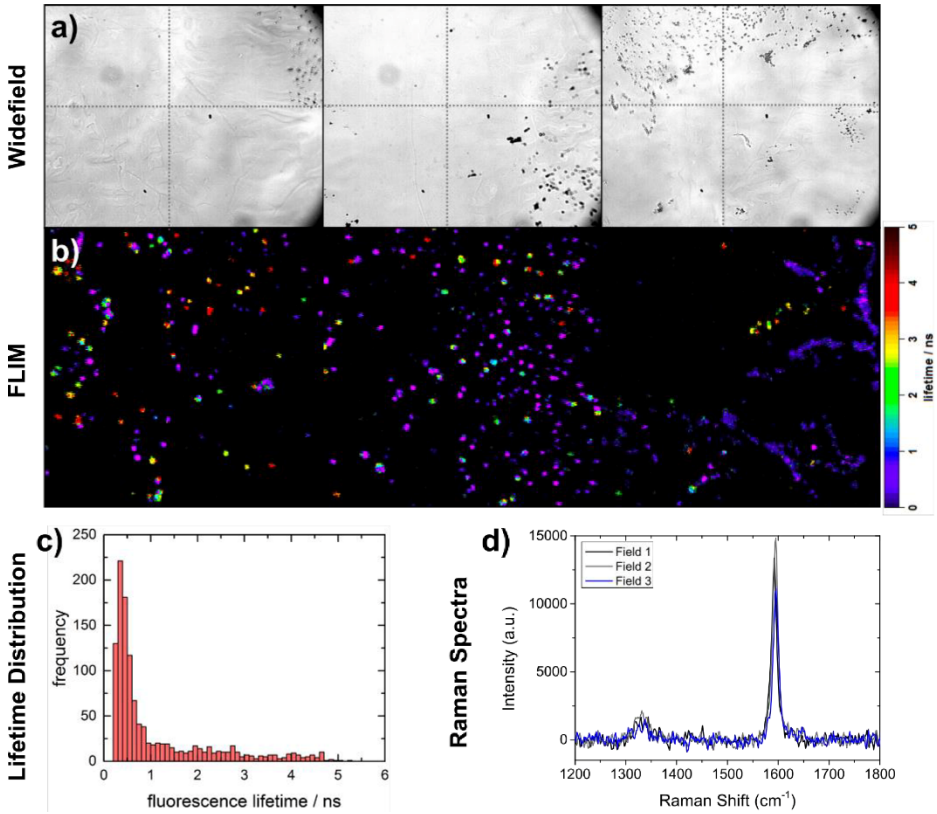

Figure S17. *R Characterization (Strategy No10). Reversing the graphene transfer method allows us to successfully transfer graphene on glass with a PMMA layered cushion in between. While no scratches are observed in widefield, PMMA/graphene forms an unequally thick, layer with crinkles and impurities. b) and c) Deposition of ATTO647N-labeled DNA origami structures on graphene is questionable since the observed fluorescence lifetimes derived from FLIM microscopy are shorter than 1 ns. Impurities within the remaining PMMA layer might be an explanation for the fluorescence spots observed within the FLIM images. d) Nevertheless, Raman spectroscopy reveals homogeneous single-layered graphene with different D:G ratios. The measurement positions are marked in the widefield images.*

5. Correlative microscopy: Light microscopy, FLIM and AFM data

Light microscopy is frequently used for visual inspection of graphene. This straight-forward, fast and nondestructive method can also reveal the number of graphene layers or wrinkles, holes, and cracks in the graphene sheet.[18, 19] Si_3N_4, or Al_2O_3 are commonly used as substrate which ensures high contrast between the areas of the substrate with and without graphene. For glass coverslips, as they are used in fluorescence microscopy, the contrast is significantly lower. Therefore, optical microscopy can be used for a rough evaluation of the transfer, but not for a detailed analysis of the quality of graphene. Scanning probe microscopy such as AFM[20-22] allows for nanoscopic access to the graphene surface quality without consuming the investigated graphene samples. Especially, residuals and wrinkles can easily be detected. This is illustrated in Figure S18 showing light microscopy, FLIM and AFM images from an intact graphene area (sample 1) and a partially destroyed graphene area (sample 2). Both sample areas are found on the same gridded glass coverslip. Surprisingly, the grid structure increases the probability of graphene rupture. The area of observation is recognized by using gridded glass coverslips with a grid repeat distance of 50 µm (Gridded Glass Coverslips Grid-50, ibidi). Light microscopy images and AFM images are overlapped by wrinkles and impurities visible in both image

types. In contrast, FLIM and light microscope images are correlated by means of an optical grid. Final overlap of the AMF and FLIM images is achieved by correlating unquenched spots from the FLIM image to impurities in the AFM image as indicated by the red triangles in Figure S18d and h. From these overlapping points it is already obvious that a correlation between inefficient quenching and residuals on the graphene surface exists to a certain extend. Nonetheless, this correlation is not always present as can be seen from the spots marked by green triangles showing a reduced fluorescence lifetime despite surface impurities in the AFM image.

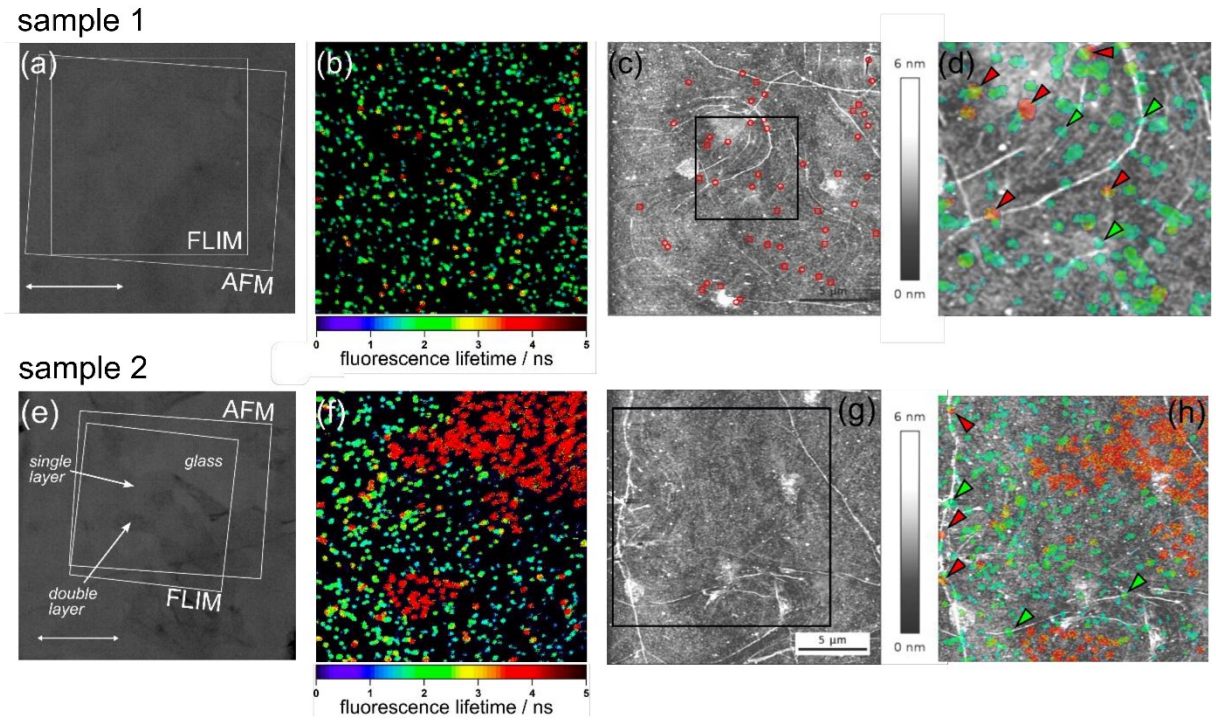

Figure S18: *a) Light microscopy image of a graphene sample (scale bar equals 15 µm). b) FLIM image of the area marked in a). c) AFM image of the area marked in a). Red circles indicate defects which can be associated with unquenched fluorescent molecules in b). Red squares mark positions of unquenched fluorescence molecules from a) which cannot be associated with any defects in the AFM image. The black frame marks the zoomed in area shown in d). d) Overlay of AFM and FLIM image. Red arrows indicate unquenched fluorescent spots which can be associated with impurities measured via AFM. Green arrows indicate fluorescent spots which show quenching despite underlying impurities visible in the AFM image. e) Light microscopy image of a graphene sample (scale bar equals 15 µm). Removed graphene (glass), single layer and double layer graphene can be identified. f) FLIM of the area marked in e). g) AFM image of the area marked in e). The black frame marks the zoomed in area shown in h). h) Overlay of AFM and FLIM image. Red arrows indicate unquenched fluorescent spots which can be associated with impurities measured via AFM. Green arrows indicate fluorescent spots which show quenching despite underlying impurities visible in the AFM image.*

6. I_D/I_G ratio versus fluorescence lifetime for the data set in Figure 3e

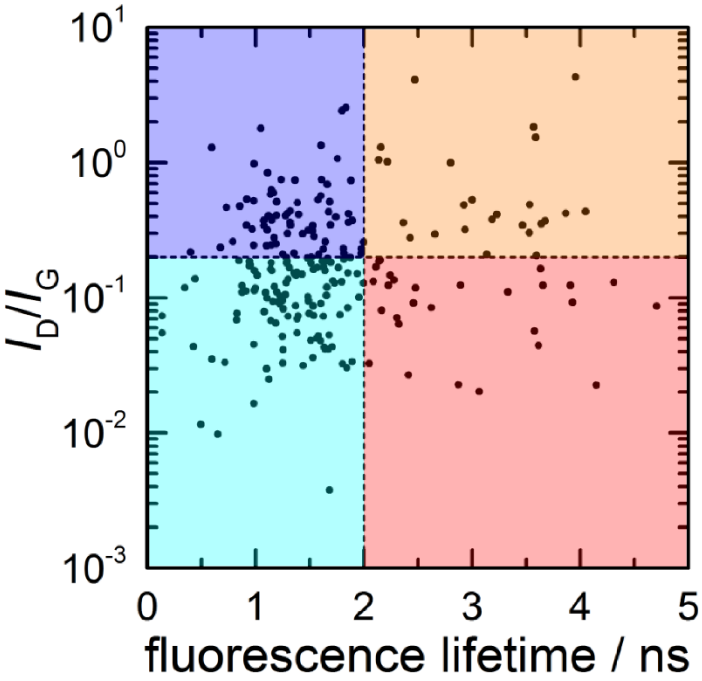

Figure S19: *Ratio of the peak intensities of D and G peak within single Raman spectra compared to the fluorescence lifetime measured at the same position. The color code marks the sections for which the four fluorescence lifetime histograms in Figure 3b) and Raman spectra in Figure 3c) are representative.*

7. Quick quality estimation procedure

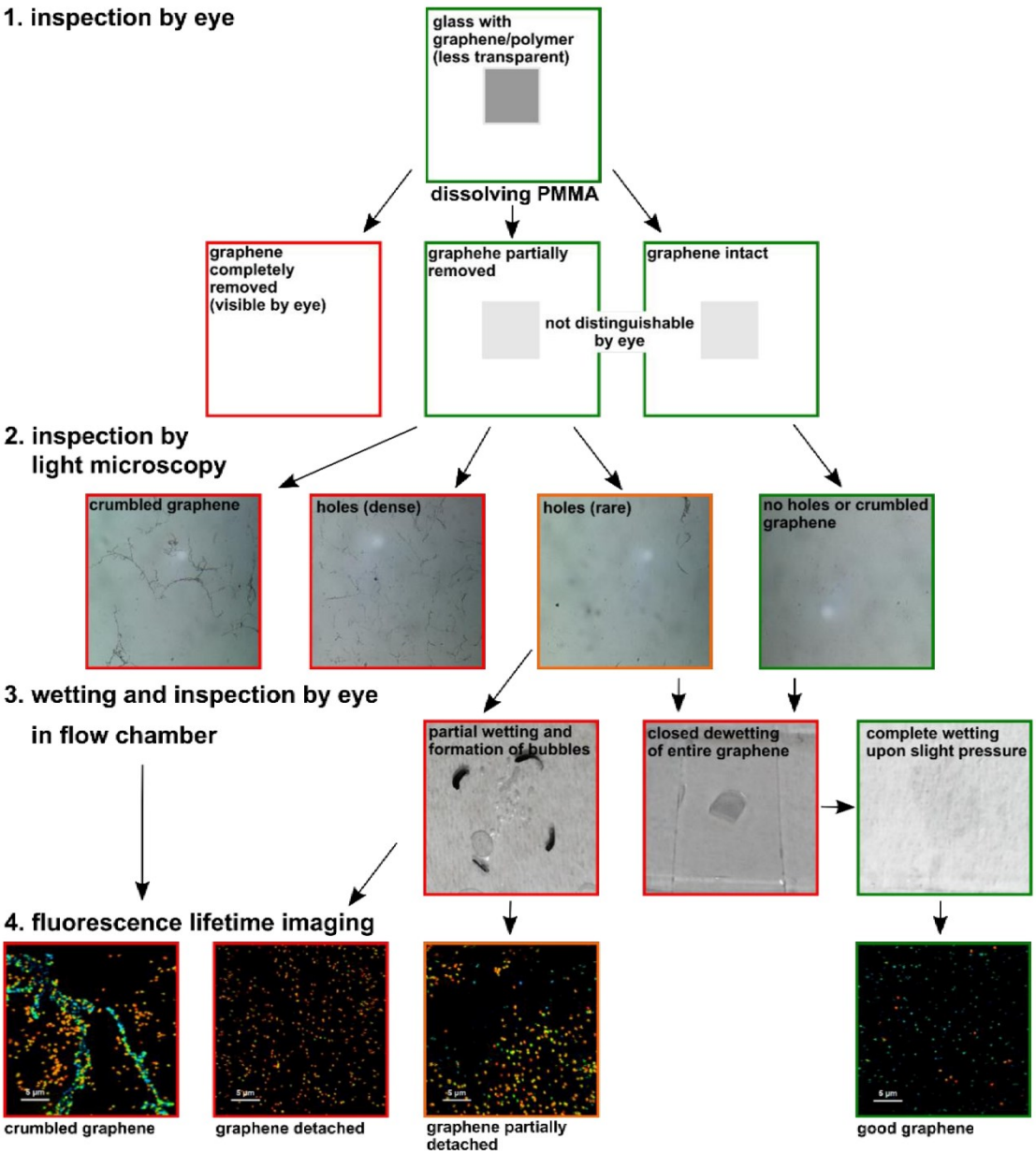

Figure S20: *Summary of procedures for a quick estimation of transferred graphene quality including example light microscopy images, standard camera images and FLIM images. The inspection starts after the removal of the protective (PMMA) layer. The Presence of graphene can be seen by eye due to the absorption (2.3 %). The quality of the graphene can be estimated in a second step via light microscopy which allows the discrimination between closed, intact graphene layer and holes or crumbled graphene. In case of rare holes (which are difficult to spot) the sample might still be useful. Care should be taken upon the formation of small bubbles during the wetting process in a flow chamber. This means in most cases detachment of the graphene from glass due to surface tension. Reduced wettability of graphene in comparison to glass, however, is usual and should lead to dewetting of graphene in a flow chamber as well as on a normal glass substrate which can also serve as an indicator for the quality of graphene. A final conclusion on the quenching properties of the transferred graphene can, however, only be drawn through fluorescence lifetime imaging. For the presented graphene transfer and cleaning procedure about nine out of ten samples showed the desired fluorescence quenching properties.*

8. DNA sequences

Table S1. Unmodified staples from the 5’ to the 3’ end for the pillar-shaped DNA origami structure.

Sequence (5’ to 3’)	Length [nt]
CTAGTCAGTTGGCAAATCAACAGTCTTTAGGTAGATAACAAA	42
CCTCATCACCCCAGCAGGCCTCTTCGCTATTACGCCAGTGCC	42
TAAGTTGGCATGATTAAAGAA	21
CAAACGGAATAGGAAACCGAGGAATAAGAAATTACAAG	38
ACCGCCACCCTCAGAACCCGTACTCTAGGGA	31
AATTTCTTAAACCCGCTTAATTGTATCGTTGCGGGCGATATA	42
GCGAATCAGTGAGGCCACCGAGTAGTAGCAACTGAGAGTTGA	42
GAATTCGTCTCGTCGCTGGGTCTGCAATCCATTGCAACACGG	42
CCCGGTTGATAAAGCATGTCAATC	24
TCACAGCGTACTCCGTGGTGAAGGGATAGCTAAGAGACGAGG	42
GGCAACACCAGGGTCTAATGAGTGAGCTCACAACAATAGGGT	42
AATAGAAAAAAATAAACGTCTGAGAGGAATATAAGAGCAACACTATGAT	49
TAGCCCGGAATAGGTGTAAGGATAAGTGCCGTCGA	35
AATAAAACGAACTATGACCCCACCAAGC	28
TGCTAAATCGGGGAGCCCCCGATTTAGAGCTAGCAGAACATT	42
AAGAAAGCGCTGAACCTCAAATATTCTAAAGGAAAGCGTTCA	42
AAATGCGGAAACATCGGTTTTCAGGTTTAACGTCAGATTAAC	42
CACGGCAACAATCCTGATATACTT	24
CGAGGGTACTTTTTCATGAACGGGGTCATAATGCCGAGCCACCACC	46
TATTTAAATTGCAGGAAGATTG	22
TTCGGTCCCATCGCATAGTTGCGCCGACATGCTTTCGAGGTG	42
TAACGACATTTTTACCAGCGCCAAAGAAAGTTACCAGAACCCAAA	45
CAAATTATTCATTTCAATTACCTGAGTA	28
GCTGTAGTTAGAGCTTAATTG	21
GAGTTAAAAGGGTAATTGAGCGCTAATATCAGAGGAACTGAACACC	46
TTAGTTTGAGTGCCCGAGAAATAAAGAAATTGCGTAGAGATA	42
GAACCGCCACCCTCCATATCATACC	25
TGCTGATTGCCGTTGTCATAAACATCGGGCGG	32
TAGCCAGCTTTCATCCAAAAATAAACGT	28
TAAAGCCTCCAGTACCTCATAGTTAGCG	28

Sequence (5’ to 3’)	Length [nt]
AGAATTTTAGAGGAAAACAATATTACCGCCAGCTGCTCATTT	42
CTCATCGGGATTGAGTGAGCGAGTAACAACCCGTC	35
GGGATATTGACGTAGCAATAGCTAAGATAGC	31
AATTGTGTCGAAATCCGCGGCACACAACGGAGATTTGTATCA	42
CCTCGTTTACCAGAAACCAAA	21
ACCAACAAACCAAAATTAACAATTTCATTTGAATTACCGAGG	42
CTGGCATTAGGAGAATAAAATGAAGAAACGATTTTTTGAGTA	42
ACCTGACGGGGAAAGCCGGCGAACCAAGTGTCTGCGCGTTGC	42
AACCGTGTCATTGCAACGGTAATATATTTTAAATGAAAGGGT	42
GAACTGGCTCATTACAACTTTAATCATTCTTGAGATTACTTA	42
AGAAATCGTTAGACTACCTTTTTAAGGCGTTCTGACCTTTTTGCA	45
CAAAATCACCGGAACCAGAGCCAGATTTTGTCACAATCACAC	42
TGCGTGTTCAGGTTGTGTACATCG	24
GAGGCCAAGCTTTGAATACCAAGTACGGATTACCTTTTCAAA	42
TAATATCAAAGGCACCGCTTCTGGCACT	28
GGCGAAGCACCGTAATAACGCCAGGGTTTTCCCAGTCATGGG	42
TATGACTTTATACATTTTTTTTTAATGGAAACAGTACACCGT	42
TTGGGCGGCTGATTTCGGCAAAATCCCT	28
CCTCGTCTTTCCACCACCGGAACCGCCTCCCTCA	34
CGTACAGGCCCCCTAACCGTCCCCGGGTACCGAGCGTTC	39
CCTAATTTAACAAACCCTCAATCAATATCTGATTCGCTAATC	42
ATTACGAGATAAATGCCAGCTTTGAGGGGACGACGACAG	39
CAGCAGCGCCGCTTGTTTATCAGCTTCACGAAAAA	35
AATATTCATTGAATCCATGCTGGATAGCGTCCAAT	35
GAGTCTGGATTTGTTATAATTACTACATACACCAC	35
AGTTTCCAACATTATTACATTATAC	25
TTGCGAATAATATTTACAGCGGAGTGAGGTAAAATTTTGAGG	42
GTCGCAGAAAAACTTAAATTTGCC	24
GCTGGCATAGCCACATTATTC	21
AGTCGCCTGATACTTGCATAACAGAATACGTGGCACAGCTGA	42
AATATCGTTAAGAGAGCAAAGCGGATTGTGAAAAATCAGGTCTTT	45
AATACCCCAACATTCATCAAAAATAATTCGCGTCT	35
AGGACAGATGAACGGTGTAACATAAGGGAACCGAAGAAT	39

Sequence (5’ to 3’)	Length [nt]
ACGTAAGAATTCGTTCTTAGAAGAACTCAAACTATCGGATAA	42
GCGAAACAAAGTGTAAAACACATGGCCTCGATTGAACCA	39
ATTGCGTTGCTGTTATCCGCTCACAATTCCAAACTCACTTGCGTA	45
CAAGCCGCCCAATAGCAAGTAAACAGCCATATTATTTTGCCATAAC	46
GCCCGAGTACGAGCCGGAAGC	21
AAAGATTACAGAACGGGAGAAGGAAACGTCACCAATGAAACCA	43
TAAAACCGTTAAAGAGTCTGTCCATCCAGAAACCACACAATC	42
CAAAGCACTAGATAGCTCCATTCAGGCTGCGCAACTGTCTTG	42
AAGGCCTGTTTAGTATCATGTTAGCTACCTC	31
TATTGAAAGGAATTGAGGTAG	21
TTTAGATTCACCAGTCACACGACCGGCGCGTGCTTTCCCAGA	42
TAACATCCAATAAATGCAAAGGTGGCATCAACATTATGAAAG	42
TTAACTCGGAATTAGAGTAAATCAATATATGTGAGTGATTCT	42
TTTTCCAGCATCAGCGGGGCTAAAGAACCTCGTAGCACGCCA	42
CCGTAATCAGTAGCGACAGAATCTAATTATTCATTAAAAAGG	42
CTGTATGGGATTACCGTTAGTATCA	25
ACTAATGCCACTACGAATAAA	21
TTTTTGCGGATGCTCCTAAAATGTTTAGATGAATTTTGCAAAAGAAGTT	49
AGTACCGCATTCCACAACATGTTCAGCCTTAAGGTAAAGTAATTC	45
CTTACGGAACAGTCAGGACGTTGGGAAGAAA	31
ACGCGAGAGAAGGCCATGTAATTTAGGCCAGGCTTAATTGAGAATCGC	48
AAGGCTCCAAAAGGAGCCTTTATATTTTTTCACGTGCTACAGTCACCCT	49
CCCCGCTAGGGCAACAGCTGGCGAAAGGGGGATGTGCTTATT	42
CCTGCGCTGGGTGGCGAGAAAGGAAGGGAAGGAGCGGGGCCG	42
TGAGTAAAGGATAAGTTTAGCTATATCATAGACCATTAGATA	42
TGAGCAAATTTATACAGGAATAACATCACTTGCCTGAGTCTT	42
CCAATGTTTAAGTACGGTGTCCAAC	25
TGAAAATCCGGTCAATAACCTAAATTTTAGCCTTT	35
CCCAGCTACAATGACAGCATTTGAGGCAAGTTGAGAAATGAA	42
CGGAATAGAAAGGAATGCCTTGCTAAACAACTTTCAAC	38
TTATAAGGGTATGGAATAATTCATCAATATA	31
CCATAATGCCAGGCTATCAAGGCCGGAGACATCTA	35
CCGACTTGTTGCTAAAATTTATTTAGTTCGCGAGAGTCGTCTTTCCAGA	49

Sequence (5’ to 3’)	Length [nt]
ACGCGGTCCGTTTTTGGGTAAGTGA	25
AGCTCTTACCGAAGCCCAATA	21
AGTTTATTGTCCATATAACAGTTGATTC	28
TTACCATTAGCAAGGCCTTGAATTAGAGCCAGCCCGACTTGAGC	44
GGCGCAGACGGTCAATCATCGAGACCTGCTCCATGTGGT	39
AAATCAGCTCATTTTTTAACCATTTTGTTAAAATTCGCATTA	42
AGGCTTGCGAGACTCCTCAAGAGAAAAGTATTCGGAAC	38
GAGAACAATATACAAAATCGCGCAGAGGCGATTCGACAAATCCTTTAAC	49
TTTAGCGATACCAACGCGTTA	21
AGGGAGCCGCCACGGGAACGGATAGGCGAAAGCATCAGCACTCTG	45
ACGAGCGGCGCGGTCAGGCAAGGCGATTAAGTTGGGTAAAAC	42
TCATACATTTAATACCGATAGCCCTAAAACATCGAACGTAAC	42
GTTAAAGGAAAGACAGCATCTGCCTATTTAAGAGGCAGGAGGTTTA	46
TAGCCTCAGAGCATACCCTGT	21
CATCGAGATAACGTCAAACATAAAAGAGCAAAAGAATT	38
GAGAAGGCATCTGCAATGGGATAGGTCAAAAC	32
TTGGTAGAACATTTAATTAAGCAAC	25
ATTTGGAAGTTTCATGCCTCAACATGTTTTA	31
AAATGACGCTAAATGGATTATTTACATTGGCGAATACCTGGA	42
TTCGGGGTTTCTGCCAGGCCTGTGACGATCC	31
AAACTCACAGGAACGGTACGCCAGTAAAGGGGGTGAGGAACC	42
GAGCATTTATCCTGAATCAAACGTGACTCCT	31
AGTAGGTATATGCGTTATACA	21
GACAATTACGCAGAGGCATTTTCGAG	26
ACTAAAGAGCAACGTGAAAATCTCCACCCACAACTAAAGGAA	42
ACATAAGTAGAAAAATCAAGAAGCAAAAGAAGATGTCAT	39
ATTTCAACCAAAAATTCTACTAATAGTTAGTTTCATTTGGGGCGCGAGC	49
TAAGTTTACACTGAGTTTCGT	21
TTTCCATGGCACCAACCTACGTCATACA	28
GTAATTAATTTAGAATCTGGGAAGGGCGATCGGTGCGGCAAA	42
ACCAGACCGGATTAATTCGAGC	22
ATAGCGAGAGGCTATCATAACCAAATCCCAAAGAAAATTTCATCCTCAT	49
AGAACTTAGCCTAATTATCCCAAGCCCCCTTATTAGCGTTTGCCA	45

Sequence (5’ to 3’)	Length [nt]
GGCTAAAACTTCAGAAAAGTTTTGCGGGAGATAGAACC	38
TGACCGCGCCTTAATTTACAATATTTTTGAATGGCTATCACA	42
CATTTCGCAAATGTCATCTGCGAACGAGAGATTCACAATGCC	42
CAAGCCCAATAGGAACCACCCTCACCCGGAA	31
GGAACCATACAGGCAAGGCAAATCAAAAAGACGTAGTAGCAT	42
AACAAGAGCCTAATGCAGAACGCGC	25
CGCGCTACAGAGTAATAAAAGGGACATTCTGATAGAACTTAG	42
CGTGTCAAATCACCATCTAGGTAATAGATTT	31
ATTGTTATCTGAGAAGAAACCAGGCAAAGCGCCATTCGTAGA	42
TGGCTTTTTACCGTAGAATGGAAAGCG	27
TCGTGCCGGAGTCAATAGTGAATTTGCAGAT	31
ATCGATGCTGAGAGTCTACAAGGAGAGGGAACGCCAAAAGGA	42
ATGAAGGGTAAAGTTCACGGTGCGGCCATGCCGGTCGCCATG	42
TTAGCCCTGACGAGAAACACCAGAAATTGGGGTGAATTATTTTAA	45
CCGTGTGATAAATAACCTCCGGCTGATG	28
TATCAGCAACCGCAAGAATGCCAATGAGCCTGAGGATCTATC	42
TATTACGAATAATAAACAAATCAGATATGCGT	32
GTAAAACGACGGCCCATCACCCAAATCAGCGC	32
CATTTGAGATAACCCACGAAACAATG	26
CTAAATCGGTCAGAATTAGCAAAATTAAGCAATAAAATAATA	42
ATTTCCTGATTATCAGATGATGGCTTTAAAAAGACGCTAAAA	42
CCAGCCTCCGATCCTCATGCCGGA	24
ATCGGTCAGATGATATTCACAAACCAAAAGA	31
CGAACACCAAATAAAATAGCAGCCAAGTTTGCCTTTAGCGTCAGA	45
ACAACGCCTGTAGCATTTACCGTATAGGAAG	31
AGCTTTCAGAGGTGGCGATGGCCAGCGGGAAT	32
TTTACCAGTCCCGGCCTGCAGCCCACTACGGGCGCACCAGCT	42
GTCGCGTGCCTTCGAATTGTCAAAG	25
AAGAAAGCTTGATACCGCCACGCATACAGACCAGGCGCTGAC	42
AAGACAAATCAGCTGCTCATTCAGTCTGACCA	32
AGCAACAAAGTCAGAAATAATATCCAATAATCGGCTCAGGGA	42
ATAAAGTCTTTCCTTATCACT	21
GAAGGAGCGGAATTATCATCATATATCATTTACATAGCACAA	42

Sequence (5’ to 3’)	Length [nt]
CTGAATATAGAACCAAATTATTTGCACGTAAAACAACGT	39
CGTACTATGGTAACCACTAGTCTTTAATGCGCGAACTGAATC	42
TGAGTGTTCCGAAAGCCCTTCACCGCCTAGGCGGTATTA	39
GCGAAAATCCCGTAAAAAAAGCCGTGGTGCTCATACCGGCGTCCG	45
AACAACAGGAAGCACGTCCTTGCTGGTAATATCCAGAAACGC	42
CGCGCCGCCACCAGAACAGAGCCATAAAGGTGGAA	35
TTCATCGGCATTTTCGGTCATATCAAAA	28
TGCAGCAAATCGGCCAACGCGCGGGGAGGGCCCTGAGAGAGT	42
GCCAGCAGTTGGGCGCAAATCAGGTTTCTTGCCCTGCGTGGT	42
GAGAGATAGACTTTACGGCATCAGA	25
TGCCATCCCACGCAGGCAGTTCCTCATTGCCGTTTTAAACGA	42
ACATAAAGCCCTTACACTGGTCGGGTTAAATTTGT	35
GCTGGTCTGGTCAGGAGCCGGAATCCGCCGTGAACAGTGCCA	42
TACGGCTGGAGGTGCGCACTCGTCACTGTTTGCTCCCGGCAA	42
CTTGTAGAACGTCAGCGGCTGATTGCAGAGTTTTTCGACGTT	42
AGACAGCAGAAACGAAAGAGGAAATAAATCGAGGTGACAGTTAAAT	46
AAGGGATATTCATTACCGTAATCTATAGGCT	31
ACGGGCCGATAATCCTGAGAAGTGTTTTTATGGAGCTAACCG	42

Table S2. Modified and extended staples from the 5’ to the 3’ end for the pillar-shaped DNA origamistructure.

Sequence (5’ to 3’)	Length [nt]	Function
ATATTTCCTCTACCACCTACATCACTAATTAGCGGGGTTTTGCTCAGTACCAGGCTGACAACAAGCTG	68	Extern labeling of pyrene
ATATTTCCTCTACCACCTACATCACTAAGAAAACGAGAATGACCATAAATCTACGCCCCTCAAATGCTTTA	71	Extern labeling of pyrene
ATATTTCCTCTACCACCTACATCACTAATAACTATATGTAAATGCTTAGGATATAAT	57	Extern labeling of pyrene
ATATTTCCTCTACCACCTACATCACTAGCATGTAGAAACCAATCCATCCTAGTCCTG	57	Extern labeling of pyrene
ATATTTCCTCTACCACCTACATCACTATGCCCGTATAAACAGTGTGCCTTCTGGTAA	57	Extern labeling of pyrene
ATATTTCCTCTACCACCTACATCACTAAGGAATCATTACCGCGTTTTTATAAGTACC	57	Extern labeling of pyrene

Sequence (5’ to 3’)	Length [nt]	Function
ATATTTCCTCTACCACCTACATCACTAGATTAGAGAGTA CCTTAACTCCAACAGG	54	Extern labeling of pyrene
ATATTTCCTCTACCACCTACATCACTACCTTAAATCAAGA TTAGCGGGAGGCTCAAC	57	Extern labeling of pyrene
GTGATGTAGGTGGTAGAGGAAATAT-**pyrene**	25	Pyrene at 3’
AATATGCAACTACCATCATAGACCGGAACCGC- **ATTO647N**	32	Dye at 3’

Table S3. Unmodified staples from the 5’ to the 3’ end for the L-shaped DNA origami structure.

Sequence (5’ to 3’)	Length [nt]
ACAAGAAATAGGAATCCCAATAGCAAGCAAATATAGCAGCATCCTGAA	48
CTGCGCGGCTAACTCACAATTCCACACAACATACGAGTACCGGGGCTCTGTGGGTGTTCAG	61
TTTTGATTAAGACGCTGAGA	20
CACAGACATTTCAGGGATCTCCAAAAAAAAGGTTCTTAAAGCCGCTTT	48
CAGTACCATTAGTACCCAGTGCCCGTATAAATTGATGAATTAAAG	45
TACAGGCATTAAATTAACCAATAGGAACGCCATCAAAGTCAATCAGAATTAGCCTAAATCG	61
TTTTGTTTCGTCACCAGTACTGTACCGTAAT	31
CCGTGCATCTGCCAGTTTTT	20
TGCTCATTCTTATGCGTTAATAAAACGAACTATATTCATTGGCTTTTG	48
AAACGGGGTTTTGCTACATAACGCCAAAAAAGGCTTGTAATCTTG	45
TAGTCAGAAGCAAAGCGGATTTT	23
TTTTTTGCATCAAAAGCCTGAGTAATTTT	29
GCGAGAAAAGGGATGACGAGCACGTATAACGTGCTTTTCACGCTGAAGAAAGC	53
CCGGCAAATCGGCGAAGTGGTGAAGGGATAG	31
TCGATAGCAGCACCGTAAAATCACGTTTTGCT	32
AAACGGCGCAAGCTTTGAAGGGCGATCGGTGC	32
GAGGGTAGTTGCAGGGTGCTAAACAACTTTCACGCCTGGAAAGAG	45
ATAAACAATCCCTTAGTGAATTTATCAAAAT	31
TTTTGCTAATATCAGAGAGATAACCCCGCCACCGCG	36
ATACGCAAAGAAAATTATTCATTAAAGGTGAATTTT	36
TTGAGAAGCCACCCTCAGAACCG	24
GGAATTAGGTAAATTTTCGGTCATAGCCCCACCGGAACCACCACC	45
AGCGAACCAGAAGCCTGGAGAATCACAAAGGCTATCAGGT	40
AACGTCAATAGACGGGGAATACCCAAAAGAACAAGACTCCGTTTTTAT	48

Sequence (5’ to 3’)	Length [nt]
CGTTGAAAATAGCAAGCCCAATA	23
ATGGCTACAATCAACTGAGAGCCAGCAGCAAATGAAAAACGAACCTAATGCGCTTGGCAGA	61
CTGAGGCCAACGGCTACAGAGGTTTCCATT	30
CCCTGAACAAATAAGAAACGCGAGGCGTT	29
ACAAGAACCGAACTGATGTTACTTAGCCGGAAAAGACAGCACTACGAA	48
CGGAATCTCAGGTCTGTTTTAAATATGCATGCGAACGAATCATTG	45
TCTTTAGGCTGAATAATGCTCATTAGTAACAT	32
TTAGAGCTATCCTGAGGCTGGTTTCAGGGCGC	32
TTATACTTAGCACTAAAAAGTTTGTGCCGCCA	32
TTTCATCGAATAATATCCAGCTACAATACTCCAGCAATTTCTTTACAG	48
CCGAGTAAGCCAACAGGGGTACCGCATTGCAA	32
ATAAAAATATCGCGTTCTCCTTTTGATAAGAGCTATAT	38
ATTCATATCAGTGATTTGGCATCAGGACGTTGTAACATAAACCAGACG	48
TAATAAGAAGAGCCACCCTTATTAGCGTTTGCCATTCAACAATAGAAA	48
TAAAGTTTAGAACCGCTAATTGTATCGCGGGGTTTAAGTTTGGCCTTG	48
GGGGCGCGCCCAATTCACTAAAGTACGGTGTCACGAGAATAGCTTCAA	48
CCTCAGAGCACAAGAAGAAAAGTAAGCAG	29
ACATTCTGAAGAGTCTCCGCCAGCAGCTCGAA	32
ATGAGTGACCTGTGCAGTTTCTGCCAGCACG	31
CTTTTGCGTTATTTCAATGATATTCAACCGTT	32
AATTACATAGATTTTCAATAACGGATTCGCC	31
CACATCCTCAGCGGTGGTATGAGCCGGGTCAC	32
CCAGAATGGAGCCGCCAATCAAGTTTGCC	29
ATATTCACCGCCAGCATTGACAGGCAAAATCA	32
CGGGAAACGAAAAACCTGATGGTGGTTCCGAA	32
CCACCCTCTGTTAGGAAGGATCGTCTTTCCAGCAGACGATTATCAGCT	48
TGCGAATAATAATCGACAATGTTCGGTCG	29
CCATTACCAAGGGCGACATCTTTTCATAGGCAGAAAGAATAGGTTGAG	48
TTTTACCGTTCCAGTAAGCGTCATACATGGCTTCAGTTAAT	41
TTCACCAGGTAGCAATGGCCTTGCTGGTAAT	31
AAAGACAAATTAGCAAGTCACCAATGAAACCA	32
CAAATCGTCAGCGTGGTGCCATCCCACGCAA	31
CAATTCATATAGATAATAAATCCTTTGCCCG	31

Sequence (5’ to 3’)	Length [nt]
CCTGCAGCCATAACGGGGTGTCCAGCATCAGC	32
AGTTGATTAGCTGAAAAGAGTACCTTTAATTGTTAATTCGGACCATAA	48
ACGCCAGATGACGGGGCGCCGCTAGCCCCAGC	32
TAATAGTATTCTCCGTGCATTAAATTTTTGTT	32
TTAGTTTGCCTGTTTAGGTCATTTTTGCGGATAGGAAGCCGACTATTA	48
GAAAGGAGCGGGCGCTAGGTTTT	23
TTTTCCATATTATTTATCCCAATCCAAAGTCAGAGA	36
TTTTGGAATTTGTGAGAGAT	20
CATTATACGGTTTACCCATAACCCTCGAAATACAATGTTTAAACAGGG	48
GCCTAATTATCATATGATAAGAGATTTAGTTAATTTCAT	39
GGAGGGAAGAGCCAGCAATCAGTAGCGACAGACCAGAACCGCCTC	45
ATTATAGCGTCGTAATAGTAAAATGTTTTTT	31
GAAACAACGCGGTCGCCGCACAGGCGGCCTTTAGTGACTTTCTCCACGTACAGACGCCAGG	61
CGCTGGCACCACGGGAGACGCAGAAACAGCGG	32
AAGCGCATAAATGAAACAGATATAGAAGGCTTAGCAAGCCTTATTACG	48
AAATTATTTGGAAACAGCCATTCGAAAATCGC	32
TTAATTAAACCATACATACATAAAGGTGGCAATTTT	36
TTTTCTTTACAAACAATTCG	20
TTTTCCCTCAGAGCCACCACCCTCAGAAAGCGCTTA	36
TCATCAACAAGGCAAATATGTACCCCGGTTG	31
CAGTTGTTTATTTTGCGAAGCCCTTTTTAATTGAGTTCTGAACA	45
ATATATATAAAGCGACGACATCGGCTGTCTTTCCTTATCATTTTT	45
TTTTATTGGGCTTGAGATGGCCAGAACGATT	31
CCGTCGGAGTAGCATTCAAAAACAGGAAGATT	32
CAGATGAATATACAGTTTTT	20
TTCAAATTTTTAGAAAAAACAGGAGCAAACAAGAGAATCGATGAAGGGTGAGATATTTTA	60
TTTTTTAATGCACGTACAAGTTACCCATTCAG	32
GTAGAATAGTTGAAACTTTCGCAAACACCGC	32
ATAACCTTATCAACAAAAATTGTATAACCTCC	32
TACCGATAGTTGCGCTTTTTCA	22
TTTTTGCCTGAGTAGAAGAA	20
CACTCATGAAACCACCTTAAATCAAGATTGAGCGTCTTTTTGTTT	45
ACCCTCATGCCCTCATTTTCTGTATGGGATTTAGTTAAAGCAGCTTGA	48

Sequence (5’ to 3’)	Length [nt]
GACAGATGGACCTTCATCAAGAGCCCTGAC	30
GCCGTCACAATATAAAAGAAACCACCAGAAGGAGCGGACTCGTATTACATTTGTCAAATAT	61
CAAAAGAATAAAATACCCAGCGATTATACCAAGCGCGAA	39
GAGCCGATATAACAACAACCATCGCCCTTTTTTT	34
CAACTAATGCAGACAGAGGGGCAATACTG	29
GCCGATTAAGGAAGGGCGCGTAACCACCACA	31
GCCAGTGCGATTGACCCACCGCTTCTGGTGCC	32
TGCTTTCGAGGTGAATCTCCAAAA	24
TTTTGGCGCATAGGCTGGCTAACGGTGTTAAATTGT	36
GGAGCCTTCACCCTCAGAGCCACC	24
TGGAGCCGGCCTCCGGGTACATCGACATAAAA	32
TGCGGGATAGCAGCGACGAGGCGCAGAGAAACGGCCGCGGTAACGATC	48
CCCCCTGCGCCCGCTTTAGCTGTTTCCTGTGT	32
TTAATTTCATGTTCTATAACTATATGTAAATGCTGATGTCAATAGAATCCTTGACAAAATT	61
CAAAGGGCCTGTCGTGTGGCCCTGAGAGAGTT	32
TGTAGCTCAACATTTACCCTCGAAAGAC	28
TTTGCGTATTGGGCGCTTTT	20
CTGATAGCCCTAAAACTTTT	20
TTTTTTTTTTTTAAAACTAG	20
GCCTGTTTGCTTCTGTTACCTTTTAACGTTAA	32
TTTTCGCAAATGGTCAATAAACCATTAGATGC	32
GGCACCAAAACCAAAAGTAAGAGCAACACTATAGCAACGTAAATCGCC	48
AACCGTTTCACACGGGAAATACCTACATTTTGACGCTAAACTATCACTTCTTTAACAGGAG	61
TTCTGAAACATGAAAGTGCCGGCCATTTG	29
AGCATGTACGAGAACAATCCGGTATTCTAAGAACGATTTTCCAGA	45
GTCGAAATCCGCGACCTGCTCCACCAACTTTTAGCATTC	39
ATTGCTTTAACAACATTTCAATTACCTGAGCAAAAGGGAGAAACAGGTTTAAGATGATGG	61
TAGTTGCCAGTTGCGGGAGGTTTTGAAGATCAATAA	36
TGAATTACCAGTGAATGGAATTACGAGGCATATAGCGAGAGAATCCCC	48
GCCCCCTGGTGTATCACCGTACTC	24
ATCAAAAAGTCATAAAACGGAACAACATTATCAACTTTAGTAGAT	45
AAATCAACACGTGGCATCAGTATTCTCAATCC	32
CAAACCCTTTAGTCTTACCAGCAGAAGATAA	31

Sequence (5’ to 3’)	Length [nt]
GTCCACTAAACGCGCGGACGGGCAACAGCTG	31
CCGGAACCGCAAGAAAGCAATAGCTATCTTACTCACAATCCGATTGAG	48
CCAACATGACGCTCAATGCCGGAGGAAATACC	32
AGAGCCGCAAACAAATGAGACTCCTCAAGAGATTAGCGGGCAGTAGCA	48
GGAACCCAAAACTACAAACAGTTTCAGCG	29
AAGGGAACCGGATATTCACTCATCTTTGACCCGTAATGCCATCGGAAC	48
TTTTCGGGCCGTTTTCACGG	20
GCCAGTACGTTATAAGGCGTTAAATAAGAATAAACACAAAT	41
AATAAGTTAGCAAAAACGCAATAATAACGAGAATTAAAAGCCCAA	45
ACAAAGTATGAGGAAGCTTTGAGGACTAAAGATTTT	36
TGTACTGGTAATAAGTTCAGTGCC	24
AGAACGTTAACGGCGTAATGGGTAAAGGTTTCTTTGCGTCGGTGGTGCTGGTCTTGCCGTT	61
TTTTCATCGGCATATTGACGGCACCACGG	29
TCTTACCATAAAGCCATAATTTAGAATGGTTTAGGGTAGC	40
TCAGCAGCAACCGCAATTTT	20
AGGAAACCGAGGACGTAGAAAAAGTACCG	29
GTTGTACCACCCTCATAAAGGCCGGAGACAG	31
TACCAGTAACGCTAACAGTTGCTATTTTGCACCCCATCCT	40
GTTTTCCCGTAGATGGCAGGAAGATCGCACT	31
TTTCGACTTGATCGAGAGGGTTGATATAAGTATTTT	36
CGCTCACTATCAGACGGTCCGTGAGCCTCCTC	32
GAGAAACATTTAATTTTACAGGTAGAAAG	29
CTCAAATGTTCAGAAATGGAAGTTTCACGCGCATTACTTCAACTGGCT	48
CTTAATTGAGACCGGAAACAGGTCAGGATTAGAGGTGGCA	40
AGAGCAAATCCTGTCCAGATACCGACAAAAGGTAATTTT	39
CGTTGGTAGTCACGACGCCAGCTGGCGAAAGGGGGATATCGGCCTGCGCATCGGCCAGCTT	61
AGGAGGTGGCGGATAAGTATTAAGAGGCTAAATCCTCTACAGGAG	45
ATCGGCCTTAAAGAATAAATCAAAAGAATAGCCCGAGACCAGTGAGGGAGAGGGGTGCCTA	61
ACAAGAAATAGGAATCCCAATAGCAAGCAAATATAGCAGCATCCTGAA	48
CTGCGCGGCTAACTCACAATTCCACACAACATACGAGTACCGGGGCTCTGTGGGTTTTCAG	61
TTTTGATTAAGACGCTGAGA	20
CACAGACATTTCAGGGATCTCCAAAAAAAAGGTTCTTAAAGCCGCTTT	48
CAGTACCATTAGTACCCAGTGCCCGTATAAATTGATGAATTAAAG	45

Sequence (5’ to 3’)	Length [nt]
TACAGGCATTAAATTAACCAATAGGAACGCCATCAAAGTCAATCAGAATTAGCCTAAATCG	61
TTTTGTTTCGTCACCAGTACTGTACCGTAAT	31
CCGTGCATCTGCCAGTTTTT	20
TGCTCATTCTTATGCGTTAATAAAACGAACTATATTCATTGGCTTTTG	48
AAACGGGGTTTTGCTACATAACGCCAAAAAAGGCTTGTAATCTTG	45
TAGTCAGAAGCAAAGCGGATTTT	23
TTTTTTGCATCAAAAGCCTGAGTAATTTT	29
GCGAGAAAAGGGATGACGAGCACGTATAACGTGCTTTTCACGCTGAAGAAAGC	53
CCGGCAAATCGGCGAAGTGGTGAAGGGATAG	31
TCGATAGCAGCACCGTAAAATCACGTTTTGCT	32
AAACGGCGCAAGCTTTGAAGGGCGATCGGTGC	32
GAGGGTAGTTGCAGGGTGCTAAACAACTTTCACGCCTGGAAAGAG	45
ATAAACAATCCCTTAGTGAATTTATCAAAAT	31
TTTTGCTAATATCAGAGAGATAACCCCGCCACCGCG	36
ATACGCAAAGAAAATTATTCATTAAAGGTGAATTTT	36
TTGAGTAAGCCACCCTCAGAACCG	24
GGAATTAGGTAAATTTTCGGTCATAGCCCCACCGGAACCACCACC	45
AGCGAACCAGAAGCCTGGAGAATCACAAAGGCTATCAGGT	40
AACGTCAATAGACGGGGAATACCCAAAAGAACAAGACTCCGTTTTTAT	48
CGTTGAAAATAGCAAGCCCAATA	23
ATGGCTACAATCAACTGAGAGCCAGCAGCAAATGAAAAACGAACCTAATGCGCTTGGCAGA	61
CTGAGGCCAACGGCTACAGAGGTTTCCATT	30
CCCTGAACAAATAAGAAACGCGAGGCGTT	29
ACAAGAACCGAACTGATGTTACTTAGCCGGAAAAGACAGCACTACGAA	48
CGGAATCTCAGGTCTGTTTTAAATATGCATGCGAACGAATCATTG	45
TCTTTAGGCTGAATAATGCTCATTAGTAACAT	32
TTAGAGCTATCCTGAGGCTGGTTTCAGGGCGC	32
TTATACTTAGCACTAAAAAGTTTGTGCCGCCA	32
TTTCATCGAATAATATCCAGCTACAATACTCCAGCAATTTCTTTACAG	48
CCGAGTAAGCCAACAGGGGTACCGCATTGCAA	32
ATAAAAATATCGCGTTCTCCTTTTGATAAGAGCTATAT	38
ATTCATATCAGTGATTTGGCATCAGGACGTTGTAACATAAACCAGACG	48
TAATAAGAAGAGCCACCCTTATTAGCGTTTGCCATTCAACAATAGAAA	48

Sequence (5’ to 3’)	Length [nt]
TAAAGTTTAGAACCGCTAATTGTATCGCGGGGTTTAAGTTTGGCCTTG	48
GGGGCGCGCCCAATTCACTAAAGTACGGTGTCACGAGAATAGCTTCAA	48
CCTCAGAGCACAAGAAGAAAAGTAAGCAG	29
ACATTCTGAAGAGTCTCCGCCAGCAGCTCGAA	32
ATGAGTGACCTGTGCAGTTTCTGCCAGCACG	31
CTTTTGCGTTATTTCAATGATATTCAACCGTT	32
AATTACATAGATTTTCAATAACGGATTCGCC	31
CACATCCTCAGCGGTGGTATGAGCCGGGTCAC	32
CCAGAATGGAGCCGCCAATCAAGTTTGCC	29
ATATTCACCGCCAGCATTGACAGGCAAAATCA	32
CGGGAAACGAAAAACCTGATGGTGGTTCCGAA	32
CCACCCTCTGTTAGGAAGGATCGTCTTTCCAGCAGACGATTATCAGCT	48
TGCGAATAATAATCGACAATGTTCGGTCG	29

Table S4. Modified and extended staples from the 5’ to the 3’ end for the L-shaped DNA origami structure.

Sequence (5’ to 3’)	Length [nt]	Function
ATATTTCCTCTACCACCTACATCACTACGTGCCTGTTCTTCGCATCCAGCGCCGGGTTA	59	Extern labeling of pyrene
ATATTTCCTCTACCACCTACATCACTAGACCGTGTGATAAATACAAATTCT	51	Extern labeling of pyrene
ATATTTCCTCTACCACCTACATCACTACCAGCTTACGGCTGGAAACGTGCCCGTCTCGT	59	Extern labeling of pyrene
ATATTTCCTCTACCACCTACATCACTATGTTGCCCTGCGGCTGATCAGATGCAGTGTCA	59	Extern labeling of pyrene
ATATTTCCTCTACCACCTACATCACTACTAGCTGATAAATTAACAGTAGGG	51	Extern labeling of pyrene
ATATTTCCTCTACCACCTACATCACTAGCTGCGCAACTGTTGGCAGACCTATTAGAAGG	59	Extern labeling of pyrene
ATATTTCCTCTACCACCTACATCACTAGGGGTCATTGCAGGCGGGAATTGACTAAAATA	59	Extern labeling of pyrene
ATATTTCCTCTACCACCTACATCACTAGGCTTAGGTTGGGTTAAGCTAATGATTTTCGA	59	Extern labeling of pyrene

Sequence (5’ to 3’)	Length [nt]	Function
ATATTTCCTCTACCACCTACATCACTATATCATTTTGCGGAACATCCTGATATAAAGAA	59	Extern labeling of pyrene
ATATTTCCTCTACCACCTACATCACTAGTATAAGCAAATATTTTAGATAAGTAACAACG	59	Extern labeling of pyrene
ATATTTCCTCTACCACCTACATCACTAGCAGTTGGGCGGTTGTCCAGTTATGGAAGGAG	59	Extern labeling of pyrene
ATATTTCCTCTACCACCTACATCACTAATCCAGAACAATATTAGTCCATCAGGAACGGT	59	Extern labeling of pyrene
ATATTTCCTCTACCACCTACATCACTAATCGGCAAAATCCCTTACGTGGACTCCAACGT	59	Extern labeling of pyrene
ATATTTCCTCTACCACCTACATCACTAGCAGCAAGCGGTCCACAAGTGTTTTGAGGCCA	59	Extern labeling of pyrene
ATATTTCCTCTACCACCTACATCACTATATTTTTGAGAGATCTGCCATATTTCCTCTACTCAATTGA	67	Extern labeling of pyrene
ATATTTCCTCTACCACCTACATCACTACCCGCCGCGCTTAATGAAAGCCGGCGAACGTG	59	Extern labeling of pyrene
ATATTTCCTCTACCACCTACATCACTATTCGTAATCATGGTCATCCATCAGTTATAAGT	59	Extern labeling of pyrene
ATATTTCCTCTACCACCTACATCACTAAACAGAGGTGAGGCGGCAGACAATTAAAAGGG	59	Extern labeling of pyrene
ATATTTCCTCTACCACCTACATCACTATATTTTGTTAAAATTCGGGTATATATCAAAAC	59	Extern labeling of pyrene
ATATTTCCTCTACCACCTACATCACTACATAGGTCTGAGAGACAAATCGTCGAATTACC	59	Extern labeling of pyrene
ATATTTCCTCTACCACCTACATCACTAAACGTTATTAATTTTACAACTAATCAGTTGGC	59	Extern labeling of pyrene
ATATTTCCTCTACCACCTACATCACTATCAAATCACCATCAATACGCAAGG	51	Extern labeling of pyrene
ATATTTCCTCTACCACCTACATCACTAGAAATTGTTATCCGCTCACATTAAATTAATGA	59	Extern labeling of pyrene
ATATTTCCTCTACCACCTACATCACTACCAGCCAGCTTTCCGGGTAATGGGGTAACAAC	59	Extern labeling of pyrene

Publication

Sequence (5’ to 3’)	Length [nt]	Function
ATATTTCCTCTACCACCTACATCACTACTTCTGACCTAAATTTGCAGAGGCCAGAACGCAATTTACG	67	Extern labeling of pyrene
ATATTTCCTCTACCACCTACATCACTAGTACTATGGTTGCTTTTTTAGACACGCAAATT	59	Extern labeling of pyrene
ATATTTCCTCTACCACCTACATCACTACATTGCCTGAGAGTCTTTATGACCATAAATCATTTCATTT	67	Extern labeling of pyrene
ATATTTCCTCTACCACCTACATCACTAGGGCCTCTTCGCTATTACGTTGTACCTCACCG	59	Extern labeling of pyrene
ATATTTCCTCTACCACCTACATCACTAAAATCAGCTCATTTTTGTGAGCGAATAGGTCA	59	Extern labeling of pyrene
ATATTTCCTCTACCACCTACATCACTAGGAAACCAGGCAAAGCGTACATAAGTGAGTGA	59	Extern labeling of pyrene
ATATTTCCTCTACCACCTACATCACTAATCAAACTTAAATTTCTGGAAGGGCCATATCA	59	Extern labeling of pyrene
ATATTTCCTCTACCACCTACATCACTACTGCAACAGTGCCACGTATCTGGTAGATTAGA	59	Extern labeling of pyrene
ATATTTCCTCTACCACCTACATCACTAACAGTTGAGGATCCCCAGATAGAACTGAAAGC	59	Extern labeling of pyrene
ATATTTCCTCTACCACCTACATCACTAGCCGGGCGCGGTTGCGCCGCTGACCCCTTGTG	59	Extern labeling of pyrene
ATATTTCCTCTACCACCTACATCACTAATTGCCCTTCACCGCCCCAGCTGCTTGCGTTG	59	Extern labeling of pyrene
ATATTTCCTCTACCACCTACATCACTACAGGAAAAACGCTCATACCAGTAAATTTTTGA	59	Extern labeling of pyrene
ATATTTCCTCTACCACCTACATCACTATGATTGCTTTGAATACAAACAGAATGTTTGGA	59	Extern labeling of pyrene
ATATTTCCTCTACCACCTACATCACTAGCAGAGGCGAATTATTTTTCATTTGCTATTAA	59	Extern labeling of pyrene
ATATTTCCTCTACCACCTACATCACTAAAATCCCGTAAAAAAACGTTTTTTGGACTTGT	59	Extern labeling of pyrene
ATATTTCCTCTACCACCTACATCACTACTCTCACGGAAAAAGAACGGATAAAAACGACG	59	Extern labeling of pyrene

Sequence (5’ to 3’)	Length [nt]	Function
ATATTTCCTCTACCACCTACATCACTAAGGCGAAAATCCTGTTGTCTATCACCCCCGAT	59	Extern labeling of pyrene
ATATTTCCTCTACCACCTACATCACTAATAATCAGAAAAGCCCAACATCCACTGTAATA	59	Extern labeling of pyrene
GTGATGTAGGTGGTAGAGGAAATAT-**pyrene**	25	Pyrene at 3’
AGAAACAGCTTTAGAAGGAAGAAAAATCTACGATTTTAAGCATATAACTTTTAAATGC	58	Lower catching site
GCACCCTCCGTCAGGTACGTTAGTAAATGAATAGTTAGCGTCAATCATTTTTAAATGC	58	Upper catching site
ACGATAAACCTAAAACAAAGAATACACTAAAACATTACCCAACAAAGCTTTTTTTTTCGGGCATTTA-**ATTO542**	67	Pointer - dye at 3’

9. References

1. Li, X.; Zhu, Y.; Cai, W.; Borysiak, M.; Han, B.; Chen, D.; Piner, R. D.; Colombo, L.; Ruoff, R. S., Transfer of Large-Area Graphene Films for High-Performance Transparent Conductive Electrodes. *Nano Lett.* **2009,** *9* (12), 4359-4363.
2. Gorantla, S.; Bachmatiuk, A.; Hwang, J.; Alsalman, H. A.; Kwak, J. Y.; Seyller, T.; Eckert, J.; Spencer, M. G.; Rümmeli, M. H., A Universal Transfer Route for Graphene. *Nanoscale* **2014,** *6* (2), 889-896.
3. An, C. J.; Kim, S. J.; Choi, H. O.; Kim, D. W.; Jang, S. W.; Jin, M. L.; Park, J.-M.; Choi, J. K.; Jung, H.-T., Ultraclean Transfer of Cvd-Grown Graphene and Its Application to Flexible Organic Photovoltaic Cells. *J. Mater. Chem. A* **2014,** *2* (48), 20474-20480.
4. Algara-Siller, G.; Lehtinen, O.; Turchanin, A.; Kaiser, U., Dry-Cleaning of Graphene. *Appl. Phys. Lett.* **2014,** *104* (15), 153115.
5. Ferrari, A. C.; Meyer, J.; Scardaci, V.; Casiraghi, C.; Lazzeri, M.; Mauri, F.; Piscanec, S.; Jiang, D.; Novoselov, K.; Roth, S., Raman Spectrum of Graphene and Graphene Layers. *Phys. Rev. Lett.* **2006,** *97* (18), 187401.
6. Graf, D.; Molitor, F.; Ensslin, K.; Stampfer, C.; Jungen, A.; Hierold, C.; Wirtz, L., Spatially Resolved Raman Spectroscopy of Single-and Few-Layer Graphene. *Nano Lett.* **2007,** *7* (2), 238-242.
7. Gupta, A.; Chen, G.; Joshi, P.; Tadigadapa, S.; Eklund, P., Raman Scattering from High-Frequency Phonons in Supported N-Graphene Layer Films. *Nano Lett.* **2006,** *6* (12), 2667-2673.
8. Nolen, C. M.; Denina, G.; Teweldebrhan, D.; Bhanu, B.; Balandin, A. A., High-Throughput Large-Area Automated Identification and Quality Control of Graphene and Few-Layer Graphene Films. *Acs Nano* **2011,** *5* (2), 914-922.
9. Pimenta, M.; Dresselhaus, G.; Dresselhaus, M. S.; Cancado, L.; Jorio, A.; Saito, R., Studying Disorder in Graphite-Based Systems by Raman Spectroscopy. *Phys. Chem. Chem. Phys.* **2007,** *9* (11), 1276-1290.
10. Wang, Y. Y.; Ni, Z. H.; Yu, T.; Shen, Z. X.; Wang, H. M.; Wu, Y. H.; Chen, W.; Shen Wee, A. T., Raman Studies of Monolayer Graphene: The Substrate Effect. *J. Phys. Chem. C* **2008,** *112* (29), 10637-10640.
11. Krause, S.; Overgaard, M. H.; Vosch, T., Photon Energy Dependent Micro-Raman Spectroscopy with a Continuum Laser Source. *Sci. Rep.-UK* **2018,** *8* (1), 1-6.

12. Cançado, L. G.; Jorio, A.; Ferreira, E. M.; Stavale, F.; Achete, C. A.; Capaz, R. B.; Moutinho, M. V. d. O.; Lombardo, A.; Kulmala, T.; Ferrari, A. C., Quantifying Defects in Graphene *via* Raman Spectroscopy at Different Excitation Energies. *Nano Lett.* **2011,** *11* (8), 3190-3196.
13. Childres, I.; Jauregui, L. A.; Tian, J.; Chen, Y. P., Effect of Oxygen Plasma Etching on Graphene Studied Using Raman Spectroscopy and Electronic Transport Measurements. *New J. Phys.* **2011,** *13* (2), 025008.
14. Yoon, D.; Cheong, H., Raman Spectroscopy for Characterization of Graphene. In *Raman Spectroscopy for Nanomaterials Characterization*, Springer: 2012; pp 191-214.
15. Heller, E. J.; Yang, Y.; Kocia, L.; Chen, W.; Fang, S.; Borunda, M.; Kaxiras, E., Theory of Graphene Raman Scattering. *ACS nano* **2016,** *10* (2), 2803-2818.
16. Malard, L.; Pimenta, M. A.; Dresselhaus, G.; Dresselhaus, M., Raman Spectroscopy in Graphene. *Phys. Rep.* **2009,** *473* (5-6), 51-87.
17. Tsoukleri, G.; Parthenios, J.; Papagelis, K.; Jalil, R.; Ferrari, A. C.; Geim, A. K.; Novoselov, K. S.; Galiotis, C., Subjecting a Graphene Monolayer to Tension and Compression. *Small* **2009,** *5* (21), 2397-2402.
18. Gao, L.; Ren, W.; Li, F.; Cheng, H.-M., Total Color Difference for Rapid and Accurate Identification of Graphene. *ACS nano* **2008,** *2* (8), 1625-1633.
19. Ni, Z.; Wang, H.; Kasim, J.; Fan, H.; Yu, T.; Wu, Y. H.; Feng, Y.; Shen, Z., Graphene Thickness Determination Using Reflection and Contrast Spectroscopy. *Nano Lett.* **2007,** *7* (9), 2758-2763.
20. Lui, C. H.; Liu, L.; Mak, K. F.; Flynn, G. W.; Heinz, T. F., Ultraflat Graphene. *Nature* **2009,** *462* (7271), 339-341.
21. Novoselov, K. S.; Geim, A. K.; Morozov, S. V.; Jiang, D.; Zhang, Y.; Dubonos, S. V.; Grigorieva, I. V.; Firsov, A. A., Electric Field Effect in Atomically Thin Carbon Films. *science* **2004,** *306* (5696), 666-669.
22. Tung, V. C.; Allen, M. J.; Yang, Y.; Kaner, R. B., High-Throughput Solution Processing of Large-Scale Graphene. *Nat. Nanotechnol.* **2009,** *4* (1), 25.

8.6. Publication IV

Graphene Energy Transfer for Single-Molecule Biophysics, Biosensing, and Super-Resolution Microscopy

by

I. Kamińska,* **J. Bohlen**,* R. Yaadav, P. Schüler, M. Raab, T. Schröder, J. Zähringer, K. Zielonka, S. Krause, P. Tinnefeld (* equal contribution)

published in

Advanced materials **2021**, *33* (24), e2101099

Author contribution:

J. B. designed the L-shaped DNA origami structure, did preliminary work on the orientation of the L-shaped DNA origami structure on graphene, designed and prepared the pointer and helped designing the tether in the part “Dynamics with GET”. Furthermore, J. B. designed, planned, executed, prepared, analyzed and interpreted all data in the parts “Expanding FRET”, “GET Tracking” and “GET-DNA PAINT Super-Resolution” (sample in “GET-DNA PAINT Super-Resolution” was supported from GATTAquant) and wrote parts of the manuscript.

RESEARCH ARTICLE

ADVANCED MATERIALS
www.advmat.de

Graphene Energy Transfer for Single-Molecule Biophysics, Biosensing, and Super-Resolution Microscopy

Izabela Kamińska, Johann Bohlen, Renukka Yaadav, Patrick Schüler, Mario Raab, Tim Schröder, Jonas Zähringer, Karolina Zielonka, Stefan Krause, and Philip Tinnefeld**

Graphene is considered a game-changing material, especially for its mechanical and electrical properties. This work exploits that graphene is almost transparent but quenches fluorescence in a range up to ≈40 nm. Graphene as a broadband and unbleachable energy-transfer acceptor without labeling, is used to precisely determine the height of molecules with respect to graphene, to visualize the dynamics of DNA nanostructures, and to determine the orientation of Förster-type resonance energy transfer (FRET) pairs. Using DNA origami nanopositioners, biosensing, single-molecule tracking, and DNA PAINT super-resolution with <3 nm z-resolution are demonstrated. The range of examples shows the potential of graphene-on-glass coverslips as a versatile platform for single-molecule biophysics, biosensing, and super-resolution microscopy.

1. Introduction

Graphene is the prototypical 2D material whose extraordinary properties including mechanical strength, electrical and thermal conductivity, as well as uniform absorption across the visible spectrum have made it attractive for many research directions.[1–5] While only 2.3% of visible light is absorbed, graphene constitutes an efficient acceptor for nonradiative energy transfer for fluorescent dyes in the near-field in analogy to FRET.[6–10] Accordingly, excited state energy is nonradiatively transferred to graphene with a d^{-4} scaling law and a wavelength independent characteristic length scale of ≈18 nm with 50% energy transfer efficiency.[6,8,9] The fluorescence quenching property has been used for graphene characterization[10–12] and for biosensors based on graphene-related materials such as graphene oxide or reduced graphene oxide[13–16] but only recently its potential for applications in the life science including super-resolution microscopy has been realized.[9,17–20] Due to graphene energy transfer (GET), the intensity of a fluorescent dye as well as its fluorescence lifetime are reduced as a function of its distance to graphene. This information can be used to determine the position of the dye molecule to graphene and to sensitively report on distance changes. We here introduce graphene-on-glass coverslips as a platform for additional functionality and information content in single-molecule biophysics and biosensing, and to provide 3D information in super-resolution microscopy and in single-molecule tracking. To make graphene chemically accessible, we use DNA origami nanostructures as chemical adapters and place demonstration assays at defined distances on top of graphene coverslips.

We exemplify the potential of graphene energy transfer with five different assay formats. First, we show height measurements of dyes based on fluorescence lifetimes. We then sense the orientation of DNA origami nanostructures with four landing surfaces by inserting two fluorescent lifetime reporting dyes. Second, we visualize switching dynamics of a DNA pointer between two binding sites with high time resolution using an autocorrelation scheme that filters for lifetime associated components. This approach also enables detecting the dynamics of a flexible DNA tether influenced by viscosity or target binding. Third, by combining FRET with GET, we determine the orientation of a donor–acceptor pair with respect to the substrate, in both static and dynamic systems. Fourth, we show a biosensing assay with single DNA molecule detection in a novel unquenching assay format that uses graphene as a quencher. Fifth, we combine GET with DNA point accumulation in nanoscale topography (DNA PAINT) super-resolution imaging and for single-molecule tracking with resolution below 3 nm in z and 6 nm in x/y on DNA origami structures.

In summary, using graphene energy transfer with graphene-on-glass coverslips[21] provides many new opportunities for biosensing, single-molecule biophysics and super-resolution, ready to be lifted with the aid of DNA origami nanopositioners.

2. Results

2.1. Distance Determination from Fluorescence Lifetimes

With the known d_0-value and the d^{-4} distance dependence, the distance of a molecule from graphene can be determined from its fluorescence intensity or analogously, from the fluorescence

Dr. I. Kamińska, K. Zielonka
Institute of Physical Chemistry of the Polish Academy of Sciences
Kasprzaka 44/52, Warsaw 01-224, Poland
E-mail: ikaminska@ichf.edu.pl

J. Bohlen, R. Yaadav, P. Schüler, Dr. M. Raab, T. Schröder, J. Zähringer, Dr. S. Krause, Prof. P. Tinnefeld
Department of Chemistry and Center for NanoScience
Ludwig-Maximilians-Universität München
Butenandtstr. 5-13, 81377 München, Germany
E-mail: philip.tinnefeld@cup.uni-muenchen.de

The ORCID identification number(s) for the author(s) of this article can be found under https://doi.org/10.1002/adma.202101099.

DOI: 10.1002/adma.202101099

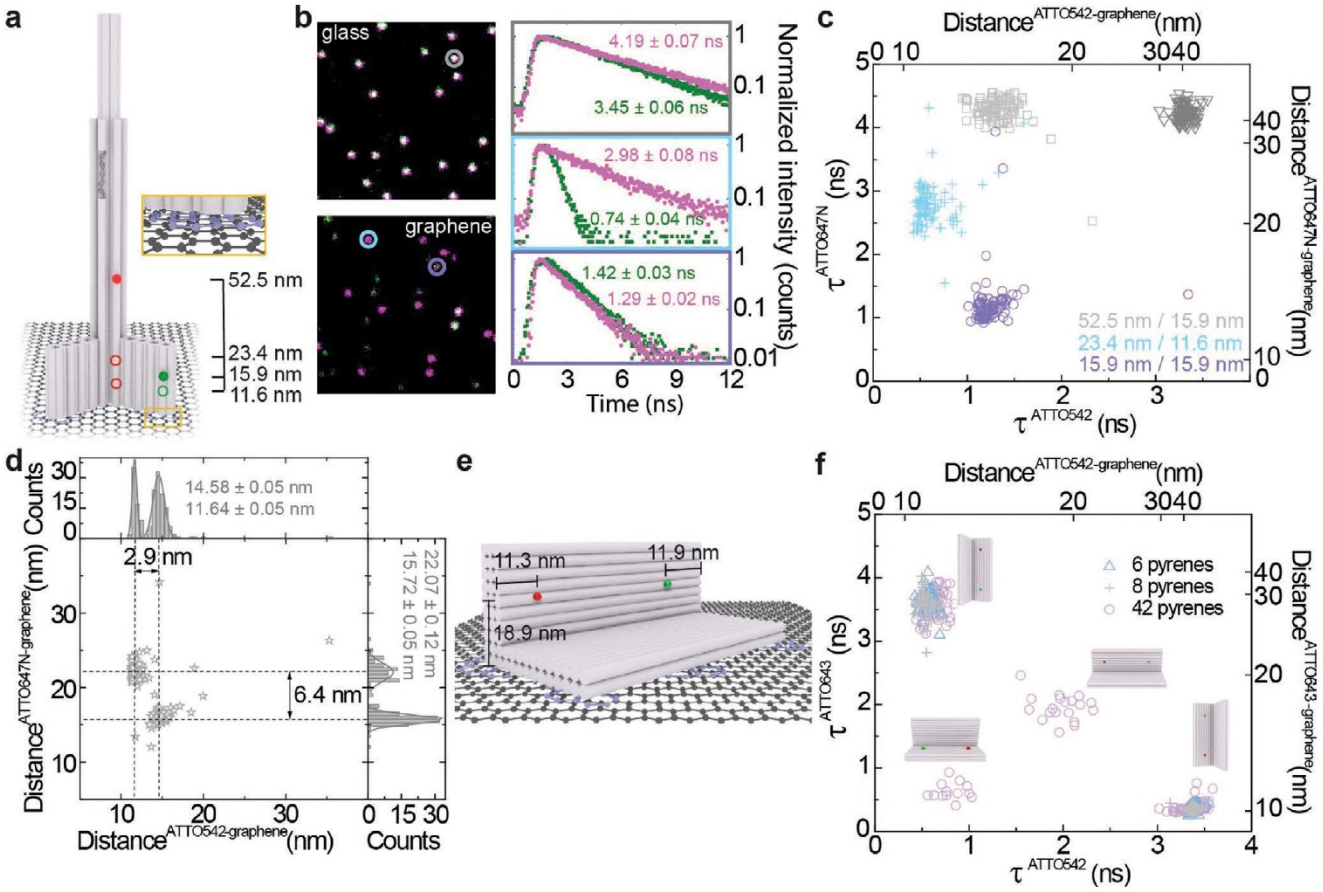

Figure 1. Distance determination from fluorescence lifetimes. a) Sketch of a pillar-shaped DNA origami structure, with the marked positions of dye molecules, and a zoom-in of pyrene molecules (orange frame) used for the immobilization of DNA origami structures on graphene. b) Fluorescence intensity maps of DNA origami structure labeled with two dye molecules immobilized on glass (top) and graphene (bottom), together with fluorescence decays and fitted fluorescence lifetime values with standard errors of the fit (right) of a green (green) and a red (magenta) dye marked on the maps: gray—on glass; cyan and violet—on graphene. c) Scatter plot of fluorescence lifetime of colocalized dye molecules (both dye molecules within one DNA origami structure), ATTO542 and ATTO647N, at various heights; each DNA origami sample measured separately on glass (∇) or graphene (□, +, ○), with ATTO542/ATTO647N at 15.9/52.5 nm (□ gray), 11.6/23.4 nm (+ cyan) or 15.9/15.9 nm (○ violet) distance from graphene. d) Scatter plot and corresponding histograms with the Gaussian fits of distances from graphene calculated from fluorescence lifetimes (for calculations check Supporting Information) of two mixed DNA origami structures with ATTO542/ATTO647N at 11.6/23.4 and 15.9/15.9 nm distance from graphene. e) Sketch of an L-shaped DNA origami structure with ATTO643 and ATTO542 positioned at the height of 18.9, and 11.3 or 11.9 nm from the side edges, respectively. f) Scatter plot of fluorescence lifetimes of colocalized dye molecules within L-shaped DNA origami structure obtained for structures labeled with 6 (Δ blue), 8 (+ gray) or 42 (○ lilac) pyrene molecules, showing four different orientations on graphene (indicated by sketches).

lifetime as proportional intensive property. Here we determine the distance of molecules from the graphene surface using their fluorescence lifetime. "Single-molecule grade" graphene-on-glass coverslips were prepared by transferring CVD-grown graphene from copper-foils to glass coverslips with an optimized protocol that avoids impurities (see Materials and Methods, Supporting Information). We used pyrene-equipped DNA origami nanopositioners to place fluorescent dyes on top of the graphene coverslips (see **Figure 1**a). Pyrene modifications ensure a selective orientation of the DNA origami nanopillar on top of graphene.[9]

Three samples were labeled with a green (ATTO542) and a red (ATTO647N) dye molecule at the heights of 15.9 and 52.5 nm (**1**), 11.6 and 23.4 nm (**2**), 15.9 and 15.9 nm (**3**), respectively.[9] Using alternating pulsed laser excitation at 532 and 639 nm, both dyes were measured quasi-simultaneously by single-molecule fluorescence lifetime imaging (Figure 1b, see also Supporting Information for sample preparation, selection of dyes, experimental conditions, and data analysis). Single molecules were identified in the fluorescence images and their fluorescence lifetime was determined (example decays are shown in Figure 1b). Reference measurements on glass show a narrow and homogenous population of fluorescence lifetime that is identical for all three samples (Figure 1c, ∇) with an average fluorescence lifetime of 4.3 ± 0.1 ns for ATTO647N and 3.4 ± 0.1 ns for ATTO542. For each nanostructure measured on graphene, shortened fluorescence lifetimes of both dye molecules indicate the proximity of graphene (Figure 1c □, +, ○), except for ATTO647N in sample **1**. This one emitter was incorporated at the height of 52.5 nm, which is too far from graphene for measurable shortening of the fluorescence lifetime. In the following experiment, samples **2** and **3** were mixed, immobilized on graphene, and imaged. An example of a fluorescence intensity map and decays obtained for the mixed sample are presented in Figure 1b (lower panel and decays in cyan and violet frames). The scatter plot of the dye–graphene distance (Figure 1d) calculated from the measured

values of the fluorescence lifetime of dye molecules (see Figure S1 and calculations, Supporting Information), confirm that the populations of the two DNA origami structures are separated equally well as in the isolated samples (Figure 1c), indicating that differences in z-direction as small as 6.4 and 2.9 nm are easily resolved from the fluorescence lifetimes of single molecules. Next, we used this sensitivity to study the orientation of a DNA origami structure that can bind to graphene in different orientations. The L-shaped DNA origami structure (Figure 1e) can bind to graphene through pyrene immobilization at the bottom of the structure but also by blunt end stacking to the sides. We placed two dye molecules in the DNA origami structure at the height of 18.9 nm (≈48% and 43% energy transfer efficiency to graphene, for ATTO643 and ATTO542, respectively)[9] and 11.3 or 11.9 nm from the side edges, for ATTO643 and ATTO542, respectively, such that the obtained combination of fluorescence lifetime directly reports on the orientation of each individual DNA origami structure. Three tested samples varied by the number of incorporated pyrene molecules. Two samples contained 6 or 8 pyrene molecules and for both, two populations of L-shaped DNA origami structure positioned on one or the other side were observed (Figure 1f, Δ and +). Increasing the number of binding strands for pyrene labeled strands to 42 resulted in the appearance of four populations (Figure 1f, ○) with the expected combination of fluorescence lifetimes showing that binding mediated by pyrenes was adopted by ≈15% of all structures. The population with very short fluorescence lifetimes of both dyes could be explained by binding of the DNA origami structure on the remaining site or by partial degradation of the DNA origami structures. We note that it is advantageous for homogeneous DNA origami nanopositioning on graphene if the π–π stacking interactions of both pyrene molecules and DNA bases with graphene are additive and not competitive.

2.2. Dynamics with GET

Next, we studied whether dynamic distance changes to graphene can be visualized by GET. We used the L-shaped DNA origami structure equipped with a Cy3B labeled 19 nucleotides (nt) single-stranded DNA pointer which can transiently bind to two protruding strands, ≈6 nm below and above the pointer position (see sketch in **Figure 2**a).

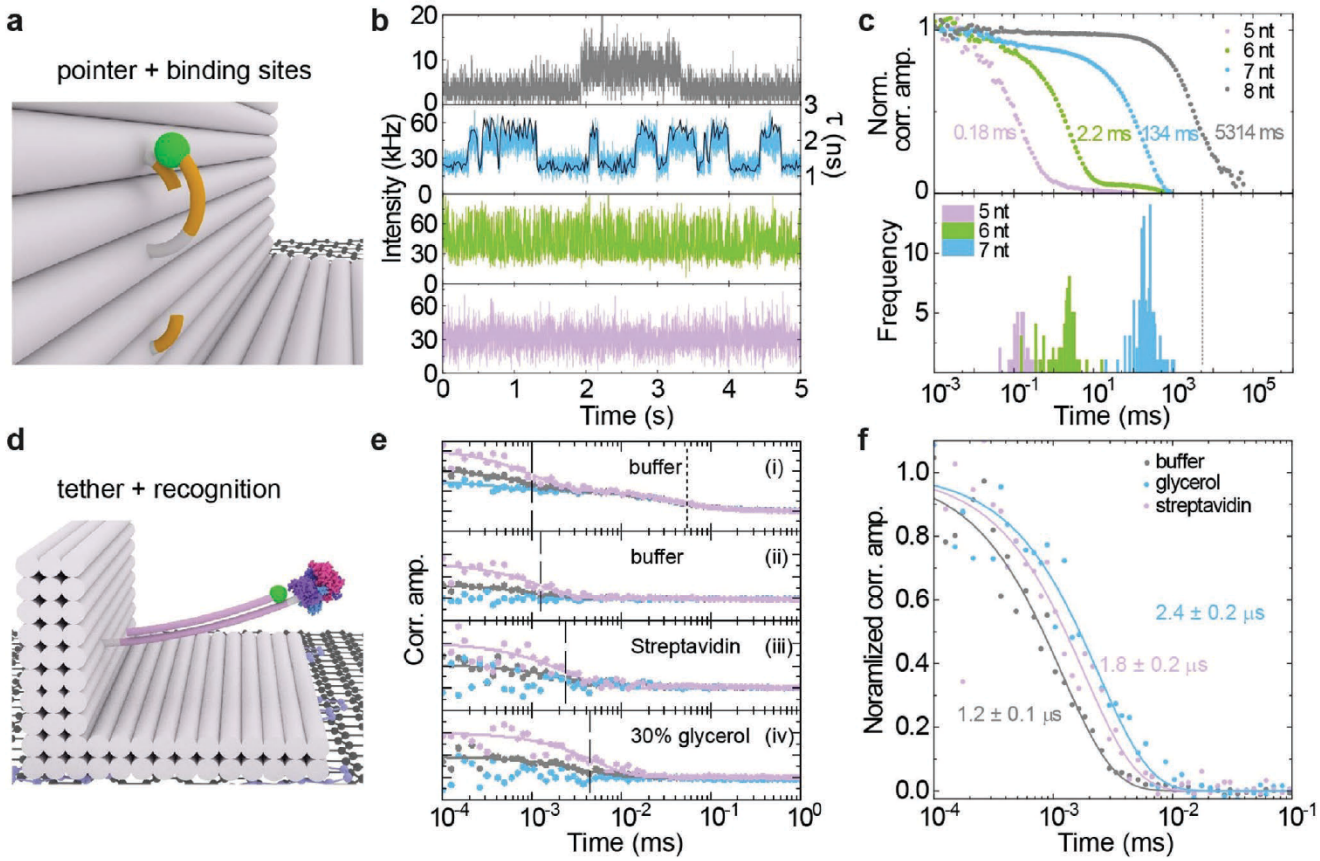

Figure 2. Dynamic DNA origami nanostructures studied with GET. a) Sketch of the L-shaped DNA origami structure with a flexible pointer with fluorescent dye (Cy3B), and upper (26.5 nm) and lower (16.1 nm) binding strands yielding GET efficiencies of 15.7% (τ_{up} = 2.6 ns) and 59.3% (τ_{low} = 1.3 ns). b) Representative transients for 8 (gray), 7 (blue), 6 (green), and 5 (lilac) nt binding. For 7 nt binding, the fluorescence lifetime (black) is also shown with 20 ms binning. All transients were acquired at 3 µW excitation power, except for eight nt binding (1 µW). c) Normalized correlation functions averaged over several transients and corresponding frequency distribution resulting from analyzing each transient individually. The gray dashed vertical line represents the correlation time for 8 nt extracted from concatenated transients. d) Sketch of the biosensing system with a 44 nt long tether, Cy3B, and a target recognizing unit (biotin) and target (streptavidin). e) Averaged correlation functions for photons with a long microtime (>2.5 ns) for measurements of the tether fluctuations in buffer (gray), in buffer with 30% glycerol (blue) and in buffer, incubated with streptavidin (lilac) after subtracting the fit of the correlation functions calculated from photons with a short microtime (<2.5 ns). See Supporting Information for a detailed description of the gating procedure.

L-shaped DNA origami structures with correct orientation exhibit strong fluctuations in the fluorescence intensity due to dynamic switching of the binding position between lower (strong quenching) and upper (weak quenching) strand. Figure 2b shows exemplary transients with decreasing strength of the binding interactions from 8 (gray) to 5 (lilac) complementary nucleotides. With 8 nt binding, switching between the two bound conformations occurs on the time scale of seconds as visualized by the two intensity levels (Figure 2b, gray). With 7 nt binding (blue), frequent transitions occur in the hundred millisecond range. For this example, a fluorescence lifetime transient is also depicted (black) verifying that intensity fluctuations are directly correlated with the fluorescence lifetime. For 6 and 5 nt (green and lilac), the transitions are too fast to be visually resolved in the transients but they are revealed by autocorrelation analysis. The correlation functions averaged over several transients are displayed in Figure 2c, together with the correlation time distribution for the different number of nucleotides per binding strand (see Supporting Information for details of autocorrelation). As the correlation time for 8 nt binding is too long to extract it from a single transient with sufficient statistical accuracy, only a single value (vertical dashed line) is given which results from concatenating all acquired transients.

We have further advanced this approach for dynamic sensing of confined diffusion changes of a flexible 44 nt double stranded tether (see sketch in Figure 2d). As the tether is able to perform a confined diffusion around the point of attachment, the distance between the Cy3B dye at the end of the tether and the graphene surface is permanently changing which causes fast intensity fluctuations. As this intensity fluctuation is directly correlated to the fluorescence lifetime, it can be distinguished from other sources of photophysical intensity fluctuations such as triplet states by correlating different subsets of photons depending on their arrival time with respect to the laser pulse (see Supporting Information for details). The resulting filtered component for tether movements on graphene (Figure 2e, averaged over several molecules) is sensitive to changes of the diffusion properties of the tether and can be used to detect binding events (streptavidin to biotin at the end of the tether (Figure 2e, lilac) as well as viscosity changes (buffer with 30% glycerol in Figure 2e, blue). Changes of the correlation time from 1.2 to 1.8 and 2.6 µs, respectively, are revealed in analogy to confocal fluorescence correlation spectroscopy (see Supporting Information for comparison and further details on analysis).

2.3. Expanding FRET

FRET is a workhorse of single-molecule biophysics.[22,23] FRET experiments require labeling with a donor and acceptor fluorophore with a distance up to 10 nm. In GET, an unbleachable, broad-band acceptor "molecule" is provided complimentary without requiring an additional labeling. GET provides the distance of the dye (acceptor and donor) to graphene. From FRET, the distance between acceptor and donor is determined. Next, we explored whether combining FRET and GET could yield additional information such as the orientation of the FRET-pair with respect to the surface. To this end, we prepared three DNA origami constructs that exhibit similar FRET efficiency but different orientation of the FRET-pair with respect to the surface (**Figure 3**a).

The arrangements are termed vertical (v), horizontal (h), and diagonal (d). We determined accurate FRET efficiency E using the acceptor bleaching approach in fluorescence transients.[24] Therefore, we first excited the donor and recorded fluorescence intensities of the green and red channel (see transients in Figure 3b, green—donor; gray—FRET). Around 1.2 s the green excitation was switched off, and at 2.1 s, we switched to red excitation and photobleached the acceptor. Finally, we probed the green emission with green excitation to obtain the intensity of the donor in the absence of the acceptor. With this data, we calculated the FRET distance r, the distances to graphene d and a, and the angle δ (see Figure 3c). The FRET efficiency was obtained from the donor lifetime in presence and absence of the acceptor (see Figure S4, Supporting Information). Under the assumption of isotopically rotating dipoles ($\kappa^2 = 2/3$), the FRET distance was calculated from measurements on glass (Figure 3d) as graphene might slightly change the FRET rate constant.[25–28]

Next, the distances to graphene (GET distance) were calculated from the acceptor lifetime and the donor lifetime after acceptor bleaching. The position of the acceptor was fixed (magenta line in Figure 3e at 15.1 nm) whereas the donor position was varied (Figure 3e; Supporting Information for details). Finally, based on the results of FRET and GET distances, the angle δ (δ_h, δ_d, δ_v) was calculated (Figure 2f) directly visualizing the additional information obtained by GET–FRET. The angles of the vertical (4° ± 14°), diagonal (28° ± 0.6°) and horizontal samples (87° ± 0.6°) are close to the designed values of 0°, 37°, and 90°. The slight differences to the designed angles are related to the limited accuracy of our design model and might also be caused by linker lengths and preferred orientations and interactions of the dyes with the DNA.

Single-molecule FRET is especially valuable for visualizing dynamic processes. We used the same L-shaped DNA origami structure as described in the previous section with a pointer that transiently hybridizes to two short oligonucleotides and added an acceptor dye closer to the lower binding position, in two binding modes, either the "up" mode where low GET and FRET is observed or the "down" mode with high GET and FRET (see sketch in **Figure 4**a). The sample on glass only shows a modulation in presence of the acceptor (until 5 s, Figure 4b), after acceptor bleaching the modulation disappears. On the graphene sample, modulation in presence and absence of the acceptor (Figure 4c) is observed. During the first excitation with green (until 6 s) the modulation is caused by the combined influence of FRET and GET, after the acceptor bleached the modulation is caused only by GET. From the FRET data on glass, the FRET distance was calculated (Figure 4d). Combining FRET data and GET data (Figure 4e) enabled determining the orientation in space (Figure 4f). The directions of FRET for binding to the lower and upper position exhibit an angle of 112° and 19°, respectively.

2.4. Graphene Biosensing

Fluorescence quenchers are often employed in biosensing assays in which a binding event yields a change of the

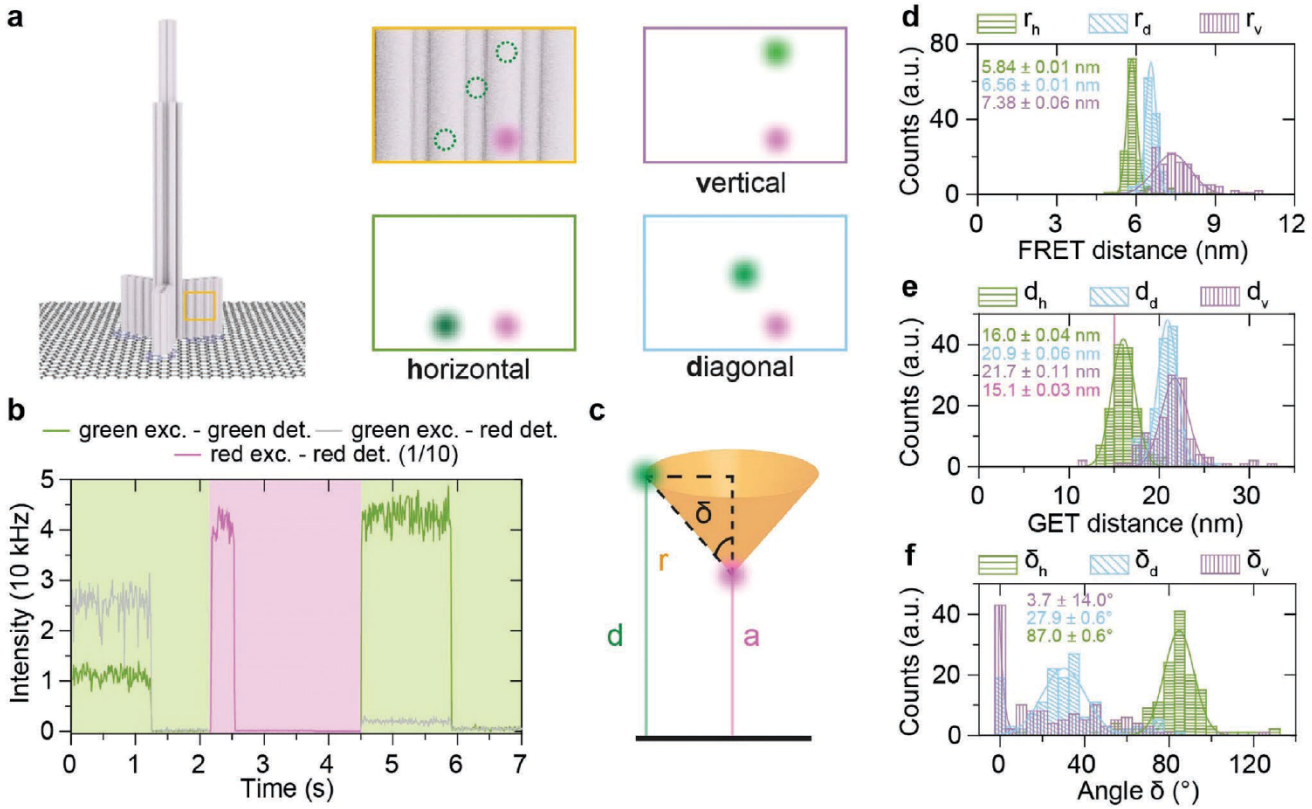

Figure 3. Static FRET/GET measurements. a) Illustration of the pillar-shaped DNA origami structure with three different acceptor–donor orientations: horizontal h, diagonal d, and vertical v. ATTO542 and ATTO647N were used as a donor and acceptor dye, respectively. b) Exemplary transient of the acceptor bleaching approach for the horizontal sample on glass. The background colors indicate the excitation laser (green: 532 nm, magenta: 640 nm). First donor (green) and FRET (gray) signal can be observed. Around 1.2 s, the green laser is switched off and the red laser is switched on (2.1 s, shown acceptor count rate is 1/10 of detected count rate) until the acceptor (magenta) bleaches (2.6 s). Green laser excitation is then used until the donor bleaches. c) Illustration of parameters accessible by FRET/GET. d) Distributions of the distance between donor and acceptor *r* calculated from the FRET data measured on glass. e) The distribution of distances of donor *d* to graphene, including the average acceptor–graphene distance (magenta line). f) The distributions of the angle δ calculated from the results presented in (d) and (e). All errors are standard errors from Gaussian distributions, besides the errors of the delta which are calculated from the error propagation.

dye–quencher interaction so that the fluorescence change is indicative of a binding event. For using graphene as quencher in nucleic acid biosensing assays, we started from the pillar-shaped DNA origami nanostructure (see Figure 3a) and equipped it with a dye-labeled protruding capturing sequence at a height of 16.3 nm (ATTO643 at the 3′ end), i.e., close to d_0-value at which the fluorescence intensity is most sensitive to height changes. An ATTO542 dye in the DNA origami structure at a height of 23.4 nm from graphene served as internal reference (**Figure 5**, sketches, Supporting Information for details on data analysis). The dye on the capture strand exhibits an intermediate fluorescence intensity with multiexponential fluorescence decays (Figure S6a, Supporting Information) and a maximum of the fluorescence lifetime distribution at 1.63 ± 0.03 ns (Figure 5a) when approximated by a single exponential decay.

Multiexponential fluorescence decays from single molecules can occur when the dye labeled strand is sampling different dye–graphene distances during the measurement. Upon hybridization with the target strand, a change of the fluorescence properties and a main population with a fluorescence lifetime around 2.79 ± 0.04 ns is observed (Figure 5b; Figure S6b, Supporting Information). We found that this increase in average fluorescence lifetime stems from an interaction of the target molecule with the DNA origami structure (Figure S8, Supporting Information). To increase the contrast, we inserted another protruding strand with 12 nt complementary to the capture strand (closing strand at 9.2 nm), which is closer to the bottom of the DNA origami structure (see Figure 5c). In the absence of target, the capturing strand binds to the closing strand yielding strongly quenched dyes with a fluorescence lifetime of 0.33 ± 0.01 ns, i.e., 92% ± 1.1% quenching efficiency (Figure 5c). Opening of this closed conformation by the target occurs via a 12 nt toehold on the capture strand and a similar fluorescence lifetime distribution was obtained as before with only a small fraction of capturing strands remaining bound to the closing strand (compare Figure 5b with Figure 5d). To further increase the contrast by maximizing the signal of the open form, we added another capture region that is able to bind the target DNA away from the graphene surface (lilac strand in Figure 5e protruding at a height of 30.6 nm above graphene). This additional capture sequence binds to a part of the target that is not binding

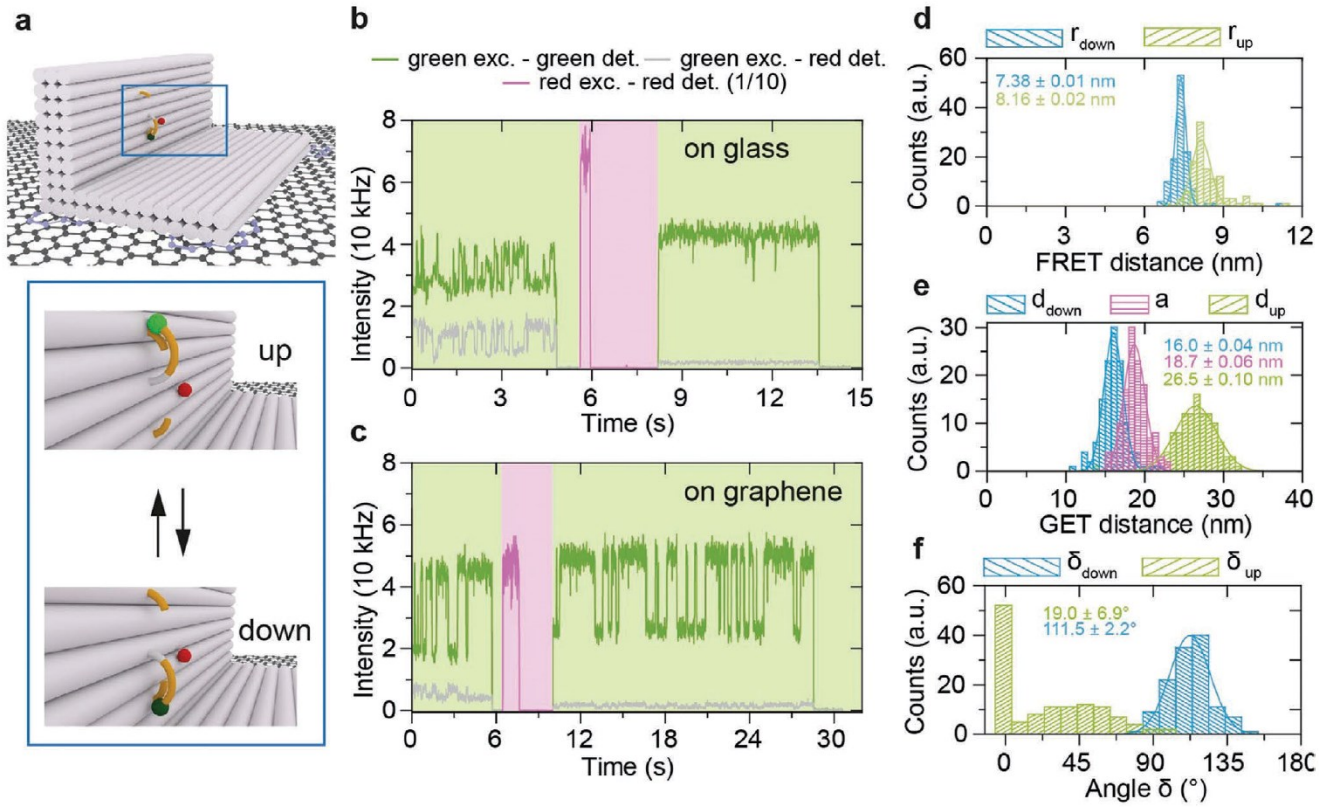

Figure 4. Dynamic FRET/GET measurements. a) Illustration of the L-shaped DNA origami structure featuring a pointer which can transiently bind to an upper and a lower binding site. ATTO542 and ATTO647N were used as a donor and acceptor dye, respectively. b,c) Transients of the FRET assay on glass (b) and graphene (c). The glass transient only shows FRET-based fluctuation in presence of the acceptor while the graphene transient show either GET-based fluctuation after acceptor bleaching or combined FRET- and GET-based fluctuation in the presence of the acceptor. d) The FRET distances (r_{down}, r_{up}) calculated from the FRET measurements on glass and e) the GET distances (d_{down}, a, d_{up}). f) From the combined results of d,e) the angles (δ_{down}, δ_{up}) were determined. All errors are standard errors from Gaussian distributions, besides the errors of the delta, which are calculated from the error propagation.

to the capture strand and it is designed so short (9 nt) that it imposes a strong pointing bias without creating a thermodynamic trap (therefore the strand is denoted "biasing strand" in the following). The short biasing strand ensures that initially the target hybridizes to the capture strand, replaces it from the closing strand and forms a new loop with the biasing strand thereby restoring the fluorescence of the dye ATTO643. Initially, the fluorescence of this construct is quenched in analogy to the sample without biasing strand (Figure 5c, compare fluorescence decays in Figure S6c,e, Supporting Information). Upon target binding, we observed almost full unquenching of the fluorescence (compare lilac population in Figure 5f with glass reference in black) with minor fractions of strong quenching ($\tau < 0.7$ ns, hybridization of capture strand with closing strand) and mild unquenching (2.3 ns $< \tau <$ 3.3 ns, target binding but not binding to biasing strand). Overall, we could stepwise increase our signal contrast upon target binding indicating the potential of designing assays with DNA origami nanopositioners on graphene.

2.5. GET Tracking

Camera-based localization methods are used to track single molecules in two dimensions and scanning a confocal spot with feedback enables recording 3D trajectories of single molecules.[29,30] Achieving isotropic nanoscale resolution in three dimensions, however, remains a challenge. Here, we show 3D tracking of a dye-labeled DNA pointer that can transiently hybridize to three single-stranded protrusions on the L-shaped DNA origami structure. Two of the three protruding strands are arranged vertically at a distance of two helices (≈6 nm) (see sketches in **Figure 6**a). The height of the third protruding strand is in the middle between the other two strands and displaced to the side by ≈5.4 nm. With respect to graphene, the three binding sites are at heights of 24 nm (high), 21 nm (mid), and 18 nm (low).

From TIRF imaging of the Cy3B-labeled pointer, we extracted intensity transients as the one depicted in Figure 6b. Three intensity levels representing binding to the different protruding strands are reflected in the intensity histogram shown next to the transient. Combining xy-information from fitting the point-spread function with the intensity z-information yields tracking trajectories such as those shown in Figure 6c and Figure S9 (Supporting Information). The y/z projection (Figure 6d) shows that all three binding positions are clearly resolved. Fitting the three populations independently yields a localization precision of 0.4 to 1.4 nm in z-direction and 1.3 to 1.8 nm in xy-direction. Such molecular precision tracking at small length scales should be able to complement single-molecule FRET, as 3D information

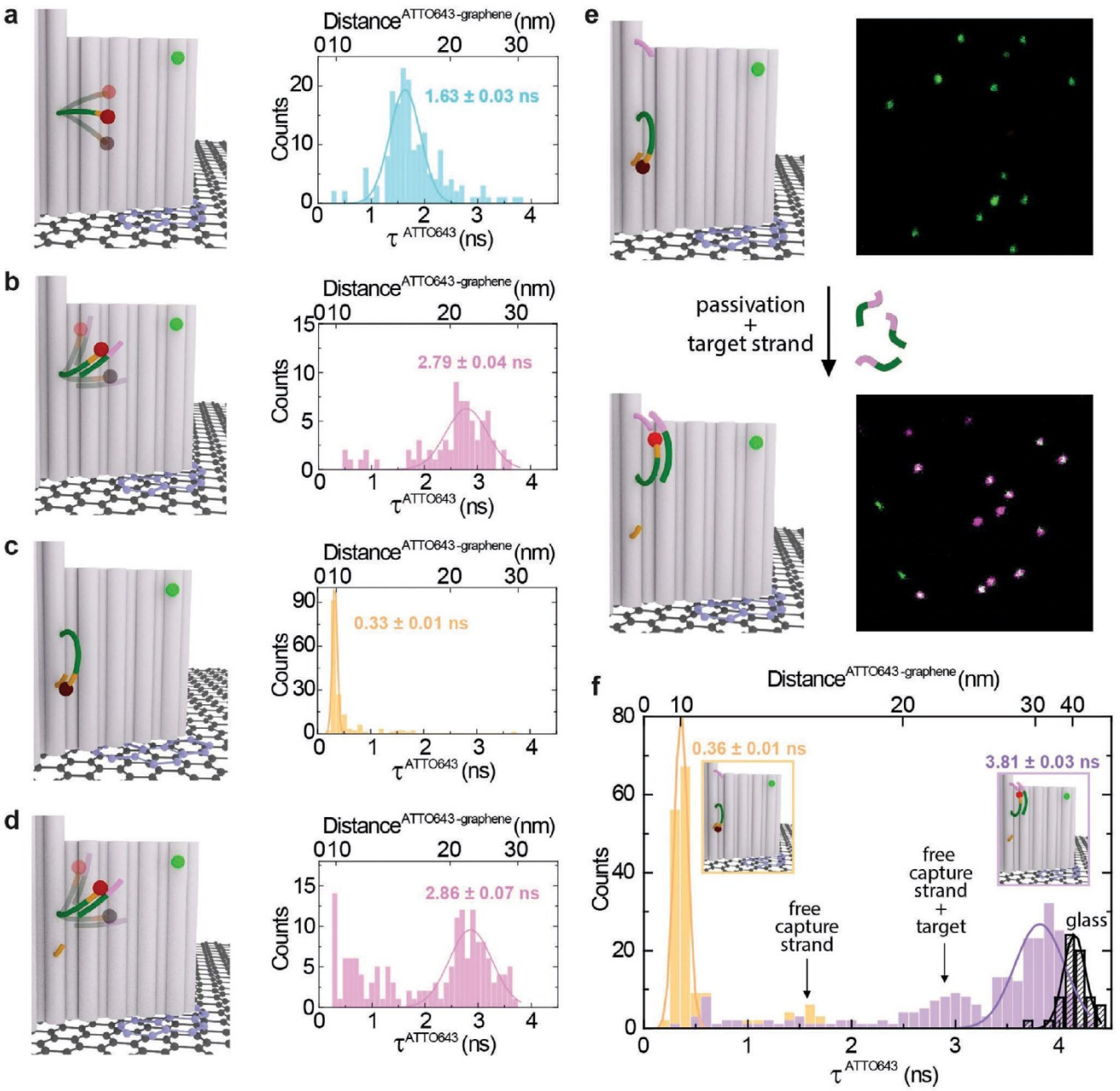

Figure 5. Graphene biosensing with a nucleic acid bioassay. a–d) Sketches and histograms of the fluorescence lifetime distributions fitted with a Gaussian function (the mean value and standard error obtained from the fit) of an ATTO643 dye attached to the capture strand which is: a) free to move (cyan), b) bound to a target strand (magenta), c) hybridized with a closing strand (orange), and d) liberated by a target strand (magenta). e) Demonstration of the full assay: sketches and fluorescence intensity maps (10 × 10 µm), on the top—before a target detection (a capture strand hybridized with a closing strand), on the bottom—a capture strand liberated by a target strand and additionally caught and stabilized by a biasing strand. f) Histogram of the fluorescence lifetime distributions fitted with Gaussian functions (the mean value and standard error obtained from the fit) of an ATTO643 dye in the full assay before (orange) and after (lilac) target detection; in black, results for the assay measured on glass.

is obtained over an extended distance range in contrast to distances only (experimental details in the Supporting Information).

2.6. GET-DNA PAINT Super-Resolution

Surface quenching was first used for super-resolution microscopy with metal-induced energy transfer to gold surfaces.[31,32] The steeper distance dependence of graphene quenching compared to gold quenching enables the determination of the z-distance of molecules from the surface with improved precision and has been used to determine the distance law of graphene quenching and the thickness of lipid membranes.[9,17] In addition, graphene creates less background and fluorescence detection can be comfortably carried out through the graphene-on-glass coverslip. Here, we explored whether graphene

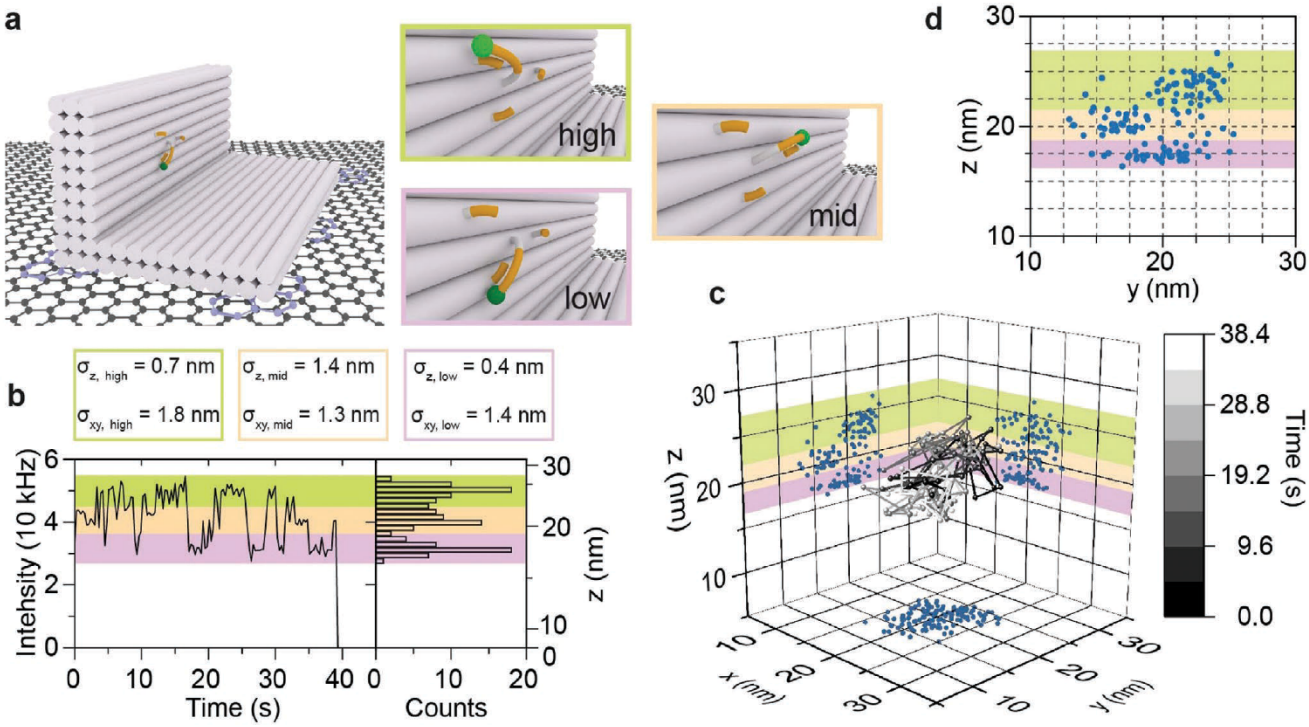

Figure 6. GET tracking. a) Sketch of the L-shaped DNA origami structure with three protruding strands "low" (light violet), "mid" (orange), and "high" (green), to which the Cy3B dye-labeled pointer can transiently hybridize. b) Intensity transient for a single pointer imaged by TIRF microscopy. An intensity histogram is shown to the right of the transient. The three intensity levels are representing the transient hybridization of the pointer to the protruding strands. c) 3D trajectory of the pointer extracted from the fluorescence intensities (*z*-resolution) and from fitting of the point-spread-functions (*xy*-resolution). Localization precision was between 1.3 and 1.8 nm in *xy* and between 0.4 and 1.4 nm in the *z*-direction. d) An inset of the *y*/*z* projection which clearly shows the well-resolved binding sites.

quenching is compatible with single-molecule localization super-resolution microscopy by DNA PAINT,[33–35] in which a DNA origami structure is super-resolved by successively visualizing the binding events of single molecules to the DNA-labeled structure of interest.

We equipped a cube-shaped DNA origami structure (obtained from GATTAquant) with DNA PAINT binding sites. On two opposing sides of the DNA cube with a side length of 24 nm, we placed 8 nt binding sites at a height of 19.2 nm above graphene. On the other two opposing sides, we placed binding sites at a height of 16.5 nm (**Figure 7**a). For DNA PAINT imaging, we used an 8 nt long ATTO542 labeled imager strand. We generated 2D images via fitting of the point-spread function and determined the *z*-position from the fluorescence intensity excluding the first and the last frame of each binding event (see the Supporting Information for details on experimental procedures and data analysis). An overview image of the DNA origami cubes is shown in Figure 7b, in which the height information is color-coded. The exemplary magnified views of the *x*/*y* and *x*/*z* projections (Figure 7c–e; Figure S10, Supporting Information) show that the structure is resolved in *xy* ($\sigma \approx 5$ nm) and in *z* with a demonstrated resolution better than 3 nm. To the best of our knowledge, this is the finest structural detail in the axial direction that has been resolved by optical microscopy. Another advantage of measuring DNA PAINT on graphene is that unspecific surface binding of imagers goes along with complete quenching instead of creating unspecific localizations.

3. Conclusion

We have introduced graphene-on-glass coverslips as a novel platform for single-molecule biophysics, biosensing, and super-resolution microscopy. Graphene represents a broadband, unbleachable energy transfer acceptor that is transparent for imaging and even reduces background by quenching unspecifically bound molecules. Using DNA origami structure nanopositioning, we carried out a series of assays with several unique and innovative abilities including the detection of the angle of a FRET pair as well as its distance with respect to a surface. GET tracking as a dynamic tool for super-resolution enables isotropic precision down to the molecular range. The combination of DNA PAINT with visualized structural details of 2.5 nm in *z*-direction provided by graphene quenching enables unique resolution. In combination with novel imaging modalities such as p-MINFLUX[36,37] and the potential to synergistically exploit graphene's electrical properties, graphene energy transfer opens new windows for single-molecule biophysics, biosensing, and super-resolution with exquisite resolution close to the coverslip.

Supporting Information

Supporting Information is available from the Wiley Online Library or from the author.

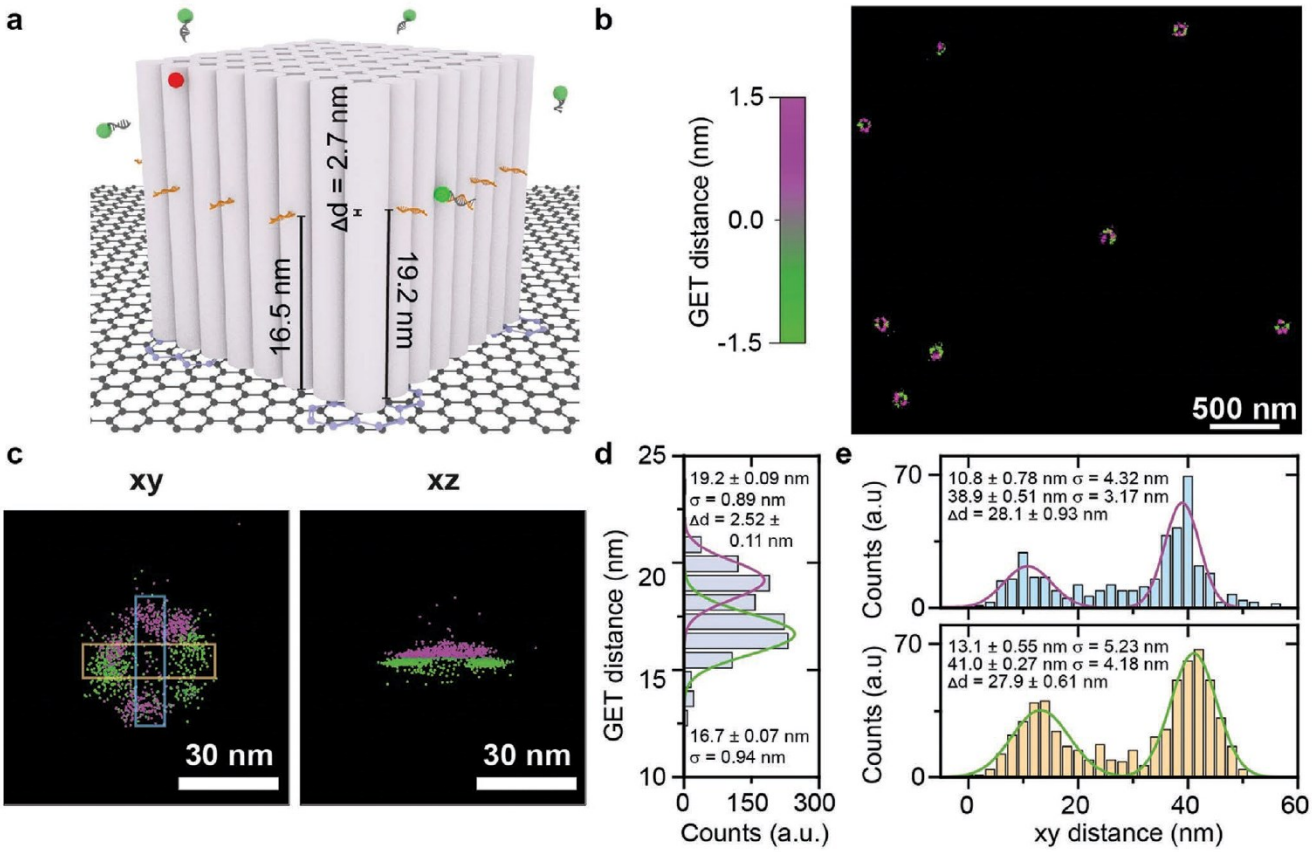

Figure 7. GET-super-resolution on a cubic DNA origami structure with DNA PAINT. a) Sketch of the DNA origami cube with DNA PAINT docking sites. Opposing sides have equal height with a difference of 2.7 nm between the adjacent sides. ATTO647N was used to monitor the DNA origami structure density. b) Super-resolution image of DNA origami cube with a heatmap. c) *x*/*y* and *x*/*z* projections of the DNA origami cube with a different height indicated by the same heatmap as in (b). d) The cross-section along the *z*-direction shows a resolution of 2.5 nm with a localization precision between 0.89 and 0.94 nm. e) Cross-sections along the *x*-axis (blue histogram) and the *y*-axis (orange histogram) in the *xy* plane with a localization precision between 3.2 nm and 5.2 nm.

Acknowledgements

I.K. and J.B. contributed equally to this work. I.K. and K.Z. acknowledge support by the Foundation for Polish Science (HOMING/2017-4/32 and POIR.04.04.00-00-42E8/17-00) and National Science Center (Sonata 2019/35/D/ST5/00958). Financial support by the Deutsche Forschungsgemeinschaft (DFG, Grant Nos. INST 86/1904-1 FUGG and TI 329/14-1, excellence cluster e-conversion under Germany's Excellence Strategy—EXC2089/1–390776260, Project-ID 201269156 – SFB1032) and by the Center for NanoScience (CeNS) is gratefully acknowledged.

Open access funding enabled and organized by Projekt DEAL.

Conflict of Interest

The invention entitled "Method of immobilization nucleic acid structure on surface of graphene, graphene modified by immobilization of nucleic acid structure and its use" has been submitted to European Patent Office (Authors: Dr. Izabela Kaminska and Prof. Dr. Philip Tinnefeld), number EP19461514.2. Prof. Dr. Philip Tinnefeld is consulting and mentoring the GATTAquant team.

Data Availability Statement

Research data are not shared.

Keywords

biophysics, biosensing, DNA origami, Förster-type resonance energy transfer, graphene, single molecules, super-resolution

Received: February 8, 2021
Revised: March 10, 2021
Published online: May 3, 2021

[1] K. S. Novoselov, V. I. Fal'ko, L. Colombo, P. R. Gellert, M. G. Schwab, K. Kim, *Nature* **2012**, *490*, 192.

[2] A. C. Ferrari, F. Bonaccorso, V. Fal'ko, K. S. Novoselov, S. Roche, P. Bøggild, S. Borini, F. H. L. Koppens, V. Palermo, N. Pugno, J. A. Garrido, R. Sordan, A. Bianco, L. Ballerini, M. Prato, E. Lidorikis, J. Kivioja, C. Marinelli, T. Ryhänen, A. Morpurgo, J. N. Coleman, V. Nicolosi, L. Colombo, A. Fert, M. Garcia-Hernandez, A. Bachtold, G. F. Schneider, F. Guinea, C. Dekker, M. Barbone, Z. Sun, C. Galiotis, A. N. Grigorenko, G. Konstantatos, A. Kis, M. Katsnelson, L. Vandersypen, A. Loiseau, V. Morandi, D. Neumaier, E. Treossi, V. Pellegrini, M. Polini, A. Tredicucci, G. M. Williams, B. Hee Hong, J. H. Ahn, J. Min Kim, H. Zirath, B. J. Van Wees, H. Van Der Zant, L. Occhipinti, A. Di Matteo, I. A. Kinloch, T. Seyller, E. Quesnel, X. Feng, K. Teo, N. Rupesinghe,

P. Hakonen, S. R. T. Neil, Q. Tannock, T. Löfwander, J. Kinaret, *Nanoscale* **2015**, *7*, 4598.
[3] R. Ye, J. M. Tour, *ACS Nano* **2019**, *13*, 10872.
[4] S. K. Krishnan, E. Singh, P. Singh, M. Meyyappan, H. S. Nalwa, *RSC Adv.* **2019**, *9*, 8778.
[5] A. Ambrosi, C. K. Chua, A. Bonanni, M. Pumera, *Chem. Rev.* **2014**, *114*, 7150.
[6] F. Federspiel, G. Froehlicher, M. Nasilowski, S. Pedetti, A. Mahmood, B. Doudin, P. Serin, J. Lee, D. Halley, B. Dubertret, P. Gilliot, S. Berciaud, *Nano Lett.* **2015**, *15*, 1252.
[7] A. Brenneis, L. Gaudreau, M. Seifert, H. Karl, M. S. Brandt, H. Huebl, J. A. Garrido, F. H. L. Koppens, A. W. Holleitner, *Nat. Nanotechnol.* **2015**, *10*, 135.
[8] L. Gaudreau, K. J. Tielrooij, G. E. D. K. Prawiroatmodjo, J. Osmond, F. J. García de Abajo, F. H. L. Koppens, *Nano Lett.* **2013**, *13*, 2030.
[9] I. Kaminska, J. Bohlen, S. Rocchetti, F. Selbach, G. P. Acuna, P. Tinnefeld, *Nano Lett.* **2019**, *19*, 4257.
[10] R. J. Stöhr, R. Kolesov, K. Xia, R. Reuter, J. Meijer, G. Logvenov, J. Wrachtrup, *ACS Nano* **2012**, *6*, 9175.
[11] J. Kim, L. J. Cote, F. Kim, J. Huang, *J. Am. Chem. Soc.* **2010**, *132*, 260.
[12] A. T. L. Tan, J. Kim, J. K. Huang, L. J. Li, J. Huang, *Small* **2013**, *9*, 3252.
[13] H. Ahmad, M. Fan, D. Hui, *Composites, Part B* **2018**, *145*, 270.
[14] E. Morales-Narváez, A. Merkoçi, *Adv. Mater.* **2019**, *31*, 1805043.
[15] H. Zhang, H. Zhang, A. Aldalbahi, X. Zuo, C. Fan, X. Mi, *Biosens. Bioelectron.* **2017**, *89*, 96.
[16] C. Zhu, D. Du, Y. Lin, *2D Mater.* **2015**, *2*, 032004.
[17] A. Ghosh, A. Sharma, A. I. Chizhik, S. Isbaner, D. Ruhlandt, R. Tsukanov, I. Gregor, N. Karedla, J. Enderlein, *Nat. Photonics* **2019**, *13*, 860.
[18] R. M. R. Adão, R. Campos, E. Figueiras, P. Alpuim, J. B. Nieder, *2D Mater.* **2019**, *6*, 045056.
[19] S. Moon, W. Li, M. Hauser, K. Xu, *ACS Nano* **2020**, *14*, 5609.
[20] A. Savchenko, V. Cherkas, C. Liu, G. B. Braun, A. Kleschevnikov, Y. I. Miller, E. Molokanova, *Sci. Adv.* **2018**, *4*, 70351.
[21] S. Krause, E. Ploetz, J. Bohlen, P. Schuler, R. Yaadav, F. Selbach, F. Steiner, I. Kamińska, P. Tinnefeld, *ACS Nano* **2021**, *15*, 6430.
[22] E. Lerner, T. Cordes, A. Ingargiola, Y. Alhadid, S. Y. Chung, X. Michalet, S. Weiss, *Science* **2018**, *359*, 1133.
[23] B. Hellenkamp, S. Schmid, O. Doroshenko, O. Opanasyuk, R. Kühnemuth, S. Rezaei Adariani, B. Ambrose, M. Aznauryan, A. Barth, V. Birkedal, M. E. Bowen, H. Chen, T. Cordes, T. Eilert, C. Fijen, C. Gebhardt, M. Götz, G. Gouridis, E. Gratton, T. Ha, P. Hao, C. A. Hanke, A. Hartmann, J. Hendrix, L. L. Hildebrandt, V. Hirschfeld, J. Hohlbein, B. Hua, C. G. Hübner, E. Kallis, A. N. Kapanidis, J. Y. Kim, G. Krainer, D. C. Lamb, N. K. Lee, E. A. Lemke, B. Levesque, M. Levitus, J. J. McCann, N. Naredi-Rainer, D. Nettels, T. Ngo, R. Qiu, N. C. Robb, C. Röcker, H. Sanabria, M. Schlierf, T. Schröder, B. Schuler, H. Seidel, L. Streit, J. Thurn, P. Tinnefeld, S. Tyagi, N. Vandenberk, A. M. Vera, K. R. Weninger, B. Wünsch, I. S. Yanez-Orozco, J. Michaelis, C. A. M. Seidel, T. D. Craggs, T. Hugel, *Nat. Methods* **2018**, *15*, 669.
[24] J. Bohlen, A. Cuartero-González, E. Pibiri, D. Ruhlandt, A. I. Fernández-Domínguez, P. Tinnefeld, G. P. Acuna, *Nanoscale* **2019**, *11*, 7674.
[25] K. A. Velizhanin, T. V. Shahbazyan, *Phys. Rev. B: Condens. Matter Mater. Phys.* **2012**, *86*, 245432.
[26] T. Bian, R. Chang, P. T. Leung, *Plasmonics* **2016**, *11*, 1239.
[27] V. D. Karanikolas, C. A. Marocico, A. L. Bradley, *Phys. Rev. B: Condens. Matter Mater. Phys.* **2015**, *91*, 125422.
[28] S. A. Biehs, G. S. Agarwal, *Appl. Phys. Lett.* **2013**, *103*, 243112.
[29] A. Yildiz, J. N. Forkey, S. A. McKinney, T. Ha, Y. E. Goldman, P. R. Selvin, *Science* **2003**, *300*, 2061.
[30] S. Hou, J. Exell, K. Welsher, *Nat. Commun.* **2020**, *11*, 3607.
[31] A. I. Chizhik, J. Rother, I. Gregor, A. Janshoff, J. Enderlein, *Nat. Photonics* **2014**, *8*, 124.
[32] S. Isbaner, N. Karedla, I. Kaminska, D. Ruhlandt, M. Raab, J. Bohlen, A. Chizhik, I. Gregor, P. Tinnefeld, J. Enderlein, R. Tsukanov, *Nano Lett.* **2018**, *18*, 2616.
[33] M. Raab, J. J. Schmied, I. Jusuk, C. Forthmann, P. Tinnefeld, *ChemPhysChem* **2014**, *15*, 2431.
[34] R. Jungmann, C. Steinhauer, M. Scheible, A. Kuzyk, P. Tinnefeld, F. C. Simmel, *Nano Lett.* **2010**, *10*, 4756.
[35] R. Jungmann, M. S. Avendaño, J. B. Woehrstein, M. Dai, W. M. Shih, P. Yin, *Nat. Methods* **2014**, *11*, 313.
[36] F. Balzarotti, Y. Eilers, K. C. Gwosch, A. H. Gynnå, V. Westphal, F. D. Stefani, J. Elf, S. W. Hell, *Science* **2017**, *355*, 606.
[37] L. A. Masullo, F. Steiner, J. Zähringer, L. F. Lopez, J. Bohlen, L. Richter, F. Cole, P. Tinnefeld, F. D. Stefani, *Nano Lett.* **2020**, *21*, 840.

CORRECTION

Graphene Energy Transfer for Single-Molecule Biophysics, Biosensing, and Super-Resolution Microscopy

Izabela Kamińska, Johann Bohlen, Renukka Yaadav, Patrick Schüler, Mario Raab, Tim Schröder, Jonas Zähringer, Karolina Zielonka, Stefan Krause, and Philip Tinnefeld**

Adv. Mater. **2021**, *33*, 2101099

DOI: 10.1002/adma.202101099

In the published article, Figure 2 contained an extra panel (e) that was not mentioned in the caption. This panel also appears in the article's Supporting Information as Figure S3. An incorrect version had been used in the production data. The corrected version of Figure 2 is provided here as it should have appeared in the article.

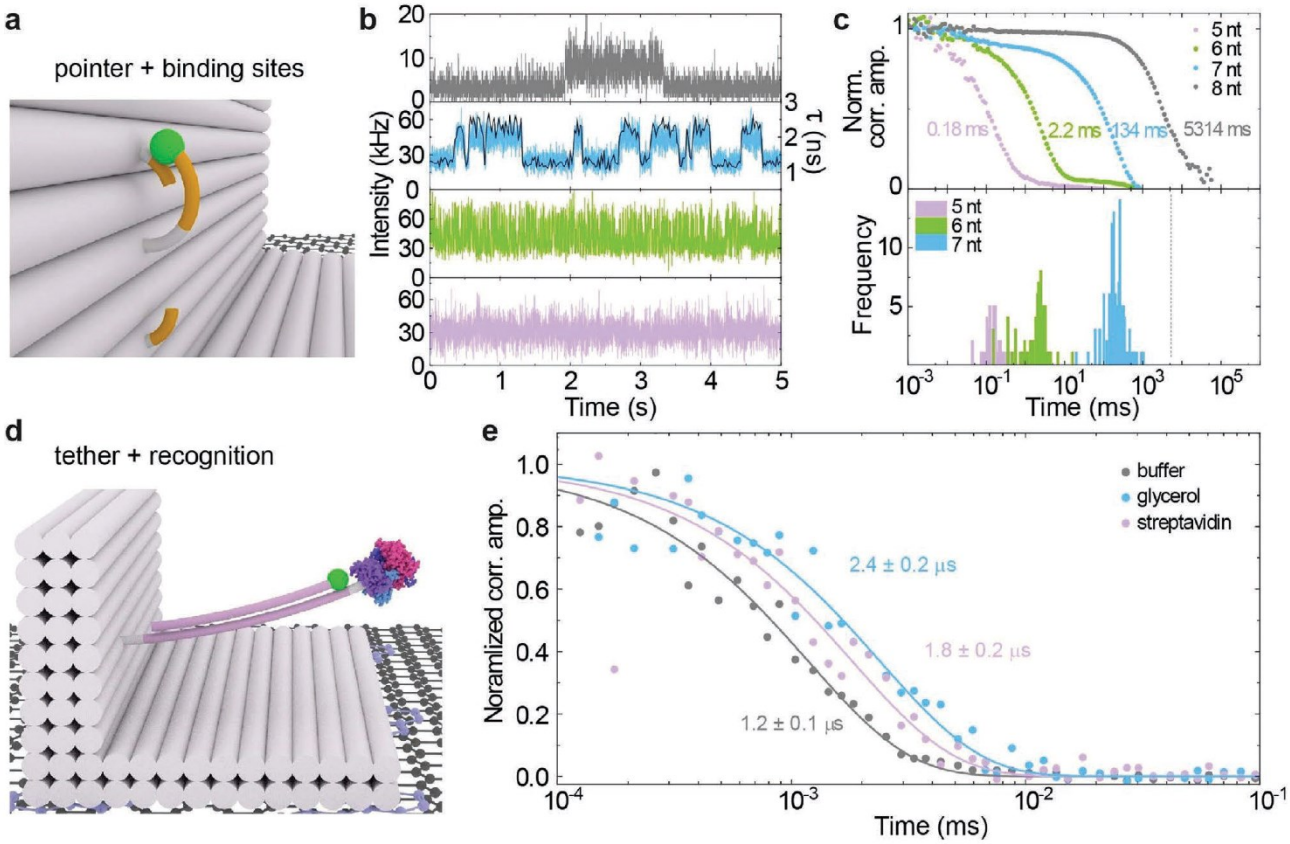

Figure 2. Dynamic DNA origami nanostructures studied with GET. a) Sketch of the L-shaped DNA origami structure with a flexible pointer with fluorescent dye (Cy3B), and upper (26.5 nm) and lower (16.1 nm) binding strands yielding GET efficiencies of 15.7% (τ_{up} = 2.6 ns) and 59.3% (τ_{low} = 1.3 ns). b) Representative transients for 8 (gray), 7 (blue), 6 (green), and 5 (lilac) nt binding. For 7 nt binding, the fluorescence lifetime (black) is also shown with 20 ms binning. All transients were acquired at 3 µW excitation power, except for eight nt binding (1 µW). c) Normalized correlation functions averaged over several transients and corresponding frequency distribution resulting from analyzing each transient individually. The gray dashed vertical line represents the correlation time for 8 nt extracted from concatenated transients. d) Sketch of the biosensing system with a 44 nt long tether, Cy3B, and a target recognizing unit (biotin) and target (streptavidin). e) Averaged correlation functions for photons with a long microtime (>2.5 ns) for measurements of the tether fluctuations in buffer (gray), in buffer with 30% glycerol (blue) and in buffer, incubated with streptavidin (lilac) after subtracting the fit of the correlation functions calculated from photons with a short microtime (<2.5 ns). See Supporting Information for a detailed description of the gating procedure.

DOI: 10.1002/adma.202105719

ADVANCED MATERIALS

Supporting Information

for *Adv. Mater.,* DOI: 10.1002/adma.202101099

Graphene Energy Transfer for Single-Molecule Biophysics, Biosensing, and Super-Resolution Microscopy

Izabela Kamińska, Johann Bohlen, Renukka Yaadav, Patrick Schüler, Mario Raab, Tim Schröder, Jonas Zähringer, Karolina Zielonka, Stefan Krause, and Philip Tinnefeld**

Supporting Information

Graphene Energy Transfer for Single-Molecule Biophysics, Biosensing & Superresolution Microscopy

Izabela Kamińska, Johann Bohlen, Renukka Yaadav, Patrick Schüler, Mario Raab, Tim Schröder, Jonas Zähringer, Karolina Zielonka, Stefan Krause, Philip Tinnefeld**

Table of Contents

1. Materials and Methods 2
1.1. Buffers and recipes 2
1.2. Dye molecules 2
1.3. Preparation of DNA origami structures 3
1.4. Preparation of graphene-on-glass coverslips 4
2. Imaging and Analysis 5
2.1. Fluorescence confocal microscope I 5
2.2. Fluorescence confocal microscope II 5
2.3. TIRF microscope I 6
2.4. TIRF microscope II 7
3. Experiments 7
3.1. Distance determination from fluorescence lifetimes. 7
3.2. Dynamics with GET. 9
3.3. Expanding FRET. 14
3.4. Graphene biosensing 21
3.5. GET tracking. 24
3.6. GET-DNA PAINT superresolution. 26
4. DNA origami structure design 29
5. DNA sequences 30
6. References 49

1. Materials and Methods

1.1. Buffers and recipes

If no other company is mentioned, chemicals were purchased from Sigma Aldrich.

Table S1. The list of buffers with recipes.

Name	Recipe
FOB20	20 mM $MgCl_2 \cdot 6H_2O$ 20 mM Tris base 20 mM acetic acid 1 mM EDTA-$Na_2 \cdot 2\ H_2O$
FOB12.5	12.5 mM $MgCl_2 \cdot 6H_2O$ 20 mM Tris base 20 mM acetic acid 1 mM EDTA-$Na_2 \cdot 2\ H_2O$
PCA/Trolox12	2 mM Trolox (6-hydroxy-2,5,7,8-tetramethylchroman-2-carboxylic acid) 25 mM PCA (protocatechuic acid) 12 mM $MgCl_2 \cdot 6H_2O$ 40 mM Tris base 20 mM acetic acid 1 mM EDTA-$Na_2 \cdot 2H_2O$
PCA/Trolox2	2 mM Trolox (6-hydroxy-2,5,7,8-tetramethylchroman-2-carboxylic acid) 25 mM PCA (protocatechuic acid) 2 M NaCl 40 mM Tris base 20 mM acetic acid 1 mM EDTA-$Na_2 \cdot 2H_2O$
50× PCD	2.8 mM PCD (protocatechuate 3,4-dioxygenase from pseudomonas sp.) 50% glycerol 50 mM KCl 100 mM Tris HCl 1 mM EDTA-$Na_2 \cdot 2H_2O$
Glox12	2mM aged Trolox 1% glycerin 12.5 mM $MgCl_2 \cdot 6H_2O$ 1× TAE 0.8 µM Glucose oxidase 0.04% Catalase

1.2. Dye molecules

Table S2. Dyes used in all experiments and the properties which determined their selection. All dye molecules are suitable for single-molecule applications and high-resolution microscopy. More information can, e.g. be found on the manufacturer's web representation and in refs.[1–3]

Dye molecule	Sections/experiments	Properties
ATTO647N	- Distance determination from fluorescence lifetimes.	- fluorescence label in the red spectral region, - exceptionally high photostability,

	- Expanding FRET. - Colocalization dye in GET superresolution.	- absorption and fluorescence independent of pH, - cationic dye, which may stick to negatively charged DNA.
ATTO643	- Distance determination from fluorescence lifetimes/orientation of L-shaped DNA origami structure. - Graphene biosensing.	- similar properties as ATTO647N, - significantly reduced tendency for unspecific binding, - anionic dye, does not stick to negatively charged DNA, - recommended for dynamic experiments.
Cy3B	- Dynamics with GET. - GET tracking.	- fluorescence label in the orange spectral region (560 nm) - bright dye in combination with PCA/PCD - negligible blinking with oxygen scavenging and ROXS - cationic dye, which may stick to negatively charged DNA.
ATTO542	- Expanding FRET. - GET superresolution. Colocalization dye in: - Distance determination from fluorescence lifetimes; - Graphene biosensing.	- fluorescence label in the green spectral region, - high photostability and high fluorescence quantum yield, - very suitable for oligonucleotide labeling, used in both static and dynamic experiments (non-sticky).

1.3. Preparation of DNA origami structures

The cube-shaped DNA origami structure was purchased from GATTAquant®. The other DNA origami nanostructures used were designed in caDNAno and utilized the p8064 scaffold derived from M13mp18 bacteriophages. DNA origami structures were folded with a 10-fold excess of unmodified and internally labeled oligonucleotides and a 100-fold excess of biotinylated or pyrene-modified oligonucleotides in comparison to the scaffold in 1× FOB20 buffer. The details of the folding program can be found here[4]. After folding, 1× Blue Juice gel loading buffer was added to the DNA origami solution which was then purified via agarose-gel electrophoresis with 1.5% agarose gel in 50 mL of FOB12.5 buffer (details in Table S2). The specific band for the nanostructure was extracted from the gel. Before putting the purified DNA origami solution onto glass or graphene, the concentration was adjusted with FOB12.5 buffer to 25 pM (GET tracking), 800 pM (GET-DNA PAINT superresolution) or 50 pM (all the other experiments).

Table S3. Agarose-gel electrophoresis protocols for each experiment.

Experiment	peqGREEN (VWR) µL/100 µL of buffer	Voltage [V]	Time [h]
Distance determination from fluorescence lifetimes	2	80	1
Dynamics with GET	2	80	1
Expanding FRET	none	60	2
Graphene biosensing	2	60	1.5
GET tracking	none	60	2

Positions and distances of dyes in DNA origami structures were estimated assuming a distance of 0.34 nm between the nucleotides along the DNA double helix and 2.7 nm between the centers of adjacent helices, in a square lattice.[5,6] Additionally, 1 nm was added to include the presence of pyrene molecules incorporated via external labeling.[7] Any deviations from the estimated values may stem from bending or tilting of DNA origami structures.[8] It also has to be taken into account that differences between the designed and measured distances may depend on the specific structure, dye-DNA interactions and salt concentration.

1.4. Preparation of graphene-on-glass coverslips

Monolayer graphene on a 60 mm × 40 mm copper substrate with poly(methyl methacrylate)(PMMA) on top was purchased from Graphenea®. Subsequently, a wet-transfer approach was used to transfer the graphene to glass coverslips.[9] All coverslips were treated with UV-Ozone cleaning at 100 ˚C for 30 minutes on each side to remove any contaminants from the surface. Smaller pieces of roughly 0.25 cm² were carefully cut from the PMMA/Gr/Cu foil. The copper was wet-etched by letting a piece float with the copper film exposed to 0.2 M ammonium persulfate for ~4 hours. A coverslip was dipped vertically while slowly moving towards the PMMA/Gr and scooped it gently out of the solution and transferred to milliQ water in order to wash out the residues of ammonium persulfate.[9] The step of washing PMMA/Gr was repeated twice with fresh milliQ water. Next, the PMMA/Gr was scooped with a glass coverslip and carefully dried using nitrogen stream. Another layer of liquid PMMA (M_w = 120,000 g/mol) dissolved in chlorobenzene (50 mg/mL) was drop-casted on top of the first PMMA/Gr layer. This allowed the dried PMMA to re-dissolve thus relaxing the underlying graphene monolayer and forming an improved contact with the substrate.[10] After 30 minutes, the PMMA/Gr on glass was first dipped in acetone for 5-10 min., then in toluene for 5-10 min., and again in fresh acetone for 5-10 min. After each washing step, in acetone or toluene, the

samples were dried with a nitrogen stream. Finally, the sample was placed on active coal, heated on a heating plate to 230°C, for 30 minutes, and then left to cool down.

2. Imaging and Analysis

2.1. Fluorescence confocal microscope I

Single-molecule fluorescence measurements (Distance determination from fluorescence lifetimes and Graphene biosensing) were performed on a custom-built confocal microscope I, based on an inverted microscope (IX-83, Olympus Corporation, Japan) and a 78 MHz-pulsed supercontinuum white light laser (SuperK Extreme, NKT Photonics A/S, Denmark) with selected wavelengths of 532 nm and 639 nm. The wavelengths are selected via an acousto-optic tunable filter (AOTF, SuperK Dual AOTF, NKT Photonics A/S, Denmark). This is controlled by a digital controller (AODS 20160 8R, Crystal Technology, USA) via a computer software (AODS 20160 Control Panel, Crystal Technology, Inc., USA). A second AOTF (AA.AOTF.ns: TN, AA Opto-Electronic, France) was used to alternate 532 nm and 639 nm wavelengths, as well as to further spectrally clean the laser beam. It is controlled via self-written LabVIEW software (National Instruments, USA). A neutral density filter was used to regulate the laser intensity, followed by a linear polarizer and a λ/4 plate to achieve circularly polarized excitation. A dichroic beam splitter (ZT532/640rpc, Chroma Technology, USA) and an oil immersion objective (UPlanSApo 100×, NA = 1.4, WD = 0.12 mm, Olympus Corporation, Japan) were used to focus the excitation laser onto the sample. Nanopositioning was performed using a Piezo-Stage (P-517.3CL, E-501.00, Physik Instrumente GmbH&Co. KG, Germany). The excitation powers at both 532 and 639 nm were set to 1 μW. Emitted light was collected using the same objective and filtered from the excitation light by the dichroic beam splitter. The light was later focused on a 50 μm pinhole (Linos AG, Germany) and detected using Single-Photon Avalanche Diodes (SPCM, AQR 14, PerkinElmer, Inc., USA) registered by a TCSPC system (HydraHarp 400, PicoQuant GmbH, Germany) after additional spectral filtering (RazorEdge 647, Semrock Inc., USA for the red channel and BrightLine HC 582/75, Semrock Inc., USA for the green channel). A custom-made LabVIEW software (National Instruments, USA) was used to process the acquired raw data.

2.2. Fluorescence confocal microscope II

Single-molecule fluorescence measurements (Dynamics with GET and Expanding FRET) were performed on another home-built confocal setup II based on an Olympus IX71 microscope. The green laser (LDH-P-FA-530B, Picoquant) is controlled by a PDL 828 “Sepia II” (Picoquant).

The green fiber (polarisation maintaining fiber with FC/APC output connector) coupled laser light is decoupled via a F220APC-532 collimator (Thorlabs) and cleaned up with a 532/2 (Z532/10 X, Chroma) filter before passing a dichroic mirror (640 LPXR, Chroma) for optional combination with the already cleaned up (Z640/10 X, Chroma) red laser (LDH-D-C-640, Picoquant). A linear polarizer (WP12L-Vis, Thorlabs) and a quarter-wave plate (AQWP05M-600, Thorlabs) are combined to obtain circularly polarized light. After passing a second dichroic mirror (zt532/640rpc, Chroma) the beam is focused via an oil immersion objective (UPLSAPO 100 XO, NA 1.40, Olympus) onto the samples. The sample is scanned with a piezo-stage (P-527.3CD, Physik Instrumente) which is controlled by an E-727 controller (Physik Instrumente). The emitted light is focused on a 50 µm pinhole (Thorlabs) and collimated with a lens (AC050-150-A-ML, Thorlabs).

For the correlation sample, the beam is cleaned with a filter set (582/75 BrightLine HC, Semrock and LP03-532RU-25, Semrock) before it is split by a 50:50 non-polarizing beam splitter cube (BS013, Thorlabs).

For FRET experiments, the beam is split with a dichroic mirror (640 LPXR, Chroma) and cleaned with a filter set (red: FESH0750, Thorlabs and LP02-647RU-25, Semrock green: 582/75 BrightLine HC, Semrock and LP03-532RU-25, Semrock). Afterwards, the beam is focused via lenses (red: AC080-020-B-ML; green: AC080-020-A-ML, Thorlabs) on two APDs (SPCM-AQRH-TR-14, Excelitas). The APDs' signal is processed with a HydraHarp 400 (PicoQuant) and controlled with the software SymPhoTime 64 (PicoQuant). Further data analysis is performed with self-written Matlab and LabVIEW routines.

2.3. TIRF microscope I

In the home-built widefield/ TIRF (total internal reflection fluorescence) microscope, a 644 nm diode laser (150 mW, iBeam smart, Toptica Photonics) and a 560 nm fiber laser (1 W, MPB Communications) are exciting the samples. After both lasers are cleaned up with filters (644 nm: Brightline HC 650/13, Semrock; 560 nm: Brightline HC 561/4, Semrock) the beams are combined with a dichroic mirror (T612lpxr, Chroma). To expand the beam profile, the laser passes through lenses (Bi-convex f50, Thorlabs; AC f120, Linos). In the microscope body (IX 71, Olympus) the beam passes a dichroic mirror (z476-488/568/647, Chroma) and is focused by an objective (100×, NA =1.4, UPlanSApo, Olympus). To avoid drift, the objective is mounted on a nose piece (IX-2NPS, Olympus). The emitted light is collected by the same objective and passes a 1.6× optical lens and an emission filter (644 nm: ET 700/75, Chroma or 560 nm: Brightline HC 561/4, Chroma). Images and movies are recorded by an EMCCD

(electron multiplying charge-coupled device) camera (iXon+ 3384, Andor). The lasers are operated with Topas iBeam smart software (Toptica Photonics, 644 nm), GUI-VFL software (MPB Communications, 560 nm) and the camera with ImageJ plugin Micro-Manager 1.4.[11]

2.4. TIRF microscope II

The second widefield/TIRF microscope is powered by a 644 nm diode laser (150 mW, ibeam smart, Toptica Photonics) and a 532 nm fiber laser (1W, MPB Communication). After both lasers are cleaned up (644 nm: Brightline HC 650/13, Semrock; 532 nm z532/647x, Chroma) and aligned, the beam is directed over a dichroic mirror (Dual Line zt532/640 rpc, AHF Analysentechnik) to the back focal plane of the objective (UPLXAPO 100×, NA = 1.45, WD = 0.13, Olympus). The microscope body (IX71, Olympus) is equipped with a nose piece (IX2-NPS, Olympus) and put on an actively stabilized optical table (TS-300, JRS Scientific Instruments) to stabilize the sample. The emission is cleaned up (644 nm: ET 700/75, Chroma; 532 nm: BrightLine 582/75, AHF Analysentechnik) and detected on an EMCCD camera (iXon X3 DU-897, Andor). The lasers are operated with Topas iBeam smart software (Toptica Photonics, 644 nm), GUI-VFL software (MPB Communications, 532 nm) and the camera with ImageJ plugin Micro-Manager 1.4.[11]

3. Experiments

3.1. Distance determination from fluorescence lifetimes.

All measurements for this part were carried out on the confocal setup I (SI chapter 2.1) with a pulsed interleaved laser excitation of 532 nm and 639 nm. Three samples of a pillar-shaped DNA origami structure were labeled with a green (ATTO542) and a red (ATTO647N) dye molecule at the heights of 15.9 and 52.5 nm (**1**), 11.6 and 23.4 nm (**2**), 15.9 and 15.9 nm (**3**), respectively. Each DNA origami nanostructure was immobilized either on neutravidin–biotinylated BSA glass coverslips using biotin modification at the base of the structure, or they were immobilized on graphene using pyrene modification. Single molecules were identified in the fluorescence images and their fluorescence lifetime was determined. Figure S1a depicts the scatter plot and corresponding histograms of the obtained fluorescence lifetime values for the measurements performed on glass (▽) or graphene (□, +, ○). All three populations of the nanostructures measured on graphene are clearly distinguishable. The distributions of the fluorescence lifetime are slightly broadened on graphene compared to glass, directly indicating minimal heterogeneity in the DNA origami structure immobilization. We can attribute this heterogeneity to several factors, including, e.g., tilting or structural heterogeneity of the DNA

origami structure, less photons recorded in the presence of graphene, as well as impurities or defects of graphene substrate.[12] Nevertheless, the differences are not substantial, and most importantly the three populations are well-separated.

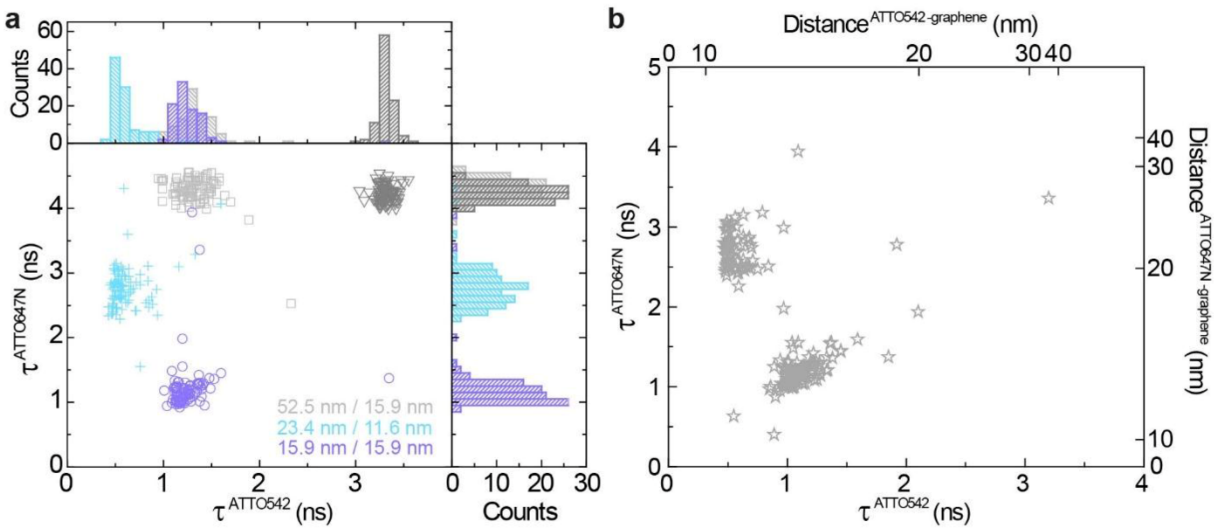

Figure S1. Distance determination from fluorescence lifetimes. (a) Scatter plot and corresponding histograms of fluorescence lifetime of colocalized dye molecules at a pillar-shaped DNA origami structure (both dye molecules within one DNA origami structure): ATTO542 and ATTO647N, at various heights; each DNA origami sample measured separately on glass (▽) or graphene (□, +, ○), with ATTO542/ATTO647N at 15.9/52.5 nm (□ grey), 11.6/23.4 nm (+ cyan) or 15.9/15.9 nm (○ violet) distance from graphene. (b) Scatter plot of fluorescence lifetime of colocalized dye molecules at a pillar-shaped DNA origami structure: two mixed DNA origami structures with ATTO542 and ATTO647N dyes molecules at the height of 11.6/23.4 nm and 15.9/15.9 nm above graphene, imaged together on one graphene substrate.

Next, samples (**2**) and (**3**) were mixed, immobilized on graphene together and imaged. Again, single molecules were identified in the fluorescence images and their fluorescence lifetime was determined (Figure S1b). From the reference measurements on glass (τ_{gl}), the mean values of the fluorescence lifetime of both dyes were obtained:

$$\overline{\tau_{gl,542}} = 3.4 \pm 0.1 \ ns$$

$$\overline{\tau_{gl,647N}} = 4.3 \pm 0.1 \ ns$$

These values were used to further calculate the energy transfer efficiency η to graphene for each dye molecule attached to DNA origami structure immobilized on graphene (τ_{gr}):

$$\eta = 1 - \frac{\tau_{gr}}{\overline{\tau_{gl}}}$$

The energy transfer efficiency from an emitter to graphene scales with d^{-4}, where d is a distance between both:

$$\eta = \frac{1}{1 + \left(\frac{d}{d_0}\right)^4}$$

d_0 is the distance of the 50% energy transfer efficiency to graphene, which equals to 17.7 nm and 18.5 nm for a dye ATTO542 and ATTO647N, respectively.[7]

Based on both equations for the energy transfer efficiency, expressed either by the fluorescence lifetime or by the distance d_0, the distance between the dye molecule and graphene can be calculated:

$$d = d_0 \sqrt[4]{\frac{1}{\eta} - 1}$$

The results from Figure S1, expressed by the height at which a dye has been positioned above graphene is presented in Figure 1.

The data was analyzed via a home-written LabVIEW software. The fluorescence lifetime was deconvoluted with FluoFit software from Picoquant.

3.2. Dynamics with GET.

Data acquisition was realized with the home built confocal microscope II (SI chapter 2.1). A 532 nm pulsed laser was used for excitation at 80 MHz repetition rate and an excitation power of 3 µW. The fluorescence was separated into two channels via a 50:50 non-polarizing beam splitter cube followed by subsequent detection by two avalanche photodiodes. This Hanbury-Brown-Twiss detection configuration allows to overcome temporal resolution limits (~ 1 µs) posed by detector dead times and after pulsing. To stabilize Cy3B, a combination of ROXS and oxygen scavenging system is used. The first buffer contains aqueous solution of aged Trolox with PCA (PCA/Trolox12) and the second a 50× PCD (for measurements both buffers were mixed in a 1:50 ratio (50× PCD : Trolox/PCA12).[13,14]

The data was analyzed with a home written Matlab routine based on the photon arrival time correlation algorithm proposed by Laurence et al.[15,16] Technically, we calculate the cross-correlation function as two different signals are correlated. Apart from the following brief description, we denote the correlation as the autocorrelation as the fluorescence coming from the same molecule is split by a 50:50 nonpolarizing beam splitter and detected by two avalanche photo detectors. The cross-correlation of discrete photon arrival time stamps t_i (arrival time of photon i in channel A) and u_j (arrival time of photon j in channel B) is defined as:

$$\hat{C}_{AB}(\tau) = \frac{n(\{(i,j) \ni t_i = u_j - \tau_l\})(T - \tau_l)}{n(\{i \ni t_i \leq T - \tau_l\})n(\{j \ni u_j \geq \tau_l\})}$$

In this equation τ_l represents the lag-time and T the duration of the experiment while $n(\{(i,j) \ni t_i = u_j - \tau_l\})$ counts the number of photon pairs in the time range $(T - \tau_l)$ which fulfill the condition $t_i = u_j - \tau_l$, $n(\{i \ni t_i \leq T - \tau_l\})$ counts the number of photons from channel A which fulfill $t_i \leq T - \tau_l$ and $n(\{j \ni u_j \geq \tau_l\})$ counts the number of photons from channel B which fulfill $u_j \geq \tau_l$.

It is commonly difficult to assign fast correlation components to physical processes as they can be masked by other processes including rotational diffusion and photophysics (e.g. triplet state formation). This problem also arises for our 44 nt tether which exhibits two components in the same time range in the autocorrelation function. With GET, the intensity fluctuation is, however, directly correlated to a change of fluorescence lifetime making it possible to disentangle fluorescence lifetime correlated components from other components by using different subsets of photons for calculating the cross-correlation function. As energy transfer to graphene reduces the fluorescence lifetime, the observed intensity fluctuations are mostly related to photons emitted later after the excitation pulse (i.e. those with higher microtimes, see section B in Figure S2a).

For this time-gated autocorrelation, photon counts in both channels with micro-time stamps according to a previously defined time-gate were neglected prior to calculating the cross-correlation function. The result of such a gating approach is illustrated in Figure S2 where a comparison of different time gates is shown for the pointer-like model system presented in Figure 2 exhibiting 7 nt binding strands. The applied short (section A in Figure S2a, 1 to 2.5 ns) and long (section B in Figure S2a, 2.5 to 12 ns) time gates are illustrated in Figure S2a. The depicted transient shows upper and lower binding events with dwell times in the 100 ms time range. The aforementioned cross-correlation function was calculated for all photons (b, c), for the short time-gate A (d, e) and for the long time-gate B (f, g). It is clearly visible, that the applied time-gates reduce (d, e) or increase (f, g) the contrast of the two observed intensity levels and thus also the resulting amplitude of the cross-correlation function. This enables us to discriminate on-off blinking processes which do not feature changes in intensities due to changes of the fluorescence lifetime but are exclusively related to off-states such as triplet-states, redox blinking or cis-trans isomerization. Applying time-gating to such blinking transients would not influence the amplitude of the cross-correlation amplitude.

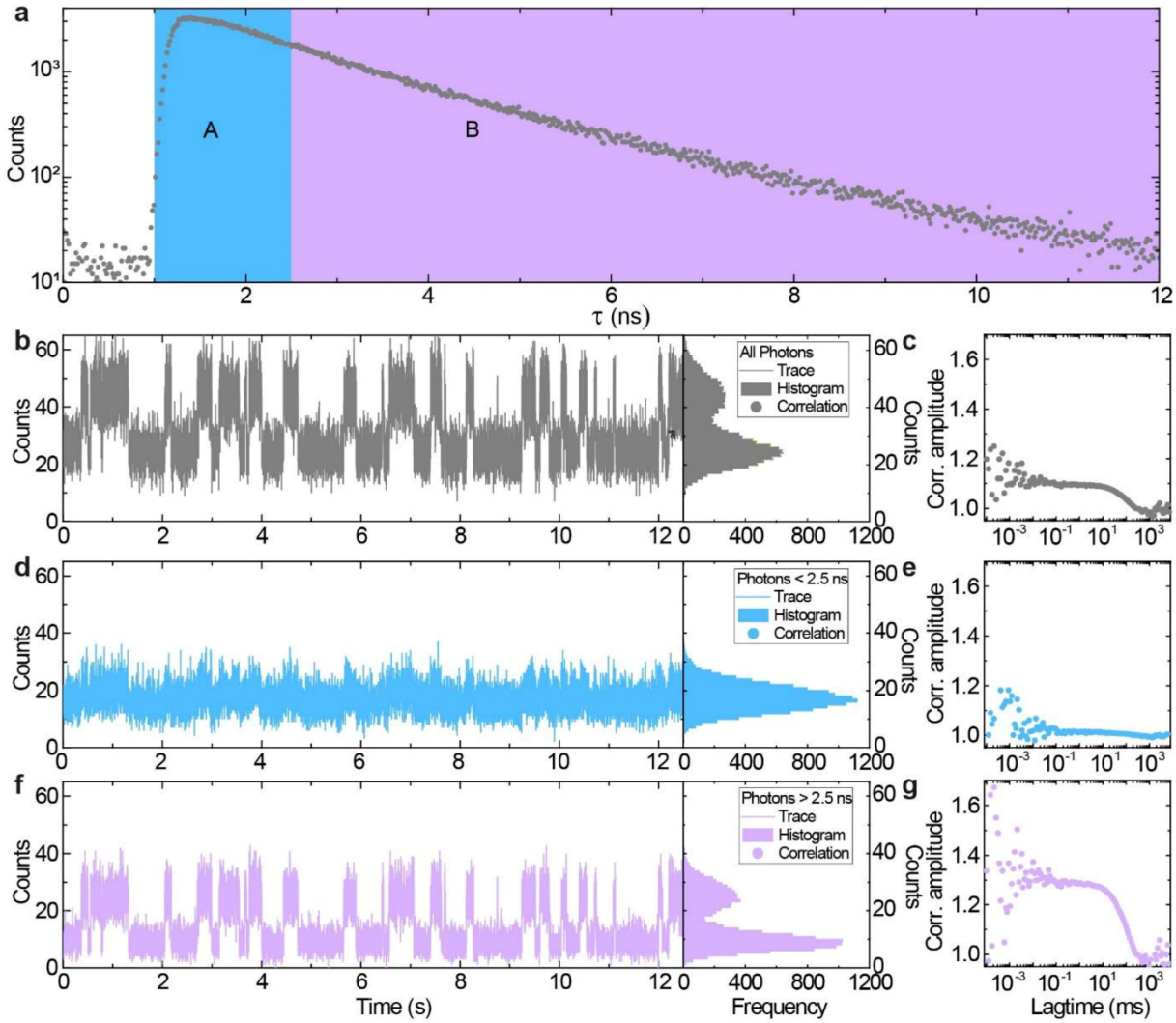

Figure S2. Dynamics with GET. a) Fluorescence decay curve of a DNA origami structure featuring a pointer with Cy3B binding to upper and lower binding strands with 7 nucleotides. The sections A (lilac) and B (blue) illustrate the short (1 to 2.5 ns) and the long (2.5 to 12 ns) time-gate. b) Example transient belonging to the fluorescence decay in (a). c) Correlation function resulting from correlating all photons of the two detection channels with each other. d) Same data as in (b) but with photons belonging to the short time-gate A. e) Correlation function resulting from correlating the photons given in (d). f) Same data as in (b) but with photons belonging to the long time-gate B. g) Correlation function resulting from correlating the photons given in (f).

By comparing cross correlations of "early photons" (short time-gate A, blue graphs in Figure S3), with cross correlations of "late photons" (long time-gate B, lilac graphs in Figure S3), one can distinguish components that are correlated with lifetime changes from those that are not. Accordingly, we assign the short component of the cross correlation shown in Figure S3 (i) to tether fluctuations. Subtraction of the photophysical component leads to a cleared correlation function (Figure S3 ii), that yields a characteristic correlation time of 1.0 ± 0.1 µs. This is in agreement with the expected time scales according to the following simplified model, where the confined diffusion of a flexible tether is approximated by calculating the diffusion coefficient of a 44 bp long dsDNA strand in water to be D = 32 µm^2/s.[17] Using the

characteristic length scale on which the strongest change in fluorescence intensity occurs, approximated with $d_0 = 18$ nm, we calculate the correlation time $\tau_C = \frac{d_0^2}{4D} = 3.1\ \mu s$. The estimated time might be slightly longer due to additional fluctuations of the flexible tether and the spherical distribution of accessible states around the point of attachment. This fast correlation time is sensitive to changes of the diffusion properties of the tether and can be used to detect binding events (streptavidin to biotin at the end of the tether in Figure S3, iii) as well as viscosity changes (buffer with 30% glycerol in Figure S3, iv) as indicated for the cross correlations of exemplary single molecule transients. For the averaged data set in Figure 2e, only transients yielding a cross correlation which could be fitted by a single component in the time range below 5 µs and with negligible further components in the time range above 5 µs were considered.

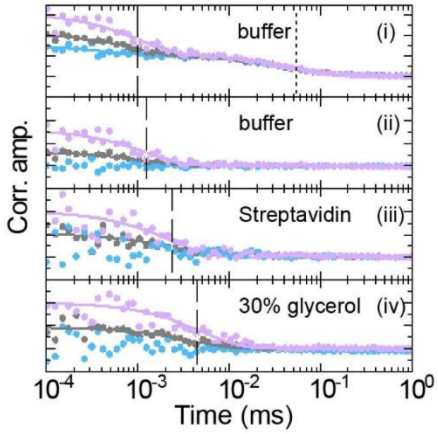

Figure S3. Dynamics with GET. Correlation functions for single transients calculated from all photons (gray), photons belonging to the long time-gate A (lilac) and short time-gate B (blue). (i) shows a raw correlation function of the tether fluctuations in buffer including a longer, photo physical time component. The mono-exponential fit of the short-gated data (blue) in (i) was subtracted to yield the data in (ii). The same correction was applied to the examples for a tether with bound streptavidin (iii) and for the tether fluctuating in buffer with additional 30% of glycerol (iv).

Reference FCS measurements

For estimating the relative change of the correlation time of the tether motion upon binding of streptavidin or changing the buffer conditions to 30% glycerol, we assume a similar effect for the confined diffusion of the tether bound to the L-shaped DNA origami structure as for the free diffusion of the tether without the L-shaped DNA origami structure in solution. Therefore, the tether was folded in absence of the DNA origami structure. The single stranded tether component with the Cy3B dye (1 µl of a 100 µM solution) was mixed with a two-fold access of the single-stranded tether component with biotin (2 µl of a 100 µM solution) to avoid unhybridized fluorescently labeled ssDNA and then folded at 37 °C for 1 h in FOB12.5 buffer. The resulting stock solution was diluted in a ratio of 1:20 with 2M NaCl buffer and then

incubated with 1 µl of streptavidin solution (1 mg/mL). Both solutions were further diluted in a ratio of 1:50 with a combination of ROXS and oxygen scavenging system. The first buffer contains aqueous solution of aged Trolox with PCA (PCA/Trolox12) and the second a 50 × PCD (for measurements both buffers were diluted in a 1:50 ratio (50× PCD:Trolox/PCA12). Afterwards, FCS measurements were performed for both solutions and the resulting normalized cross correlation functions are depicted in Figure S4a. Both curves show negligible components for triplet blinking in the time range between 1 to 50 µs. More important, the binding of streptavidin to the biotin recognition unit can be seen from fitting a 3D diffusion component. Fitting of the data reveals a correlation time (260 ± 10) µs for the pure tether diffusion and (330 ± 10) µs for the tether diffusion with bound streptavidin which gives an increase of the correlation time of a factor of 1.27 due to the increase in hydrodynamic radius.

The changes in correlation time upon increase of the buffer viscosity were measured in a similar way. Therefore, the diffusion was compared via FCS in a combination of ROXS and oxygen scavenging system. The first buffer containing aqueous solution of aged Trolox with PCA (PCA/Trolox12) and the second a 50× PCD (for measurements both buffers were diluted in a 1:50 ratio (50× PCD:Trolox/PCA12) and in buffer with additional 30% of glycerol. The corresponding normalized cross correlation curves are shown in Figure S4b and clearly reveal a reduced diffusion coefficient and thus an increased correlation time for the increased viscosity. While the diffusion in buffer agrees with the data in Figure S4a (280 ± 40 µs), the correlation time in buffer with glycerol increases by a factor of 2.4 to 680 ± 30 µs as revealed by fitting with a 3D diffusion model.

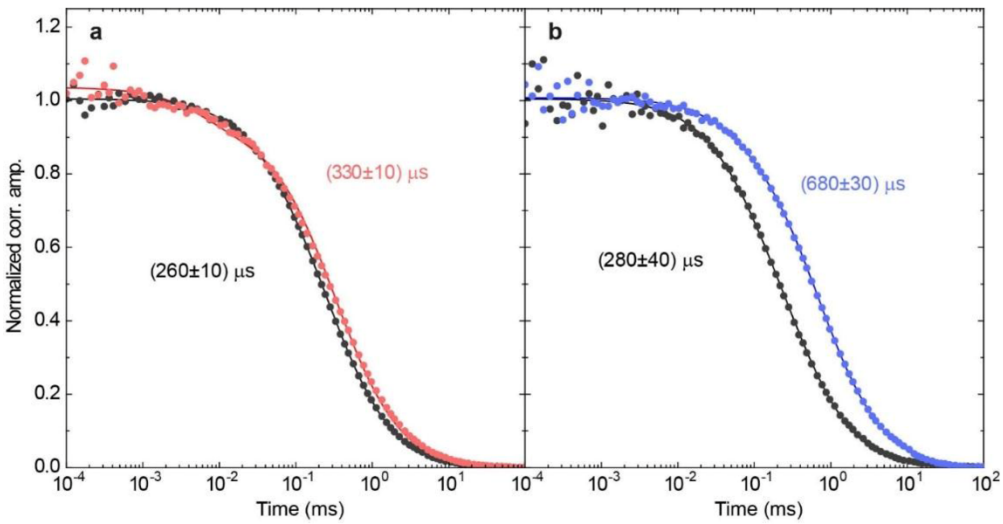

Figure S4. Dynamics with GET. a) Fluorescence correlation curve of the 44 nt long tether without (black) and with (red) incubation with streptavidin. The curves were fitted with a 3D-diffusion component and an additional triplet component. b) Fluorescence correlation curve of the 44 nt long tether in buffer (black) and in buffer with additional 30% of glycerol (blue), curve fitting in analogy to (a).

3.3. Expanding FRET.

The whole data from the FRET experiments were measured on the confocal setup II (SI chapter 2.1) with the acceptor bleaching approach. In case of the static FRET sample, the 532 nm and 640 nm laser powers were set to 1 µW and 9 µW, respectively. For the dynamic FRET sample, the 532 nm laser power was switched to 0.5 µW. The DNA origami stock solution was diluted to a concentration of 25 pM with FOB12.5. To stabilize the FRET pair (ATTO542/ATTO647N) a combination of ROXS and oxygen scavenging system was used.[13,14] The first buffer contains aqueous solution of aged Trolox with PCA (PCA/Trolox12) and the second a 50× PCD (for measurements, both buffers were diluted in a 1:50 ratio (50× PCD:Trolox/PCA12). To verify the correct orientation of the L-shaped DNA-origami structure on graphene, only transients with modulation before and after acceptor bleaching were considered.

The data was analyzed via a home-written LabVIEW software. The fluorescence lifetime was deconvoluted with FluoFit software from Picoquant.

The FRET efficiency E and the FRET rate k_{ET} are calculated with the fluorescence lifetime of the donor in presence of the acceptor τ_{DA} and after acceptor bleaching τ_D.

$$E = 1 - \frac{\tau_{DA}}{\tau_D}$$

$$k_{ET} = \frac{1}{\tau_{DA}} - \frac{1}{\tau_D}$$

Based on E and including the distance r_0 where 50% of the energy is transferred to the acceptor (for ATTO542/ATTO647N r_0 = 6.32 nm), the distance between donor and acceptor is calculated. The FRET distance is calculated from data measured on glass to avoid influence of a potentially slightly changed energy transfer rate constant on graphene.[18–21]

$$r = \sqrt[6]{\frac{1}{E_{gl}} - 1}\, r_0$$

The GET efficiency η and GET rate constant k_G are calculated with the fluorescence lifetime of species on glass (index gl) and graphene (index gr). A line above results indicates an average from previous calculations (exemplary shown for the acceptor species):

$$\eta_A = 1 - \frac{\tau_{A,gr}}{\overline{\tau_{A,gl}}}$$

$$k_{G,A} = \frac{1}{\tau_{A,gr}} - \frac{1}{\overline{\tau_{A,gl}}}$$

The GET distance is calculated from η and the distance d_0 from the dye to graphene where 50% energy transfer is observed (17.7 nm for ATTO542 and 18.5 nm for ATTO647N).[7] For these calculations, only the acceptor and the donor after acceptor bleaching are taken into account because the donor in presence of the acceptor shows a lower η compared to the donor after acceptor bleaching due to the additional FRET rate constant k_{ET}, (exemplary shown for the donor):

$$d = \sqrt[4]{\frac{1}{\eta_D} - 1}\, d_{0,D}$$

Finally, the angle between donor and acceptor δ was extracted.

$$\delta = \mathrm{acos}\left(\frac{a-d}{\bar{r}}\right)$$

When the direction of FRET is close to vertical, e.g., for the vertical structure of the static FRET experiment (Figure 3f) and for the "up" binding mode of the dynamic FRET experiment (Figure 4f), the numerator can be bigger than the mean distance $\bar{r}$ (the denominator). In this case, δ is not defined and the angle is set to 0° or 180°, respectively (also see bars at 0° for Figure 3f and 4f). To obtain meaningful mean angles for the underlying populations, we calculated the mean angles from the mean distances to the surface: $\bar{\delta} = \mathrm{acos}\left(\frac{\overline{a-d}}{\bar{r}}\right)$.

The evaluated data is illustrated in Figure S5. The fluorescence lifetime of the acceptor on glass (red line, 4.0 ns) and graphene (orange line, 1.2 ns) for every subspecies (h, d, v) is the same indicating that the distance to graphene is the same (Figure S5a). Whereas the same behavior is observed by the donor after acceptor bleaching on glass (turquoise line, 3.0 ns), the donor after acceptor bleaching on graphene is varying because of the different distance of the donor to graphene. The donor lifetime in presence of the acceptor on glass shows the influence of FRET and the same sample on graphene has an additional GET contribution.

The FRET efficiency E decreases from horizontal over diagonal to vertical on glass as well as on graphene (Figure S5b,d). In addition, the FRET efficiency also decreases on graphene in comparison to glass. The FRET rate constant k_{ET} (d) is not affected by the graphene in the diagonal and vertical case but in the horizontal case k_{ET} is slightly increasing on graphene compared to the glass sample. This might indicate an enhanced energy transfer from the donor to the acceptor mediated by graphene which has been postulated in theoretical works.[18–21]

The GET data (Figure S5c, e) also shows the influence of FRET. In the presence of the acceptor (DA), the donor is always shifted to lower GET efficiencies η than after acceptor bleaching (D).

This is caused by the competing FRET rate constant k_{ET}. The GET efficiency and the rate constant k_G stay constant for every acceptor as expected (Figure S4c,e).

The calculated FRET distance (Figure S5f) for the glass sample shows a decrease from horizontal over diagonal to vertical which is already observed in the fluorescence lifetime and FRET data. While the acceptor GET distance is constant, the donor distance d to graphene varies as designed (Figure S5g). From the combined information of Figures S4f and g the angle δ is calculated. The horizontal sample has an angle of $87.0 \pm 0.6°$ which is close to the designed angle of 90°. The angle for the diagonal (ex: $27.9 \pm 0.6°$, designed: 37°) and vertical samples ($3.7 \pm 14.0°$, designed: 0°) agree well with the designed angles.

In conclusion, the combination of FRET and GET shows a novel approach to determine the position of a donor-acceptor pair in space.

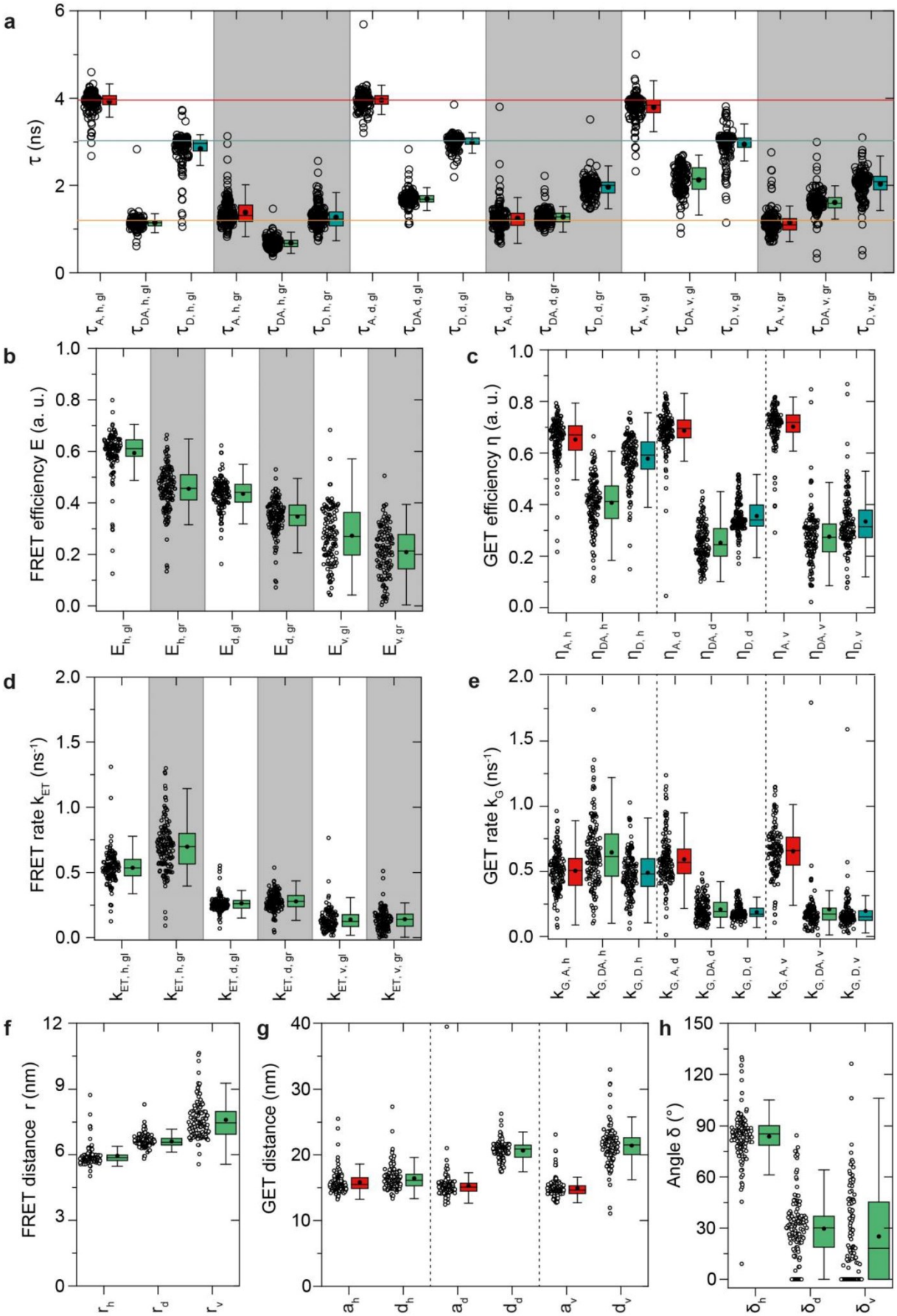

Figure S5. Measured and calculated data of the static FRET experiments. The data is illustrated by hollow dots (∘) and a box plot. In the box plot, the dot (•) indicates the mean average, while the line (-) is the median. The

percentile ranging from 25% to 75% and the whiskers are in the range of 1.5 IQR. A gray background implies a measurement on graphene. a) shows the fluorescence lifetime of all species with average fluorescence lifetime of the acceptor on glass (red line, $\overline{\tau_{A,gl}}$ =4.0 ns), donor after acceptor bleaching (turquoise line, $\overline{\tau_{D,gl}}$ = 3.0 ns) and acceptor on glass (orange line, $\overline{\tau_{A,gr}}$ = 1.2 ns). Overall a quenching in presence of FRET and/or GET is observed. On the one hand, the FRET efficiencies on graphene are lower compared to the FRET efficiency of the same species on glass due to the additional graphene rate constant (b)). On the other hand, the FRET rate constant is similar besides the horizontal case where the FRET rate constant is slightly increased in presence of graphene (d)). The GET efficiencies are similar for all acceptor species and increase for the donor with smaller distance to graphene and FRET (c)). The GET rate constant is not influenced by the presence of FRET (e)). Based on E and with a r_0 of 6.32 nm for ATTO542 and ATTO647N, the FRET distance was calculated and is shown in f). The illustrated GET distances (g)) were calculated with a d_0 of 17.7 nm for ATTO542 and 18.5 nm for ATTO647N. h) Finally, the angle was calculated and shows the expected tendency of lower angle for the different species.

For the dynamic FRET samples, information about the conformational dynamics is additionally obtained. The dynamics can be extracted by the fluctuation of FRET (on glass, Figure 4b), GET (on graphene, after acceptor bleaching Figure 4c) or both (on graphene in presence of the acceptor, Figure 4c). The sample on glass only shows a modulation in presence of the acceptor (until 5 s), after acceptor bleaching the modulation disappears. On the graphene sample, modulation in presence and absence of the acceptor is observed. During the first excitation with green (until 6 s) the modulation is caused by the combined influence of FRET and GET, after the acceptor bleached the modulation is caused only by GET.

The "on" time, t_{on} (binding time) is extracted from autocorrelation analysis and the modulation M is calculated from the fluorescence lifetime of the "up" and "down" position.

$$M = \frac{\tau_{up} - \tau_{down}}{\tau_{up} + \tau_{down}}$$

The analysis of the dynamic FRET experiment is summarized in Figure S6. The fluorescence lifetime is decreasing in the presence of GET and FRET (Figure S6a). The conformational dynamics of the pointer are not influenced by GET and/or FRET, and the on time (t_{on}) for "up" binding event is always 80 ms, while a "down" binding event has 150 ms (Figure S6b). As expected, the modulation is the smallest for FRET only ($M_{DA,\,gl}$), and is increasing from GET only ($M_{D,\,gr}$) to the combination of both ($M_{DA,\,gr}$) (Figure S6c).

The FRET data (d, f) shows a similar behavior as the static FRET samples. The FRET efficiency is lower on graphene which is caused by the additional GET rate constant k_G. Interestingly, the FRET rate constant k_{ET} is increasing on graphene for the binding closer to graphene while k_{ET} for the upper binding site is the same on glass and on graphene.

The GET efficiency η (Figure S6e) is increasing after the acceptor bleaches as the competing FRET process disappears. η gives an idea of the relative orientation of the acceptor to both binding sites of the flexible donor strand. The acceptor is closer to the lower binding site than to the upper binding site. The GET rate constant k_G (Figure S6g) is smaller for the upper than for the lower binding site with the acceptor exhibiting an intermediate value.

The FRET distance (Figure S6h) which is calculated from the glass dataset shows a narrow distribution. The GET distance (Figure S6i) gives a first impression of the relative orientation of acceptor and both donor binding modes. Only the angle δ yields the whole information about orientation between donor and acceptor molecule (Figure S6j). For the "up" binding, the δ distribution shows a peak at 0°, as we set all data points for which the dye distance determined by GET is larger than the distance determined by FRET to zero (see discussion for static GET-FRET). Using the averages of the FRET distance and the GET values, we determine an average angle of $\delta = 19.0 \pm 6.9°$. An angle of $111.5 \pm 2.17°$ for the lower position indicates that the donor is lower than the acceptor, because the angle is above 90°.

To sum up, the combination of FRET with GET is not only limited to static systems but can also be expanded for dynamic systems to verify the orientation of a donor and acceptor in space. Importantly, the dynamics are not influenced by GET.

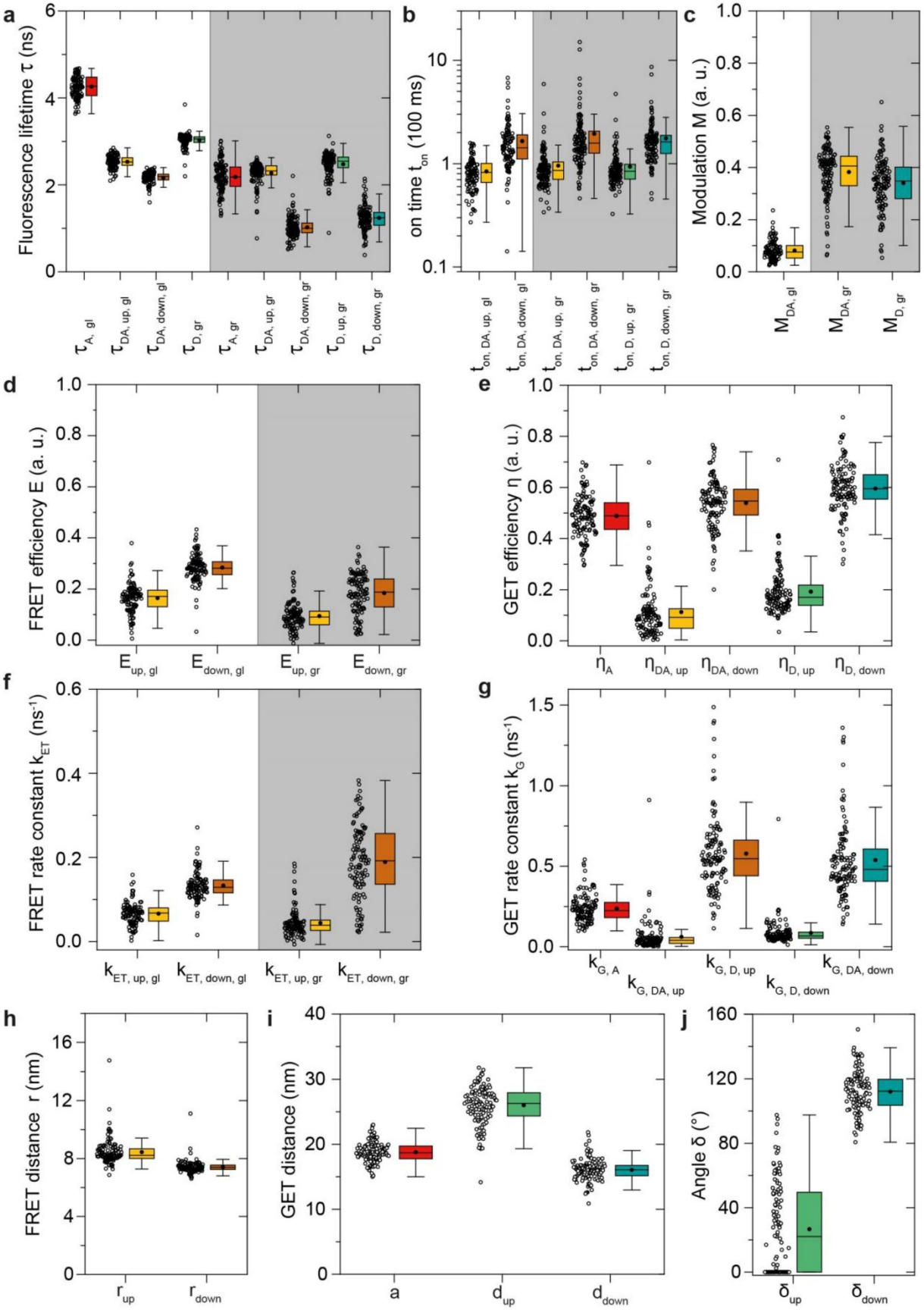

Figure S6. Measured and calculated data of the dynamic FRET experiments. The data is illustrated by hollow dots (∘) and a box plot. In the box plot the dot (•) indicates the mean average, while the line (-) is the median. The percentile ranging from 25% to 75% and the whiskers are in the range of 1.5 IQR. A gray background implies a measurement on graphene. The influence of graphene, FRET and subspecies (up and down) to the fluorescence

lifetime is illustrated in a). The on times for the "up" and "down" binding are independent of FRET and GET as expected (b)). c) shows the modulation which is higher in present of FRET and GET ($M_{DA,\ gr}$) followed by the Get only sample ($M_{D,\ gr}$) and FRET only sample ($M_{DA,\ gl}$), The FRET efficiencies are lower on graphene compared to glass due to the additional GET rate constant (d)). The FRET rate constant increased slightly closer to the graphene surface (f)). The competing FRET process decreases the GET efficiencies (e)), while the GET rate constants remained constant (g)). Based on the FRET efficiency and including the r_0 of 6.32 nm for ATTO542 and ATTO647N the FRET distance was calculated and is shown in f). The illustrated GET distances (g)) were calculated with a d_0 of 17.7 nm for ATTO542 and 18.5 nm for ATTO647N. Finally, based on h) and i) the angle for the "up" and "down" position was extracted (j).

3.4. Graphene biosensing.

A Secure Seal™ hybridization chamber was first glued on a glass coverslip in a way that the entire surface of previously transferred graphene was fully covered. The concentration of the pillar-shaped DNA origami labeled with pyrene-modified oligos was adjusted to 50 pM in 1× FOB12.5. Then the chamber was filled with 150 µL of the diluted sample, and after 1-2 minutes, the chamber was washed thrice with 1× FOB12.5 buffer. The sample was measured to collect fluorescence lifetime and intensity information for the free-capture strand and capture strand hybridized with a closing strand. Afterwards, the chamber was filled with 150 µL of 5 µM ssDNA (GTGGTATTCGAAAACAAAATCACCATCAATAACCCTCAATAAAT) and incubated for 30 minutes at room temperature, for graphene surface passivation. This was followed by the incubation with a target strand (38 nucleotides at 5 nM concentration) for 3 hours at 37 °C. Afterwards, the chamber was washed thrice with 1× FOB12.5 buffer. The sample was measured again to collect fluorescence lifetime and intensity information for the capturing strand hybridized with a target.

For these experiments, three types of the pillar-shaped DNA origami structures with the hairpin-like assay were prepared: 1) a structure with a freely moving capture strand (39 nucleotides long) with an attached ATTO643 at the height of 16.3 nm, 2) same as (1) with an additional closing strand at 9.2 nm, to which a capture strand may hybridize (getting into closed form of the assay), 3) like (2) with additional biasing strand incorporated at 30.6 nm to catch and stabilize the capture strand after the target detection (open form of the assay). Each type of the nanostructure (sketches depicted in Figure 5 and S7) was measured before and after the incubation with a target, such that six forms in total could be imaged in order to get insight into the influence of all the components on the performance of the bioassay.

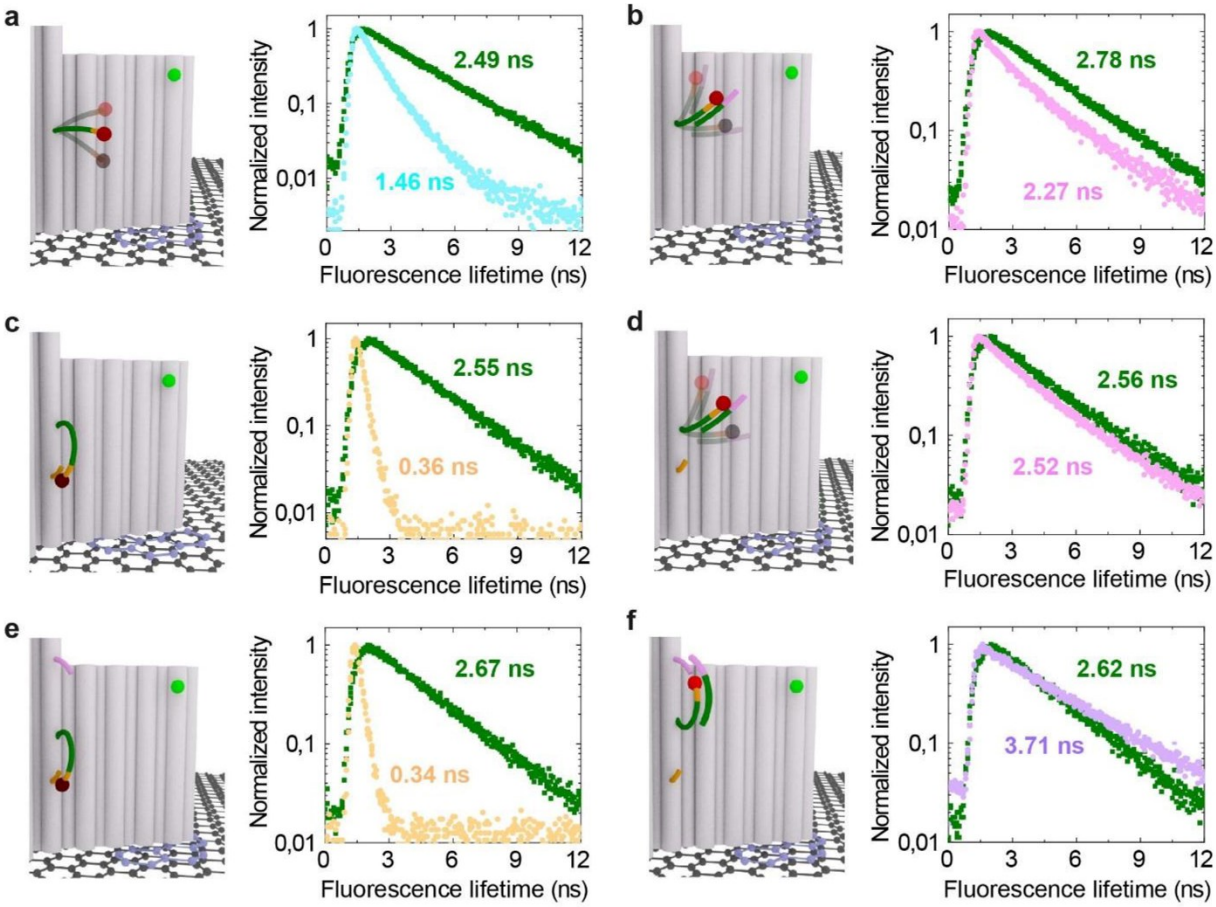

Figure S7. Graphene biosensing with a nucleic acid bioassay. Sketches (left panels) and fluorescence decays with fluorescence lifetime values obtained from the monoexponential fit (right panels) of an ATTO542 dye (internal reference) and an ATTO643 dye attached to the capture strand which is: (a) free to move (pale cyan), (b) bound to a target strand (pale magenta), (c and e) hybridized with a closing strand (orange), (d) liberated by a target strand (pale magenta), (f) liberated by a target strand and additionally caught and stabilized by a biasing strand (lilac). In all cases an ATTO542 dye was used as an internal reference, to monitor the proper orientation of a DNA origami structure on graphene and high quality of graphene.

Each pillar-shaped DNA origami structure was additionally labeled with an ATTO542 dye at a height of 23.4 nm from graphene, serving as an internal reference. It was used as an indicator of the quality of graphene as well as the functionality of the DNA origami structure itself. All measurements for this part were carried out on the confocal setup I (SI chapter 2.1) with a pulsed interleaved laser excitation of 532 nm and 639 nm. Single molecules were identified in the fluorescence images and their fluorescence lifetime was determined. For further analysis, only the colocalized spots were considered, assuring the presence of the assay with an ATTO643 dye and a reference ATTO542 dye. As an example of the entire population of all the measured colocalized molecules within one assay, we present the results obtained for the pillar-shaped DNA origami structure with a freely moving capture strand in Figure S8. Using the equations from part 3.1 of the SI, we calculated that an ATTO542 at the height of 23.4 nm, should have the fluorescence lifetime of 2.7 ± 0.3 ns. In the upper histogram in Figure S8, in

green we marked the population of the structures assigned as those with properly quenched fluorescence of the reference dye (fluorescence lifetime in the range of 2.4 – 2.9 ns). This indicates properly oriented DNA origami structure on graphene, keeping its full functionality, as well as the high quality and clean graphene. In the scatter plot, these nanostructures were marked with grey squares filled with cyan circles. On the other hand, the presence of all spots out of this range (grey histogram and empty squares in the scatter plot), may result from various deviations, such as tilting of a pillar-shaped DNA origami structure, but also defects or polymer residues on graphene. For example, the population around $\tau_{ATTO643}$ = 4.3 ns and $\tau_{ATTO542}$ = 3.4 ns indicates no fluorescence quenching of both dye molecules, resulting most probably from the presence of holes or defects in graphene or of PMMA residues. This analysis based on the fluorescence lifetime of the reference dye ATTO542 was applied for all the measured samples (final results depicted in Figure 5).

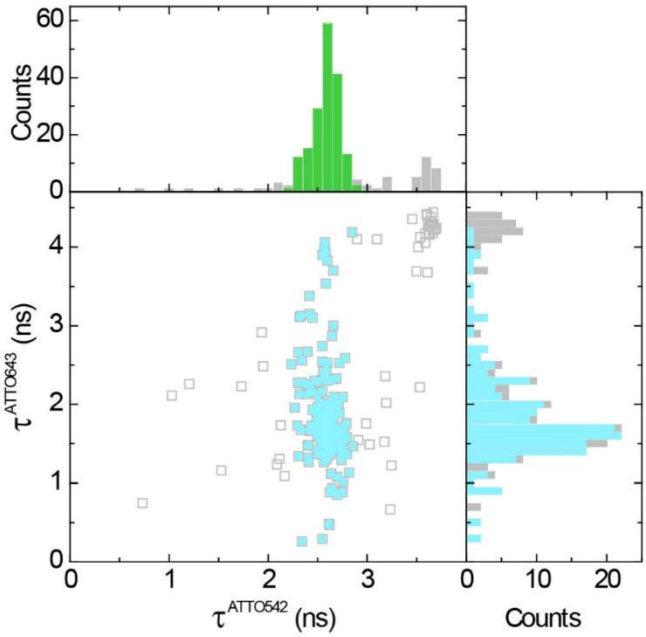

Figure S8. Graphene biosensing with a nucleic acid bioassay. Scatter plot of fluorescence lifetime of colocalized dye molecules (both dye molecules within one pillar-shaped DNA origami structure): ATTO643 at the 3' end of the freely moving capture strand (check sketch in Figure 5a and Figure S6a) and ATTO542 as an internal reference at the fixed height of 23.4 nm. In grey (□) all acquired data points and in cyan (●) population of only properly oriented pillar-shaped DNA origami structures and clean graphene (fluorescence lifetime of ATTO542 in the range between 2.3 and 2.9 ns). In the further analysis for all measured samples, such threshold for the fluorescence lifetime of ATTO542 is applied. In the top panel histogrammed fluorescence lifetime of ATTO542: in grey for all data points, in green for properly oriented DNA origami structure and high-quality graphene samples. In the right panel analogous histogram for an ATTO643 dye at the capture strand: in grey all acquired results, in cyan – data points selected for further analysis.

In order to explain the presence of the population at around 3 ns in the full assay after target binding (gray arrow in Figure 5f), called "free capture strand + target", we checked with a self-written Python code, whether the target can unintentionally bind to the DNA origami structure.

Indeed, it turned out that a fragment of the target (TA**T**AC) can stick to one of the staples in the pillar-shaped DNA origami structure at the height of ~23.1 nm, which exactly matches to the population at around 3 ns. Therefore, we modified the highlighted sequence of the target by one nucleotide (T → A) and performed the measurements again. In Figure S8, we compare both sets of measurements, (a) with the old and (b) with the new target sequence. While in the closed form (a capture strand caught by the closing strand, orange population), a very similar narrow distribution < 0.5 ns is obtained, there is a significant difference for the open form (target hybridized to the capture strand and additionally caught by the biasing strand at about 31 nm distance from graphene, lilac population). The population at about 3 ns is significantly smaller and the distribution of the fluorescence lifetime is narrower. With this small modification of the target molecule, we could further improve the performance of the GET-based bioassay.

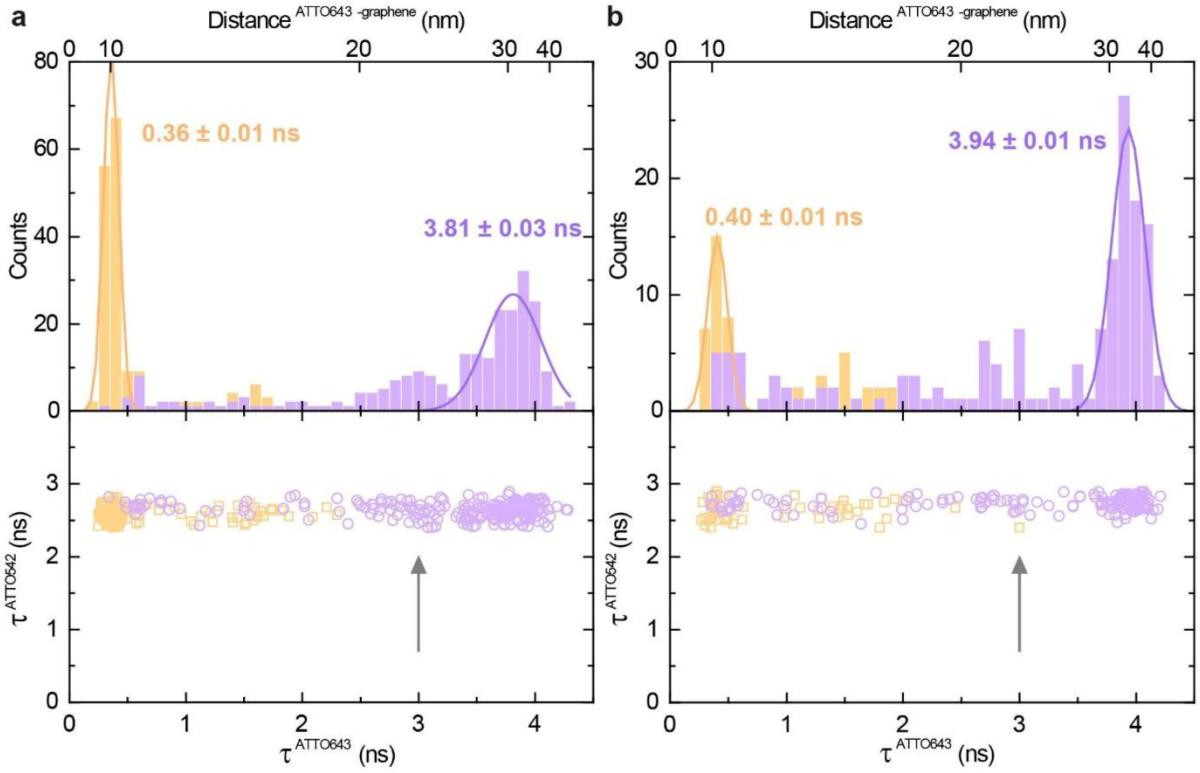

Figure S9. Graphene biosensing with a nucleic acid bioassay. Scatter plots (bottom panels) and corresponding histograms (top panels, fitted with a Gaussian function (the mean value and standard error obtained from the fit)) of fluorescence lifetime of colocalized dye molecules: ATTO643 at the 3' end of the capture strand and ATTO542 as an internal reference at the fixed height of 23.4 nm (check sketches in the Figure 5f and S7e-f). The full assay before (orange) and after (lilac) the detection of (a) the old target and (b) the new target. A significant reduction of the population at around 3 ns (marked with the arrow) is noted after exchanging just one nucleotide (T→A) of the target sequence, thereby eliminating a fragment (TA**T**AC) causing unspecific sticking to one of the staple strands of the DNA origami structure at the height of ~23.12 nm. For more details check Table S8.

3.5. GET tracking.

The data for the tracking experiments was measured on widefield setup I with a 560 nm laser power of 8 mW (200 × 200 pixel, 93 nm/pixel) with an EM-gain of 10, exposure time of 300

ms and an overall time of 400 frames. The DNA-origami structure concentration was adjusted to 25 pM and stabilized with 1:50 50× PCD:PCA/Trolox12.

The superresolution image was generated via Picasso software package, for fitting of the PSF, the MLE (maximal likelihood estimation) analysis was used and further processed with a homewritten LabVIEW software.[22] For the GET tracking analysis, one out of the triple Gaussian distribution (see Figure 6 in the main text) was defined to be at a distance of 24 nm from graphene for referencing, in accordance with the DNA origami nanostructure design.

Examples of the tracking are illustrated in Figure S10 (animated trajectories are illustrated in Supplementary video 1-3). As a reminder, in the x/y projection only two populations should be observed because the “up” and “low” binding site only differ by the z component. The distance to “mid” binding site should be around 5.4 nm. The two populations are most of the time only hard to distinguish in the x/y projection. But the additional GET superresolution shows three defined populations along either y/z or x/z or both.

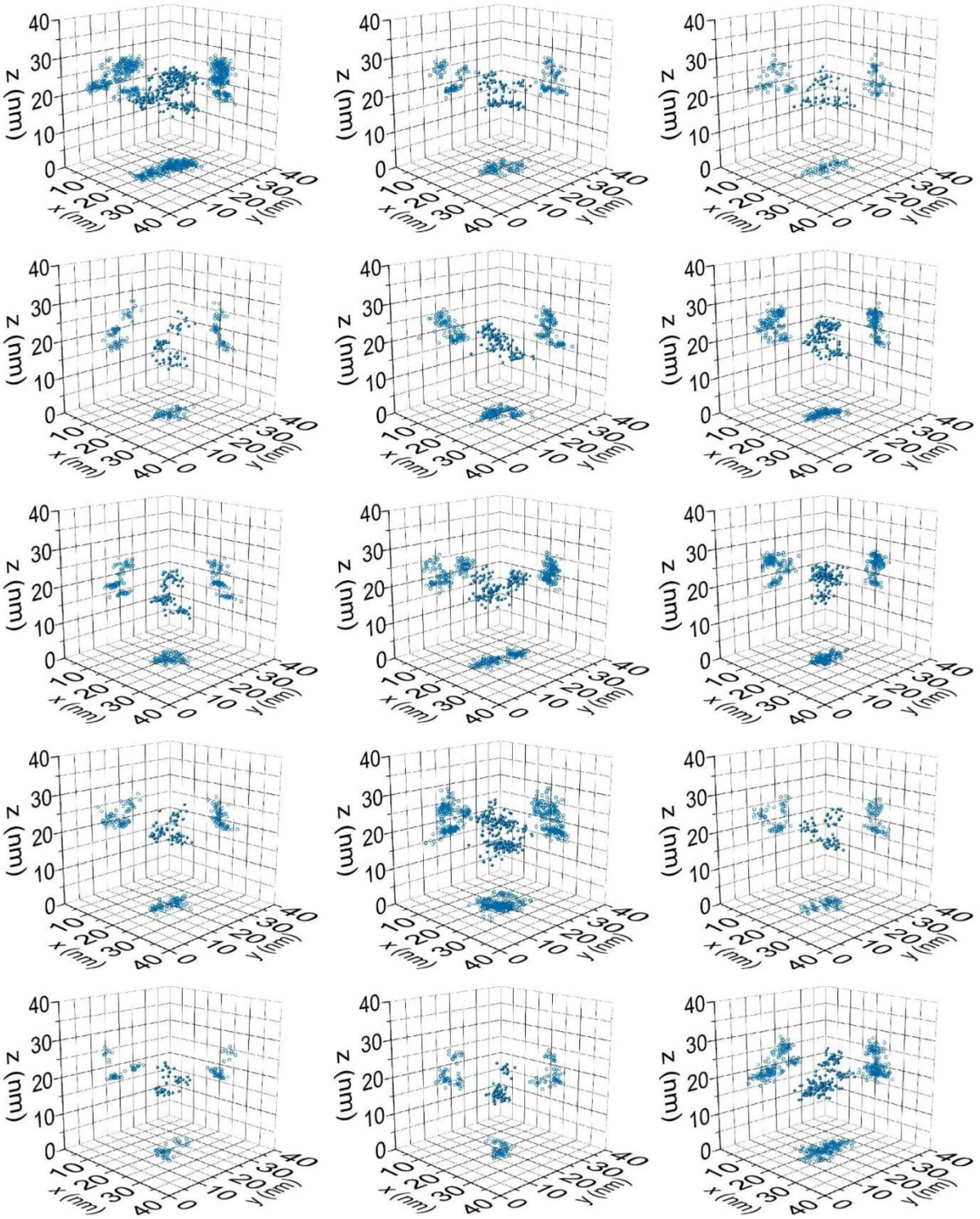

Figure S10. Superresolution tracking images. The blue spheres in the center illustrate the binding events. On the sides the projection along x/y, x/z and y/z are shown. For analyzing, the highest population is always put to 24 nm.

3.6. GET-DNA PAINT superresolution.

The data for the GET-superresolution was measured on widefield setup II (SI chapter 2.1) with a 560 nm laser power of 200 mW (200 × 200 pixel, 100 nm/pixel) with an EM-gain of 10, exposure time of 100 ms and 65000 frames in total. After incubation of the DNA origami

structures with a concentration of 800 pM in FOB12, the graphene surface was passivated to avoid sticking of the paint oligonucleotides. For the passivation, an oligonucleotide with an unspecific sequence (50 µL, 1 µM) was incubated for 1h at room temperature. The sample was measured with 2 nM Imager (ATTO542, 8 nt, sequence: CGGGCATT-ATTO542) in Glox12 buffer.

The superresolution image was generated via Picasso software package, for fitting of the PSF, the MLE (maximal likelihood estimation) analysis was used and further processed with a home-written LabVIEW software.

For the analysis, the average intensity $\bar{I}$ from the whole data was set to the height d = 17.9 nm (average between upper binding site (19.2 nm) and lower binding site (16.5 nm)).

Including d_0 (17.7 nm), the reference intensity I_{ref} (intensity without any energy transfer to the graphene) was calculated.

$$I_{ref} = \frac{\bar{I}}{\left(1 - \frac{1}{1 + \left(\frac{d}{d_0}\right)^4}\right)}$$

Based on this result, the GET distance was calculated from every intensity value.

$$d = d_0 \sqrt[4]{\frac{1}{\left(1 - \frac{I}{I_{ref}}\right)} - 1}$$

Additional superresolved images are illustrated in Figure S11. In every odd row the x/y image is shown and in every even row the x/z projection is shown. The color scale is centered between the lines of the DNA origami cube with positive values shown in green and negative values shown in lilac.

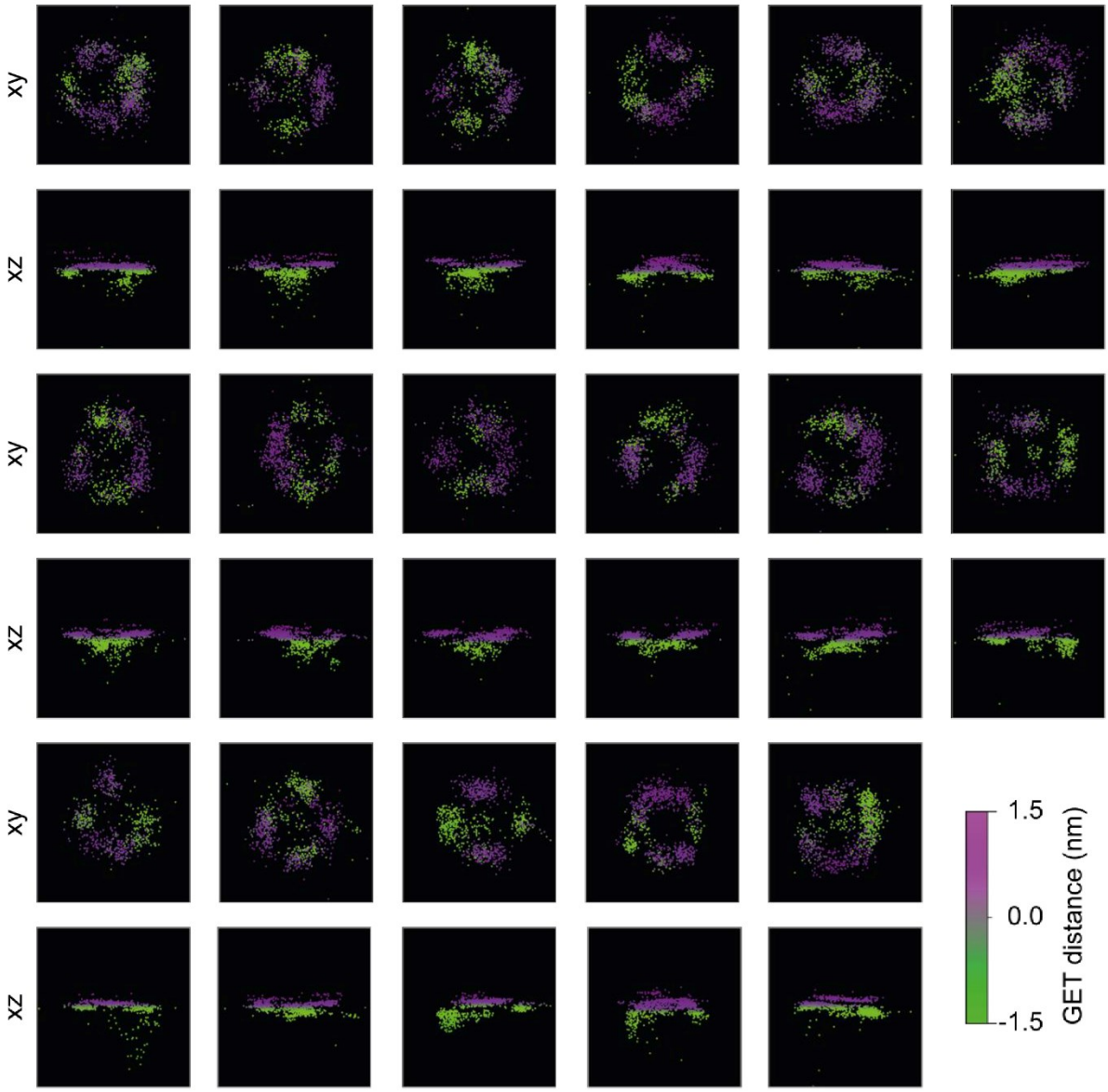

Figure S11. GET-DNA PAINT superresolution. Superresolved 70 × 70 nm images of the DNA origami cube. On the upper row the x/y projection is shown and on the lower, the x/z. The color scale is put to the center of the DNA origami structure binding events below this center are illustrated in green and above are in lilac.

4. DNA origami structure design

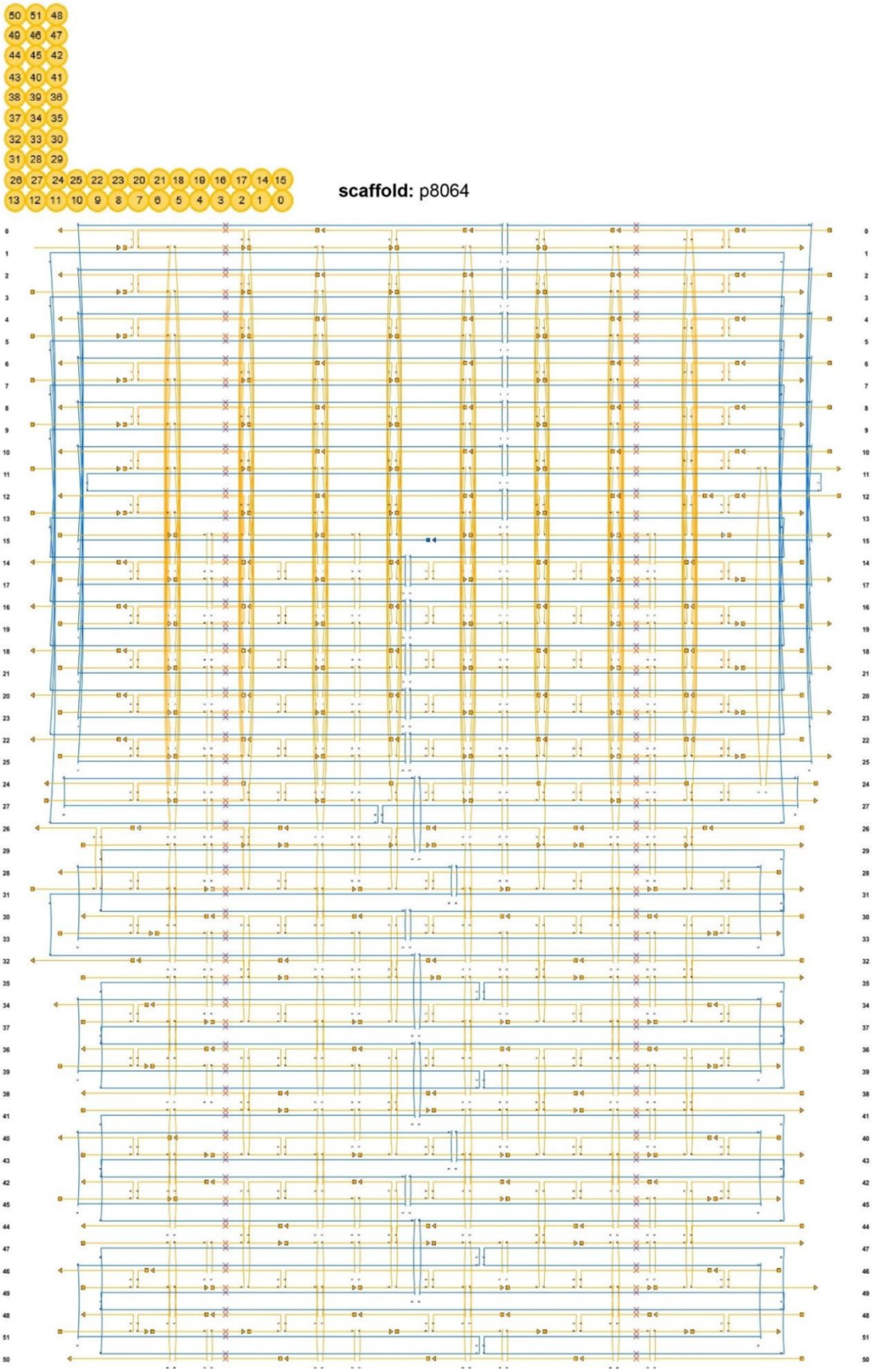

Figure S12. Cadnano design of the L-shaped DNA origami structure. Zoom in to see details.

5. DNA sequences

Table S4. Core staples from the 5' to the 3' end for the pillar-shaped DNA origami structure.

Staple ID	Sequence (5' to 3')
P1	GAGAAGGCATCTGCAATGGGATAGGTCAAAAC
P2	AACCGTGTCATTGCAACGGTAATATATTTTAAATGAAAGGGT
P3	ATCGGTCAGATGATATTCACAAACCAAAAGA
P4	GCTGGCATAGCCACATTATTC
P5	CTGTATGGGATTACCGTTAGTATCA
P6	CCATAATGCCAGGCTATCAAGGCCGGAGACATCTA
P7	CTCATCGGGATTGAGTGAGCGAGTAACAACCCGTC
P8	TAGCCAGCTTTCATCCAAAAATAAACGT
P9	TAGCCTCAGAGCATACCCTGT
P10	AATACCCCAACATTCATCAAAAATAATTCGCGTCT
P11	GGCTAAAACTTCAGAAAAGTTTTGCGGGAGATAGAACC
P12	CCCGGTTGATAAAGCATGTCAATC
P13	ATCGATGCTGAGAGTCTACAAGGAGAGGGAACGCCAAAAGGA
P14	GACAATTACGCAGAGGCATTTTCGAG
P15	TAAGTTGGCATGATTAAAGAA
P16	CCAATGTTTAAGTACGGTGTCCAAC
P17	CGGAATAGAAAGGAATGCCTTGCTAAACAACTTTCAAC
P18	GAGTTAAAAGGGTAATTGAGCGCTAATATCAGAGGAACTGAACACC
P19	TTTAGCGATACCAACGCGTTA
P20	TTTTTGCGGATGCTCCTAAAATGTTTAGATGAATTTTGCAAAAGAAGTT
P21	AATAAAACGAACTATGACCCCACCAAGC
P22	AATATCGTTAAGAGAGCAAAGCGGATTGTGAAAAATCAGGTCTTT
P23	ATTACGAGATAAATGCCAGCTTTGAGGGGACGACGACAG
P24	ACAACGCCTGTAGCATTTACCGTATAGGAAG
P25	TTACCATTAGCAAGGCCTTGAATTAGAGCCAGCCCGACTTGAGC
P26	CAGCAGCGCCGCTTGTTTATCAGCTTCACGAAAAA
P27	CTTACGGAACAGTCAGGACGTTGGGAAGAAA
P28	AGCTCTTACCGAAGCCCAATA
P29	TATTACGAATAATAAACAAATCAGATATGCGT
P30	CACGGCAACAATCCTGATATACTT
P31	CATCGAGATAACGTCAAACATAAAAGAGCAAAAGAATT
P32	CAAGCCCAATAGGAACCACCCTCACCCGGAA
P33	CATTTCGCAAATGTCATCTGCGAACGAGAGATTCACAATGCC
P34	GGCGCAGACGGTCAATCATCGAGACCTGCTCCATGTGGT
P35	CAAACGGAATAGGAAACCGAGGAATAAGAAATTACAAG
P36	ACCAACAAACCAAAATTAACAATTTCATTTGAATTACCGAGG

Staple ID	Sequence (5' to 3')
P37	CATTTGAGATAACCCACGAAACAATG
P38	AGGACAGATGAACGGTGTAACATAAGGGAACCGAAGAAT
P39	TGGCTTTTTACCGTAGAATGGAAAGCG
P40	GTTAAAGGAAAGACAGCATCTGCCTATTTAAGAGGCAGGAGGTTTA
P41	AGTAGGTATATGCGTTATACA
P42	CGAACACCAAATAAAATAGCAGCCAAGTTTGCCTTTAGCGTCAGA
P43	GCGAAACAAAGTGTAAAACACATGGCCTCGATTGAACCA
P44	AAGAAAGCTTGATACCGCCACGCATACAGACCAGGCGCTGAC
P45	CTGAATATAGAACCAAATTATTTGCACGTAAAACAACGT
P46	AGACAGCAGAAACGAAAGAGGAAATAAATCGAGGTGACAGTTAAAT
P47	CGAGGGTACTTTTTCATGAACGGGGTCATAATGCCGAGCCACCACC
P48	TAAAGCCTCCAGTACCTCATAGTTAGCG
P49	AATATGCAACTACCATCATAGACCGGAACCGC
P50	AGAAATCGTTAGACTACCTTTTTAAGGCGTTCTGACCTTTTTGCA
P51	CTAAATCGGTCAGAATTAGCAAAATTAAGCAATAAAATAATA
P52	AAATCAGCTCATTTTTTAACCATTTTGTTAAAATTCGCATTA
P53	ATAGCGAGAGGCTATCATAACCAAATCCCAAAGAAAATTTCATCCTCAT
P54	GAACTGGCTCATTACAACTTTAATCATTCTTGAGATTACTTA
P55	ACGCGAGAGAAGGCCATGTAATTTAGGCCAGGCTTAATTGAGAATCGC
P56	TAATATCAAAGGCACCGCTTCTGGCACT
P57	TTTCCATGGCACCAACCTACGTCATACA
P58	AAGACAAATCAGCTGCTCATTCAGTCTGACCA
P59	CCGTAATCAGTAGCGACAGAATCTAATTATTCATTAAAAAGG
P60	CTGGCATTAGGAGAATAAAATGAAGAAACGATTTTTTGAGTA
P61	CGCGCCGCCACCAGAACAGAGCCATAAAGGTGGAA
P62	TAGCCCGGAATAGGTGTAAGGATAAGTGCCGTCGA
P63	AAGGCTCCAAAAGGAGCCTTTATATTTTTTCACGTGCTACAGTCACCCT
P64	CAAAATCACCGGAACCAGAGCCAGATTTTGTCACAATCACAC
P65	AATTGTGTCGAAATCCGCGGCACACAACGGAGATTTGTATCA
P66	CCTCGTCTTTCCACCACCGGAACCGCCTCCCTCA
P67	CCGTGTGATAAATAACCTCCGGCTGATG
P68	CCCAGCTACAATGACAGCATTTGAGGCAAGTTGAGAAATGAA
P69	TATTTAAATTGCAGGAAGATTG
P70	AAGGGATATTCATTACCGTAATCTATAGGCT
P71	ACCAGACCGGATTAATTCGAGC
P72	AAGGCCTGTTTAGTATCATGTTAGCTACCTC
P73	AGCAACAAAGTCAGAAATAATATCCAATAATCGGCTCAGGGA
P74	TGAGTAAAGGATAAGTTTAGCTATATCATAGACCATTAGATA

Staple ID	Sequence (5' to 3')
P75	GAGTCTGGATTTGTTATAATTACTACATACACCAC
P76	TTCGGTCCCATCGCATAGTTGCGCCGACATGCTTTCGAGGTG
P77	CGTGTCAAATCACCATCTAGGTAATAGATTT
P78	GGAACCATACAGGCAAGGCAAATCAAAAAGACGTAGTAGCAT
P79	ATTTGGAAGTTTCATGCCTCAACATGTTTTA
P80	AATTTCTTAAACCCGCTTAATTGTATCGTTGCGGGCGATATA
P81	GAGCATTTATCCTGAATCAAACGTGACTCCT
P82	TTATAAGGGTATGGAATAATTCATCAATATA
P83	TAACGACATTTTTACCAGCGCCAAAGAAAGTTACCAGAACCCAAA
P84	AAAGATTACAGAACGGGAGAAGGAAACGTCACCAATGAAACCA
P85	GCTGTAGTTAGAGCTTAATTG
P86	AGTTTCCAACATTATTACATTATAC
P87	GGGATATTGACGTAGCAATAGCTAAGATAGC
P88	AACAAGAGCCTAATGCAGAACGCGC
P89	AGTTTATTGTCCATATAACAGTTGATTC
P90	TATTGAAAGGAATTGAGGTAG
P91	AATAGAAAAAAATAAACGTCTGAGAGGAATATAAGAGCAACACTATGAT
P92	TCGTGCCGGAGTCAATAGTGAATTTGCAGAT
P93	TTAGTTTGAGTGCCCGAGAAATAAAGAAATTGCGTAGAGATA
P94	TTGGTAGAACATTTAATTAAGCAAC
P95	TAACATCCAATAAATGCAAAGGTGGCATCAACATTATGAAAG
P96	TAAGTTTACACTGAGTTTCGT
P97	AGAACTTAGCCTAATTATCCCAAGCCCCCTTATTAGCGTTTGCCA
P98	ACCGCCACCCTCAGAACCCGTACTCTAGGGA
P99	TTAGCCCTGACGAGAAACACCAGAAATTGGGGTGAATTATTTTAA
P100	ATAAAGTCTTTCCTTATCACT
P101	ATTTCCTGATTATCAGATGATGGCTTTAAAAAGACGCTAAAA
P102	ACATAAGTAGAAAAATCAAGAAGCAAAAGAAGATGTCAT
P103	TTCATCGGCATTTTCGGTCATATCAAAA
P104	GAACCGCCACCCTCCATATCATACC
P105	ACTAATGCCACTACGAATAAA
P106	CAAGCCGCCCAATAGCAAGTAAACAGCCATATTATTTTGCCATAAC
P107	TGAAAATCCGGTCAATAACCTAAATTTTAGCCTTT
P108	CCTCGTTTACCAGAAACCAAA
P109	CAAATTATTCATTTCAATTACCTGAGTA
P110	ATTTCAACCAAAAATTCTACTAATAGTTAGTTTCATTTGGGGCGCGAGC
P111	AGGCTTGCGAGACTCCTCAAGAGAAAAGTATTCGGAAC
P112	AATATTCATTGAATCCATGCTGGATAGCGTCCAAT

Staple ID	Sequence (5' to 3')
P113	CTAGTCAGTTGGCAAATCAACAGTCTTTAGGTAGATAACAAA
P114	TATGACTTTATACATTTTTTTTTAATGGAAACAGTACACCGT
P115	ACTAAAGAGCAACGTGAAAATCTCCACCCACAACTAAAGGAA
P116	TTGCGAATAATATTTACAGCGGAGTGAGGTAAAATTTTGAGG
P117	CCGACTTGTTGCTAAAATTTATTTAGTTCGCGAGAGTCGTCTTTCCAGA
P118	ATTGTTATCTGAGAAGAAACCAGGCAAAGCGCCATTCGTAGA
P119	AGTACCGCATTCCACAACATGTTCAGCCTTAAGGTAAAGTAATTC
P120	AAACTCACAGGAACGGTACGCCAGTAAAGGGGGTGAGGAACC
P121	CGCTTTCCAGTTAGCTGTTTAAAGAACGT
P122	GGCGAAGCACCGTAATAACGCCAGGGTTTTCCCAGTCATGGG
P123	TTTACCAGTCCCGGCCTGCAGCCCACTACGGGCGCACCAGCT
P124	GGCAACACCAGGGTCTAATGAGTGAGCTCACAACAATAGGGT
P125	GAAGGAGCGGAATTATCATCATATATCATTTACATAGCACAA
P126	CGCGCTACAGAGTAATAAAAGGGACATTCTGATAGAACTTAG
P127	GTAATTAATTTAGAATCTGGGAAGGGCGATCGGTGCGGCAAA
P128	GGATGTGGTTTGCCCCAGCAG
P129	GCCAGCAGTTGGGCGCAAATCAGGTTTCTTGCCCTGCGTGGT
P130	TATCAGCAACCGCAAGAATGCCAATGAGCCTGAGGATCTATC
P131	GAGAACAATATACAAAATCGCGCAGAGGCGATTCGACAAATCCTTTAAC
P132	GTAAAACGACGGCCCATCACCCAAATCAGCGC
P133	ACGGGCCGATAATCCTGAGAAGTGTTTTTATGGAGCTAACCG
P134	TGCTAAATCGGGGAGCCCCCGATTTAGAGCTAGCAGAACATT
P135	ACGCGGTCCGTTTTTGGGTAAGTGA
P136	GCGTCCACTATTCCTGTGTGAAATGCTCACTGCC
P137	CGTACTATGGTAACCACTAGTCTTTAATGCGCGAACTGAATC
P138	AGAATTTTAGAGGAAAACAATATTACCGCCAGCTGCTCATTT
P139	TTGGGCGGCTGATTTCGGCAAAATCCCT
P140	TGGTGGTTGTTCCAGTTTGGAACA
P141	AGTCGCCTGATACTTGCATAACAGAATACGTGGCACAGCTGA
P142	TGCTGATTGCCGTTGTCATAAACATCGGGCGG
P143	TGAGTGTTCCGAAAGCCCTTCACCGCCTAGGCGGTATTA
P144	TGAGCAAATTTATACAGGAATAACATCACTTGCCTGAGTCTT
P145	CCTGCGCTGGGTGGCGAGAAAGGAAGGGAAGGAGCGGGGCCG
P146	CGTACAGGCCCCCTAACCGTCCCCGGGTACCGAGCGTTC
P147	TTTAGATTCACCAGTCACACGACCGGCGCGTGCTTTCCCAGA
P148	CCCCGCTAGGGCAACAGCTGGCGAAAGGGGGATGTGCTTATT
P149	TCACAGCGTACTCCGTGGTGAAGGGATAGCTAAGAGACGAGG
P150	TGCGTGTTCAGGTTGTGTACATCG

Staple ID	Sequence (5' to 3')
P151	AGGGAGCCGCCACGGGAACGGATAGGCGAAAGCATCAGCACTCTG
P152	AAGAAAGCGCTGAACCTCAAATATTCTAAAGGAAAGCGTTCA
P153	AGCGCAGCTCCAACCGTAATCATGGTCACGGGAAACCT
P154	CCTCATCACCCCAGCAGGCCTCTTCGCTATTACGCCAGTGCC
P155	GTCGCGTGCCTTCGAATTGTCAAAG
P156	TTCGGGGTTTCTGCCAGGCCTGTGACGATCC
P157	AGAGAAAATCCAGAGAGTTGCAGCAAATC
P158	TGCCATCCCACGCAGGCAGTTCCTCATTGCCGTTTTAAACGA
P159	GCCCGAGTACGAGCCGGAAGC
P160	GAGGCCAAGCTTTGAATACCAAGTACGGATTACCTTTTCAAA
P161	ACGTAAGAATTCGTTCTTAGAAGAACTCAAACTATCGGATAA
P162	TAAAACCGTTAAAGAGTCTGTCCATCCAGAAACCACACAATC
P163	ACGAGCGGCGCGGTCAGGCAAGGCGATTAAGTTGGGTAAAAC
P164	TTTTCCAGCATCAGCGGGGCTAAAGAACCTCGTAGCACGCCA
P165	CAAAGCACTAGATAGCTCCATTCAGGCTGCGCAACTGTCTTG
P166	ATTGCGTTGCTGTTATCCGCTCACAATTCCAAACTCACTTGCGTA
P167	GAGAGATAGACTTTACGGCATCAGA
P168	TGACCGCGCCTTAATTTACAATATTTTTGAATGGCTATCACA
P169	CCTAATTTAACAAACCCTCAATCAATATCTGATTCGCTAATC
P170	TTAACTCGGAATTAGAGTAAATCAATATATGTGAGTGATTCT
P171	ATGAAGGGTAAAGTTCACGGTGCGGCCATGCCGGTCGCCATG
P172	ACATAAAGCCCTTACACTGGTCGGGTTAAATTTGT
P173	AAATGCGGAAACATCGGTTTTCAGGTTTAACGTCAGATTAAC
P174	GTCGCAGAAAAACTTAAATTTGCC
P175	GAATTCGTCTCGTCGCTGGGTCTGCAATCCATTGCAACACGG
P176	GCGAAAATCCCGTAAAAAAAGCCGTGGTGCTCATACCGGCGTCCG
P177	CTTGTAGAACGTCAGCGGCTGATTGCAGAGTTTTTCGACGTT
P178	TCATACATTTAATACCGATAGCCCTAAAACATCGAACGTAAC
P179	TACGGCTGGAGGTGCGCACTCGTCACTGTTTGCTCCCGGCAA
P180	AAATGACGCTAAATGGATTATTTACATTGGCGAATACCTGGA
P181	AACAACAGGAAGCACGTCCTTGCTGGTAATATCCAGAAACGC
P182	TGCATTAATGAGCGGTCCACGCTCACTGCGCCACGTGCCAGC
P183	ACCTGACGGGGAAAGCCGGCGAACCAAGTGTCTGCGCGTTGC
P184	CCAGCCTCCGATCCTCATGCCGGA
P185	GCTGGTCTGGTCAGGAGCCGGAATCCGCCGTGAACAGTGCCA
P186	GCGAATCAGTGAGGCCACCGAGTAGTAGCAACTGAGAGTTGA
P187	GGCCAACGCGCGGGGAGGGCCCTGTGTTTGA
P188	AGCTTTCAGAGGTGGCGATGGCCAGCGGGAAT

Staple ID	Sequence (5' to 3')
P189	ATTAGCGGGGTTTTGCTCAGTACCAGGCTGACAACAAGCTG
P190	TGCCCGTATAAACAGTGTGCCTTCTGGTAA
P191	AGAAAACGAGAATGACCATAAATCTACGCCCCTCAAATGCTTTA
P192	ATAACTATATGTAAATGCTTAGGATATAAT
P193	AGGAATCATTACCGCGTTTTTATAAGTACC
P194	GATTAGAGAGTACCTTAACTCCAACAGG
P195	CCTTAAATCAAGATTAGCGGGAGGCTCAAC
P196	GCATGTAGAAACCAATCCATCCTAGTCCTG

Table S5. Biotin-modified staples from the 5' to the 3' end for the pillar-shaped DNA origami structure.

Sequence (5' to 3')	Function	Replace
Biotin-AGAAAACGAGAATGACCATAAATCTACGCCCCTCAAATGCTTTA	Biotin at 5'	P189
Biotin-ATTAGCGGGGTTTTGCTCAGTACCAGGCTGACAACAAGCTG	Biotin at 5'	P190
Biotin-GCATGTAGAAACCAATCCATCCTAGTCCTG	Biotin at 5'	P191
Biotin-GATTAGAGAGTACCTTAACTCCAACAGG	Biotin at 5'	P192
Biotin-TGCCCGTATAAACAGTGTGCCTTCTGGTAA	Biotin at 5'	P193
Biotin-CCTTAAATCAAGATTAGCGGGAGGCTCAAC	Biotin at 5'	P194
Biotin-AGGAATCATTACCGCGTTTTTATAAGTACC	Biotin at 5'	P195
Biotin-ATAACTATATGTAAATGCTTAGGATATAAT	Biotin at 5'	P196

Table S6. Staples from the 5' to the 3' end for the pillar-shaped DNA origami structure with extensions for pyrene-modified staples binding.

Sequence (5' to 3')	Function	Replace
ATATTTCCTCTACCACCTACATCACTAATTAGCGGGGTTTTGCTCAGTACCAGGCTGACAACAAGCTG	External labeling with pyrene	P189
ATATTTCCTCTACCACCTACATCACTAAGAAAACGAGAATGACCATAAATCTACGCCCCTCAAATGCTTTA	External labeling with pyrene	P190
ATATTTCCTCTACCACCTACATCACTAATAACTATATGTAAATGCTTAGGATATAAT	External labeling with pyrene	P191
ATATTTCCTCTACCACCTACATCACTAGCATGTAGAAACCAATCCATCCTAGTCCTG	External labeling with pyrene	P192
ATATTTCCTCTACCACCTACATCACTATGCCCGTATAAACAGTGTGCCTTCTGGTAA	External labeling with pyrene	P193
ATATTTCCTCTACCACCTACATCACTAAGGAATCATTACCGCGTTTTTATAAGTACC	External labeling with pyrene	P194

Sequence (5' to 3')	Function	Replace
ATATTTCCTCTACCACCTACATCACTAGATTAGAGAGTACCTTAACTCCAACAGG	External labeling with pyrene	P195
ATATTTCCTCTACCACCTACATCACTACCTTAAATCAAGATTAGCGGGAGGCTCAAC	External labeling with pyrene	P196
GTGATGTAGGTGGTAGAGGAAATAT-**pyrene**	Pyrene at 3'	-

Table S7. Staples from the 5' to the 3' end for the pillar-shaped DNA origami structure for Distance determination from fluorescence lifetimes.

Sequence (5' to 3')	Function	Replace
AGACAGCAGAAACGAAAGAGGAAATAAATCGAGGTGACAGTTAAAT-**ATTO542**	Dye ATTO542 at 3' (11.6 nm)	P46
AATATGCAACTACCATCATAGACCGGAACCGC-**ATTO542**	Dye ATTO542 at 3' (15.9 nm)	P49
CATTTGAGATAACCCACGAAACAATG-**ATTO647N**	Dye ATTO647N at 3' (15.9 nm)	P37
AAGGGATATTCATTACCGTAATCTATAGGCT-**ATTO647N**	Dye ATTO647N at 3' (23.4 nm)	P70
ACGGGCCGATAATCCTGAGAAGTGTTTTTATGGAGCTAACCG-**ATTO647N**	Dye ATTO647N at 3' (52.5 nm)	P133

Table S8. Staples from the 5' to the 3' end for the pillar-shaped DNA origami structure for Expanding FRET (horizontal orientation).

Sequence (5' to 3')	Function	Replace
TGCAATGGGATAGGTCAAAAC	Exchange staple	P1
ATGAAAGGGTGAGAAGGCATC	Exchange staple	P1
AACCGTGTCATTGCAACGGTAATATATTTTAA-**ATTO647N**	Dye ATTO647N at 3' (FRET acceptor)	P2
ACATCTAGCTGGCATAGCCACATTATTCATCGGTCAGATGATATTCACAAACCAA	Exchange staple	P3/P4
CTGTATGGGATTACCGTTAGTATCA	Exchange staple	P5
CCATAATGCCAGGCTATCAAGGCCGGAG-**ATTO542**	Dye ATTO542 at 3'	P6

Table S9. Staples from the 5' to the 3' end for the pillar-shaped DNA origami structure for Expanding FRET (diagonal orientation).

Sequence (5' to 3')	Function	Replace
TGCAATGGGATAGGTCAAAAC	Exchange staple	P1
ATGAAAGGGTGAGAAGGCATC	Exchange staple	P1
AACCGTGTCATTGCAACGGTAATATATTTTAA-**ATTO647N**	Dye ATTO647N at 3' (FRET acceptor)	P2
AAACTTCAGAAAAGTTTTGAATACCCCAAC	Exchange staple	P7

Sequence (5' to 3')	Function	Replace
ATTCATCAAAAATAATTCGCGTCTTAGCCAGACCCGTC	Exchange staple	P8
CATCCAAAAATAAACGTTAGCCTCAGA	Exchange staple	P9
GGATTGAGTGAGCGAGTAACACTTT	Exchange staple	P10
GCATACCCTGTCGGGAGATAGAACCCTCATCGTA-**ATTO542**	Dye ATTO542 at 3'	P11

Table S10. Staples from the 5' to the 3' end for the pillar-shaped DNA origami structure for Expanding FRET (vertical orientation).

Sequence (5' to 3')	Function	Replace
TGCAATGGGATAGGTCAAAAC	Exchange staple	P1
ATGAAAGGGTGAGAAGGCATC	Exchange staple	P1
AACCGTGTCATTGCAACGGTAATATATTTTAA-**ATTO647N**	Dye ATTO647N at 3' (FRET acceptor)	P2
ATGCTGAGAGTCTACAAGGAGAGGGAACGCCAAAAG GA	Exchange staple	P12
CCCGGTTGATAAAGCATGTCAATCATATTTTTAACAAG AGAATCG-**ATTO542**	Dye ATTO542 at 3'	P13

Table S11. Staples from the 5' to the 3' end for the pillar-shaped DNA origami structure for Graphene biosensing.

Sequence (5' to 3')	Function	Replace
AAGGGATATTCATTACCGTAATCTATAGGCT-**ATTO542**	Colocalization dye ATTO542 at 3' (23.4 nm)	P70
AATATGCAACTACCATCATAGACCGGAACCGCCGCGC CGCCA**TTAAGTGGGATGGACAGACGCGCG**CATCCC ACTTAA-**ATTO643**	Capture strand with dye ATTO643 at 3'	P49
AGAAATCGTTAGACTACCTTTTTAAGGCGTTCTGACCT TTTTGCATTTTAAGTGGGATG	Closing strand	P50
TTAGTTTGAGTGCCCGAGAAATAATTTAGCGTATAGC ATA	Biasing strand "old"	P93
TTAGTTTGAGTGCCCGAGAAATAATTTAGCGTTTAG	Biasing strand "new"	P93
TATGCTATACGCTATTAAGTGGGATGCGCGCGTCTGTC	Target strand "old"	-
CTAAACGCTATTAAGTGGGATGCGCGCGTCTGTC	Target strand "new"	-

Table S12. Core staples from the 5' to the 3' end for the L-shaped DNA origami structure for Distance determination from fluorescence lifetimes, Dynamics with GET and Expanding FRET. Staples L197-L252 were left out in the experiments with the L-shaped DNA origami structure labeled with 42 pyrene molecules.

Staple ID	Sequence (5' to 3')
L1	ATCCAGAACAATATTAGTCCATCAGGAACGGT

Staple ID	Sequence (5' to 3')
L2	CGTGCCTGTTCTTCGCATCCAGCGCCGGGTTA
L3	ATAATCAGAAAAGCCCAACATCCACTGTAATA
L4	CATAGGTCTGAGAGACAAATCGTCGAATTACC
L5	ATTGCCCTTCACCGCCCCAGCTGCTTGCGTTG
L6	TTCGTAATCATGGTCATCCATCAGTTATAAGT
L7	CCCGCCGCGCTTAATGAAAGCCGGCGAACGTG
L8	AGGCGAAAATCCTGTTGTCTATCACCCCCGAT
L9	GCTGCGCAACTGTTGGCAGACCTATTAGAAGG
L10	CTGCAACAGTGCCACGTATCTGGTAGATTAGA
L11	AACAGAGGTGAGGCGGCAGACAATTAAAAGGG
L12	AAATCCCGTAAAAAAACGTTTTTTGGACTTGT
L13	GGCTTAGGTTGGGTTAAGCTAATGATTTTCGA
L14	TATTTTGTTAAAATTCGGGTATATATCAAAAC
L15	GTATAAGCAAATATTTTAGATAAGTAACAACG
L16	CCAGCCAGCTTTCCGGGTAATGGGGTAACAAC
L17	GGGGTCATTGCAGGCGGGAATTGACTAAAATA
L18	TGTTGCCCTGCGGCTGATCAGATGCAGTGTCA
L19	GGAAACCAGGCAAAGCGTACATAAGTGAGTGA
L20	CTCTCACGGAAAAAGAACGGATAAAAACGACG
L21	ATCGGCAAAATCCCTTACGTGGACTCCAACGT
L22	TCAAATCACCATCAATACGCAAGG
L23	GCAGTTGGGCGGTTGTCCAGTTATGGAAGGAG
L24	CTTCTGACCTAAATTTGCAGAGGCCAGAACGCAATTTACG
L25	ATCAAACTTAAATTTCTGGAAGGGCCATATCA
L26	TATCATTTTGCGGAACATCCTGATATAAAGAA
L27	GACCGTGTGATAAATACAAATTCT
L28	TGATTGCTTTGAATACAAACAGAATGTTTGGA
L29	GCCGGGCGCGGTTGCGCCGCTGACCCCTTGTG
L30	GTACTATGGTTGCTTTTTTAGACACGCAAATT
L31	GGGCCTCTTCGCTATTACGTTGTACCTCACCG
L32	GCAGCAAGCGGTCCACAAGTGTTTTGAGGCCA
L33	AACGTTATTAATTTTACAACTAATCAGTTGGC
L34	GAAATTGTTATCCGCTCACATTAAATTAATGA
L35	CCAGCTTACGGCTGGAAACGTGCCCGTCTCGT
L36	GCAGAGGCGAATTATTTTTCATTTGCTATTAA
L37	CATTGCCTGAGAGTCTTTATGACCATAAATCATTTCATTT
L38	CTAGCTGATAAATTAACAGTAGGG

Staple ID	Sequence (5' to 3')
L39	AAATCAGCTCATTTTTGTGAGCGAATAGGTCA
L40	TATTTTTGAGAGATCTGCCATATTTCCTCTACTCAATTGA
L41	CAGGAAAAACGCTCATACCAGTAAATTTTTGA
L42	ACAGTTGAGGATCCCCAGATAGAACTGAAAGC
L43	ACGATAAACCTAAAACAAAGAATACACTAAAACATTACCCAACAAAGC
L44	AGAAACAGCTTTAGAAGGAAGAAAAATCTACGATTTTAAGCATATAAC
L45	GCACCCTCCGTCAGGTACGTTAGTAAATGAATAGTTAGCGTCAATCAT
L46	AGTTGATTAGCTGAAAAGAGTACCTTTAATTGTTAATTCGGACCATAA
L47	CTCAAATGTTCAGAAATGGAAGTTTCACGCGCATTACTTCAACTGGCT
L48	TTTCATCGAATAATATCCAGCTACAATACTCCAGCAATTTCTTTACAG
L49	TGCTCATTCTTATGCGTTAATAAAACGAACTATATTCATTGGCTTTTG
L50	GGCACCAAAACCAAAAGTAAGAGCAACACTATAGCAACGTAAATCGCC
L51	AAGGGAACCGGATATTCACTCATCTTTGACCCGTAATGCCATCGGAAC
L52	ATATTCACCGCCAGCATTGACAGGCAAAATCA
L53	CGGAATCTCAGGTCTGTTTTAAATATGCATGCGAACGAATCATTG
L54	AAAGACAAATTAGCAAGTCACCAATGAAACCA
L55	TCGATAGCAGCACCGTAAAATCACGTTTTGCT
L56	TGAATTACCAGTGAATGGAATTACGAGGCATATAGCGAGAGAATCCCC
L57	TAGTTGCCAGTTGCGGGAGGTTTTGAAGATCAATAA
L58	GCCCCCTGGTGTATCACCGTACTC
L59	AATAAGTTAGCAAAAACGCAATAATAACGAGAATTAAAAGCCCAA
L60	CAAAAGAATAAAATACCCAGCGATTATACCAAGCGCGAA
L61	TTTTCATCGGCATATTGACGGCACCACGG
L62	GGGGCGCGCCCAATTCACTAAAGTACGGTGTCACGAGAATAGCTTCAA
L63	CCGGCAAATCGGCGAAGTGGTGAAGGGATAG
L64	ATCAAAAAGTCATAAAACGGAACAACATTATCAACTTTAGTAGAT
L65	TTAGTTTGCCTGTTTAGGTCATTTTTGCGGATAGGAAGCCGACTATTA
L66	GCGAGAAAAGGGATGACGAGCACGTATAACGTGCTTTTCACGCTGAAGAAAGC
L67	CCCTGAACAAATAAGAAACGCGAGGCGTT
L68	CTGAGGCCAACGGCTACAGAGGTTTCCATT
L69	ACATTCTGAAGAGTCTCCGCCAGCAGCTCGAA
L70	AAATCAACACGTGGCATCAGTATTCTCAATCC
L71	TTATACTTAGCACTAAAAAGTTTGTGCCGCCA
L72	CCAACATGACGCTCAATGCCGGAGGAAATACC
L73	CCGGAACCGCAAGAAAGCAATAGCTATCTTACTCACAATCCGATTGAG
L74	GTAAGAATAGTTGAAACTTTCGCAAACACCGC
L75	GCCAGTGCGATTGACCCACCGCTTCTGGTGCC

Staple ID	Sequence (5' to 3')
L76	AGGAAACCGAGGACGTAGAAAAAGTACCG
L77	CTGCGCGGCTAACTCACAATTCCACACAACATACGAGTACCGGGGCTCTGTGGGTG TTCAG
L78	AATTACATAGATTTTCAATAACGGATTCGCC
L79	ATAACCTTATCAACAAAAATTGTATAACCTCC
L80	CCAGAATGGAGCCGCCAATCAAGTTTGCC
L81	TTTTTTAATGCACGTACAAGTTACCCATTCAG
L82	CATTATACGGTTTACCCATAACCCTCGAAATACAATGTTTAAACAGGG
L83	CTTTTGCGTTATTTCAATGATATTCAACCGTT
L84	GACAGATGGACCTTCATCAAGAGCCCTGAC
L85	ACAAGAAATAGGAATCCCAATAGCAAGCAAATATAGCAGCATCCTGAA
L86	AAATTATTTGGAAACAGCCATTCGAAAATCGC
L87	CACTCATGAAACCACCTTAAATCAAGATTGAGCGTCTTTTTGTTT
L88	GCCTAATTATCATATGATAAGAGATTTAGTTAATTTCAT
L89	GAGGGTAGTTGCAGGGTGCTAAACAACTTTCACGCCTGGAAAGAG
L90	AGAGCCGCAAACAAATGAGACTCCTCAAGAGATTAGCGGGCAGTAGCA
L91	ATTGCGTTTAACAACATTTCAATTACCTGAGCAAAAGGGAGAAACAGGTTTAAGAT GATGG
L92	CCACCCTCTGTTAGGAAGGATCGTCTTTCCAGCAGACGATTATCAGCT
L93	GCCAGTACGTTATAAGGCGTTAAATAAGAATAAACACAAAT
L94	CAATTCATATAGATAATAAATCCTTTGCCCG
L95	GCCGTCACAATATAAAAGAAACCACCAGAAGGAGCGGACTCGTATTACATTTGTCA AATAT
L96	TACCAGTAACGCTAACAGTTGCTATTTTGCACCCCATCCT
L97	GTCGAAATCCGCGACCTGCTCCACCAACTTTTAGCATTC
L98	GTCCACTAAACGCGCGGACGGGCAACAGCTG
L99	AACCGTTTCACACGGGAAATACCTACATTTTGACGCTAAACTATCACTTCTTTAACA GGAG
L100	CGCTGGCACCACGGGAGACGCAGAAACAGCGG
L101	CAAATCGTCAGCGTGGTGCCATCCCACGCAA
L102	GCCGATTAAGGAAGGGCGCGTAACCACCACA
L103	TGTAGCTCAACATTTACCCTCGAAAGAC
L104	GAGAAACATTTAATTTTACAGGTAGAAAG
L105	TTGAGTAAGCCACCCTCAGAACCG
L106	TTAGAGCTATCCTGAGGCTGGTTTCAGGGCGC
L107	TTCACCAGGTAGCAATGGCCTTGCTGGTAAT
L108	CGCTCACTATCAGACGGTCCGTGAGCCTCCTC
L109	ATTCATATCAGTGATTTGGCATCAGGACGTTGTAACATAAACCAGACG
L110	GGAGGGAAGAGCCAGCAATCAGTAGCGACAGACCAGAACCGCCTC

Staple ID	Sequence (5' to 3')
L111	AACGTCAATAGACGGGGAATACCCAAAAGAACAAGACTCCGTTTTTAT
L112	TGTACTGGTAATAAGTTCAGTGCC
L113	TTCAAATTTTTAGAAAAAACAGGAGCAAACAAGAGAATCGATGAAGGGTGAGATA TTTTA
L114	TAATAAGAAGAGCCACCCTTATTAGCGTTTGCCATTCAACAATAGAAA
L115	TTCTGAAACATGAAAGTGCCGGCCATTTG
L116	CAAACCCTTTAGTCTTACCAGCAGAAGATAA
L117	AAACGGGGTTTTGCTACATAACGCCAAAAAAGGCTTGTAATCTTG
L118	TGGAGCCGGCCTCCGGGTACATCGACATAAAA
L119	CCGAGTAAGCCAACAGGGGTACCGCATTGCAA
L120	ACAAGAACCGAACTGATGTTACTTAGCCGGAAAAGACAGCACTACGAA
L121	AGAACGTTAACGGCGTAATGGGTAAAGGTTTCTTTGCGTCGGTGGTGCTGGTCTTG CCGTT
L122	GGAGCCTTCACCCTCAGAGCCACC
L123	CCCCCTGCGCCCGCTTTAGCTGTTTCCTGTGT
L124	TGCGGGATAGCAGCGACGAGGCGCAGAGAAACGGCCGCGGTAACGATC
L125	TAATAGTATTCTCCGTGCATTAAATTTTTGTT
L126	CACATCCTCAGCGGTGGTATGAGCCGGGTCAC
L127	CACAGACATTTCAGGGATCTCCAAAAAAAAGGTTCTTAAAGCCGCTTT
L128	CCATTACCAAGGGCGACATCTTTTCATAGGCAGAAAGAATAGGTTGAG
L129	ATGAGTGACCTGTGCAGTTTCTGCCAGCACG
L130	AAGCGCATAAATGAAACAGATATAGAAGGCTTAGCAAGCCTTATTACG
L131	ATAAAAATATCGCGTTCTCCTTTTGATAAGAGCTATAT
L132	ATCGGCCTTAAAGAATAAATCAAAAGAATAGCCCGAGACCAGTGAGGGAGAGGGG TGCCTA
L133	CCTGCAGCCATAACGGGGTGTCCAGCATCAGC
L134	ATGGCTACAATCAACTGAGAGCCAGCAGCAAATGAAAAACGAACCTAATGCGCTT GGCAGA
L135	TACAGGCATTAAATTAACCAATAGGAACGCCATCAAAGTCAATCAGAATTAGCCTA AATCG
L136	CCGTCGGAGTAGCATTCAAAAACAGGAAGATT
L137	GTTTTCCCGTAGATGGCAGGAAGATCGCACT
L138	GCCTGTTTGCTTCTGTTACCTTTTAACGTTAA
L139	AAACGGCGCAAGCTTTGAAGGGCGATCGGTGC
L140	TACCGATAGTTGCGCTTTTTCA
L141	CAGTACCATTAGTACCCAGTGCCCGTATAAATTGATGAATTAAAG
L142	CAACTAATGCAGACAGAGGGGCAATACTG
L143	ACCCTCATGCCCTCATTTTCTGTATGGGATTTAGTTAAAGCAGCTTGA
L144	ATAAACAATCCCTTAGTGAATTTATCAAAAT

Staple ID	Sequence (5' to 3')
L145	CCTCAGAGCACAAGAAGAAAAGTAAGCAG
L146	CAGTATGTTTATTTTGCGAAGCCCTTTTTAATTGAGTTCTGAACA
L147	CGGGAAACGAAAAACCTGATGGTGGTTCCGAA
L148	CTTAATTGAGACCGGAAACAGGTCAGGATTAGAGGTGGCA
L149	TCATCAACAAGGCAAATATGTACCCCGGTTG
L150	TGCTTTCGAGGTGAATCTCCAAAA
L151	AGCATGTACGAGAACAATCCGGTATTCTAAGAACGATTTTCCAGA
L152	TCTTACCATAAAGCCATAATTTAGAATGGTTTAGGGTAGC
L153	CGTTGAAAATAGCAAGCCCAATA
L154	GTTGTACCACCCTCATAAAGGCCGGAGACAG
L155	GAAACAACGCGGTCGCCGCACAGGCGGCCTTTAGTGACTTTCTCCACGTACAGACG CCAGG
L156	CAAAGGGCCTGTCGTGTGGCCCTGAGAGAGTT
L157	TTAATTTCATGTTCTATAACTATATGTAAATGCTGATGTCAATAGAATCCTTGACAA AATT
L158	AGCGAACCAGAAGCCTGGAGAATCACAAAGGCTATCAGGT
L159	CGTTGGTAGTCACGACGCCAGCTGGCGAAAGGGGGATATCGGCCTGCGCATCGGCC AGCTT
L160	GGAACCCAAAACTACAAACAGTTTCAGCG
L161	AGGAGGTGGCGGATAAGTATTAAGAGGCTAAATCCTCTACAGGAG
L162	GGAATTAGGTAAATTTTCGGTCATAGCCCCACCGGAACCACCACC
L163	TCTTTAGGCTGAATAATGCTCATTAGTAACAT
L164	TGCGAATAATAATCGACAATGTTCGGTCG
L165	ACGCCAGATGACGGGGCGCCGCTAGCCCCAGC
L166	TAAAGTTTAGAACCGCTAATTGTATCGCGGGGTTTAAGTTTGGCCTTG
L167	ATTATAGCGTCGTAATAGTAAAATGTTTTTT
L168	TTTTTTTTTTTTAAAACTAG
L169	TTTTTGCCTGAGTAGAAGAA
L170	TTTTGATTAAGACGCTGAGA
L171	TTTTGGCGCATAGGCTGGCTAACGGTGTTAAATTGT
L172	TTTGCGTATTGGGCGCTTTT
L173	TAGTCAGAAGCAAAGCGGATTTT
L174	TTTTCGCAAATGGTCAATAAACCATTAGATGC
L175	TTTTTTGCATCAAAAGCCTGAGTAATTTT
L176	TTTTCCATATTATTTATCCCAATCCAAAGTCAGAGA
L177	GAAAGGAGCGGGCGCTAGGTTTT
L178	ATATATATAAAGCGACGACATCGGCTGTCTTTCCTTATCATTTTT
L179	TCAGCAGCAACCGCAATTTT

Staple ID	Sequence (5' to 3')
L180	TTTTGTTTCGTCACCAGTACTGTACCGTAAT
L181	TTTTCTTTACAAACAATTCG
L182	TTTTACCGTTCCAGTAAGCGTCATACATGGCTTCAGTTAAT
L183	TTTTGGAATTTGTGAGAGAT
L184	AGAGCAAATCCTGTCCAGATACCGACAAAAGGTAATTTT
L185	ATACGCAAAGAAAATTATTCATTAAAGGTGAATTTT
L186	TTAATTAAACCATACATACATAAAGGTGGCAATTTT
L187	CTGATAGCCCTAAAACTTTT
L188	TTTTATTGGGCTTGAGATGGCCAGAACGATT
L189	CAGATGAATATACAGTTTTT
L190	TTTTCGGGCCGTTTTCACGG
L191	CCGTGCATCTGCCAGTTTTT
L192	TTTTGCTAATATCAGAGAGATAACCCCGCCACCGCG
L193	ACAAAGTATGAGGAAGCTTTGAGGACTAAAGATTTT
L194	TTTCGACTTGATCGAGAGGGTTGATATAAGTATTTT
L195	TTTTCCCTCAGAGCCACCACCCTCAGAAAGCGCTTA
L196	GAGCCGATATAACAACAACCATCGCCCTTTTTTT
L197	CCGAATCTAAAGCATCTTTT
L198	TTTTACCTTGCTGAACCAGG
L199	AGTGTGCTGCAAGGCGTTTT
L200	TTCCGGAATCATAATTTTTT
L201	CATAATAATTCGCGTCTTTT
L202	TTTTAGAGCGGGAGCTAGAT
L203	TTTTGGAACCTAAGTCTCTGAATTTTTTTTTT
L204	AATGCAATAGATTAAGGGCTTAGAGCTTATTTT
L205	TTTTACTGTAGCCTCAGAACCGCCATTTT
L206	TTTTCAGGGTGGTTTTTCTT
L207	TTTTCATATAAAAGAAAGCCGAACATTTT
L208	CATGTTTACCAGTCCCTTTT
L209	TTTTAAACATCAAGAAAAAA
L210	TTTTAACAGTACCTTTTACA
L211	ATTTAGAAGTATTAGATTTT
L212	TTTTAGAACGCGAGAAAACTTT
L213	TTTTATTGCTGAATATAATACATTTTTTT
L214	TTTTTTAGGAATACCACAGTAGTAATTTT
L215	TTTTGTGTAAAGCCTGGCGG
L216	TTTTATCGCCATTAAAAATA

Staple ID	Sequence (5' to 3')
L217	TTTTGAACAACTAAAGGAACACTGATTTT
L218	TTTTTTATCACCGTCACAGCGTCAGTTTT
L219	TTTTTGGCCTTCCTGTATAA
L220	TTTTTCCAAGAACGGGTGCGAACCTTTTT
L221	TTTTTGGATTATTTACAGAA
L222	TCACCGGAAGCATAAATTTT
L223	TTTTCTTTTTCACAACGGAGATTTGTTTT
L224	ACAAATTATCATCATATTTT
L225	TTTTACGCATAATGAGAATAGAAAGTTTT
L226	TTTTGCCTCAGAGCATAAAGAAAATTAAGCAATAAATTTT
L227	TAGTAATAACATCACTTTTT
L228	TTTTCCCTTACACTGGTTGC
L229	AGATGAAGGGTAAAGTTTTT
L230	TTTTCCCGACTTACAAAATAAACAGTTTT
L231	TTTTTAAACGATGCTGATGG
L232	ACATAGCGATAGCTTATTTT
L233	TTTTATTAAGTTGGGTACGC
L234	TTTTTTGTTCCAGTTTGGAACAAGA
L235	TCGAAGATGATGAAACTTTT
L236	TTTTTATCATCGCCTGAACAGACCATTTT
L237	ACCTCGTCATAAACATTTTT
L238	TTTTGCGCTGGCAAGTGTAG
L239	TTTTTTGAGGGGACGACGAC
L240	CTCCAATCGTCTGAAATTTT
L241	AAAACGGTAATCGTTTTTTT
L242	TTTTTTCCTGATTATCACGT
L243	TTTTTAGACTGGCATCAGTTGAGATTTTTT
L244	CGGCCTCGTTAGAATCTTTT
L245	TTTTTAGCCCGGAATAGCCTATTTCTTTT
L246	TTTTGTGTAGGTAAAGATTC
L247	TTCATAGGGTTGAGTGTTTT
L248	TTTTGAATGCCAACGGCAGC
L249	TTTTACTAGAAAAAGCCTGTT
L250	TTTTAAGTTACCAGGGTAATTGAGCTTTT
L251	TGCGGCCAGAATGCGGTTTT
L252	TTTTAGTAATTCAATCGCAAGACAATTTT

Table S13. Biotin-modified staples from the 5' to the 3' end for the L-shaped DNA origami structure.

Sequence (5' to 3')	Function	Replace
Biotin-ATCCAGAACAATATTAGTCCATCAGGAACGGT	Biotin at 5'	L1
Biotin-CGTGCCTGTTCTTCGCATCCAGCGCCGGGTTA	Biotin at 5'	L2
Biotin-ATAATCAGAAAAGCCCAACATCCACTGTAATA	Biotin at 5'	L3
Biotin-CATAGGTCTGAGAGACAAATCGTCGAATTACC	Biotin at 5'	L4

Table S14. Staples from the 5' to the 3' end for the L-shaped DNA origami structure with extensions for pyrene-modified staple binding. Staples marked with the numbers 1-6 or 1-8 were used in the measurements with only 6 or 8 pyrene molecules, respectively (Distance determination from fluorescence lifetimes). In all other measurements, 42 staples were used for external labeling with pyrene molecules.

Sequence (5' to 3')	Function	Replace
ATATTTCCTCTACCACCTACATCACTAATCCAGAACAATATTAGTCCATCAGGAACGGT	External labeling with pyrene (1)	L1
ATATTTCCTCTACCACCTACATCACTACGTGCCTGTTCTTCGCATCCAGCGCCGGGTTA	External labeling with pyrene (2)	L2
ATATTTCCTCTACCACCTACATCACTAATAATCAGAAAAGCCCAACATCCACTGTAATA	External labeling with pyrene (3)	L3
ATATTTCCTCTACCACCTACATCACTACATAGGTCTGAGAGACAAATCGTCGAATTACC	External labeling with pyrene (4)	L4
ATATTTCCTCTACCACCTACATCACTAATTGCCCTTCACCGCCCCAGCTGCTTGCGTTG	External labeling with pyrene	L5
ATATTTCCTCTACCACCTACATCACTATTCGTAATCATGGTCATCCATCAGTTATAAGT	External labeling with pyrene	L6
ATATTTCCTCTACCACCTACATCACTACCCGCCGCGCTTAATGAAAGCCGGCGAACGTG	External labeling with pyrene	L7
ATATTTCCTCTACCACCTACATCACTAAGGCGAAAATCCTGTTGTCTATCACCCCCGAT	External labeling with pyrene	L8
ATATTTCCTCTACCACCTACATCACTAGCTGCGCAACTGTTGGCAGACCTATTAGAAGG	External labeling with pyrene	L9
ATATTTCCTCTACCACCTACATCACTACTGCAACAGTGCCACGTATCTGGTAGATTAGA	External labeling with pyrene (5)	L10
ATATTTCCTCTACCACCTACATCACTAAACAGAGGTGAGGCGGCAGACAATTAAAAGGG	External labeling with pyrene	L11
ATATTTCCTCTACCACCTACATCACTAAAATCCCGTAAAAAAACGTTTTTTGGACTTGT	External labeling with pyrene	L12
ATATTTCCTCTACCACCTACATCACTAGGCTTAGGTTGGGTTAAGCTAATGATTTTCGA	External labeling with pyrene	L13
ATATTTCCTCTACCACCTACATCACTATATTTTGTTAAAATTCGGGTATATATCAAAAC	External labeling with pyrene	L14

Sequence (5' to 3')	Function	Replace
ATATTTCCTCTACCACCTACATCACTAGTATAAGCAAATATTTTAGATAAGTAACAACG	External labeling with pyrene	L15
ATATTTCCTCTACCACCTACATCACTACCAGCCAGCTTTCCGGGTAATGGGGTAACAAC	External labeling with pyrene	L16
ATATTTCCTCTACCACCTACATCACTAGGGGTCATTGCAGGCGGGAATTGACTAAAATA	External labeling with pyrene	L17
ATATTTCCTCTACCACCTACATCACTATGTTGCCCTGCGGCTGATCAGATGCAGTGTCA	External labeling with pyrene	L18
ATATTTCCTCTACCACCTACATCACTAGGAAACCAGGCAAAGCGTACATAAGTGAGTGA	External labeling with pyrene	L19
ATATTTCCTCTACCACCTACATCACTACTCTCACGGAAAAAGAACGGATAAAAACGACG	External labeling with pyrene	L20
ATATTTCCTCTACCACCTACATCACTAATCGGCAAAATCCCTTACGTGGACTCCAACGT	External labeling with pyrene	L21
ATATTTCCTCTACCACCTACATCACTATCAAATCACCATCAATACGCAAGG	External labeling with pyrene	L22
ATATTTCCTCTACCACCTACATCACTAGCAGTTGGGCGGTTGTCCAGTTATGGAAGGAG	External labeling with pyrene	L23
ATATTTCCTCTACCACCTACATCACTACTTCTGACCTAAATTTGCAGAGGCCAGAACGCAATTTACG	External labeling with pyrene	L24
ATATTTCCTCTACCACCTACATCACTAATCAAACTTAAATTTCTGGAAGGGCCATATCA	External labeling with pyrene	L25
ATATTTCCTCTACCACCTACATCACTATATCATTTTGCGGAACATCCTGATATAAAGAA	External labeling with pyrene	L26
ATATTTCCTCTACCACCTACATCACTAGACCGTGTGATAAATACAAATTCT	External labeling with pyrene	L27
ATATTTCCTCTACCACCTACATCACTATGATTGCTTTGAATACAAACAGAATGTTTGGA	External labeling with pyrene	L28
ATATTTCCTCTACCACCTACATCACTAGCCGGGCGCGGTTGCGCCGCTGACCCCTTGTG	External labeling with pyrene	L29
ATATTTCCTCTACCACCTACATCACTAGTACTATGGTTGCTTTTTTAGACACGCAAATT	External labeling with pyrene	L30
ATATTTCCTCTACCACCTACATCACTAGGGCCTCTTCGCTATTACGTTGTACCTCACCG	External labeling with pyrene (6)	L31
ATATTTCCTCTACCACCTACATCACTAGCAGCAAGCGGTCCACAAGTGTTTTGAGGCCA	External labeling with pyrene (7)	L32
ATATTTCCTCTACCACCTACATCACTAAACGTTATTAATTTTACAACTAATCAGTTGGC	External labeling with pyrene	L33
ATATTTCCTCTACCACCTACATCACTAGAAATTGTTATCCGCTCACATTAAATTAATGA	External labeling with pyrene	L34
ATATTTCCTCTACCACCTACATCACTACCAGCTTACGGCTGGAAACGTGCCCGTCTCGT	External labeling with pyrene	L35
ATATTTCCTCTACCACCTACATCACTAGCAGAGGCGAATTATTTTTCATTTGCTATTAA	External labeling with pyrene	L36
ATATTTCCTCTACCACCTACATCACTACATTGCCTGAGAGTCTTTATGACCATAAATCATTTCATTT	External labeling with pyrene	L37

Sequence (5' to 3')	Function	Replace
ATATTTCCTCTACCACCTACATCACTACTAGCTGATAAATTAACAGTAGGG	External labeling with pyrene	L38
ATATTTCCTCTACCACCTACATCACTAAAATCAGCTCATTTTTGTGAGCGAATAGGTCA	External labeling with pyrene	L39
ATATTTCCTCTACCACCTACATCACTATATTTTTGAGAGATCTGCCATATTTCCTCTACTCAATTGA	External labeling with pyrene (8)	L40
ATATTTCCTCTACCACCTACATCACTACAGGAAAAACGCTCATACCAGTAAATTTTTGA	External labeling with pyrene	L41
ATATTTCCTCTACCACCTACATCACTAACAGTTGAGGATCCCCAGATAGAACTGAAAGC	External labeling with pyrene	L42
GTGATGTAGGTGGTAGAGGAAATAT-**pyrene**	Pyrene at 3'	-

Table S15. Staples from the 5' to the 3' end for the L-shaped DNA origami structure for Distance determination from fluorescence lifetimes.

Sequence (5' to 3')	Function	Replace
ATTO542-AATAAGTTAGCAAAAACGCAATAATAACGAGAATTAAAAGCCCAA	ATTO542 at 5' at the height of 18.9 nm	L59
ATTO643-GAGAAACATTTAATTTTACAGGTAGAAAG	ATTO643 at 5' at the height of 18.9 nm	L104

Table S16. Staples from the 5' to the 3' end for the L-shaped DNA origami structure for Dynamics with GET.

Sequence (5' to 3')	Function	Replace
GGCACCAAAACCAAAAGTAAGAGCAACACTATAGCAACGTAAATCGCCTTTTTTTTTCGGGCATTTA- **Cy3B**	Pointer-Cy3B at 3'	L43
AGAAACAGCTTTAGAAGGAAGAAAAATCTACGATTTTAAGCATATAACTTTTAAAT	Lower binding site 5nt	L44
GCACCCTCCGTCAGGTACGTTAGTAAATGAATAGTTAGCGTCAATCATTTTTAAAT	Upper binding site 5nt	L45
AGAAACAGCTTTAGAAGGAAGAAAAATCTACGATTTTAAGCATATAACTTTTAAATG	Lower binding site 6nt	L44
GCACCCTCCGTCAGGTACGTTAGTAAATGAATAGTTAGCGTCAATCATTTTTAAATG	Upper binding site 6nt	L45
AGAAACAGCTTTAGAAGGAAGAAAAATCTACGATTTTAAGCATATAACTTTTAAATGC	Lower binding site 7nt	L44
GCACCCTCCGTCAGGTACGTTAGTAAATGAATAGTTAGCGTCAATCATTTTTAAATGC	Upper binding site 7nt	L45
AGAAACAGCTTTAGAAGGAAGAAAAATCTACGATTTTAAGCATATAACTTTTAAATGCC	Lower binding site 8nt	L44
GCACCCTCCGTCAGGTACGTTAGTAAATGAATAGTTAGCGTCAATCATTTTTAAATGCC	Upper binding site 8nt	L45

Table S17. Staples from the 5' to the 3' end for the L-shaped DNA origami structure for Dynamics with GET – tether.

Sequence (5' to 3')	Function	Replace
AATCTACGATTTTAAGAACTGGCTTTTTTTGATCGATCGGATCGATCAAGATCGATCGATGCTATAAACGTCCTTT	Tether	L44
AATCTACGATTTTAAGAACTGGCTTTTTTTGATCGATCGGATCGATCAAGATCGATCGATGCTATAAACGTCCTTT-**Biotin**	Tether Biotin at 3'	L44
CATATAACAGTTGATTAGCT	Exchange staple	L46
GAAAAGAGTACCTTTAATTGTTAATTCGGACCATAA	Exchange staple	L46
CTCAAATGTTCAGAAATGGAAGTTTCACGCGCATTACTTC	Exchange staple	L47
CAATTTCTTTACAGAGAAACAGCTTTAGAAGGAAGAAA	Exchange staple	L48
TTTCATCGAATAATATCCAGCTACAATACTCCAG	Exchange staple	L48
AGGACGT-**Cy3B**-TATAGCATCGATCGATCTTGATCGATCCGATCGATC	Tether complementary Cy3B internally labeled at a T-base	-

Table S18. Staples from the 5' to the 3' end for the L-shaped DNA origami structure for dynamic FRET.

Sequence (5' to 3')	Function	Replace
GGCACCAAAACCAAAAGTAAGAGCAACACTATAGCAACGTAAATCGCCTTTTTTTTTCGGGCATTTA-**ATTO542**	Pointer-ATTO542 at 3'	L43
TGCTCATTCT-**ATTO647N**-ATGCGTTAATAAAACGAACTATATTCATTGGCTTTTG	Acceptor-ATTO647N-internal	L49
AGAAACAGCTTTAGAAGGAAGAAAAATCTACGATTTTAAGCATATAACTTTTAAATGC	Lower binding site 7nt	L44
GCACCCTCCGTCAGGTACGTTAGTAAATGAATAGTTAGCGTCAATCATTTTTAAATGC	Upper binding site 7nt	L45

Table S19. Staples from the 5' to the 3' end for the L-shaped DNA origami structure for GET tracking.

Sequence (5' to 3')	Function	Replace
GGCACCAAAACCAAAAGTAAGAGCAACACTATAGCAACGTAAATCGCCTTTTTTTTTCGGGCATTTA-**Cy3B**	Pointer-Cy3B at 3'	L43
AACGAATCATTGTGAATTACCTTTTTTAAATGCC	Lower binding site	L49
GGCACCAAAACCAAAAGTAAGAGCAACACTATAGCAACTTTTAAATGC	Middle binding site	L50
AGCGTCAATCATAAGGGAACCGGTTTTAAATGCC	Upper binding site	L51
GCACCCTCCGTCAGGTACGTTAGTAAATGAATAGTT	Exchange staple	L45
TGCTCATTCAGTGAATGGAATTACGAGGCATATAGCGAGAGAATCCCC	Exchange staple	L49

Sequence (5' to 3')	Function	Replace
ATATTCACTCATCTTTGACCCGTAATGCCATCGGAAC	Exchange staple	L51
ATATTCACCGCCAGCATCGATAGCAGCACCGTAAAAT CACGTTTTGCT	Exchange staple	L52
CGGAATCTCAGGTCTGTTTTAAATATGCATGCG	Exchange staple	L53
GTAAATCGCCAAAGACAAATTA	Exchange staple	L54
GCAAGTCACCAATGAAACCATTGACAGGCAAAATCA	Exchange staple	L55
ATGCGTTAATAAAACGAACTATATTCATTGGCTTTTG	Exchange staple	L56

6. References

[1] L. M. Hall, M. Gerowska, T. Brown, *Nucleic Acids Res.* **2012**, *40*, e108.

[2] A. Gust, A. Zander, A. Gietl, P. Holzmeister, S. Schulz, B. Lalkens, P. Tinnefeld, D. Grohmann, *Molecules* **2014**, *19*, 15824.

[3] J. J. Schmied, R. Dijkstra, M. B. Scheible, G. M. R. De Luca, J. J. Sieber, available at https://www.leica-microsystems.com/science-lab/measuring-the-3d-sted-psf-with-a-new-type-of-fluorescent-beads/, **2016**.

[4] P. C. Nickels, B. Wünsch, P. Holzmeister, W. Bae, L. M. Kneer, D. Grohmann, P. Tinnefeld, T. Liedl, *Science* **2016**, *354*, 305.

[5] Y. Ke, S. M. Douglas, M. Liu, J. Sharma, A. Cheng, A. Leung, Y. Liu, W. M. Shih, H. Yan, *J. Am. Chem. Soc.* **2009**, *131*, 15903.

[6] S. Fischer, C. Hartl, K. Frank, J. O. Rädler, T. Liedl, B. Nickel, *Nano Lett.* **2016**, *16*, 4282.

[7] I. Kaminska, J. Bohlen, S. Rocchetti, F. Selbach, G. P. Acuna, P. Tinnefeld, *Nano Lett.* **2019**, *19*, 4257.

[8] M. Raab, I. Jusuk, J. Molle, E. Buhr, B. Bodermann, D. Bergmann, H. Bosse, P. Tinnefeld, *Sci. Rep.* **2018**, *8*, 1780.

[9] S. Krause, E. Ploetz, J. Bohlen, P. Schuler, R. Yaadav, F. Selbach, F. Steiner, I. Kamińska, P. Tinnefeld, *ACS Nano,* in revision.

[10] X. Li, Y. Zhu, W. Cai, M. Borysiak, B. Han, D. Chen, R. D. Piner, L. Colombo, R. S. Ruoff, *Nano Lett.* **2009**, *9*, 4359.

[11] A. Edelstein, N. Amodaj, K. Hoover, R. Vale, N. Stuurman, *Curr. Protoc. Mol. Biol.* **2010**, *92*, 14.20.1.

[12] J. J. Schmied, C. Forthmann, E. Pibiri, B. Lalkens, P. Nickels, T. Liedl, P. Tinnefeld, *Nano Lett.* **2013**, *13*, 781.

[13] T. Cordes, J. Vogelsang, P. Tinnefeld, *J. Am. Chem. Soc.* **2009**, *131*, 5018.

[14] C. E. Aitken, R. A. Marshall, J. D. Puglisi, *Biophys. J.* **2008**, *94*, 1826.

[15] T. A. Laurence, S. Fore, T. Huser, *Opt. Lett.* **2006**, *31*, 829.

[16] B. Spokoyny, "Photon arrival time correlation," can be found under https://www.mathworks.com/matlabcentral/fileexchange/64605-photon-arrival-time-correlation, **2017**.

[17] G. L. Lukacs, P. Haggie, O. Seksek, D. Lechardeur, N. Freedman, A. S. Verkman, *J. Biol. Chem.* **2000**, *275*, 1625.

[18] K. A. Velizhanin, T. V. Shahbazyan, *Phys. Rev. B - Condens. Matter Mater. Phys.* **2012**, *86*, 245432.

[19] T. Bian, R. Chang, P. T. Leung, *Plasmonics* **2016**, *11*, 1239.

[20] V. D. Karanikolas, C. A. Marocico, A. L. Bradley, *Phys. Rev. B - Condens. Matter Mater. Phys.* **2015**, *91*, 125422.

[21] S. A. Biehs, G. S. Agarwal, *Appl. Phys. Lett.* **2013**, *103*, 243112.

[22] J. Schnitzbauer, M. T. Strauss, T. Schlichthaerle, F. Schueder, R. Jungmann, *Nat. Protoc.* **2017**, *12*, 1198.

9. List of Figures

Figure 1: Influence of different orientations between dye, NP, and excitation laser beam. a) When the dye and NP are orthogonal orientated to the propagation direction of the laser beam the fluorescence intensity is enhanced. b) The orientation of the dye and NP aligned with the propagation direction of the excitation laser beam results in a quenching of the fluorescence intensity. 2

Figure 2: Hairpin as a biosensor. Before addition of the target the dye (red) is quenched by the quencher (grey). The target binds to the blue region of the hairpin and opens the hairpin, which separates the dye and quencher from each other that no energy transfer from the dye to the quencher occurs. 6

Figure 3: Jablonski diagram illustrating transition of a fluorescence molecule, including the singlet states S_1 and S_0 and the triplet state T_1 with the corresponding vibrational levels v. Besides the radiative transitions of absorption (purple arrow), fluorescence (blue arrow) and phosphorescence (red arrow), which are depicted as continuous lines, also non-radiative transitions in waved lines like internal conversion (green arrow) and inter system crossing (orange arrow) are shown. For a better overview, not all possible transitions as well as higher singlet and triplet states are illustrated. 10

Figure 4: Schematic presentation of the Franck Condon principle. a) Transition of a molecule between to singlet states S_1 and $S_{0'}$, including the vibrational wave functions illustrated in orange. b) Absorption and fluorescence spectra of a molecule as a results of a). In both figures the absorption is purple and the fluorescence is blue. 11

Figure 5: Jablonski diagram for Förster resonance energy transfer (FRET). Similar to Figure 3 the donor dye is excited through light absorption (continuous purple arrow) to a higher singlet state ($S_{1,D}$) and the molecule relaxes back to the singlet ground state $S_{0,D}$ via emission (continuous blue arrow) after internal conversion (waved green arrow). If another dye (acceptor) is in close proximity to the first dye (donor) an additional path is possible. Via non-radiative energy transfer the acceptor can get excited (continuous orange arrow) during the relaxation of the donor (waved turquois arrow). The excited acceptor ($S_{1,A}$) after internal conversion can relax radiatively (continuous red arrow) to the singlet ground state ($S_{0,A}$). For a better overview not all possible transitions as well as higher singlet states and vibrational levels are illustrated. 12

Figure 6: FRET requirements. a) Top: Angles to determine κ^2. Button: Example orientations of acceptor (red) and donor dipoles (blue) including the corresponding κ^2 values, a free rotating dye pair has a κ^2 of 2/3. b) Donor emission (blue) and acceptor absorption spectra (red) including the overlap integral J (orange) are illustrated. Here Atto542 is chosen as a donor and Atto647N as an acceptor were chosen. c) Distance dependence of the FRET efficiency for the FRET pair described in b) is shown with an r_0 of 5.5 nm. 13

Figure 7: a) Chemical structure of sp^2-hybridized carbon lattice graphene. b) Jablonski diagram of a fluorophore close to the graphene surface (< 40 nm). The excited electron can not only relax back to the ground state S_0 via radiative emission (straight blue) also a relaxation via non-radiative energy transfer (waved turquois arrow) known as graphene energy transfer (GET) can occur. In case of GET an electron from the valence band (VB) of the graphene is excited (orange arrow) to the conduction band (CB) and relaxes back to the VB (red arrow). c) Illustration of the GET efficiency η against the distance d. Besides the measured distance dependence of Atto542 with a d_0 of 17.7 nm (blue) also the theoretical calculations of the same fluorophore with perpendicular (red) of parallel (purple) orientation of the dipole based on equation 2.7 are shown. 15

Figure 8: a) Interaction of a spherical gold nanoparticle with the electromagnetic field of light. The light displaces the electrons (blue) in the NP from the nucleus. A counterforce (gray arrow) from the positively charged nucleus (salmon) is replacing the electrons back to its starting position. b) The collective oscillation of the electrons is creating an electric field which can interact with the dyes in close proximity to the NP. The dashed line illustrates the orientation of the electrical component of light (modified from [111]). 16

Figure 9: Jablonski diagram for ROXS. Besides the already explained transition to the S_1 and from the S_1 to the T_1 (Figure 3), the transitions for ROXS are pictured. In presence of ROXS the molecule can get reduced (waved turquois) and afterwards oxidized (waved gray) via a radical anion state (F^{*-}) or vice versa over a radical cation state (F^{*+}). 19

Figure 10: Chemical agents for the stabilization of fluorophores. a) Ageing from trolox to trolox quinone under UV radiation. b) Chemical reaction of the oxygen scavenging system glucose oxidase (GOD), catalase (Cat) and glucose with oxygen. GOD oxidizes glucose to glucono lactone under the production of H_2O_2. The product H_2O_2 is converted to water and oxygen in presence of Cat. c) In the oxygen scavenging system protocatechuic acid (PCA) and protocatechuate decarboxylase the PCA is transformed to beta-carboxy –cis,cis-muconate (CM). 20

Figure 11: Illustration of the DNA double helix including the gray phosphate deoxyribose backbone with the color coded base pairs. The complimentary oligonucleotides cytosine (purple) and guanine (green) as well as adenine (orange) and thymine (blue) form hydrogen bonds. The inset shows the chemical structures of the base pairs. For a better overview not all valence electrons are shown. 21

Figure 12:Illustration of the DNA origami structure folding process. To a scaffold (blue) an excess of up to 200 staple strands (gray) is added in a buffered environment, heated up and slowly cooled down (a). The correct folding can be observed with AFM. The DNA origami structure is modified with strands protruding from the DNA origami structure to externally bind a Hfq molecule (from methanocaldococcus jannaschii) which is illustrated as a white dot in the

center of the rectangular DNA origami structure (b) (scalebar: 50nm, Reproduced from [134] with permission from the Royal Society of Chemistry). 22
Figure 13: Exemplary two-color confocal microscope (a)) with illustration of time correlation single photon counting (TCSPC) (b)). Every detected arrival time is summed up into an decay (b) lower panel). 23
Figure 14: Laser path of a wide-field microscope operating in epi fluorescence (a)) and TIRF (b)) with detailed illustration of TIRF in c). Furthermore, the decaying fluorescence intensity ratio (I/I_0) along the distance d is shown in c), calculated from Eq. 3.2. Epi fluorescence is penetrating the whole sample while the evanescence field of TIRF decays after a few hundred nanometers. 25
Figure 15: Illustration of the Abbe limit and DNA-PAINT. Two dyes (orange Gaussian) won´t be distinguishable as different light sources when those are limited by the Abbé criterion, leading to the observation of only one elliptical light source (blue Gaussian; (a))). To circumvent the Abbe limitation both dyes have to blink independently from each other (gray: dark fluorophore, b)). Finally, instead of observing one elliptical spot it is possible to detect the single fluorophores. After detecting multiple blinking events and fitting the spots a super-resolution image can be generated (c), scalebar: 30 nm). One way to make the molecules blink is the DNA-PAINT technique. Here oligonucleotides labeled with dyes are transiently binding to the structure of interest (d)). The fluctuation of “off” (unbinding, gray) and “on” (binding, orange) is shown in the intensity transient (e)). 26
Figure 16: a) Operation principle of an atomic force microscope (AFM) including laser, cantilever and SPD (segmented photo diode)with lateral (blue double headed arrow) and vertical detection (green double headed arrow). b) AFM image of the DNA origami structure. 28
Figure 17: a) Rectangular DNA origami structure immobilized on a glass surface (for a better overview BSA-biotin and neutrAvidin are not illustrated). FRET pair (Atto542/Atto647N) is located underneath the spherical gold NP. b) Illustration of the acceptor bleaching approach: The background colors indicate the excitation laser (green: 532 nm, red: 640 nm). First fluorescence from the green dye (green) and FRET (orange) occurs afterwards the red dye (red) is bleached and in the finale step the green dye is bleached. c) The results demonstrated that with increasing NP diameter the FRET efficiency E decreases while the FRET rate constant k_{ET} stays constant. (both quantities are normalized to corresponding data without any NP). 30
Figure 18: a) Illustration of the three different DNA origami structures investigated in GET studies. b) Distance dependence between graphene and dye with the designed GET distance on top of the graph. The data points from Atto542 (green hollow circle with standard errors) are fitted with the green curve to obtain d_0 (orange). Also the calculated curves for parallel (purple) and perpendicular (purple) oriented dipoles are shown. 31

Figure 19: DNA origami structures for GET applications. a) Multiple possible binding geometries of the L-shaped DNA origami structure to graphene due to additional π-π stacking of the helices. b) Dynamic investigations and a bioassay was realized by adding a tether the L-shaped DNA origami structure. c) As a biosensing assay a dye is more quenched by graphene and after binding of the target strand a higher binding site is accessible (right part of c)). d) For FRET measurements a dynamic DNA origami structure which can transiently bind to two binding sites at different heights. e) The cubic DNA origami structure contains different binding sites only 2.7 nm apart for super-resolution imaging of the z-distance with DNA-PAINT. f) Tracking of a dye was realized by equipping the L-shaped DNA origami structure with three different binding sites. 34

Figure 20: Outlook for FRET samples close to a spherical plasmonic NP. a) Based on the extracted FRET efficiencies the shifted distance dependence in presence of a 20 nm Au NP is calculated. The distance dependence can be proven by designing DNA origami structures with a constant distance between donor and NP surface ($d_{D\text{-}NP}$) and varying the distance between donor and acceptor r (b)). 37

Figure 21: Adapting the L-shaped DNA origami design. a) Illustration of the established L-shaped DNA origami structure with the π-system of the helices highlighted in light blue. b) Improved L-shaped DNA origami structure “L2” with 90° kink (light red), helical π-System (light blue) and uneven helical edges which should enhance the correct standing of the DNA origami structure. The side view and the view from the bottom(c)) are shown. For better overview not all π-systems are highlighted. 38

Figure 22: Jablonski diagram of undoped (a)) and p-doped graphene (b)). In case of the undoped graphene an electron from graphene is excited from the VB to the CB (orange arrow) and decays back to the VB (red arrow) after excited from a dye in close proximity (waved torques arrow). The contacting of graphene with a negative voltage yields in a removing of the electron in the VB of graphene. When the applied voltage is large enough the energy transfer from the donor dye is too low to excited an electron from the VB to the CB. Measurements with and without voltage make it possible to implemented graphene as a switchable acceptor. 40

Figure 23: Expanding the distance dependence of GET. a) Calculations of multilayers show a minor increase of d_0 and the working range from monolayer (blue) to pentalayer (green). b) Illustration of GET (blue), SIMPLER (light orange, light green) and the combination of both (orange, green). As both methods are contrary to each other a fluorescence intensity value shows ambiguity in height as it can belong to two different distances. When a measurement m_1 (θ = 69°, light orange, orange) is performed and a fluorescence intensity of 25% relative to the maximum fluorescence intensity is measured this could either be a height of 8 nm or 145 nm. A second measurement m_2 with a different TIRF angle θ (65°, light green, green) delivers a relative fluorescence intensity of 37%, which gives an unambiguous result for distance d_1 of 145 nm. 41

10. Table of Abbreviations

abbreviation	meaning
A	adenine
AA	ascorbic acid
AFM	atomic force microscopy
APD	avalanche photo diode
BSA	bovine serum albumin
C	cytosine
CB	conduction band
CM	beta-carboxy-cis,cis-muconate
COT	cyclooctatetraene
DC	dichroic mirror
DNA	deoxyribonucleic acid
ds	double stranded
dSTORM	direct stochastical optical reconstruction microscopy
EMCCD	electron multiplying charged coupled device
Eq.	equiation
FIFI	flat Illumination for field independent imaging
FLIM	fluorescence lifetime imaging
FRET	Förster resonance energy transfer
FWHW	full width half maximum
G	guanine
GET	graphene energy transfer
GOD	glucose oxidase
GPET	graphene plasmon energy transfer
GSD	ground state depletion)
LSPR	localized surface plasmon resonance
L	lens
MINFLUX	minimal photon flux
MV	methylviologen
NA	numerical aperture
NP	nanoparticle
OSS	oxygen scavenging system
P	pinhole
PAINT	points accumulation for imaging in nanoscale topography
PALM	photoactivated localization microscopy
PCA	protocatechuic acid
PCD	protocatechuate decarboxylase

Table of Abbreviations

abbreviation	meaning
PSF	point spread function
ROI	region of interest
ROXS	reducing and oxidizing system
SEM	scanning electron microscope).
SIMPLER	Supercritical Illumination Microscopy Photometric z-Localization with Enhanced Resolution
SPD	segmented photo diode
ss	single stranded
STED	stimulated emission depletion
T	thymine
TCSPC	time correlated single photon counting
TEM	transmission electron microscope
TIRF	total internal reflection fluorescence
TQ	trolox quinone
TX	trolox
VB	valence band
ZMW	zero mode waveguides

11. Acknowledgement

At this point I would like to thank everyone, who supported me the last years and make this work possible.

First I would like to thank Philip for the outstanding working environment, always looking for high impact in the data and pushing the resolution to the limit. Furthermore, I would like to thank him for the scientific discussions we had and the possibility to work on different cooperation projects.

I would like to thank Don for showing me a world beyond DNA origami structures and for not being afraid to combine DNA origami structures with three color FRET.

I would like to thank to Ralf Jungmann, Achim Hartschuh, Hermann Gaub and Oliver Trapp, who took their time to read this work.

Thanks to Guillermo for the whole scientific input on NPs and FRET and making me aware of how important Super Block is.

I would also like to thank Izabela for always coming up with new ideas on how to use GET on the single-molecule level and being super optimistic, when it comes down to tackle the next graphene crisis.

Thanks to the old Braunschweig guys: Mario, Ija, Enrico and Bettina. Thanks to Enrico for all the relationship advices regrading Enrica. Special thanks goes to Mario for the introduction and implementation of the schmiedschen Tiefpassfilter. Thanks to Ija for making me laugh on the daily basis.

I also have to thank the “informal discussion group”: Tim, Jonas, Mario, Stephan, Lars, Kristina, Kateryna, Frank and Evelyn for way too much beer events.

Thanks to Tim and Jonas for the outstanding scientific input and listening to my trash talk. Thanks to Tim for convincing me that every problem can be solved by bouldering and thanks to Jonas for not being a biologist.

I also would like to thank all cooperation partners: The whole team from the Enderlein group, especially Jörg and Roman, for combing MIET with DNA-PAINT. Thanks to PTB-Flo for electrical tapping of the DNA origami structures and the Stefani group for the p-Minflux. Thanks to Lars, Fabian, Frank and Evelyn for the whole investigation on multilayer graphene. I would also like to thank the Piehler group (Lara and Chang) for the scientific curiosity to find the real d_0 of GET. Thanks to Sarah and Jonas from the Stigler group as well as Michi for highlighting the last month of my PhD time with biological samples under the AFM. It is always nice to discuss results with someone from a different field.

Acknowledgement

Thanks to Fiona and Jonas for pushing the clock idea to the next level, I cannot tell how much this means to me. I hope that Jonas will succeed to combine PEI on the clock with the help of Benjamin. Fingers crossed that Fiona and Martina together with Michele will manage to make one binding site EDC-switchable. However, even from your unpublished data and the thousand ideas you have in your mind I know that you will succeed. In this context I also would like to thank Simon, Pooyeh, Frank, Evelyn and Don for the whole three color clock experiments and this cool AI.

I would also like to thank the people, who moved from Braunschweig to München, for the whole cocktail Fridays. Thanks to Sarah, Kateryna, Ija, Mario, Carsten, Tim, Kristina, Andres, NP-Flo. and Lennart.

Furthermore, I would like to thank Kristina, Jonas, Lars and Laser-Flo for proof reading of this work.

Thanks to all other highly skilled people I worked with during the last 5+ years and didn't mention so far: Viktorija, Alan, Lorena, Julian, Ece, Cindy, Patrick, Renukka, Melanie, Karina, Monique and Luna.

I would like to thank the permanent employees like Frau Talk and Sabine as well as Angelika, Herr Ehrl, Frau Steger and Frau Lipfert who are keeping the show running.

Thanks to the whole working group for the social events like hiking, drinking, eating and using the moon as a laser, you rock.

Thanks to my family who weren´t that excited when I told them that I was going to München, but still were super supportive.

Thanks to Kristina for the last 10 years, especially the last 8, for always motivating me and for all the trips I always wanted to make and you organized. Hopefully we will have many more trips and years.